Loughborough University

This item was submitted to Loughborough University as a PhD thesis by the author and is made available in the Institutional Repository (https://dspace.lboro.ac.uk/) under the following Creative Commons Licence conditions.

creative commons

COMMONS DEED

Attribution-NonCommercial-NoDerivs 2.5

You are free:

- to copy, distribute, display, and perform the work

Under the following conditions:

Attribution. You must attribute the work in the manner specified by the author or licensor.

Noncommercial. You may not use this work for commercial purposes.

No Derivative Works. You may not alter, transform, or build upon this work.

- For any reuse or distribution, you must make clear to others the license terms of this work.
- Any of these conditions can be waived if you get permission from the copyright holder.

Your fair use and other rights are in no way affected by the above.

This is a human-readable summary of the Legal Code (the full license).

Disclaimer

For the full text of this licence, please go to:
http://creativecommons.org/licenses/by-nc-nd/2.5/

BLDSC no.:- DX 92758

LOUGHBOROUGH
UNIVERSITY OF TECHNOLOGY
LIBRARY

AUTHOR/FILING TITLE

JASSIM, I K

ACCESSION/COPY NO.

03424402

VOL. NO. | CLASS MARK

LOAN COPY

25 MAY 1994

LB 0034244026

MAGNETIC AND LATTICE INTERACTION IN 3D TRANSITION METAL COMPOUNDS

by

ISHMAEEL KHALIL JASSIM
M.Sc. Kent, United Kingdom

A Doctoral Thesis submitted in partial fulfilment of the requirements for the award of Doctor of Philosophy of the Loughborough University of Technology

September 1990

Supervisor: Professor Kurt Ziebeck
Head of Department of Physics
Loughborough University of Technology

© by Ishmaeel Khalil Jassim 1990

Loughborough University
of Technology Library
Date Dec 90
Class
Acc No. 03424402

99908833

Name: Ishmaeel Khalil Jassim

Date of Birth: 1.7.1956 Iraq, Baghdad

1976 – 1980 B.Sc Physics Department, Mosul University, Iraq.

1980 – 1984 Physics Teacher, Falluja–Al–Anbbar, Iraq.

1985 – 1987 M.Sc Physics Department , University of Kent, Canterbury, United Kingdom.
(Molecular motion in Ionic Crystals using NMR technique).

1987 – 1990 Ph.D. Physics Department, University of Technology, Loughborough, United Kingdom.
(Magnetic and Lattice Interaction in 3D Transition Metal Compounds)

For my mother who gave me the gift of life, who wept for my sorrows and rejoiced in my achievement; who was, is, and ever will be, my greatest supporter in my travels and throughout my life.

CONTENTS

Page No.

ABSTRACT

ACKNOWLEDGEMENTS

CHAPTER 1 INTRODUCTION [1]

1.1 Scope [4]

CHAPTER 2 REVIEW OF MAGNETISM AND LATTICE DYNAMICS [6]

2.1 Transition Metal Magnetism [6]

2.1.1 Magnetic moment of free atoms [7]
2.1.2 Localised magnetic moment and Weiss theory of ferromagnetism [8]
2.1.3 The Stoner model for itinerant electrons [10]
2.1.4 Finite temperature and excitation mechanisms [12]
2.1.5 Instability at the $(\gamma - \alpha)$ transition in $Fe_x - Ni_{1-x}$ [13]

2.2 Interaction between Magnetic and Lattice Degrees of Freedom [14]

2.2.1 The effect of magnetism on phonon frequencies in FeNi Invar [16]
2.2.2 Elastic constants [17]
2.2.3 Specific heat contributions [20]
2.2.4 Magnetic contribution to elastic constants [21]
2.2.5 Magnetic entropy [22]
2.2.6 Vibrational modes of a monatomic lattice [23]
2.2.7 Phonons and Magnons [24]

CHAPTER 3 NEUTRON SCATTERING THEORY [27]

3.1 Introduction [27]

3.2 Neutron scattering cross section [27]

3.3 Spin dependent interactions [29]

3.4 Coherent and Incoherent scattering amplitudes [30]

3.5 Neutron scattering by phonons [32]

3.6 Polarised Neutrons [34]

3.6.1 Introduction [34]
3.6.2 Elastic coherent scattering [35]
3.6.3 Inelastic coherent scattering [36]
3.6.4 Magneto–vibrational scattering [37]

CHAPTER 4 EXPERIMENTAL TECHNIQUES AND EQUIPMENT [38]

4.1 Alloy preparation [38]
4.2 X–ray diffraction [38]

4.3 Neutron scattering measurements [39]

4.3.1 Neutron diffraction and structural refinements [39]
4.3.2 Inelastic neutron scattering [43]
4.3.3 Production of a polarised monochromator beam [44]
4.3.4 Half wavelength contamination in the polarised incident beam [47]
4.3.5 Measuring phonon dispersion relations [47]

4.4 Magnetic Measurements [48]

4.4.1 Automation of Magnetic susceptibility measurements [50]

4.5 Specific Heat Measurements [51]

4.5.1 The Differential Scanning Calorimeter (DSC) [51]
4.5.2 Pulse heating technique [51]

CHAPTER 5 A REVIEW OF THE VARIOUS ORDERING SCHEMES FOUND IN MAGNETIC COMPOUNDS [53]

5.1 Structure Factor of Heusler [53]

5.2 The structure of the Fe_xNi_{1-x} alloys [54]

5.3 Antiferromagnetism of the fcc lattice [55]

5.4 Magnetic Structure determination to various magnetic modes [56]

5.5 Application of molecular field theory to various magnetic models [57]

5.6 Frustration on antiferromagnetic fcc lattice [59]

5.7 Antiferromagnetism in Fe–Ni Invar [60]

CHAPTER 6 EXPERIMENTAL RESULTS – $Pd_{2-x}Ag_xMnIn$ [62]

6.1 Introduction [62]

6.2 $Pd_{1.8}Ag_{0.2}MnIn$ [63]

6.3 $Pd_{1.6}Ag_{0.4}MnIn$ [68]

6.4 $Pd_{1.4}Ag_{0.6}MnIn$ [70]

6.5 $Pd_{1.2}Ag_{0.8}MnIn$ [72]

CHAPTER 7 EXPERIMENTAL RESULTS – $Pd_{2-x}Au_xMnIn$ [75]

7.1 Introduction [75]

7.2 $Pd_{1.8}Au_{0.2}MnIn$ [76]

7.3 $Pd_{1.6}Au_{0.4}MnIn$ [80]

7.4 $Pd_{1.4}Au_{0.6}MnIn$ [82]

7.5 $Pd_{1.2}Au_{0.8}MnIn$ [86]

7.6 PdAuMnIn [88]

7.7 $Pd_{0.8}Au_{1.2}MnIn$ [89]

7.8 $Pd_{2-x}Au_xMnIn$ $(1{\cdot}4 \leq x \leq 2)$ [92]

CHAPTER 8 DISCUSSION AND CONCLUSIONS [94]

8.1 Introduction [94]

8.2 Discussion [94]

8.3 Conclusion [100]

CHAPTER 9 DYNAMIC FORM FACTOR IN THE INVAR ALLOY $Fe_{65}Ni_{35}$

9.1 Introduction [107]

9.2 Inelastic Measurements [108]

9.2.1 The [111] and [001] directions [110]
9.2.2 The [100] direction [112]
9.2.3 The [110] direction [114]
9.2.4 Temperature dependence [114]
9.2.5 Polarisation dependence [117]

9.3 Specific heat measurements [117]

9.4 Elastic constants determination [117]

9.5 Discussions and Conclusions. [119]

References

Publication

ABSTRACT

MAGNETIC AND LATTICE INTERACTION IN 3D TRANSITION METAL COMPOUNDS

The importance and nature of magnetic and lattice degrees of freedom and their interaction in transition metal magnets has been investigated

Two different alloy systems in which the magnetic 3d electrons either had localised or itinerant characteristics were chosen. As an example of localised behaviour, Heusler alloys in which the magnetic moment was confined to Mn atoms were chosen, e.g. Pd_2MnIn. The manganese atoms are separated by more than 4.6Å These materials provide a good approximation to a Heisenberg system, having long–range interactions. By systematically changing Pd for either Ag or Au the electron concentration can be varied in a continuous manner. Dependent upon the electron concentration several different antiferromagnetic structures consistent with an fcc lattice are observed at low temperatures. The type of magnetic order gives rise to distinct lattice distortion characteristic of the magnetic symmetry. High resolution powder neutron diffraction was used to investigate the dependence of the lattice distortion on the magnetic structure as a function of temperature.

A wide range of bulk measurements were carried out to characterise the materials, e.g. X–ray, neutron diffraction, magnetic susceptibility and specific heat (using both pulse and continuous heating techniques). From these measurements it was revealed that the magnetic structures were, in some instances, frustrated as may be expected for antiferromagnetism on an fcc lattice. The results are discussed on the basis of current models.

As an example of itinerant behaviour the Fe–Ni system was chosen. Fe_{1-x} Ni_x alloy systems have long been of considerable interest since $Fe_{65}Ni_{35}$ shows an anomalously small thermal expansion below T_c. Numerous experiments have been carried out to understand this phenomenon, which has come to be known as the Invar effect. The effect is most pronounced close to the composition defining the phase boundary between the bcc and fcc structures. Thus the interplay between the magnetic and lattice

degrees of freedom are of great importance, and so were investigated on an atomic scale using inelastic polarised neutron scattering.

In this study, the polarisation dependence of the magneto vibrational scattering of the one phonon cross–sections have been investigated as a continuous function of $\underline{q}$ throughout the Brillouin zone in the Invar alloy $Fe_{65}Ni_{35}$, and in two other FeNi samples outside the Invar region. The results show that the magneto vibrational scattering is strongly dependent on the energy and wave vector of the phonon, indicating that the effective magnetic moments are reduced as the phonon energy increases.The results also show the presence of a "forbidden" phonon mode propagating in the [001] direction. From the nature of the dispersion the "forbidden" mode was identified as being the transverse [001] phonon, the observation being made possibly by strong coupling of the two degrees of freedom. Possible mechanisms are proposed to account for this observation.

ACKNOWLEDGEMENTS

This thesis describes work carried out in the laboratory of the Department of Physics, University of Technology, Loughborough, United Kingdom, and the Institut Laue–Langevin, Grenoble, France, between 1987 and 1990.

I am indebted to the staff and director of both laboratories for supporting me to complete my project throughout this period. I should like to express my gratitude to my country, Iraq, for the scholarship award which enabled me to undertake this work.

At the Department of Physics, Loughborough University, first and foremost I would like to thank above all, my research supervisor Professor Kurt Ziebeck, for his guidance and encouragement throughout the course of this work, the stimulating discussions and through every stage of my work. He has contributed greatly to my interest in, and knowledge of, the field of Neutron Scattering and Magnetism.

All the experiments at ILL, Grenoble, France on Fe–Ni alloys were performed in collaboration with Professor Jane Brown whose comments and ideas have been greatly appreciated and I would like to express my deepest gratitude for her assistance with the experiments and contribution to many valuable discussions.

I am grateful to Dr Klaus Neumann for his assistance with several of the computer programs and for his guidance and friendship over the last three years. Thanks are also certainly due to Dr Dick Visser for his continuing help and sincere cooperation.

In addition I would like also to thank my friends and colleagues, Professor Herbert Capellmann, Dr David Williams, Dr John Samson and Dr Gerry Swallowe, for numerous useful discussions, guidance and encouragement.

I extend my thanks to all my friends at the University of Technology, Loughborough, particularly Iraqi students for their contribution in various forms throughout my stay in the United Kingdom.

Thanks also go to Miss Debby Smith for her friendship and assistance in variable cases.

I would also like to thank my wife Lamyaa who showed great patience and encouraged me throughout the period of my research and , of course, to my son Ali who deserves a special mention because for me he is a source of comfort and joy.

Finally, I should like to thank Mrs Carole Ann Torr in the Mathematical Sciences Department, University of Technology, Loughborough, for her help in the typing of this thesis.

All this work described here is my own. This thesis has not been submitted to any other university.

CHAPTER ONE

INTRODUCTION

Transition metal compounds provide good systems for studying 3d magnetism. By suitable choice of compounds it is possible to investigate localised 3d magnetism (Heisenberg model) as well as itinerant electron magnetism (band model) in metals.

Band theory accounts for the ground state properties of metallic systems, in particular their non–integral magnetic moments. In this model exchange interactions between Bloch states give rise to an inbalance of up and down spins thus producing a nett moment. However, band theory is less successful at finite temperatures, particularly in accounting for the thermal variation of the bulk susceptibility. The strong thermal variations of many physical properties are easier to describe using a localised model. Consequently, the inclusion of many body effects are required to account for these observations.

In localised magnetism, well–localised electron wave functions give rise to localised magnetic moments. The magnetism can then be discussed by concentrating on the magnetic degrees of freedom alone, i.e. via a Heisenberg Hamiltonian. For itinerant magnets, however, the possibility of the electrons to move around relatively freely through the crystal lattice means their wave functions are delocalised and thus their translational degrees of freedom cannot be separated from their magnetic degrees of freedom alone, making a Heisenberg description inadequate. The delocalised wave functions for the 3d type electrons are characterised by a band structure with bandwidth W, which for the 3d electrons (which carry the magnetism) is typically of order W = 5ev. The degree of itinerancy is measured by the band width W and therefore the degree of overlap of the d wave functions. This may be controlled by choosing specimen in which the separation of the magnetic atoms are different or can be systematically varied, the radial extent of 3d functions is typically of the order 1–2Å.

The magnetic and lattice degrees of freedom are closely related in magnetic materials through several properties such as volume, structure, and elasticity in transition metal compounds. These effects arise from the interatomic cohesive forces through the exchange interaction.

In order to understand the nature of magnetic and lattice interactions, two different systems of the 3d electrons, itinerant or localised, have been chosen.

We have selected Heusler alloys as typical materials with localised 3d moments. This is because the magnetic atoms are separated by more than 4·6Å. In the alloy series chosen the magnetic moment is large ~ $4\mu_B$ and confined to the Mn atoms. Heusler alloys with the chemical formula X_2MnY are ordered 3d transition metal compounds with the cubic $L2_1$ type structure. The Mn atoms lie on an fcc sublattice, and each Mn atom has eight X atoms as nearest neighbours which form a simple cubic sublattice. The X atoms are either a noble metal or a transition metal with a nearly full outer d shell. The Y atoms are non–transition metal atoms, normally from one of the B subgroups 3, 4, or 5. These Heusler alloys containing manganese are valuable in understanding magnetism and also provide an ideal test for investigating the long range exchange interaction in 3d metals. Additionally, the effects of immediate neighbours, average electron concentrations and lattice parameter changes can be investigated.

Several theoretical models have been proposed to account for long–range exchange interactions in 3d metals and the magnetic properties of the Heusler alloys. Spin wave measurements [1] have shown that the long range magnetic interactions in Heusler alloys have an oscillatory nature of the RKKY type or the double resonance type proposed by Caroli and Blandin [2]. By Fourier transformation of the magnon dispersion curves, the Mn–Mn exchange interaction J(r) can be obtained. This was carried out for Pd_2MnSn and Ni_2MnSn by Ishikawa and Noda (1974) [3], who found that J(r) changed both in magnitude and sign as a function or r.

In the present thesis, two new series of intermetallic compounds with compositions $Pd_{2-x}Ag_xMnIn$ and $Pd_{2-x}Au_xMnIn$ for $0 \leq x \leq 2$ have been investigated. A large amount of work has been devoted to determining the magnetic structure and thermal properties of compounds in this series.

Preliminary structural information including lattice parameters were determined from X–ray and neutron diffraction measurements. Specific heat measurements were designed to provide information relating to the magnetic entropy and to establish ordering temperatures. Susceptibility measurements have been made, and the extent and type of long range chemical and magnetic order has been determined from neutron diffraction measurements. A temperature dependent lattice distortion is also observed in some Heusler alloys which order antiferromagnetically. This is due to the magnetostriction which arises from the coupling between the crystalline lattice and the atomic moments. The results provide us with experimental support that the magnetic properties of the metallic system with localised moments can be analysed in terms of the Heisenberg model.

As an example of itinerant behaviour we have selected the $Fe_{1-x}Ni_x$ alloy system with x = 22, 35, 50. The most interesting of these compounds $Fe_{65}Ni_{35}$ has an anomalously small thermal expansion below the Curie temperature. This phenomenon is known as the Invar effect and has been studied extensively. It is in fact one of the most important problems of the 3d magnetism at finite temperatures. These Invar characteristics are closely related to the magnetic anomalies such as deviation of the magnetic moment from the Slater–Pauling curve with increasing Fe concentration [4], large volume magnetostriction [5], the large pressure dependence of the Curie [6] temperature and the enhancement of the high field susceptibility [7]. All these properties suggest that the Invar effect is associated with the nature of the 3d magnetism. The $Fe_{1-x}Ni_x$ system is also of fundamental importance from the structure point of view since Ni has a fcc structure and Fe is bcc. The bcc phase occurs below ~ 33 at % Ni and does not exhibit the Invar effect. In the concentration range 10 to 70% Ni there is a mixed phase ($\alpha + \gamma$) region. The magnetic excitations in the Invar alloy consist of well defined spin waves up to an energy transfer of 80 meV, the spin wave disperion is well described by [114]

$$\hbar w = Dq^2(1 - \beta q^2) \text{ with } D = 143 \text{ meV}\text{Å}^2 \text{ and } \beta = 0{\cdot}12\text{Å}^2.$$

The magnon line width was found [115] to be significantly greater than those or normal ferromagnets and to increase linearly with q^2. The fact that such damping is not shown

by the non–Invar alloy $Fe_{50}Ni_{50}$ suggests that it is characteristic of the Invar effect, it's q dependence shows that it is not due to magnon–magnon interaction. The temperature variation of the magnetisation calculated from the magnon dispersion and intensities does not completely account for the temperature decrease in the bulk magnetisation. To account for these descrepancies a "hidden" mode was suggested [115], this mode should have a quadratic dispersion $\hbar\omega q \simeq Dq^2$ with $D \sim 85$ meVÅ^2.

Various models have been proposed to explain the Invar effect, and include latent antiferromagnetism, which is believed to be characteristic of fcc iron, or the collapse of the local moment, etc. Ultrasonic measurements on $Fe_{65}Ni_{35}$ reveal that the shear constants $\frac{1}{2}(C_{11} - C_{12})$ and C_{44} decrease below the Curie temperature [8]. On the basis of the bulk measurements, it may be concluded that a coupling of magnetisation to the lattice is essential for the Invar effect. Neutron scattering therefore provides a unique possibility of studying the temporal and spatial variation of the lattice and magnetic degrees of freedom and their possible interaction. Polarised neutron measurements on $Fe_{65}Ni_{35}$, $Fe_{50}Ni_{50}$ and $Fe_{78}Ni_{22}$ are discussed. In our study, magneto–vibrational scattering has been investigated through the polarisation dependence in the $Fe_{65}Ni_{35}$ Invar alloy. The results show the presence of a "forbidden" phonon mode which is closely related to the Invar effect. This anomaly occurs due to a strong interaction of the lattice and magnetic degrees of freedom.

1.1 SCOPE

The magnetic and lattice interactions in metal compounds is the main topic of the thesis. It was decided to perform extensive studies on two different types of 3d transition metal alloys. One is the Heusler alloy system and the other is the $Fe_{1-x}Ni_x$ alloys.

Chapter 2 includes a brief discussion of excitation mechanisms, magnetic and lattice interaction, elastic constants, and vibrational modes.

The theoretical work that provides the background for the neutron scattering is reported in Chapter 3.

Chapter 4 is concerned with the various experimental techniques used in this work. It includes a description of the principles of the new polarised neutron triple axis spectrometer IN20 and other diffractometers such as D1A and D2B which are used at the Institut Laue–Langevin, Grenoble, France. This chapter also includes a description of the principles and apparatus used for magnetic susceptibility, specific heat and X–ray measurements.

In Chapter 5 a review of the various types of magnetic order is presented.

In Chapters 6 and 7 the results obtained for the two series of intermetallic compounds formed at the compositions $Pd_{2-x}Ag_xMnIn$ and $Pd_{2-x}Au_xMnIn$, where $0 \leq x \leq 2$, are presented.

In Chapter 8, the discussion and conclusions for the results of chapters 6 and 7 are given. The results and discussion study of the dynamic form factor in $Fe_{1-x}Ni_x$ alloys, are presented in chapter 9

CHAPTER TWO

REVIEW OF MAGNETISM AND LATTICE DYNAMICS

2.1 TRANSITION METAL MAGNETISM

Elements in the 3d transition metal series have been the subject of intensive studies for many years. The magnetic behaviour of this series is to a large extent governed by the electrons of the 3d band. With increasing atomic number, the elements progress from those with a nonmagnetic ground state (Sc, Ti, V) via the antiferromagnets Cr and Mn to the ferromagnets Fe, Co and Ni. The 3d electrons which give rise to the magnetic properties of these transition metals lie at the Fermi surface [116] and are therefore free to move through the metal. This electron itinerancy distinguishes the magnetism of the 3d metals and their magnetic alloys from the localised magnetism of the transition metal insulating compounds, where the magnetic moments are due to the electrons with highly localised wavefunctions lying well below the Fermi surface. A good description of the ground state properties of itinerant ferromagnets is given by the band model of magnetism based on the local density functional theory of Hohenberg, et al [117] which correctly predicts ferro–magnetism in Fe,Co and Ni and yields the observed non–integral magnetic moments.

At finite temperatures the Stoner model predicts a transition to the paramagnetic state via the thermal repopulation of one–electron states. At the Curie temperature T_C, a Stoner ferromagnetic should resemble an exchange enhanced Pauli paramagnet.

A general theory of spin fluctuations, in an attempt to produce a unified model for transition metal magnetism, has been presented by Moriya [118]. In

Moriya's model the temperature dependence of the longitudinal component of the spin fluctuations causes the susceptibility of a weakly ferromagnetic system above T_c to follow a Curie–Weiss law.

The ferromagnetism of iron, nickel and their alloys is thought to arise from 3d electrons which are not strictly localised (see for example: Herring 1966 [16]). This "itinerant electron" approach involves correlated fluctuations in the 3d shell configurations of each atom. Thus the average saturation moment per atom may be a non–integral number of Bohr magnetons. The saturation moments of the 3d series is thought to be largely due to electron spin or the 3d series.

The behaviour of an itinerant magnetic system in the paramagnetic state became a controversial topic since Mook et al [11] and Lynn [12] reported the existence of spin wave excitations in Ni and Fe above Curie temperature, T_c. The excitations were observed in neutron inelastic scattering studies performed using a triple–axis spectrometer. The reported observation of spin waves above T_c and the paramagnetic diffuse neutron scattering data of Deportes et al [14] and Brown et al [13] provide the experimental evidence for short–range magnetic order (SRMO) above T_c.

In the fluctuating band theory Prange and Korenman [119], (Capellmann [17], Sokolloff [18]) transverse fluctuations, i.e. fluctuations of the direction of the moment, are responsible for destruction of large range magnetic order (LRMO). Capellmann [17, 19] has obtained a value of T_c = 1050K for Fe which is very close to the measured value of 1044K. Also he used his theory to obtain a Curie–Weiss law for the uniform static susceptibility [19] and to account for spin waves with wavelengths up to the characteristic length suggested by the SRMO.

This chapter is concerned with a brief summary of fundamental concepts in the theory of Magnetism followed by a discussion of the difference in behaviour between a localised and itinerant magnetic material, and how these differences are revealed in experiments.

2.1.1 Magnetic moment of free atoms

In a simple model, magnetism can be visualised as originating from the motion of electric charges, i.e. moving electrons. Four quantum numbers, n, s, l and m_s, are required to describe the state of an electron in an atom for

a single atom. The moment formation in a free atom is determined by the way these electrons combine in an atom to produce a stable state of least energy. It is found experimentally [20] that spin–spin coupling and orbit–orbit coupling predominate, i.e. the individual spin and orbital momenta combine to form a total spin and orbital momenta, S and L respectively. S and L can be determined by applying Hund's rules. These total orbital and spin momenta then combine via Russell–Saunders coupling to give a total angular momentum J.

The magnetic moment associated with this is [20, 21]:

$$M^2 = g^2 J(J+1)\mu_B^2 \tag{2.1}$$

where g is the Lande factor given by:

$$g = 1 + \frac{J(J+1) + S(S+1) - L(L+1)}{2J(J+1)} \tag{2.2}$$

2.1.2 Localized magnetic moment and the Weiss theory of ferromagnetism

Modern theory of magnetism (Langevin) started with the concept of non–interacting local magnetic moments of fixed amplitude. By using this concept Langevin [25] (1905) derived the Curie law of magnetic susceptibility. In this model he considered a set of atomic magnetic moments each of which has fixed magnitude M, under an external magnetic field H applied along the Z direction. The statistical average of the magnetisation, parallel to the external field and its value per atom at temperature T is given by:

$$\langle M_z \rangle = \frac{\int d\Omega\, M\cos\theta \exp(MH\cos\theta)/K_B T}{\int d\Omega \exp(MH\cos\theta)/K_B T} = M\,L(Z) \tag{2.3}$$

where $M\cos\theta$ is the Z component of the magnetic moment and the integrals are over the solid angle $d\Omega$. The solution to equation (2.3) is called the Langevin function, which can be written as [20]:

$$L(Z) = \mathrm{Coth}Z - 1/Z \sim Z/3 - Z^3/45 \qquad (2.4)$$

where:

$$Z = MH/K_BT$$

By using an expansion form for L(Z), the following expression for the magnetic susceptibility is obtained:

$$\chi = N \lim_{H \to 0} <M_z>/H = NM^2/3K_BT = C/T \qquad (2.5)$$

where N is the number of atoms in the crystal and C is called the Curie constant. Subsequently, Weiss [23] (1907) introduced an interaction between the atomic magnetic moments in solids and approximated its effect by a mean molecular field which he assumed to be proportional to the average magnetisation. This is equivalent to the introduction of a term γM_Z to the external field in equation (2.3), therefore:

$$<M_Z> M L(Y)$$

where (2.6)

$$Y = M(H + \gamma <M_Z>)/K_BT$$

The solution for $<M_Z> > 0$ when $H = 0$ is the condition for ferro–magnetism and is satisfied when:

$$L(Y) = \frac{M^2\gamma}{3K_B} \text{ for } T < T_C \qquad (2.7)$$

The susceptibility above the Curie temperature is:

$$\chi = \frac{C}{T - T_C}$$

where

$$C = \frac{N g^2 \mu_B^{\ 2} J(J+1)}{3 K_B} \qquad (2{\cdot}8)$$

However, molecular field theory is purely phenomenological and so gives no indication of the origin of the internal molecular field. The idea of exchange coupling between spins of two or more atoms first appeared in the work of Heitler and London [24] (1927) on chemical bonding. These ideas were applied to ferromagnetism by Heisenberg [25] in 1928. The interaction mechanism put forward by Heisenberg was a direct exchange between atomic spins localised on atoms and is essentially an electrostatic effect and, a consequence of the Pauli exclusion principle, the Hamiltonian being:

$$H_{Heis} = \sum_{i,j} 2J_{ij} S_i S_i \qquad (2\cdot9)$$

where i, j specify atomic sites in the crystal, J_{ij} the interatomic exchange interaction is constant.

The type of coupling depends on the sign of the exchange integral J. Slater [26 (1930) derived a relation between J and the interatomic distance, d, of metals with incomplete d or f shells. J changes from a negative value at small d to positive values at large d and vanishes rapidly with increasing d.

Other forms of exchange have been proposed since Heisenberg's original paper, to account for ordered magnets in which direct exchange between well separated atoms is not possible. These include super exchange interactions in ionic solids, Anderson [27] (1950) and indirect exchange mechanisms via the conduction electrons in metallic systems, such as the RKKY interaction (Rudermann and Kittel [28]) (1954).

2.1.3 The Stoner Model for Itinerant Electrons

Although the Weiss theory was successful in being able to account for ferromagnetism via exchange interactions, when applied to the transition metal ferromagnets, iron, nickel and cobalt, it was unable to account for a moment which is a non–integral number of Bohr magnetons.

Stoner [35, 36] (1938, 1947) realised that an atomic orbital description of an electron in a metallic magnet was inadequate, and that a better description of the magnetic electrons could be obtained if they were

distributed in electronic energy bands. His model has one immediate advantage in that an electron in a band state had no orbital momentum. Stoner's basic premis was to assume that the electrons in a metal formed a free electron gas (Pauli [15] (1927)), in which the interaction was taken into account by a Weiss molecular field. The introduction of the molecular field causes the band to split into two sub–bands by an amount Δ_{ex} (called the exchange splitting).

Thus at T = 0 all the electron states within the band are occupied up to the Fermi energy, while those above are empty. There is therefore a net excess population of electrons in one sub–band (the majority band), compared with the other (the minority band), resulting in a net magnetisation as shown in Fig (2.1).

As in the theory of Weiss [23] (1907), Stoner assumed the molecular field to be proportional to the magnetisation of the sample (i.e. to the difference in the number of electrons in the two sub–bands $n_+ - n_-$):

$$\gamma M = \gamma (n_+ - n_-) \mu_B \tag{2.10}$$

where γ is the molecular field constant. Thus the exchange splitting Δ_{ex} is given by:

$$\Delta_{ex} = E_\uparrow - E_\downarrow = -\frac{1}{2}\gamma(n_+ - n_-) = Im \tag{2.11}$$

where I is the Stoner parameter. By considering a state with magnetic moment m and density of states per spin at the Fermi level $N(E_F)$, m can related to the exchange splitting by:

$$m = \Delta N(E_F) \tag{2.12}$$

The total energy of the system with magnetic moment m is given by:

$$U_{fm} = U_{pm} + m/2\,[m/2NaN(E_F)] - Im^2/4Na \tag{2.13}$$

where U_{fm}, U_{pm} are the energy of the ferromagnet and paramagnetic states respectively. Thus the ferromagnetic state is stable if:

$$IN(E_F) > 1 \tag{2.14}$$

which is the famous Stoner criterion for ferromagnetism.

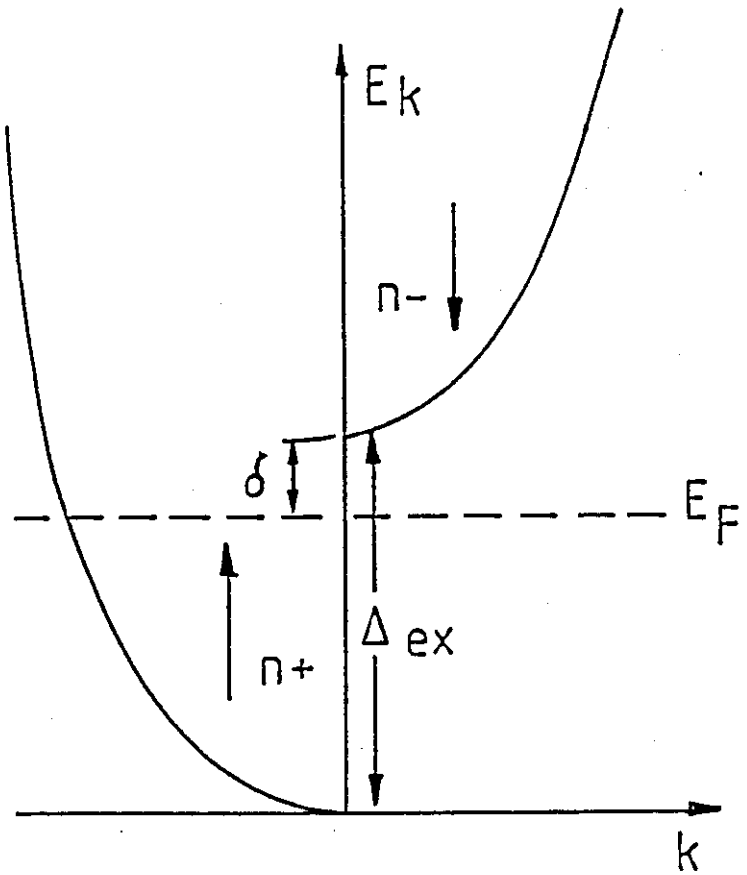

Figure (2.1). Schematic representation of the exchange split band in a simple Stoner model. Thermal excitation of the electrons from the majority band to the minority band occur.

2.1.4 Finite Temperatures and Excitation Mechanisms

Although the Stoner theory of ferromagnetism is applicable to itinerant metallic magnets, severe difficulties occur at finite temperatures.

In the Weiss model, with increasing temperature the moments maintain the same amplitude, but become increasingly disordered, until the Curie temperature is reached and $< M_z > = 0$. Thus, above the Curie temperature the paramagnetic state can be described by the thermal disordering of well defined atomic spins, resulting in a static susceptibility which follows the Curie–Weiss law as given by equ (2.8).

The properties of a Stoner magnet at finite temperature are remarkably different; at any given temperature T the probability P_i of any given electron state i being occupied is governed by Fermi–Dirac statistics:

$$P_i = \frac{1}{\exp (E_i - E_F) / K_B T + 1} \tag{2.15}$$

With increasing temperature in the Stoner model, electrons from the majority band are thermally excited into the minority band, and the ferro–magnetism is thus destroyed by the reduction of the exchange splitting.

The Curie temperature T_c is then given by

$$T_c \sim \Delta_{ex} \tag{2.16}$$

Above the Curie temperature the system becomes a simple Pauli para–magnet, in which the static susceptibility χ is:

$$\chi \alpha T/T_F \tag{2.17}$$

where T_F is the Fermi temperature.

The excitation spectrum at low temperatures consists of the two types of excitation which are the single particle or Stoner modes in which just a single electron is excited and the collective mode or spin wave in which the excitation is shared by all the electrons. The single particle excitations which correspond to transitions from a spin–up to spin–down band, form a continuum (the Stoner continuum).

Excitations with small or vanishing energy transfer ω, are in general possible for finite momentum transfer Q only; single particle excitations with zero momentum transfer (Q = 0) cost a finite amount of energy, the exchange splitting Δ_{ex}. The fact that no single particle excitations for small Q and ω exist, leads to well defined collective excitations in that region, i.e. spin–waves in the ground state. For large Q, the spin–waves enter the single particle continuum and become damped and therefore disappear, as shown in figure (2.2).

At finite temperatures the atomic moments can themselves fluctuate, and it is these fluctuations that are responsible for the phase transition from the ordered ferromagnetic state to disordered paramagnetic state.

2.1.5 Instability at the ($\gamma - \alpha$) Transition in the $Fe_x - Ni_{1-x}$

In order to get a better understanding of the structural instability in the Fe_xNi_{1-x} alloy system, several physical properties have been investigated by others and are reproduced in figure (2·3).

In this figure one achieves a continuous magnetic phase diagram, which starts from the (FM) FeNi system, through the Invar composition $Fe_{65}Ni_{35}$ to a Re–entrant–Spin–Glass (RSG) and Spin Glass state (SG) phase to around $Fe_{65}Ni_{35}Mn_{10}$, and reaches with increasing Mn concentration continuously a purely (AF) phase.

In Fig. 2.3 a, b, we show the variation of the lattice constant at zero K, a_o [29, 30], which initially increases from $a_o = 3.57\text{Å}$ at $Fe_{45}Ni_{55}$ (while T_c is falling), reaches an intermediate maximum at $Fe_{65}Ni_{35}$ and then decreases in parallel with T_c, until the SG state is reached. Because of the growing influence of Mn, a_o afterwards rises continuously in the (AF) phase.

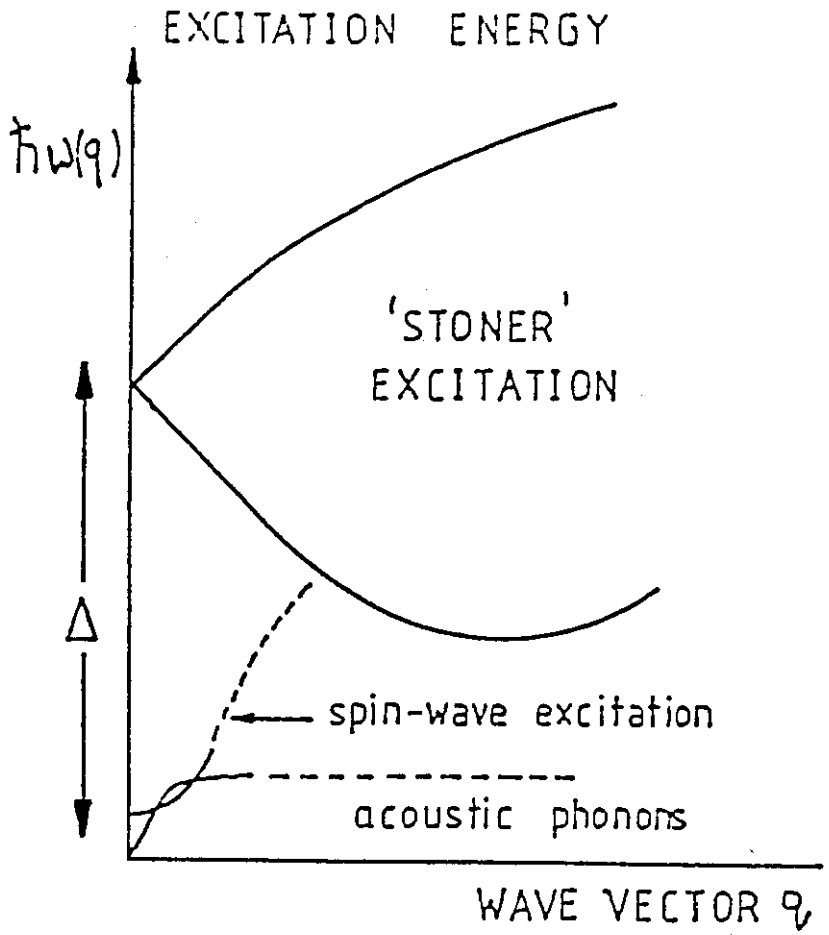

Fig (2.2) Spin wave spectra of an itinerant magnet. The spin-waves enter the Stoner continuum of single particle excitations and become overdamped.

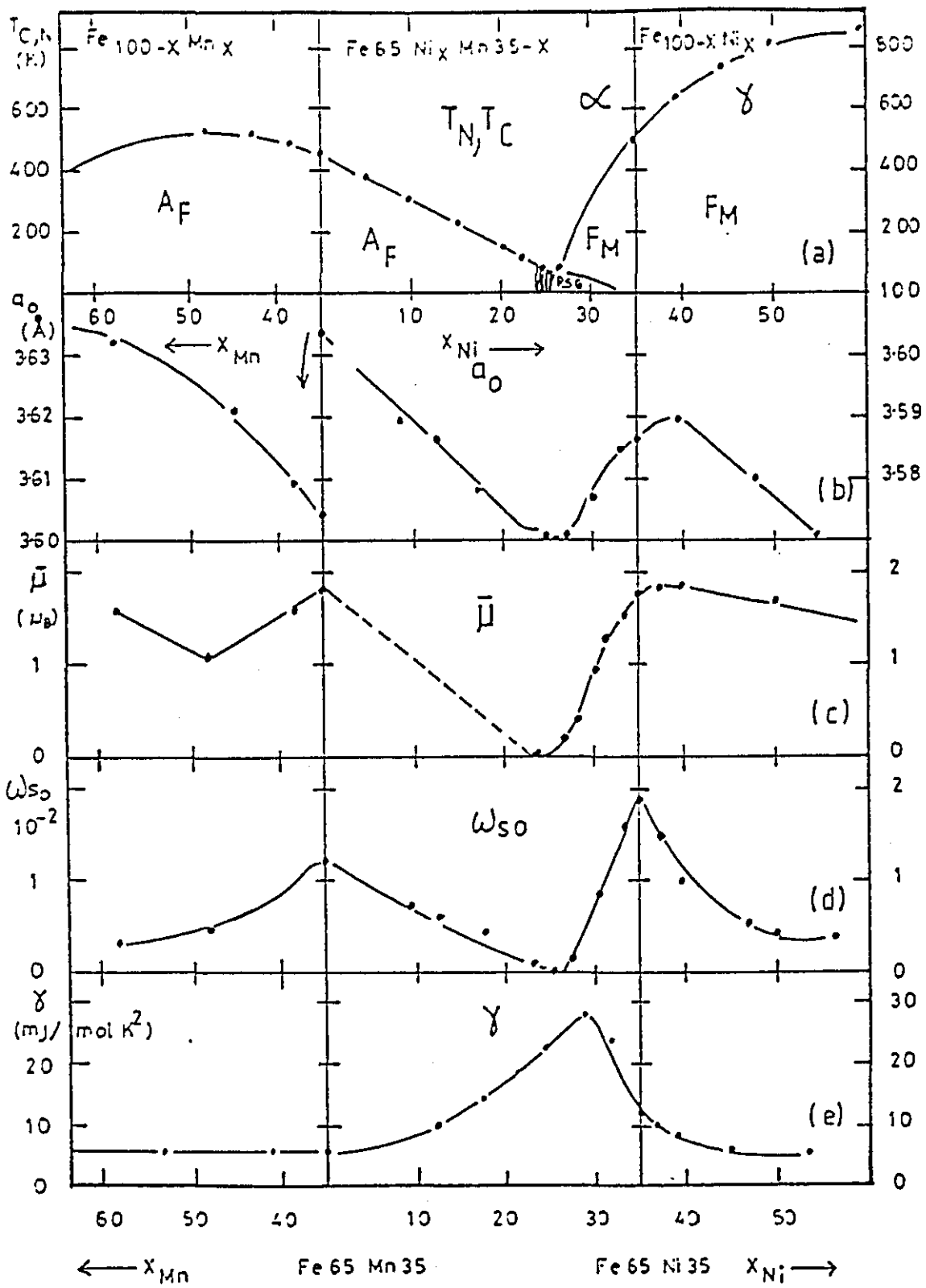

Fig (2.3)

Magnetic phase diagram of the ternary system FeNiMn

A surprising result is now that the average magnetic moment $\bar{\mu}$ per formula unit [29, 31, 32] shown in Fig (2.3c) follows the concentration variation of the lattice constant. $\bar{\mu}$ increases along the Slater–Pauling curve in the FeNi system, and then deviates from the Slater–Pauling curve to zero average moment in the SG Phase, near $Fe_{66}Ni_{34}$ ($\gamma - \alpha$ transition). This transition is, however, suppressed here, because the f.c.c phase of FeNi is stabilised by Mn.

The variation of the spontaneous volume magnetostriction at zero temperature, $\omega_{so} = 3\int_{T_1}^{T} \alpha_m \, dT$, where T_1 is a reference temperature and α_m is the magnetic contribution to the thermal expansion coefficient. In ferro– and antiferromagnetic Invar, ω_{so} is large and positive, but in the SG phase ω_{so} is zero. This is seen from figure (2.3d). Maximum values of $\omega_{so} = 1{\cdot}9 \times 10^{-2}$ are reached on the ferromagnetic side in the FeNi system.

Finally fig(2.3e) shows the concentration dependence of the electronic term of the specific heat γ [130, 131]. γ reaches a maximum value of more than 25mJ mole k^{-2} in the SGand RSG range. For other concentrations it remains at normal level. The observed increase in γ where ω_{so} vanishes has nothing to do with the Invar effect [33]. It is caused by low energy magnetic excitations associated with the SG or RSG phases, which are present at low temperature.

Also several band calculations have shown moment instabilities in 3d elements. Roy and Pettifor [132] predicted the existence of two ferro–magnetic states for fcc Fe using hybridized density of states. These authors [132] also showed, that the instability of the Fe moment in a fcc lattice is directly responsible for the very marked softening in the shear constants, observed experimentally in FeNi [120] and Fe_3Pt [133].

2.2 INTERACTION BETWEEN MAGNETIC AND LATTICE DEGREES OF FREEDOM

In this section, we turn from a consideration of magnetism to the lattice properties. The magnetic contribution to the elasticity of magnetic materials is

closely related to the magnetostriction, which arises from interatomic cohesive forces through the exchange interactions. The elastic moduli associated with the interatomic cohesive forces are closely related to the Invar properties as observed in ferromagnetic FeNi alloys. The elastic constant of these alloys changes quite sensitively with temperature; around and below the Curie temperature T_c the elastic constant decreases with decreasing temperature and the size of the change is large, as shown in Figure (2.4a) [38].

Such anomalous elastic behaviour of Invar alloys, particularly that below T_c, is associated with their magnetic properties and is called the magnetoelastic effect. However, the relation between magnetism and elastic properties is not simple. In Ni, for example, the elastic constant shows quite ordinary behaviour as shown in fig (2.4c) [39]; with decreasing temperature the elastic constant slowly increases reflecting the volume contraction.

In magnetic metals, thermal volume expansion also often shows anomalous behaviour, especially in the temperature region below Tc. In the case of FeNi alloys, fig (2.4d), the temperature dependence of the volume which drastically deviates from the simple linear extrapolation is called magneto–volume or magneto–striction effects. A system with a very small or negative thermal expansion coefficient , such as FeNi alloys, is called an Invar [39].

The origin of those anomalous magneto–elastic and magneto–volume effects are not yet satisfactorily understood [40], Electron Phonon Interaction (EPI) can effect the volume of a ferromagnetic metal and cause negative thermal volume expansion [33]. The free energy of a metal with magnetisation $M = (n_+ - n_-)/(n_+ - n_-)$ and volume V can be divided into an electron part, F_{el}, and the phonon part, F_{ph} as [41]:

$$F(V, M) = F_{el}(V,M) + F_{ph}(V,M) \qquad (2.18)$$

The M dependence of F_{ph} comes from the phonon frequency wq(V, M); wq is influenced by the M since the screening of the ion–ion interaction depends on the splitting of the energy bands of the screening conduction electrons.

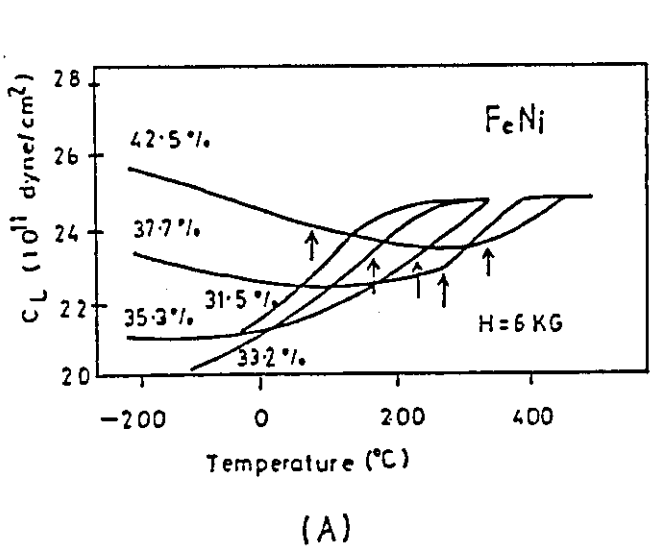

(A)

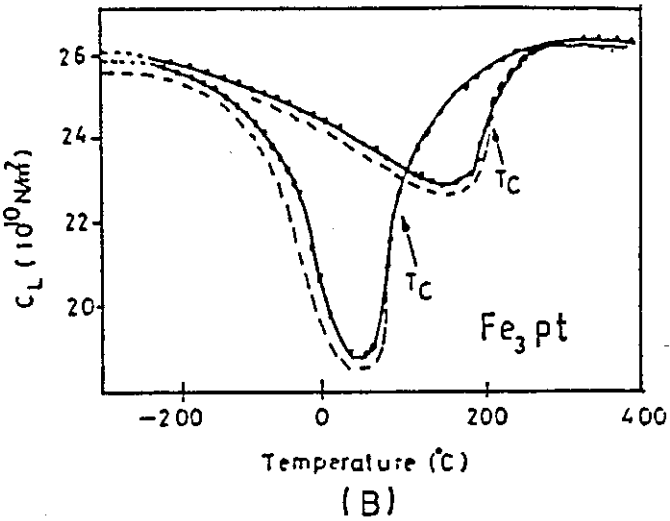

(B)

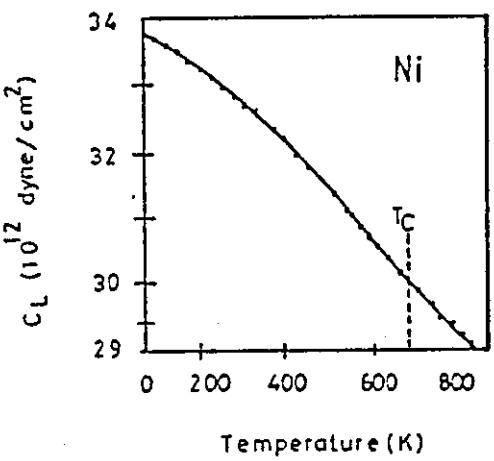

(C)

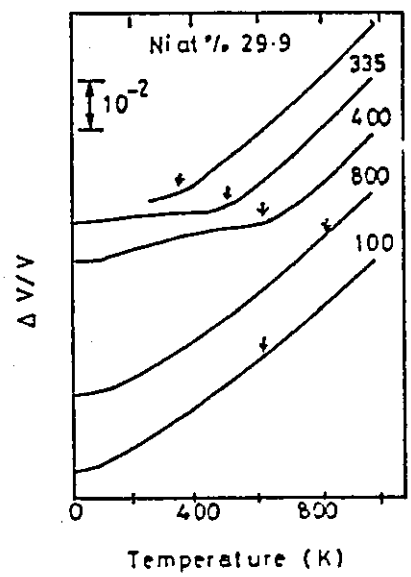

(D)

Fig (2.4)

The temperature dependence of

(a) the elastic constant $C_L = 1/2\,(C_{11} + C_{12} + C_{44})$ of FeNi alloys

(b) the elastic constant C_L of Fe_3Pt

(c) the elastic constant C_L of Ni

(d) volume for FeNi alloys

The change in volume due to phonons is given as the product of the inverse of the bulk modulus B and the pressure Pp; both B and Pp are magnetisation dependent in the ferromagnetic state as [41, 42]:

$$\frac{\Delta Vp(M)}{V} = Pp(M).\frac{1}{B(M)} \tag{2.19}$$

where Pp(M) is the phonon pressure defined by:

$$Pp(M) = \frac{N\theta_D(M)}{V}\gamma_D(M) \tag{2.20}$$

where $\theta_D(M)$ is the magnetisation dependent Debye temperature, $\gamma_D(M)$ is the phonon Grüneisen constant, N is the total number of atoms and B(M) is the bulk modulus of free electrons defined as:

$$B(M) = \frac{1}{K(M)}\frac{S^2(M)}{s_0^2} \tag{2.21}$$

where K(M) is the electron compressibility [46], S(M) is the sound velocity in the magnetic state, and s_0 is the Bohm–Staver sound velocity.

Measurements of the phonon Grüneisen constant $\gamma_D(M)$ suggest the possibility of having a negative value in the ferromagnetic state of metal. With such behaviour phonons can play an important role in causing zero or negative thermal volume expansion often observed in ferromagnetic metals [43, 44].

In the following subsections we discuss the fundamental concepts of the Magnetic Lattice interaction

2.2.1 The effect of magnetism on phonon frequencies in FeNi Invar.

The unusual elastic softening as well as the lattice dynamical anomaly particularly for the [ξξ0] TA mode in the Invar FeNi alloys, are reasonably understood by the Electron–Phonon Interactions (EPI). This interaction is enhanced by the detailed structure of the d–bands in Invar alloys. The

argument that the d–band has a very important role in explaining Invar property was originally made by Kanamori et al [45], who developed a theory to relate the electron structure with the crystal volume.

The Hamiltonian of EPI can be written as [43, 44]:

$$H_{ep} = \sum_{\mu} |g_{q\mu}| Q_{q\mu} \rho_k \qquad (2.22)$$

where $g_{q\mu}$ and $Q_{q\mu}$ represent, respectively, the coupling coefficient and the normal coordinates of a phonon with wave number q and polarisation μ; ρ_k is the electron density.

The frequency wq of longitudinal acoustic phonon in the [111] direction, below Tc in the ferromagnetic state of a metal is given by [46]:

$$w^2 q = \Omega^2 q - |gq|^2 \chi^e q \qquad (2.23)$$

where Ωq is the bare phonon frequency and $\chi^e q$ is the charge susceptibility at the Fermi energy. The expression to shows how the phonon frequency is renormalized from Ωq to wq by the effect of EPI, or, the screening effect of conduction electrons.

We next consider the enhancement of the electron–phonon coupling constant $gq\mu$ in equ (2.24). This constant depends on the density of states at the Fermi energy, $n(E_F)$ and is given by [47]:

$$gq\mu \ \alpha \ n(E_F) \ < I^2 > \qquad (2.24)$$

where $< I^2 >$ is the matrix element averaged over the Fermi surface. In both Invar metals $Fe_{65}Ni_{35}$ and $Fe_{72}Pt_{28}$ the d electron density of states is large [46].

2.2.2 Elastic Constants

Acoustic modes of a long wavelength propagate as in a continuous medium and their frequencies are related to the elastic constants of the crystal.

Hook's law states that for small deformation, stress components σ_{ij} are linear functions of the strain components e_{kl} of the form [49]:

$$\sigma_{ij} = c_{ijkl}\, e_{kl} \tag{2.25}$$

where C_{ijkl} is the elastic constant which consists of 81 independent elastic constants. This number is reduced if the crystal possesses symmetry elements [48].

In cubic crystals there are only three independent elastic constants, C_{11}, C_{12} and C_{44}. There are also three different modes i of propagation for a sound wave with velocities V_i (V_L, V_{T1} and V_{T2}). These velocities are related to the elastic constants as indicated in table (2.1). One can see that a measurement of sound velocities in the (110) direction enables the three independent constants C_{11}, C_{12} and C_{44} to be determined.. Commonly one expresses the elastic properties of crystals with cubic symmetry through three elastic constants C_L, $\bar{C}$ and C_{44} which are defined by linear combinations of C_{ij} (see Table 2.1).

For propagation in the (110) direction, the elastic constants are given by [50, 48]: (see figure (2.5)

$$\begin{aligned} C_L &= \rho V_L^2 = \frac{1}{2}(C_{11} + C_{12} + 2C_{44}) \\ \bar{C} &= \rho V_{T1}^2 = \frac{1}{2}(C_{11} - C_{12}) \\ C_{44} &= \rho V_{T2}^2 \end{aligned} \tag{2.26}$$

where V_L and V_T are longitudinal and tranverse wave velocities, C_{11}, C_{12} and C_{44} are the elastic constants of cubic crystals, and ρ is the density.

For a wave parallel to the (100) direction:

Direction of Propagation	Mode i	$\rho . v_i^2 = C_{ij}$
[100]	L	C_{11}
[100]	T	C_{44}
[110]	L	$\frac{1}{2}(C_{11} + C_{12} + 2C_{44}) = C_L$
[110]	T1	$\frac{1}{2}(C_{11} - C_{12}) = \overline{C}$
[110]	T2	C_{44}
[111]	L	$\frac{1}{3}(C_{11} - C_{12} + C_{44})$
[111]	T1	$\frac{1}{3}(C_{11} + 2C_{12} + 4C_{44})$

Table (2.1)

Propagation of sound waves and respective elastic constants for a crystal with cubic symmetry

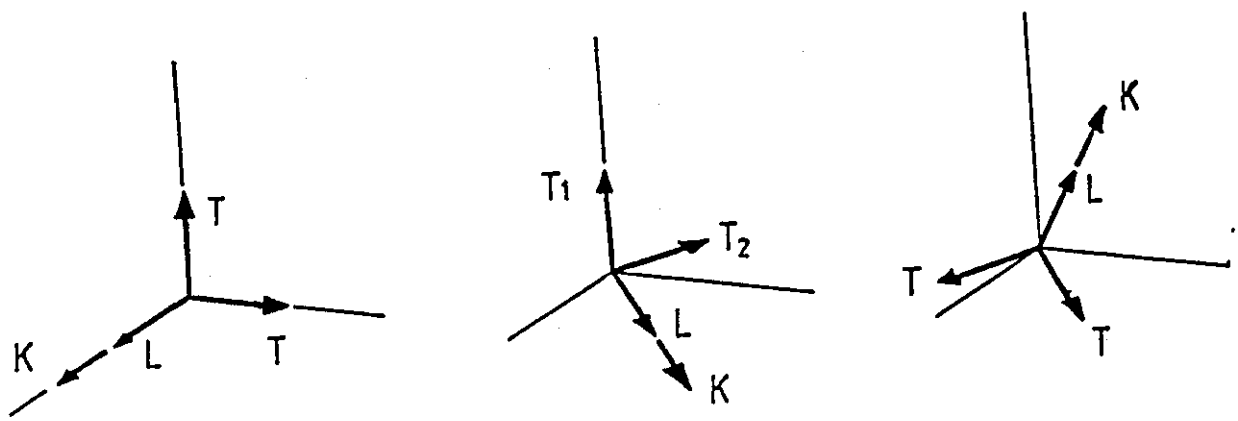

Fig (2.5)

Effective elastic constants for three modes of elastic waves in the principal propagation direction in cubic crystals

$$\rho V^2_L = C_{11} \quad \text{and} \quad \rho V^2_T = C_{44} \tag{2.27}$$

and for a wave parallel to the (111) direction:

$$\rho V^2_L = \frac{1}{3}(C_{11} + 2C_{12} + 4C_{44})$$
$$\rho V^2_T = \frac{1}{3}(C_{11} - C_{12} + C_{44}) \tag{2.28}$$

The bulk modulus is given by [50]:

$$B = C_L - \bar{C}/3 - C_{44} = \left(\frac{1}{3}\right)(C_{11} + 2C_{12}) \tag{2.29}$$

C_L expresses a compression mode accompanied by a change in volume, $\bar{C}$ corresponds to a pure shear mode with an expansion along the (110) axis (tetragonal distortion). C_{44} corresponds to a pure shear mode with an expansion occurring along the (111) axis (trigonal distortion). For ferro–magnetic Invar alloys, Hausch [51] (1974) found that the elastic constant shows anomalous behaviour, exhibiting a continuous decrease in the shear constants $(C_{11} - C_{12})/2$ and C_{44} with decreasing temperature below the Curie temperature T_c. The origin of the anomaly could be magnetoeleastic coupling as suggested by Hausch [51] . The anomaly begins to occur around T_c, and is approximately proportional to the square of the relative magnetisation.

Expressions for the magnetoelastic coupling constant and the pressure dependence of the Curie temperature $\frac{\partial Tc}{\partial p}$ have been given by Shiga [52]:

$$\frac{\partial Tc}{\partial p} = \frac{5}{3} K\, Tc - \frac{\alpha}{Tc}$$

where (2.30)

$$\alpha = 2KCN\, N(\varepsilon o)\mu_B{}^2\, T^2_F$$

where K are the compressibility, C is magnetoelastic coupling constant.

For positive C, the Curie temperature decreases under pressure as observed for all known Invar type materials.

The volume magnetostriction ω_m and the spontaneous magnetisation M may be expressed as [53]

$$\omega_m = -2k\frac{\partial A}{\partial w}M^2 = -\frac{2}{B}\frac{\partial A}{\partial w}NM^2 \qquad (2.31)$$

where A is the exchange stiffness constant, ω is volume strain and

$B = \frac{1}{3}(C_{11} + 2C_{12})$ is the bulk modulus.

2.2.3 Specific heat contributions

Specific heat is a successful probe for obtaining information about electronic and lattice contributions, magnetic entropy and transition temperatures. The thermodynamic concept of heat capacity measured at constant volume or pressure is defined by:

$$C = \lim_{\Delta T \to 0} \frac{\Delta U}{\Delta T} \qquad (2.32)$$

where ΔU is the quantity of heat given to the specimen and ΔT is the corresponding rise in temperature of the specimen. A more useful quantity is the molar heat capacity which is defined by:

$$C = \frac{c}{m} \qquad (2.33)$$

where m is the specimen mass in gram molecules. As a solid absorbs heat, its temperature rises and its internal energy is increased. The heat capacity of metals is zero at 0°K, and rise rapidly as the temperature increases to an approximately constant value at higher temperatures. The total specific heat at low temperature proportional to the electrons and lattice contributions is written as:

$$C = \gamma T + \beta T^3 \qquad (2.34)$$

where γ and β are coefficients related to the electron and lattice

contributions. Values of γ and β can be obtained by fitting equation (2.34) to measured values of specific heat. The electronic specific heat C_e is given by:

$$C_e = \frac{\pi^2}{3} N K_\beta^2 n(\varepsilon_F) T = \gamma T \tag{2.35}$$

where N is Avogadros's number and K_β is Boltzmanns constant. The coefficient γ is directly proportional to the density of states, $n(\varepsilon_F)$, at the Fermi level εo. The lattice specific heat is expressed by:

$$C_L = \frac{12}{5} \pi^4 N K \left(\frac{T}{\theta_D} \right)^3 = \beta T^3 \tag{2.36}$$

where θ_D is the Debye temperature.

Elastic constant measurements may be used to derive the values of β and θ_D.

2.2.4 Magnetic Contribution to Elastic Constants

The magnetic contribution to the elastic constants of fcc materials originates from the occurrence of a spontaneous magnetization.

Considering only the nearest neighbour exchange interaction , the elastic constants can be expressed using a localised model by the following equations [39, 54].

$$\begin{aligned} C_{44} &= C_p - \frac{1}{4} N Z_1 \left(\frac{I}{I_o} \right)^2 (r_o^2 \bar{\bar{J}}_1 + 3 r_o \bar{J}_1) \\ \bar{C} &= \bar{C}p - \frac{1}{8} N Z_1 \left(\frac{I}{I_o} \right)^2 (r_o^2 \bar{\bar{J}}_1 + 7 r_o J_1^2) \end{aligned} \tag{2.37}$$

where C_{44} and $\bar{C}$ are the elastic constants, while C_p and $\bar{C}_p$ can be determined by extrapolation from the paramagnetic region. N is the number

of atoms per unit volume, Z_1 the number of nearest neighbours, r_o the equilibrium interatomic distance, J_1 the exchange energy between nearest neighbour atoms, and $\bar{J}_1$ and $\bar{\bar{J}}_1$ are the first and second derivatives of J_1, with respect to the interatomic distance.

Hausch and Warlimont [38] (1972) approximate the temperature dependence of the exchange contribution to the elastic constants using the Landau–Belov relation [55]

$$\left(\frac{I}{I_o}\right)^2 = A\left(1-\frac{T}{T_c}\right) \tag{2.38}$$

where A is a constant. From magnetization measurements, Belov found A = 6.75 for both Fe and Ni .

2.2.5 Magnetic entropy

The change in magnetic order, as the temperature varies, is revealed by specific heat measurements. The relationship between the magnetic entropy S_M, and the thermal capacity C, follows directly from the thermodynamic equation:

$$S_M = \frac{dQ}{T} = C\frac{dT}{T} \tag{2.39}$$

where dQ is the amount of heat absorbed by the system. S_M is the magnetic entropy which is a measure of the disorder or randomness of a system: the greater the disorder the higher is the entropy. In particular, sharp maxima in specific heat are expected near the transition temperatures. The variation of S_M can be quantitatively estimated from the area under the specific heat curve near and above the transition temperature. By integrating the equation (2.39):

$$S_M = \int_0^T \frac{C}{T} dT \tag{2.40}$$

The entropy of the magnetic state is related to the spin quantum number s (and hence the magnetic moment) of the magnetic atoms by:

$$\Delta S_M = CR \ln (2s + 1) \tag{2.41}$$

where C is the fraction of the atoms carrying magnetic moment and R is the gas constant.

2.2.6 Vibrational Modes of a Monatomic lattice

Atoms in a crystal do not in general move independently. The general motion is complicated even in simple crystals with high symmetry. This is partly because there are significant force constants between each atom which extend to more distant neighbours than just its nearest neighbours. In three dimensions many subscripts are required to keep account of these forces.

Consider a linear chain of monatomic atoms with forces only between nearest neighbours. If the force constant is α and the atoms have small displacements U_n the equation of motion of the n^{th} atom is [56, 48]:

$$m d^2U_n/dt^2 = \alpha (U_{n+1} - U_n + U_{n-1} - U_n) \tag{2.42}$$

If we suppose a normal mode solution is $u = u_o\ e^{i(nqa - wt)}$ and differentiate, we obtain:

$$-mw^2U_n = \alpha [\exp(qa) + \exp(-iqa) - 2] U_n \tag{2.43}$$

The frequency w_q is now given by [48, 50]:

$$w_q = \sqrt{\frac{4\alpha}{m}} \sin\left(\frac{qa}{2}\right) = w_m \sin\left(\frac{qa}{2}\right) \tag{2.44}$$

This is the dispersion curve for acoustic phonons. The frequency is a function of the wave vector q and fig (2.6) shows the results. The significant range of q for the periodic system is $-\pi/a \leq q \leq \pi/a$. This range of values of q is referred to as the first Brillouin Zone of the linear lattice in reciprocal space.

If we now consider the chain with the different atoms of mass m and M, then the w_q is given by [48, 56]

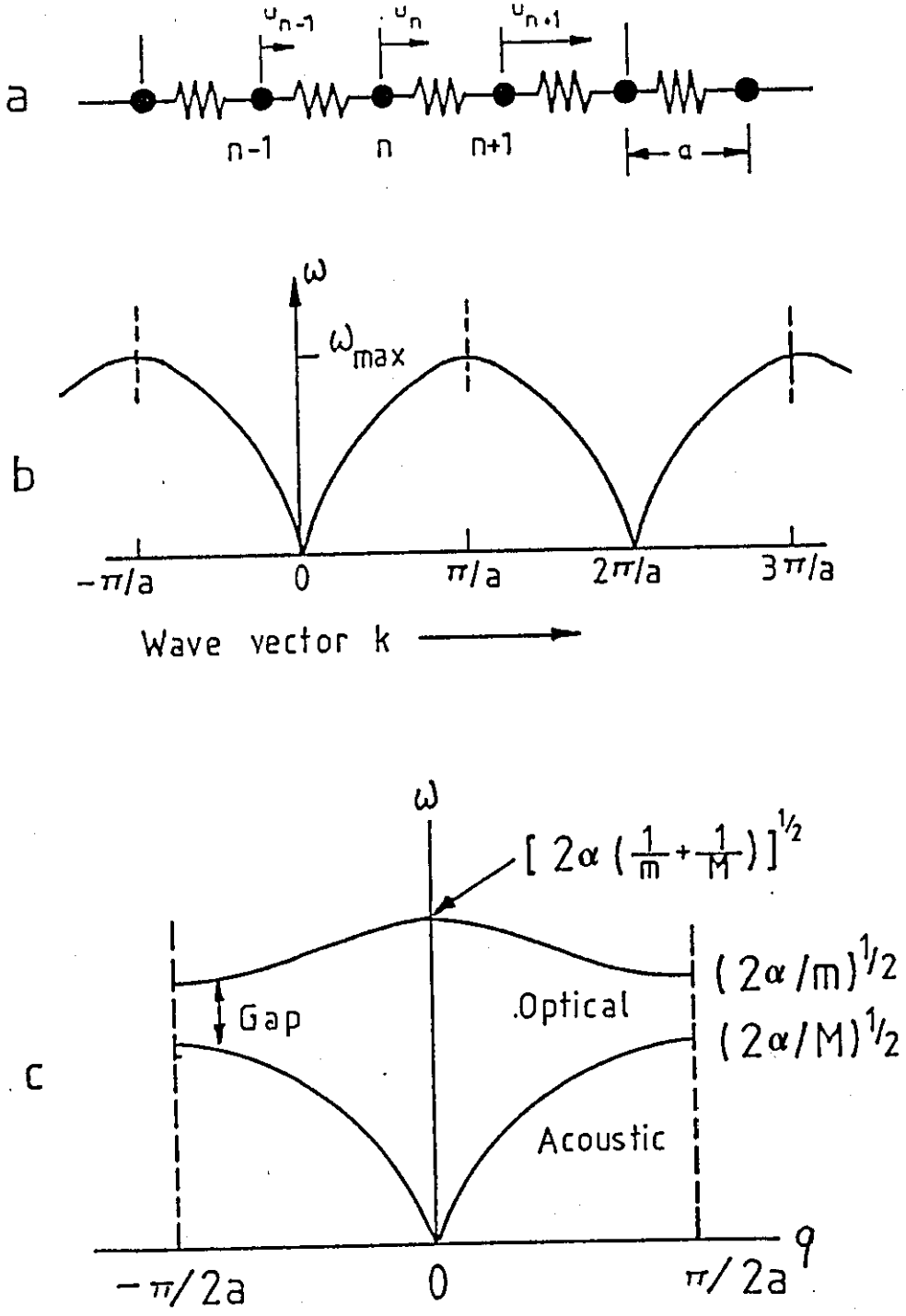

Fig. (2.6)

(a) a segment of a one–dimensional lattice

(b) the dispersion of curve, w versus q, for a one–dimensional lattice with nearest neighbour interaction

(c) two dispersion branches of a diatomic lattice showing frequency gap

$$w^2_q = \alpha\left(\frac{1}{m} + \frac{1}{M}\right) \pm \alpha\left[\left(\frac{1}{m} + \frac{1}{M}\right)^2 - \frac{4\sin^2(qa)}{mM}\right]^{1/2} \qquad (2.45)$$

In equation (2.45) the modes corresponding to the negative sign before the square root are the acoustic ones, and those with the positive sign are the optical modes. An important feature of equation (2.45) is the zone boundaries defined by $-\pi/2a \leq \pi/2a$.

The acoustic and optical frequencies for M > m are given by:

$$w_{acous} = \sqrt{\frac{2\alpha}{M}}$$

and (2.46)

$$w_{opti} = \sqrt{\frac{2\alpha}{m}}$$

The dependence of w on q is shown in fig (2.6c). It can be seen that an acoustic curve is not qualitatively different from the dispersion found for the monatomic case. The acoustic curve begins at the q = o, w = o and the curve saturates at the value $q = \pi/2a$. The optical curve begins at q = o with a finite frequency $w = \left[2\alpha\left(\frac{1}{m} + \frac{1}{M}\right)\right]^{1/2}$ and then decreases slowly, until $q = \pi/2a$.

The frequency range between the top of the acoustic curve and the bottom of the optical curve is forbidden, and the lattice cannot transmit such a wave; waves in this region are strongly attenuated.

2.2.7 Phonons and Magnons

The motion of atoms in a crystal is described by the properties of the normal modes of vibration and in particular by their frequency, w(q),which depends on the magnitude and direction of the wave vector q of the normal mode.

Any dynamic problem that can be described as a collection of harmonic oscillators can be quantized in energy; this includes phonons and magnons. The energy quantized of the qth normal mode is given by:

$$Eq = \left(n_q + \frac{1}{2}\right)\hbar w_q \qquad n_q = 0, 1, 2 \ldots \tag{2.47}$$

When exciting the qth normal mode from n_q to $n_q + 1$, a magnon is created (or emitted) and the energy of vibrational system increases by $\hbar w_q$. When de–exciting a normal mode from n_q to n_q–1, a magnon is annihilated (or absorbed) and the energy of the vibrational system decreases by $\hbar w_q$.

Magnons, just as phonons, are described by Bose–Einstein Statistics

$$< n_q > = \frac{1}{\exp(\hbar w_q / K_B T - 1)} \tag{2.48}$$

where $< n_q >$ is the average occupation number for magnons or phonons at thermal equilibrium.

At very high temperatures the oscillator is excited to very high quantum states since for $K_B T >> \hbar w_q$, $< n_q >$ and $< E_q >$ become:

$$< n_q > \approx K_B T / \hbar w_q$$

and (2.49)

$$< E_q > = < n_q > \hbar w_q \approx K_B T$$

At low temperatures, $\hbar w_q >> K_B T$ then:

$$< n_q > \approx \exp(-\hbar w_q / K_B T) \tag{2.50}$$

In spin waves, the spins precess around the equilibrium magnetization and their precessions are correlated through exchange forces. The dispersion relation for spin wave–like phonons but with maximum frequencies of $4JS^2/h$ and can be written as:

$$w = \left(\frac{4JS^2}{h}\right) \sin^2\left(\frac{aq}{2}\right) \tag{2.51}$$

where a is the lattice spacing and q is the wave vector of the spin wave. For small q, w is also very small because the spins at long wavelengths are still almost parallel to each other, and hence the restoring exchange force is small. For long wavelengths, the dispersion curve of spin wave is $w \approx A q^2$ differs from the case of lattice waves, in which $w \approx q$. This is because the phase and group velocities of the spin wave are unequal even in the long wavelength region.

CHAPTER THREE

NEUTRON SCATTERING THEORY

3.1 INTRODUCTION

In this Chapter a brief account of neutron scattering will be given. More detailed accounts of the various aspects of thermal neutron scattering are available in a number of texts [57, 58, 59, 60].

The neutron beam is directed on to the sample and the scattered neutron intensity in various directions is measured. Unlike electrons, neutrons are uncharged and penetrate deeply into most solid materials. Diffraction patterns, characteristic of the crystal structure, occur as a result of the interaction of the neutron with the atomic nuclei. Furthermore, since the neutron possesses a magnetic moment, it may interact with any atomic moments in the sample to yield magnetic scattering. If long range magnetic order is present, the coherent magnetic scattering will enable the magnetic structure to be determined. Inelastic scattering of neutrons provides direct information about both nuclear and magnetic dynamical processes in condensed matter. In particular, direct measurements of the energy E and moment q of phonons or magnons is possible, i.e. by using a triple axis neutron spectrometer. The instruments used in performing the thermal neutron scattering experiments discussed in Chapter 4 were D1A, D2B, D1B, diffractometers and triple axes neutron spectrometer (IN20) which uses polarised neutrons, all located at the Institut Laue–Langevin, Grenoble, France.

3.2 NEUTRON SCATTERING CROSS SECTION

The incident neutrons may be considered to be plane waves characterised by their wave functions $|>$ which interact via some potential $\underline{V}$ of the target. The neutrons are selected (monochromator, collimators, etc.) to have some well defined initial state $|\, k_i\, \sigma_i\, \alpha_i >$ where k_i, σ_i, α_i are the neutron's initial wavevector, spin state, and the scattering system respectively. The general arrangement of a scattering experiment is shown in figure (3.1).

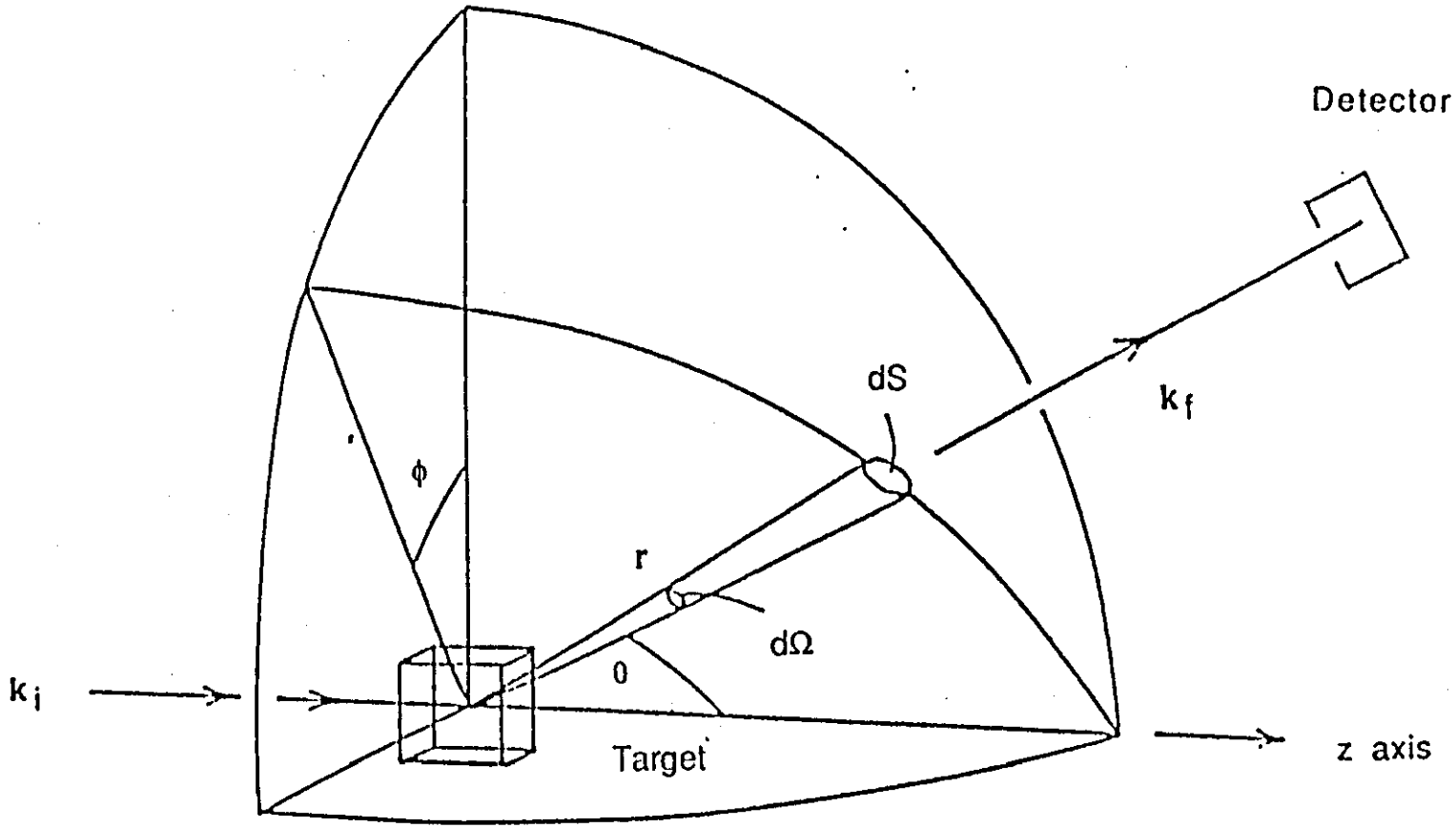

Figure (3.1) Geometry for scattering

The interaction of a monochromatic beam of neutrons (a neutron beam in which all the neutrons have the same wavelength or energy) may be defined in terms of three cross-- sections. These are:

(i) the total scattering cross-section

$$\sigma = \text{(total number of neutrons scattered/unit time)} / \phi \qquad (3.1)$$

where ϕ is the flux of the incident neutrons (number of neutrons/cm^2/sec)

(ii) the differential cross–section of the system:

$$\frac{d\sigma}{d\Omega} = \text{(number of neutrons scattered/unit time/unit solid angle)}/\ \phi\ d\Omega \qquad (3.2)$$

(iii) the partial differential cross–section:

$$\frac{d^2\sigma}{d\Omega dE} = \text{(number of neutrons scattered/unit time/ unit solid angle with energies between } \underline{E}_f \text{ and } \underline{E}_f + d\underline{E}_f / \phi\ d\Omega E \qquad (3.3)$$

In the Born approximation, the partial differential cross–section for a process in which the neutron changes its wave vector from $\underline{K}_i$ to $\underline{K}_f$, its spin state from $\underline{\sigma}_i$ to $\underline{\sigma}_f$ and in which the scattering system also changes from state $\underline{\alpha}_i$ to $\underline{\alpha}_f$, is:

$$\left(\frac{d^2\sigma}{d\Omega dE}\right)_{\underline{K}i\,\underline{\sigma}i\,\underline{\alpha}i \rightarrow \underline{K}f\,\underline{\sigma}f\,\underline{\alpha}f} = \frac{\underline{K}_f}{\underline{K}_i}\left(\frac{m}{2\pi h}\right)^2 \left| <\underline{K}_f \underline{\sigma}_f \underline{\alpha}_f | V | \underline{K}_i \underline{\sigma}_i \underline{\alpha}_i > \right|^2 x\ \delta(E_{\underline{\alpha}i} - E_{\underline{\alpha}f} + \underline{E}_i - \underline{E}_f) \qquad (3.4)$$

where V is the interaction potential between the system and the neutron. $\delta(X)$ is the Dirac delta function and represents mathematically the energy distribution of the scattered neutrons (i.e. energy conservation). $E_{\underline{\alpha}i}$, $E_{\underline{\alpha}f}$ are energies of initial and final states of the scattering system, and $\underline{E}_i$, $\underline{E}_f$ are energies of initial and final states of the neutrons, $\frac{\hbar^2}{2m}\underline{K}_i^2$, $\frac{\hbar^2}{2m}\underline{K}_f^2$ respectively.

To evaluate equation (3.4), the matrix elements must be calculated. If the potential V is assumed to be very short range then it can be shown that for a single fixed nucleus [57]:

$$\frac{d\sigma}{d\Omega} = b^2 \qquad (3.5)$$

where b is called the nuclear scattering amplitude, and has dimensions of length. At present b cannot be calculated but is often expressed in terms of potential and resonance levels in the compound nucleus. The potential term is always positive having a scattering length of the same magnitude as the nuclear radius. The resonance term is a function of energy. Under certain conditions, the resonance term may be negative and also sufficiently large numerically to outweigh the potential term, thus giving a resultant scattering amplitude b which is negative. The experimentally determined coherent scattering amplitudes for the different elements and isotopes have been tabulated by Sears [62].

Furthermore, since the nuclear interaction potential V_{nucl} is short range (the radius of the nucleus $r << \lambda$), the scattering will be isotropic and there will be no form factor dependence.

3.3 SPIN DEPENDENT INTERACTIONS

If the spin state of the neutron is also considered, then sources of scattering other than the nuclear scattering mentioned above can occur. The additional scattering can be divided into two components: nuclear spin scattering and magnetic scattering. The nuclear spin scattering will be discussed later. Magnetic scattering arises from the interaction of the neutron's magnetic moment with the electronic moments in the scattering system. To evaluate the partial differential cross–section (Equation 3.4)) it is necessary to consider a magnetic interaction potential V_{mag}. The matrix elements $\langle \underline{K}_f | V_{mag} | \underline{K}_i \rangle$ are given by Squires [59]:

$$\langle \underline{K}_f | V_{mag} | \underline{K}_i \rangle = 4\pi\gamma\mu_N \ \mu_B \ \sigma Q_\perp (\underline{K}_i - \underline{K}_f) \qquad (3.6)$$

where μ_B is Bohr magnetons, σ is the Pauli spin operator, $Q_\perp$ is the magnetic interaction operator and γ is the magnetic moment of the neturon, $-1{\cdot}91\ \mu_B$.

The cross-section (Equation (3.4)) after evaluating the matrix elements can be written

$$\left(\frac{d^2\sigma}{d\Omega dE}\right) = (\gamma r_o)^2 \frac{K_f}{K_i} <\underline{\sigma}_f \underline{\alpha}_f|\sigma.Q_\perp|\underline{\sigma}_i\ \underline{\alpha}_i>^2 \delta(\underline{E}_{\underline{\alpha}i} - \underline{E}_{\underline{\alpha}f} + \underline{E}_i - \underline{E}_f) \tag{3.7}$$

where r_o is the classical electron radius.

The magnetic interaction operator $\hat{Q}\perp$ can be written as:

$$\hat{Q}_\perp = \hat{\underline{K}}x(\hat{\underline{Q}}x\hat{\underline{K}}) \tag{3.8}$$

where $\hat{K}$ is a unit vector parallel to the scattering vector and the operator $\hat{Q}$ represents the Fourier transform of the magnetisation density:

$$\hat{Q} = -\frac{1}{2\mu_B}\int M(r)\exp(ik.r)dr \tag{3.9}$$

The magnetic interaction operator $\hat{Q}$ represents all the magnetic scattering, i.e. both spin and orbital contributions.

Thus, unlike nuclear scattering, magnetic scattering is a vector interaction. An important implication of equation (3.8) is that only magnetic components perpendicular to the scattering vector give rise to scattering.

Furthermore, since the magnetic electrons have a finite radial extent, comparable with a typical neutron wavelength (~ 1 Å), the magnetic scattering has a form factor dependence. This form factor falls off with $\sin\theta/\lambda$, similar to X-ray scattering.

3.4 COHERENT AND INCOHERENT SCATTERING AMPLITUDES

A scattering system which is a single atom may consist of a mixture of several different isotopes each with a well defined abundance or relative frequency ω. These isotopes will each have their own characteristic values of the scattering length b, and will be distributed at random among the atomic

positions, so that the average value of b for the system is:

$$\bar{b} = \sum_i \omega_i b_i$$

and the average value of b^2 is (3.10)

$$\overline{b^2} = \sum_i \omega_i b_i^2$$

This effect will produce coherent and disorder nuclear isotopic scattering, the cross–section of which are:

$$\left(\frac{d^2\sigma}{d\Omega d\omega}\right)_{coh} \alpha (\bar{b})^2 \qquad (3.11)$$

and

$$\left(\frac{d^2\sigma}{d\Omega d\omega}\right)_{disorder} \alpha \left(\overline{b^2} - (\bar{b})^2\right) \qquad (3.12)$$

It could be clearly seen from equations (3.11) and (3.12) that there is a marked difference between the coherent and disorder cross–sections. Whereas the coherent cross–section is proportional to the mean square of the scattering lengths b_i, the disorder cross–section is proportional to the mean–square deviation of the scattering length from their mean value. If a system contains nuclei of equal scattering lengths then the phase shifts of the scattered waves are all equal and the scattering is said to be entirely coherent.

In addition to the isotopic disorder scattering (resulting from disorder amongst the various isotopes), incoherent scattering arises if the spin of the nucleus is non zero. A neutron of spin 1/2 may combine with a nucleus having spin I, to form one of two compound nuclei, having spins (I + 1/2) and (I – 1/2) respectively. Each of these compound nuclei will have an associated scattering length, labelled b_+ and b_-. The coherent and incoherent scattering resulting from this process are:

$$\left(\frac{d^2\sigma}{d\Omega dE}\right)_{coh} \alpha (W_+ b_+ + W_- b_-)^2 \qquad (3.13)$$

and

$$\left(\frac{d^2\sigma}{d\Omega dE}\right)_{disorder} \alpha (W_+ b_+^2 + W_- b_-^2) - (W_+ b_+ + W_- b_-)^2 \qquad (3.14)$$

The weighting factor of each spin is given by Bacon [57]:

$$W_+ = \frac{I+1}{(2I+1)}, \qquad W_- = \frac{I}{(2I+1)} \qquad (3.15)$$

3.5 NEUTRON SCATTERING BY PHONONS

The neutron interacts with the target atom via nuclear forces, and the strength of interaction will depend on the isotope. If the nuclear spin is non zero, it will depend on whether the spins of neutron and the nucleus are parallel or antiparallel.

If we assume the nuclear motion to be spin and mass independent, and the range of the nuclear interaction ($\sim 10^{-12}$cm) to be small compared with the relevant neutron wavelength ($\sim 10^{-8}$cm), we can use a pseudopotential for the interaction of the form:

$$V_{nuc} = \frac{2\pi h^2}{m} \sum_j b_j \, \delta(\underline{r} - \underline{R}_j) \qquad (3.16)$$

where $\underline{R}_j$ is the position of the ith nucleus and b_j its scattering length.

For harmonic solids where the atoms undergo oscillations given by

$$\underline{R}_j(t) = \underline{L}_j + \underline{U}_j(t) \qquad (3.17)$$

where the $\underline{L}_j$ define is the equilibrium positions, and $\underline{U}_j$ (t) are small displacements from $\underline{L}_j$.

The lattice displacement expressions considered in the previous chapter can be quantised (e.g. for details see Kittel [48]) so that the dynamics are discussed in terms of phonons (of characteristic frequencies ω and wavevectors q).

For a collection of nuclei, using the above approach, the one phonon coherent scattering cross–section is [58, 59]

$$\left(\frac{d^2\sigma}{d\Omega dE}\right)_{\substack{coh \\ 1\,ph}} = \frac{K_f}{K_i} \sum_{q,j} \delta\,(E_i - E_f - \hbar w_j(q)] \sum_{\tau} \delta\,(Q \pm q - 2\pi\tau) \times |G_j(Q)|^2 \qquad (3.18)$$

where $\underline{Q} = \underline{K}_i - \underline{K}_f$ is the momentum transfer τ is a reciprocal lattice vector and G(Q) is the structure factor for one phonon scattering and is given by:

$$G(Q) = \sum_{K} \frac{b_k}{\sqrt{m}} [\underline{Q}.\hat{\underline{z}}(l)] \exp[-W_k(Q)] \exp(i\underline{Q}.Rl) \qquad (3.19)$$

where R_l is the position of the lth unit cell, $\hat{\underline{z}}$ is the polarization vector of the l th atom, defining the direction of the displacement. Exp $(-W_k)$ is the Debye–Waller factor originating from the harmonic motion of the ions, W depends on temperature and momentum $\hbar Q$ and is a measure of the mean square ionic displacements.

The upper and lower sign in Equation (3.18) refer to phonon annihilation and creation respectively.

Two–phonons and higher order processes are usually regarded as background but can be important at higher temperatures.

For coherent scattering the zero phonon term corresponds to the well known elastic Bragg scattering with cross–section:

$$\left(\frac{d\sigma}{d\Omega}\right)_{coh} + \sum_{\tau} \delta\,(Q - 2\pi\,\underline{\tau})\,|F(\underline{\tau})|^2 \qquad (3.20)$$

Equations (3.18) and (3.20) contain δ functions for energy and crystal momentum conservation, and these conditions enable the determination of dispersion curves. The conservation equations are:

$$E_i - E_f = \pm \hbar w_j(\underline{q}) \qquad \text{(energy)} \qquad (3.21)$$

$$\hbar(\underline{K}_i - \underline{K}_f) = \hbar\underline{Q} = \hbar(\underline{G} - \underline{q}) \qquad \text{(momentum)}$$

The measurement of phonon scattering, with the triple axis polarised neutron spectrometer (IN20) will be described in detail in the next chapter.

The incoherent one–phonon cross–section does not involve a momentum δ function, and is given by [58, 59]:

$$\left(\frac{d^2\sigma}{d\Omega dE}\right)_{\substack{\text{incoh}\\ 1\text{ ph}}} = \frac{\sigma_{in}}{4\pi}\frac{N}{\hbar}\frac{K_f}{K_i}e^{-2W}\left[\frac{\hbar Q^2}{2m}\cdot\frac{Z(\omega)}{\omega} < n(\omega)+1 >\right] \qquad (3.22)$$

where n(w) is the number of quanta in the mode and is given by:

$$n(\omega) = [\exp(h\omega)/K_B T) - 1] \qquad (3.23)$$

$Z(\omega)$ is the phonon frequency distribution function, m is the mass of a nucleus and N is the number of atoms in the sample.

3.6 POLARISED NEUTRONS

3.6.1 Introduction

The polarised beam technique has been widely utilized for the study of spin density distributions in ferromagnets, following the pioneering work of Shull and Nathans [63] in the 1950's. This technique requires only a double axis configuration, without analyzer. Then in 1969, the classic paper by Moon, Riste and Koehler [64] appeared, which advocated the use of polarisation analysis after scattering.

Polarised neutrons provide a very precise method of separating magnetic from non–magnetic scattering, since a magnetic interaction can change the spin state of a neutron, whilst a non–magnetic interaction cannot. This is particularly valuable when the magnetic and

nuclear unit cells are coincident. If the magnetic moments of the sample all point upwards, neutrons with spin–up will be scattered with amplitude $|b + e|^2$ and neutrons with spin–down with amplitude $|b - e|^2$ (due to the presence of the orientation factor $p.q^{\perp}$). Measurement of the scattering amplitude for some reflection (hkl) with incident neutrons polarised first parallel and then antiparallel to an external magnetic field applied to the sample, enables the ratio of magnetic to nuclear scattering e/b to be determined for that reflection. This ratio is of crucial importance in measurements of the magnetic form factor. This technique is employed using the polarised neutron diffractometer D3B at the ILL, Grenoble.

The instrument used in performing the polarised neutron scattering experiments is discussed in the next chapter.

3.6.2 Elastic Coherent Scattering

The polarisation dependence of the differential neutron elastic scattering cross–section may be written [65]:

$$\frac{d\sigma}{d\Omega} \alpha [b^2 + 2be\hat{q}.\hat{\lambda} + p^2q^2] \qquad (3.24)$$

where e and b are the magnetic and nuclear scattering amplitudes respectively. $\hat{\lambda}$ is a unit vector in the direction of the spin of the incident neutron and $\hat{q}$, the magnetic interaction vector. p is an effective magnetic scattering amplitude and, for a spin moment only, can be written as, $p = 0{\cdot}2695\ 10^{-12}\ \mu.f$ cm. Where f is the form factor and μ is the magnetic moment per magnetic atom. The crystal is magnetised perpendicular to the scattering vector and the Bragg intensities measured with the neutron polarisation both parallel and anti–parallel to the applied field directions. The ratio of the Bragg intensities for the two polarisation directions is given by [65, 66, 67]:

$$R = (b+e)^2/(b-e)^2 \qquad (3.25)$$

$$= (1+\gamma)^2/(1-\gamma)^2$$

where $\gamma = e/b$ is the ratio of magnetic to nuclear structure factors.

For 3d metals the solution $|\gamma| < 1$ is usually correct, thus knowing the value of b, the magnetic structure factor can be obtained. This is, on the other hand, proportional to the neutron magnetic form factor f(k) whose Fourier transform gives information about the spatial distribution of the magnetic moment densities.

This method is used extensively by Ziebeck, Brown, and their collaborators [68] in a series of pioneering studies of magnetic scattering from 3d metals and compounds.

3.6.3 Inelastic coherent scattering

The cross–section for the vibrational scattering of polarised neutrons from a magnetic crystal may be written [65, 66]

$$\frac{d^2\sigma}{d\Omega dE} \alpha \{b_v^2 + 2b_v m_v p \cdot S^{\perp} + P^2 (S^{\perp})^2] \cdot \delta[K + q - 2\pi\tau] \cdot \delta[\frac{h^2}{2m_o}(K_f^2 - K_i^2 \pm \hbar w] \qquad (3.26)$$

where b_v is the nuclear vibrational scattering amplitude, q is the phonon momentum or propagation vector, m_o is the neutron mass, $\hbar w$ is a quantum of vibrational energy and m_v is the magneto–vibrational scattering. It is again seen that the polarisation dependence of the scattered intensity is similar to equation (3.32).

The polarisation ratios of the intensities of Bragg peaks associated with phonons propagating in the principle symmetry direction may be measured as a continuous function of $\underline{q}$ throughout the Brillouin Zone.

For a ferromagnetic sample, the magnetic electrons are expected to follow the nuclei in their thermal oscillation. Thus, in addition to usual

follow the nuclei in their thermal oscillation. Thus, in addition to usual coherent nuclear scattering by phonons there is also coherent magnetic scattering, called magneto–vibrational scattering, with the same dependence on energy and momentum transfer as for the nuclear scattering.

3.6.4 Magneto–vibrational scattering

The interaction between the vibrational and magnetic degrees of freedom are of great importance. Information about the way in which phonon modes are coupled to the magnetisation may be obtained by measurements of the phonon intensities of Bragg peaks. Consequently, the polarisation ratios may be measured for different phonon polarisations. To the extent that the magnetic electrons follow the nuclei exactly, the form factor of the magneto–vibrational scattering will be identical with that obtained from the elastic scattering experiment.

This technique was first used by Steinsvoll et al to study iron and nickel [66]. Their measurements demonstrated that, whereas for nickel the magnetic density giving rise to the magneto–vibrational scattering was indistinguishable from that giving rise to elastic scattering, for iron there was a small but significant difference.

The ratio of the magneto–vibrational to the nuclear vibrational scattering is:

$$\gamma^2 = (f(K)\,\mu/b)^2 \qquad (3.27)$$

where f(K) is the magnetic form factor, μ is the mean magnetic moment per atom and b is the mean nuclear scattering length.

CHAPTER FOUR

EXPERIMENTAL TECHNIQUES AND EQUIPMENT

4.1 ALLOY PREPARATION

All the Heusler alloys used in this project were prepared by P. J. Webster and M. R. M. Mankikar at Salford University in the Department of Physics.

The alloys were prepared by arc melting the appropriate proportions of spectrographically pure constituents. After the initial melt, the alloys were turned over and re–melted to ensure good mixing. Care was taken to minimise any loss by vaporization. The resulting ingots were crushed into a fine powder using a steel pestle and mortar. These powders were used for X-ray, specific heat, neutron diffraction and magnetic susceptibility studies. All the samples were slow cooled after being sealed in a quartz tube under vacuum and annealed for 24 hours at 800°C.

Single crystals of Fe_xNi_{1-x} alloys containing x = 66, 50, 22 and were prepared in the Department of Metal Science, Kyoto, Japan, and kindly supplied by Y. Nakamura.

4.2 X-RAY DIFFRACTION

The structure of the Heusler alloys were initially investigated using X–ray diffraction techniques at room temperature with a Philips diffractometer. A broad focus PW2103/100 copper radiation (Cu(kα)) tube was used in conjunction with a PW1050/25 vertical goniometer. A compact amount of the finest fraction of the powder was enclosed in an aluminium sample holder, which was mounted at the centre of the goniometer. A proportional detector PW1965/20/30 was used with the diffractometer, and after electronic processing the ouput was displayed on a servoscribe pen recorder.

A small error in the measurement of the Bragg angle θ produces an error in the calculated value of the lattice constant a_0. To obtain the lattice parameter more accurately, the Nelson–Riley extrapolation is used [69].

This method uses a plot of the lattice constants, a_0, against the functions $1/2(\cos^2\theta/\sin\theta + \cos^2\theta/\theta)$. The line is extrapolated back to $\theta = 90°$ to give the exact value of a_0.

4.3 NEUTRON SCATTERING MEASUREMENTS

All the results presented in this thesis were obtained using the high flux reactor (HFR) at the Institut Laue–Langevin, Grenoble, France. The high neutron flux is provided by the nuclear fission of uranium 235 within a single fuel element. This fuel element consists of approximately 9kg of uranium enriched to 93% by uranium 235. The thermal neutron flux, in equilibrium with the D_2O moderator (300K), has a peak in the Maxwellian distribution at 1.2Å. The range of neutron wavelength is extended by the inclusion of a hot source (10 dm^3 graphite at 2400K) or the cold source (25 dm^3 of liquid deuterium at 25K) giving an enhancement of the neutron intensity in the wavelength range $0{\cdot}4 < \lambda < 0{\cdot}8$ Å and $\lambda < 4{\cdot}0$ Å respectively [70] (figure 4.1). The experimental data was collected mainly on three different thermal neutron instruments, D2B, D1A and IN20.

4.3.1 Neutron diffraction and structural refinements

Accurate determination of the magnetic and chemical order of the Heusler alloys were made using neutron powder diffraction techniques. Results were obtained on D1A and D2B at ILL, Grenoble. The D2B instrument is a high resolution, high intensity version of D1A and is installed on the thermal reactor beam H11. The arrangement of the diffractometer is shown schematically in figure 4.2. A wide choice of the wavelengths from 1·05 to 3·155 Å can be obtained by using different reflections from a germanium monochromator. The instrument has 64He^3 detectors which are spaced at 2·5° intervals to cover the full 165° scattering range [71]. The detector angle, sample angle, monochromator angle (wavelength) and sample

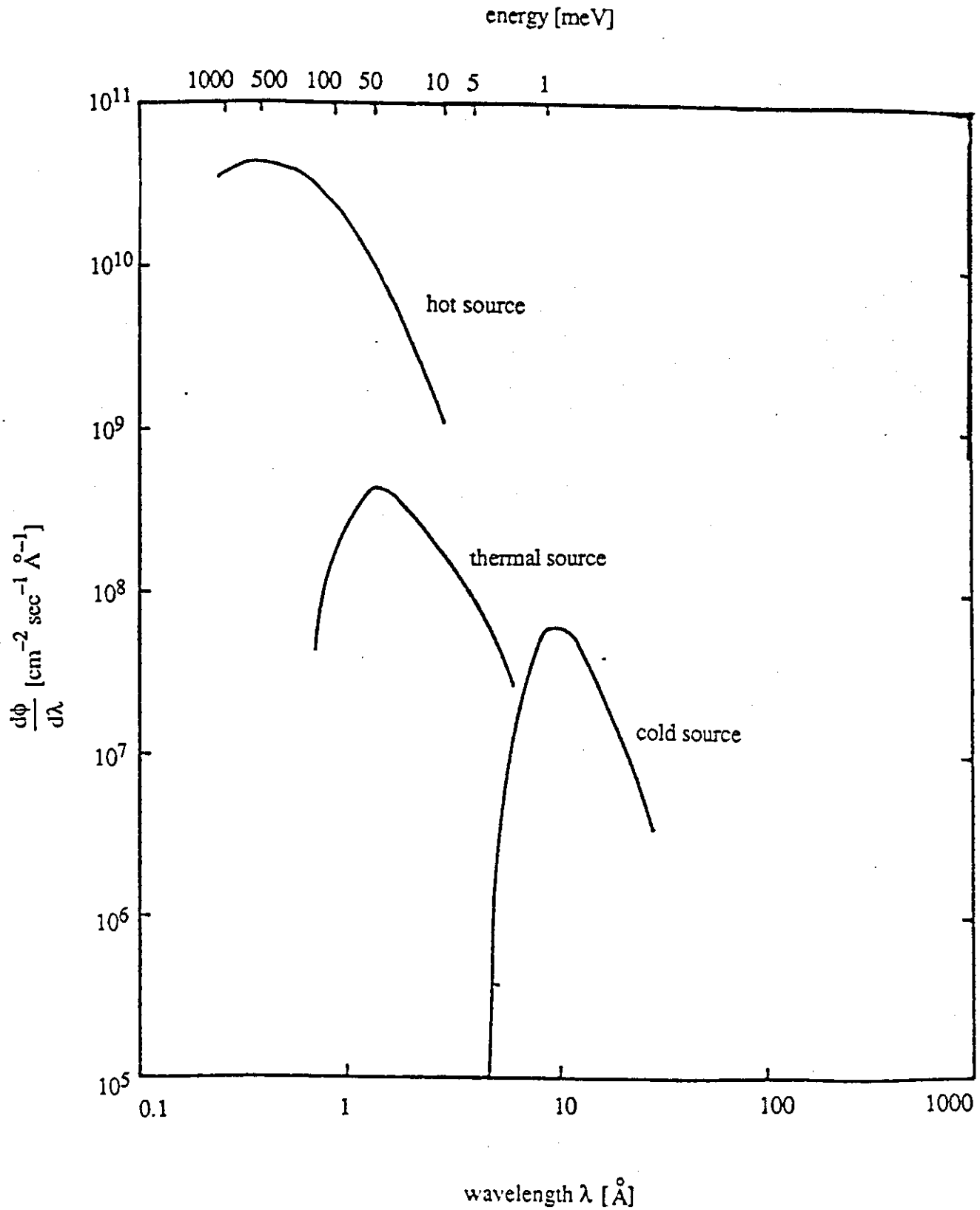

Figure (4.1) Neutron flux produced by the three principle neutron sources available at the Institut Laue Langevin

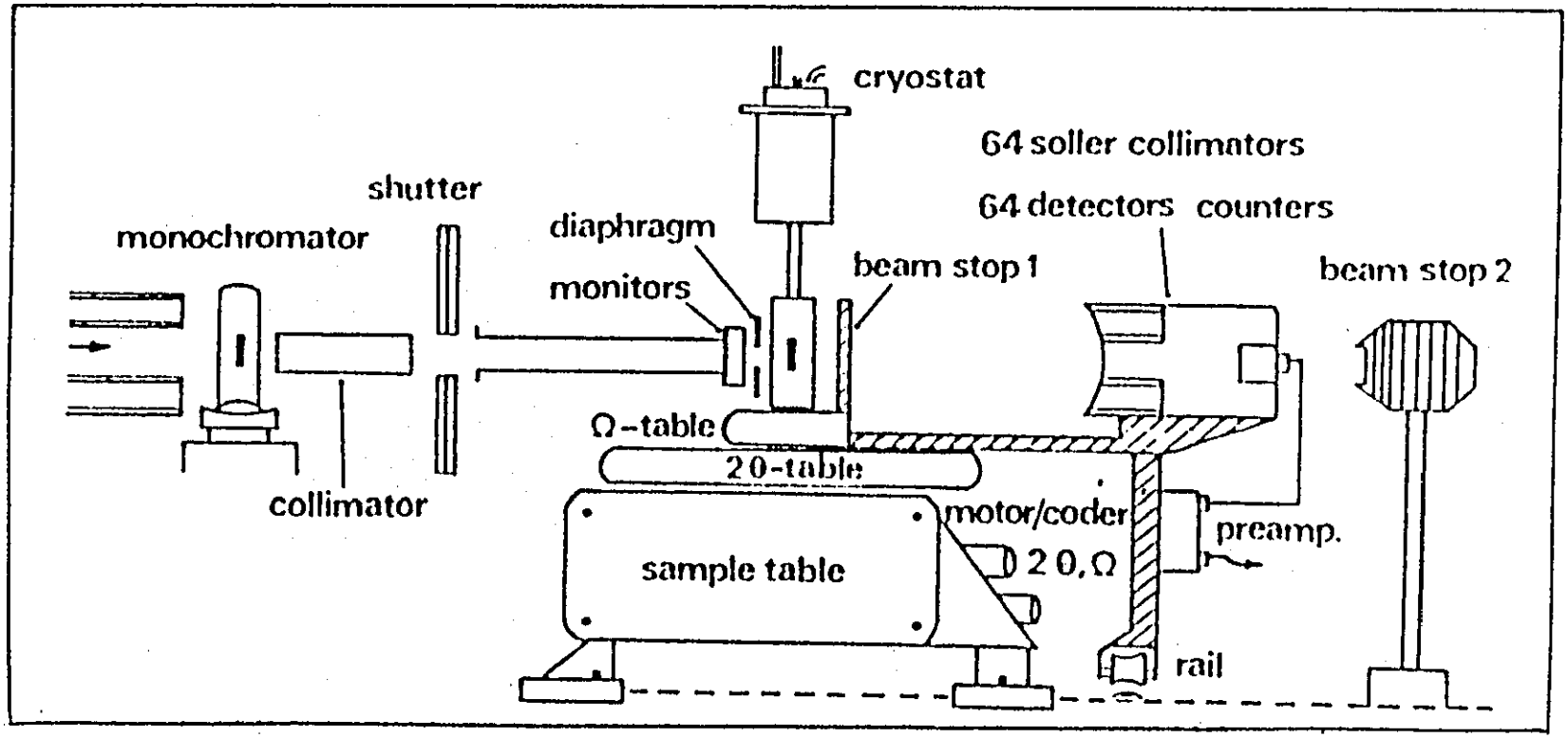

Figure (4.2) Schematic view of D2B

temperature range are set by individual microprocessor controllers receiving commands from a PDP11/24 computer

The powder specimens was contained in a cylindrical sample can made out of vanadium, for which the coherent scattering is negligible. Cans of 5 mm diameter and 40 mm length were used and were mounted in a standard orange ILL flow cryostat on the table of the diffractometer. A polaroid camera fitted with a LiF scintillator sensitive to thermal neutrons was used to position the specimen in the neutron beam. The safety window blocking the neutron beam was opened for approximately one second, sufficiently long enough for the neutrons to expose the film. Scans were made at several temperatures between 5K and room temperature. The 2–theta angle covered in each scan ranged from 0° to 165° with a step width of 0·025° in 2–theta. The wavelength of the diffractometer was 1·594 Å which was produced by the (335) plane of the germanium monochromator. A fixed monitor count was used for each run and the integrated intensities were obtained by subtraction of the back–ground count from the count obtained for the Bragg peak.

Manual integration of Bragg peak is unreliable for complex structures because of the overlap of adjacent Bragg peaks. For this reason, a structure refinement program was used to determine the structure of each Heusler alloy [72]. This program is in two parts which should be run separately. The first is the Multipattern Preprofile Program (MPREP). This particular program required the specification of an input file, containing the following information:

(i) The number of phases (maximum of three)

(ii) The unit cell parameters of each phase and the neutron wavelength

(iii) The half width parameters U, V and W of the Bragg reflections which are described by a Gaussian peak of full width H viz: $H^2 = U\tan^2\theta + V\tan\theta + W$

(iv) Background values from the original diffraction profile

(v) 2θ regions to be excluded from the calculations

(vi) Approximate zero 2θ angle of the counter.

The second part is the Multipattern Rietveld Program (MPROF) [72]. This program needed different parameters to construct a model for a crystal structure such as:

(i) space group

(ii) atomic scattering factors

(iii) site occupation factor

(iv) atomic positions

etc.

The refinement was carried out using the appropriate space groups e.g. $Fm\bar{3}m$, $R\bar{3}m$ and I4/mm, with the atoms located at positions as listed in Table 7.6.

The space groups that we have used are suitable in describing the symmetry relationships which have fixed magnetic moment orientations relative to the antiferromagnetic AF_3A and AF_2 structures. The AF_3A magnetic structures occur as a result of the lattice distortion from the cubic cell below the Neel temperatures, with the magnetic unit cell being twice that of the chemical cell (using cubic indices).

A program GETSFZ was used to generate a listing of the reflections expected for these space groups with relevant lattice parameters using the Cambridge Crystallographic Subroutine Library. These were compared with the data and it was found that all the reflections listed were present in the profile.

The refined parameters included the positional parameters, peak shape parameters, temperature factor and the lattice constant, together with other parameters such as zero offset, scale factor etc. Altogether there were 15 parameters to be determined by the least square fit for each diffraction pattern. The intensity of 52 nuclear reflections for both space groups were observed.

The R factor is defined by:

$$R = \frac{\sum_{i=1}^{n} |S\, F_i\, obs - F_i\, calc|}{\sum_{i=1}^{n} S\, F_i\, obs} \qquad (4.1)$$

where

F_i obs = observed structure factor

F_i calc = calculated structure factor

S = scale factor

The scale factor S is defined by:

$$S = \frac{\sum_{i=1}^{n} F_i \text{ calc}}{\sum_{i=1}^{n} F_i \text{ obs}} \qquad (4.2)$$

In a least square fit, one attempts to minimise the function M as:

$$M = \sum_{i=1}^{n} W_i \left| S\, F_i \text{ obs} - F_i \text{ calc} \right|^2 \qquad (4.3)$$

W_i is the weighting associated with each structure factor, where:

$$W_i = \frac{1}{(\Delta F_i \text{ obs})^2} \qquad (4.4)$$

The agreement between the powder diffraction pattern and theoretical model is measured by the nuclear R factor R_n. The R factor is defined as:

$$R_n = 100 \frac{\sum_{i=1}^{n} \left| \left(F_N \text{ obs (i)}\right)^2 - \left(F_N \text{ calc (i)}\right)^2 \right|}{\sum_{i=1}^{n} \left(F_N \text{ obs (i)}\right)^2} \qquad (4.5)$$

where F_N(i) is the nuclear structure factor of the ith reflection out of a total number of n reflections with obs and calc indicating either the observed or calculated values of the nuclear structure factors.

The main technique used to separate the nuclear and magnetic contribution was to repeat the experiment twice; once above and once below the transition temperature. In magnetic scattering, the form factor falls off with $\sin\theta/\lambda$, and the detailed shape depends upon the distribution of the unpaired electron spins. The nuclear scattering amplitude shows no regular variation with atomic number, and does not change with the scattering angle 2θ.

4.3.2 Inelastic Neutrons Scattering

One very sensitive way to study the interaction between the magnetic and lattice degrees of freedom is through the polarisation dependence of the magneto–vibrational scattering.

The instrument IN20 is ideal for this purpose. IN20 is a three–axis spectrometer equipped for polarisation analysis and is installed on the thermal beam H13 figure (4.3). The principle features of this instrument are described briefly as follows:

The incident wavevector $\underline{k}_i$ is selected using a Cu(200) monochrometer crystal to produce an unpolarised monochromatic incident beam. If d_M is the spacing between the appropriate scattering planes of that crystal, then by Bragg's law:

$$|k_i| = \pi/d_M \sin\theta_M \qquad (4.6)$$

similarly, the (111) reflection of Cu_2MnA1 was used as analyser to define a final wavevector $\underline{k}_f$ for neutron reaching the detector where:

$$|k_f| = \pi/d_A \sin\theta_A \qquad (4.7)$$

The neutrons scattered from the monochromator pass through a collimator towards the sample. This collimator is mounted in a drum of shielding which surrounds the monochromator to protect against radiation. The collimation used starting from the monochromator was 30', 40', 40', 40' and the spectrometer was operated in the constant $\underline{k}_f$ mode with $\underline{k}_f$ either 2·66 or 4·1 A^{-1}. A graphite filter was used to eliminate higher order contamination of the beam, and a Mezei flipper was placed just in front of the analyser crystal.

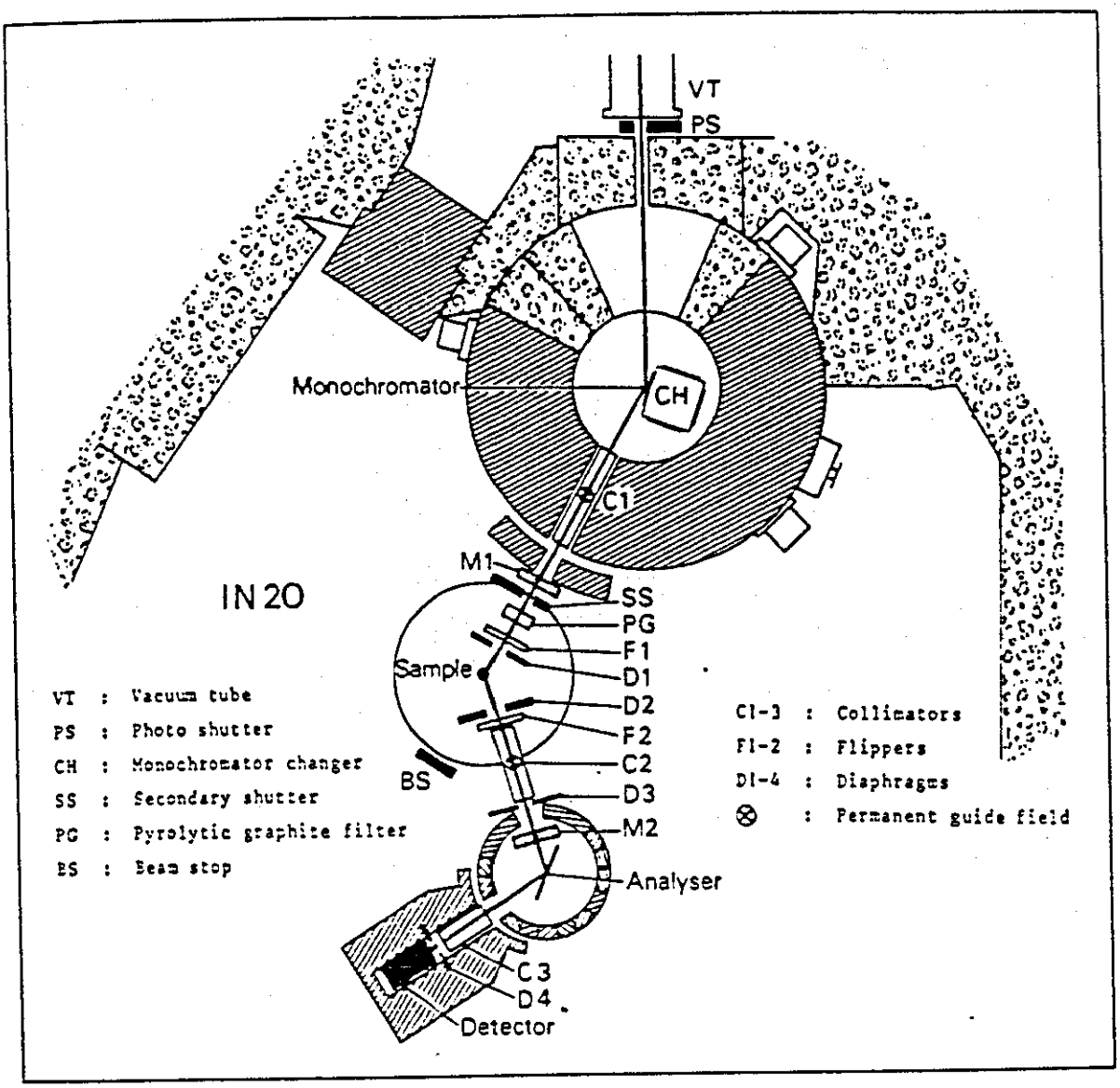

Figure (4.3) Schematic view of the triple axis spectrometer with polarisation analysis, IN20

The instrument has a He^3 detector, and most operations of the spectrometer and power supplies are controlled by the instrument computer PDP11/73.

The measurements were made with the sample placed in a vertical magnetic field provided by a superconducting magnet: the field at the sample was set to 2T which was sufficient to saturate the sample at 100 K.

Dispersion curves for the phonon and magnon modes in the three principle symmetry directions of $Fe_{65}Ni_{35}$ were investigated. A series of constant E scans were carried out. In each scan the scattered intensity was measured at each point with the flipper on, and then with it off, to obtain the polarisation dependence of the scattered intensity.

The ratio between the counting rates for the polarisation state is known as the "flipping ratio" is recorded for each reflection and these ratios are the data of the experiment. The polarisation ratio is given by:

$$R = \frac{b^2 + 2be + e^2}{b^2 - 2be + e^2} = \frac{(1+\gamma)^2}{(1-\gamma)^2} \text{ where } \gamma = \frac{e}{b} \qquad (4.8)$$

where b and e are the nuclear and magnetic structure factors respectively.

4.3.3 Production of a polarised Monochromator beam

Neutrons are spin 1/2 particles whose direction are normally random in space. If the neutron beam can be polarised then a significant increase in information concerning the scattering process can be obtained.

The technique of polarisation involves arranging for all incident neutrons impinging on the sample to have their spins aligned in the same direction. This is normally achieved by using a ferromagnetic monochromating crystal for which the magnetic and nuclear structure factors for a low angle reflection have the same amplitude i.e. b = e. The scalar product $\hat{p} \cdot \hat{\lambda}$ in

the cross section for Bragg scattering (equation 3.24) becomes +1 for upward (+) and −1 for downward (−) pointing spin vectors, so that scattering amplitudes for upward and downward pointing spins will be (b + e) and (b − e) respectively. The corresponding intensities are proportional to $(b + e)^2 = (2b)^2$ and $(b - e)^2 = 0$ respectively, so that the reflected beam will consist of upward pointing spins only.

There are several monochromators which fulfil this condition, in particular the (002) reflection of $Co_{92}Fe_{08}$ and (111) reflection of Cu_2MnAl (Heusler Alloy). The choice of monochromator is determined by the degree of polarisation, it's reflectivity and the resolution $\Delta\lambda/\lambda$ required.

Face–centered cubic cobalt containing 8% iron ($Co_{92}Fe_{08}$) has equal nuclear and magnetic cross sections for the 002 reflections. For this reflection $\gamma = 1$, the d spacing is 1·767Å and $\lambda/2$ contamination is small. Unfortunately, cobalt has a relatively high thermal neutron absorption cross–section (37 barns) so that only thin crystals can be used and hence the intensity of the polarised beam is limited. An alternative polariser that is sometimes used is the (111) superlattice reflection of the Heusler alloy Cu_2MnAl. The polarisation ratio for the (111) reflection is $\gamma \sim -1$ and ~ 95% polarisation is usually achieved. The Heusler crystal is much less absorbing and large crystals may be used to increase the intensity by a factor of 4 times the intensity achieved with Co/Fe. The Heusler alloy has particular application for wavelengths greater than 2Å because of the large d spacing of the polarising reflection. For long polarised wavelengths crystals are now being replaced by polarising mirrors and multi–layer devices (supermirrors) [37], for certain specialist applications.

The spectrometer was aligned using a Heusler alloy (Cu_2MnAl) as both monochromator and analyser. A Mezei flipper placed in front of the analyser crystal enabled the polarisation of the beam to be reversed.

The polarisation of the instrument was checked by driving the spectro–meter into the straight through position and measuring the ratio of the spin up and spin down count in the absence of a sample. The ratio of the two

counts "flipping ratio" was found to be 16. An estimate of the polarisation was determined using:

$$P = \frac{R-1}{R+1} \qquad (4.9)$$

The ratios of the magnetic to nuclear structure factor γ of the sample were obtained from the polarisation flipping ratios after making corrections for incomplete polarisation reversal in the manner suggested by Brown and Forsyth (1964) [67, 122]:

$$R = (1 + 2P_i\gamma + \gamma^2)/(1 - 2P_i e\gamma + \gamma^2) \qquad (4.10)$$

where P_i is the incident polarisation and $e = 2E-1$, where E is the fraction of spins reversed by the flipper, and e is the flipping efficiency. Thus

$$\gamma = \frac{P_i(eR+1) \pm [P_i^2(eR+1)^2 - (R-2)^2]^{1/2}}{R-1} \qquad (4.11)$$

The values of P_i using standard crystals of Cu_2MnA1 for which $\gamma = -1$ and Co/Fe for which $\gamma = +1$ in place of the specimen and a Cu(200) mono-chromator, and e were determined.

Thus

$$R(111)\,(\text{Heusler}) = \frac{1-P_i}{1+eP_i}$$

and (4.12)

$$R(200)\,(\text{Co/Fe}) = \frac{1+P_i}{1-eP_i}$$

Typically R(Heusler) = 0·029 and R(Co/Fe) = 16·0, yielding e = 0·94 and P_i = 0·94.

4.3.4 Half wavelength contamination in the polarised incident beam

A monochromator set to diffract neutrons of wavelength λ from a set of Bragg planes (hkl) will also be correctly oriented to diffract neutrons of wavelength $\lambda/2$ from the planes (2h, 2k, 2l). If the structure factor for this reflection is not zero, there will be a $\lambda/2$ contamination in the monochromatic beam. For a Cu_2MnA1 monochromator, the nuclear scattering amplitude of the (222) reflection is more than twice that of the (111) used to polarise the beam and hence significant $\lambda/2$ contamination occurs. This is minimised to a negligible level by a suitable choice of filter which captures unwanted neutrons by a resonant absorption process.

The $\lambda/2$ component is very weak for a $Co_{0.92}Fe_{0.8}$ monochromator working at $\lambda < 1\text{Å}$ on a thermal reactor hole. However in the case of a hot source instrument, the $\lambda/2$ contribution may need to be attenuated and corrected for. The maximum intensity in the neutron spectrum from the hot source occurs between $0{\cdot}4 - 0{\cdot}5\text{Å}$ and the $\lambda/2$ contribution becomes important for wavelengths greater than $0{\cdot}7\text{Å}$.

By measuring the integrated intensity of the same reflection at both λ and $\lambda/2$ one obtains the fluxes $J(\lambda)$ and $J(\lambda/2)$ which allow corrections to be made in deriving a true value of γ from the observed flipping ratio [73]:

$$C = \frac{J(\lambda/2)}{8J(\lambda)} \qquad (4.13)$$

4.3.5 Measuring Phonon Dispersion Relations

The advantage of a three axis spectrometer over a two axis diffractometer is that in addition to measuring the neutron intensity as a function of momentum transfer Q, the use of the third axis enables the neutron intensity to be measured as a function of energy hw, i.e the inelastic in the scattering.

The energy transfer hw in inelastic neutron scattering meaasurement is given by

$$\hbar\omega = E_i - E_f = \frac{\hbar^2}{2m}(K_i^2 - K_f^2) \qquad (4.14)$$

and the momentum transfer is defined by:

$$\hbar Q = \hbar(K_i - K_f) \qquad (4.15)$$

where K_i and K_f are the incident and final wavevectors and E_i and E_f are the corresponding energies of the neutron. From equation (4.14) the Bragg condition is obtained when $|K_i| = |K_f|$ and the scattering vector $Q = \tau$, a reciprocal lattice vector. For inelastic scans, $\hbar\omega \neq 0$, and either $|K_i|$ or $|K_f|$ is fixed. For fixed $|K_f|$ the measured intensity is directly proportional to the dynamic structure factor $S(Q, \omega)$. Inelastic scans are usually performed with either Q fixed and $\hbar$w varied or $\hbar$w fixed and Q varied. These two scans are diagrammatically represented in figure (4.4). The choice of scans depends on the resolution in energy and momentum of the spectrometer and the nature of the scattering surface to be studied.

4.4 MAGNETIC MEASUREMENTS

The magnetic properties of the Heusler alloys were investigated using a Cahn RH Automic Electrobalance (as shown in figure 4.5). The susceptibilities of the alloys were measured in five applied fields over the temperature range 77K to 300K. The balance measured the force F_Z exerted on a small specimen of mass m, by a magnetic gradient $\left(\frac{\partial H}{\partial Z}\right)$. The force is given by:

$$F_Z = m\chi H\frac{\partial H}{\partial Z} \qquad (4.16)$$

where χ is the susceptibility.

The measurement of magnetic susceptibility by using equation (4.16), is called the Faraday method. Since it is difficult to measure $\partial H/\partial Z$ accurately the absolute value of the susceptibility was measured by comparison of the force acting on standard specimen of known susceptibility and with that of the specimen under investigation.

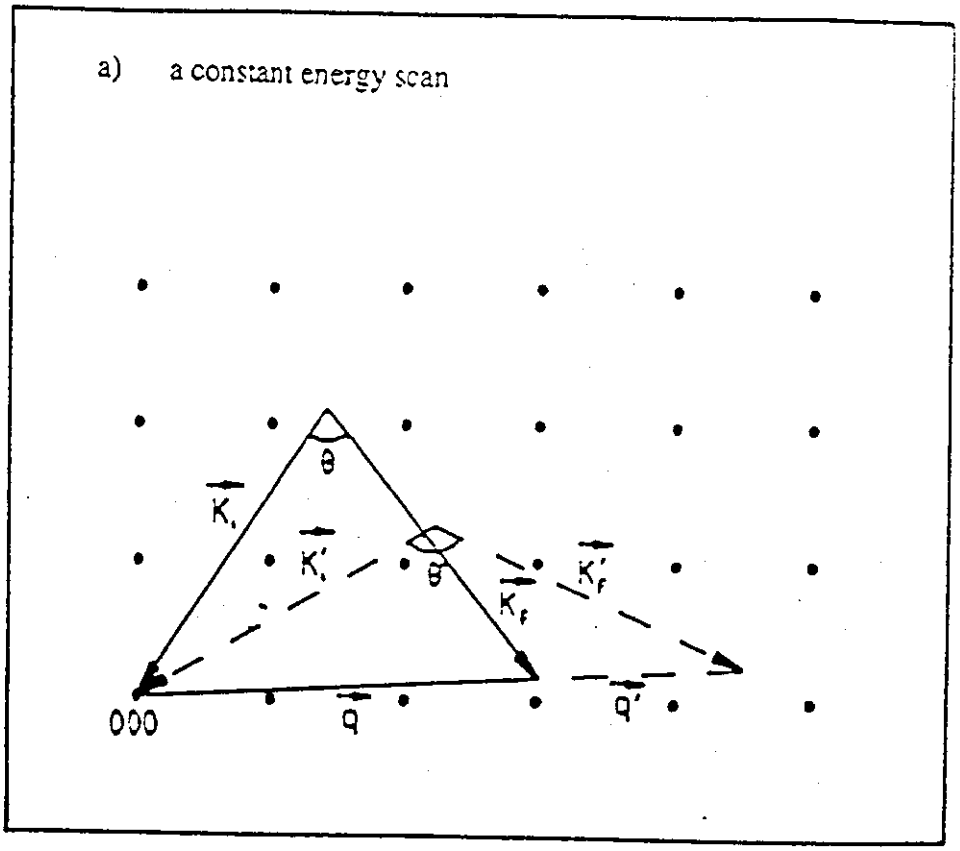

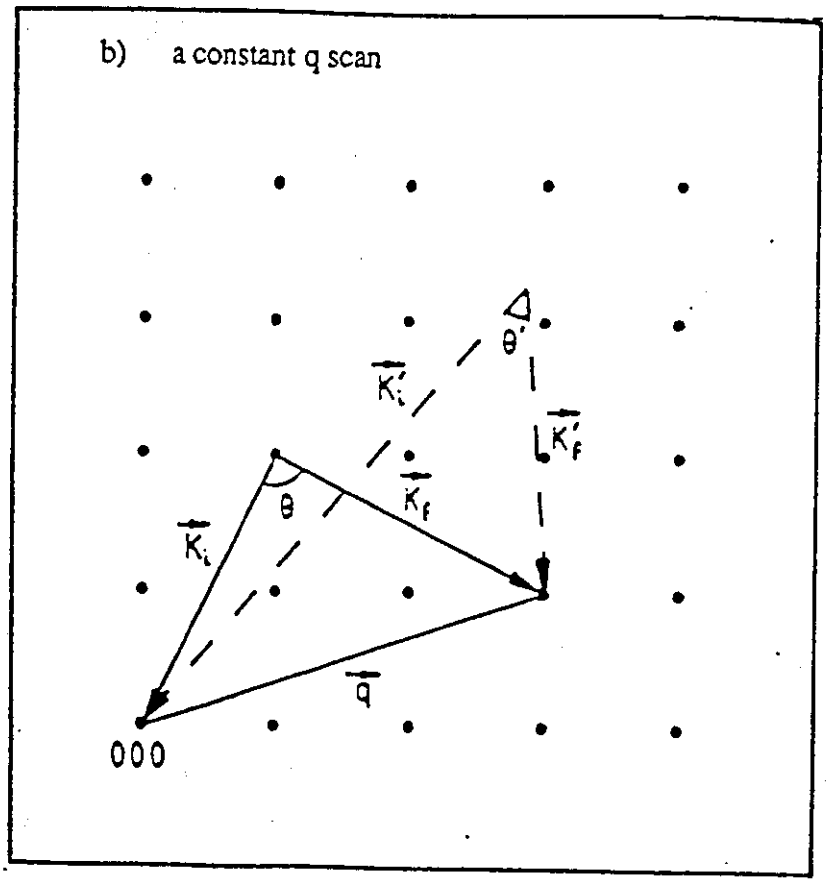

Figure (4.4) Schematic representation of:

a) a constant energy scan in reciprocal space
b) a constant q scan in reciprocal space

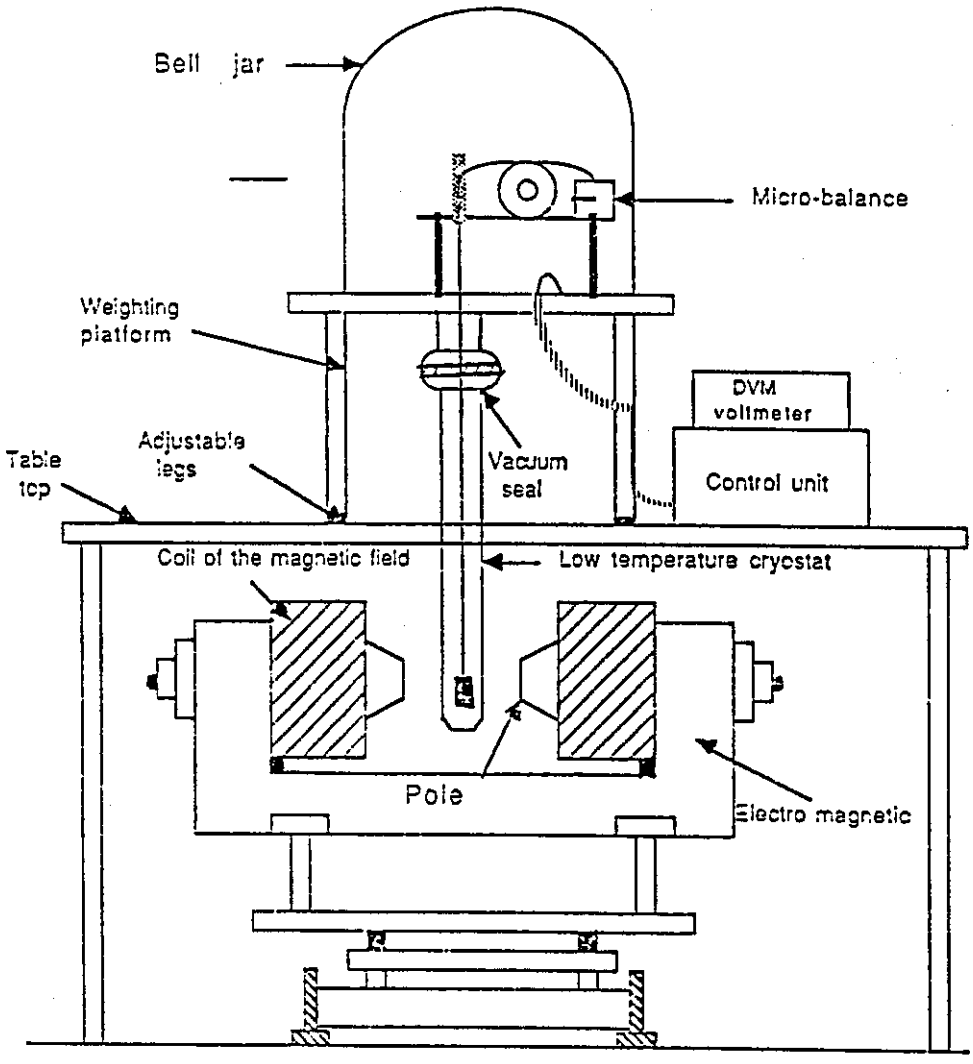

Figure (4.5) Low Temperature Magnetic susceptibility System

The instrument was calibrated using pure materials of known susceptibility for example solid cylindrical samples (4 x 3 mm) of pure palladium and niobium and a powder sample of Pd_2MnIn.

A Newport electromagnet was used to produce magnetic fields of sufficiently large gradient to measure magnetic susceptibilities of antiferro–magnetic materials. The magnet had 10 cm diameter plane pole tips separated by a 3·5 cm gap. The power supply for the electromagnet was a 240 VDC(ST-240) supply, which was capable of producing a maximum current of 20 amps. The optimum vertical position of the specimen, i.e. the region of constant $H\frac{\partial H}{\partial Z}$, was determined from a plot of $H\frac{\partial H}{\partial Z}$ against the vertical position of a fluxmeter.

The copper specimen holder was suspended from the Micro–balance by a lightweight rod of material with high resistance, e.g. a thin walled stainless tube of length 52 cm and 4 mm diameter. The Micro–balance assembly was placed at the top of an aluminium supporting plate and this plate was fixed on a wall. The cryostat was sealed to the bottom of this plate by an 'O' ring seal. The Micro–balance assembly was enclosed in an airtight glass Bell jar, as shown in figure (4.5).

An ACF 1200 continuous flow cryostat and a 3120 temperature controller, both manufactured by Oxford Instruments was used. Stable temperatures were determined using a gold–iron (Au–0·03% Fe) thermocouple.

The vacuum jacket of the cryostat was maintained to a pressure of 10^{-5} mbar. The vacuum equipment consisted of an oil diffusion pump and a rotary pump. The rotary pump was used to evacuate the cryostat to a pressure less than 10^{-1} mbar, and the diffusion pump was used to achieve vacuums to less than 10^{-5} mbar.

Corrections for the specimen holder were obtained by measuring the magnetic forces exerted with the empty rod and these values were subtracted from readings observed with the sample. The magnetic susceptibility of a specimen can be determined from the following relationship:

$$\chi_{Heusler} = \frac{F}{M}\left(\frac{M}{F}\right)_{Standard} \qquad (4.17)$$

where χ, M and F are susceptibility, mass and the exerted magnetic force respectively.

4.4.1 Automation of Magnetic Susceptibility Measurements

The experiment involves the measurements of the magnetic susceptibility of the specimen as a function of both field and temperature. If carried out manually the measurements are time consuming with one run taking at least one day. For this reason, a computer control measurement was designed by W. Hussen. The data acquisition was controlled by a BBC micro–computer. A block diagram of the apparatus is given in figure (4.6).

The temperature of the sample is set by a temperature controller through the computer and the electromagnetic current is set by the control unit through the user port of the computer. The voltage from the microbalance, which is proportional to the magnetic force acting on the sample for different magnetic fields, is measured by a DVM. The measured voltage signal is transferred from the DVM to the computer through an IEEE Interface. The magnetic susceptibility of the sample for several fields was then obtained by using equation (4.17). The same measured sequence procedure is repeated for the next temperature.

Susceptibility and reciprocal susceptibility versus temperature curves were plotted for paramagnetic and antiferromagnetic Heusler alloys. Neel temperatures θ_N were measured, and paramagnetic Curie temperatures θp were extrapolated. From the slope of the reciprocal susceptibility the Bohr magneton numbers were obtained.

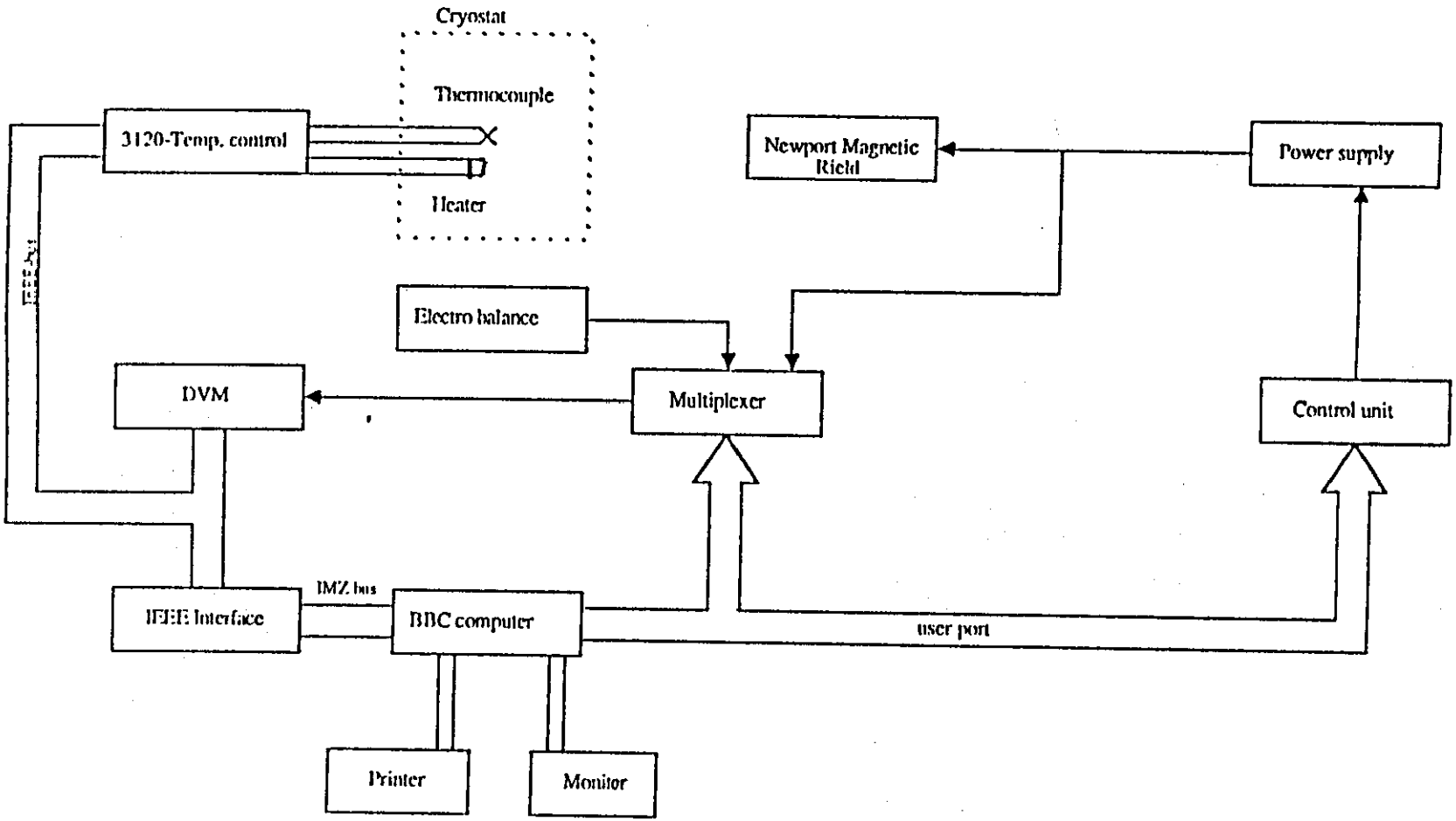

Figure (4.6) Schematic Magnetic Susceptibility

4.5 SPECIFIC HEAT MEASUREMENTS

Two methods of determining the specific heats between liquid nitrogen 77°K and room temperature have been used. The first method involved continuous heating using a Differential Scanning Calorimeter (TA 3000 System), and the second method involved a pulse technique. The principle procedure of using these techniques are described briefly as follows:

4.5.1 The Differential Scanning Calorimeter (DSC)

The DSC is a device for making rapid and accurate evaluations of the thermal properties of materials. The basic idea is that a sample which is enclosed in a small container (pan) and a reference pan, which is empty, are heated at a selected rate. The energy required to heat both sample and reference is monitored and the difference between them provides a measure of the energy needed to heat the sample through a known temperature step and hence its specific heat. The basic output of the device is the difference in the energy flow rate as a function of temperature. The output can either be presented graphically or printed out in a table.

In most measurements a blank run using an empty pan was done and the resulting data stored and subtracted from the results for the sample.

4.5.2 Pulse Heating Technique

Pulse calorimetry is a technique, in which a measured amount of electrical heating power is injected into the specimen over a fixed period of time. The sequence of operations of a pulse calorimeter is illustrated in terms of a temperature time curve in figure (4.7).

During the period AB, the temperature is measured repeatedly whilst the specimen is maintained in good thermal isolation. During the heat pulse, BC, it is not necessary to measure the temperature, but the heating power (EI) must be measured from the dc voltage drop E across the heater and the current I through a series resistor heater. The heating power (EI) is almost constant, as the heater resistance changes slightly with temperature.

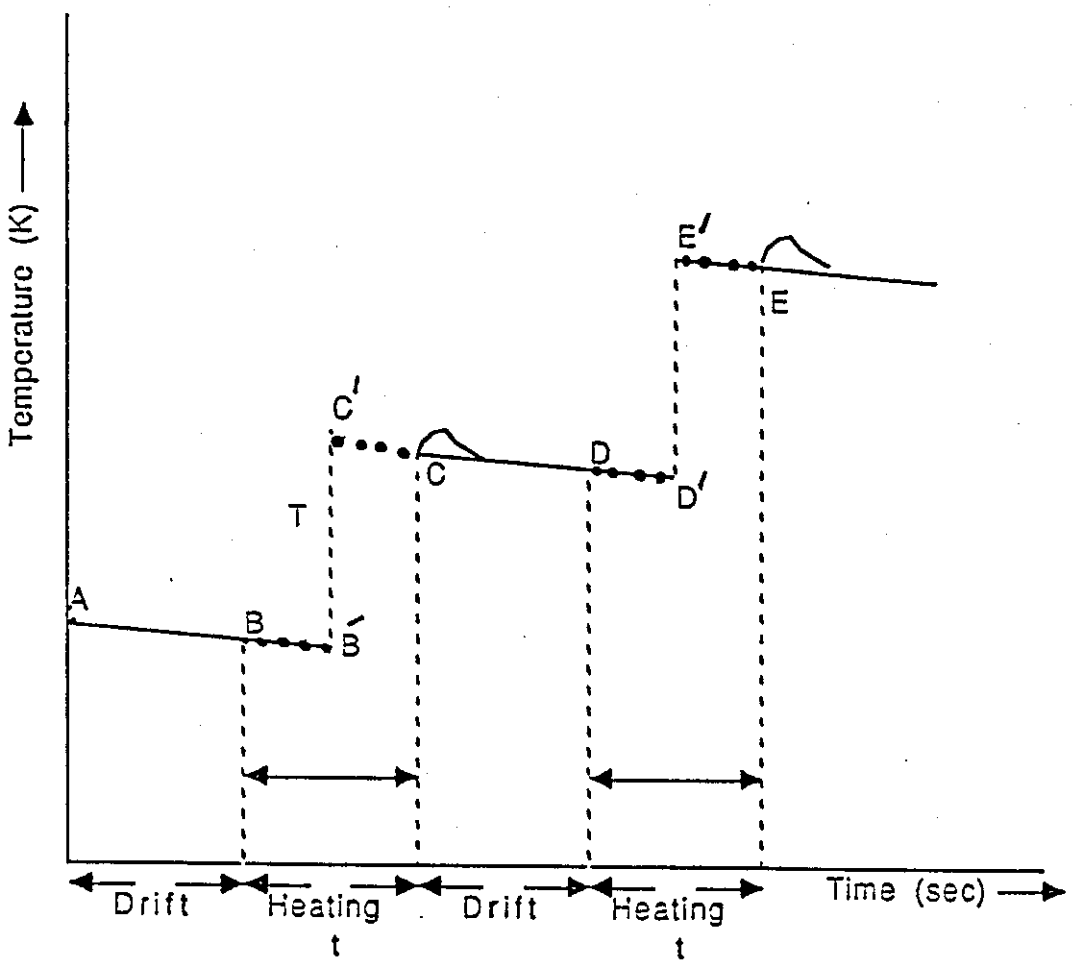

Figure (4.7) Schematic pulse specific heat technique

Following the heat pulse, the temperature is measured in the drift period CD, after which a further heat pulse DE can be applied. The temperature rise ΔT and the average temperature (T) are calculated at the mid–point of the heating period from a line extrapolation of the lines fitted to the temperature points in the pre and post drift periods. The calculated energy supplied to the specimen ($EI/\Delta t$) during the heating and the temperature rise (ΔT) yield the specific heat at the average temperature point (T) by [74]:

$$Cp = \frac{EI\Delta t}{M\Delta T} \qquad (4.18)$$

The specific heat system was automated by using a BBC computer using the above equation to calculate the specific heat as a function of temperature between 77–300K.

CHAPTER FIVE

A REVIEW OF THE VARIOUS ORDERING SCHEMES FOUND IN MAGNETIC COMPOUNDS

5.1 STRUCTURE FACTOR OF HEUSLER ALLOYS

Heusler compounds X_2MnY are intermetallic compounds which have the cubic type $L2_1$ structure and space group $Fm\bar{3}m$ [134]. The structure of the compounds may be visualised as a system of four inter–penetrating fcc sub–lattices A, B, C and D as shown in figure (5.1).

X atoms occupy the A $\left(\frac{1}{4}\frac{1}{4}\frac{1}{4}\right)$ and C $\left(\frac{3}{4}\frac{3}{4}\frac{3}{4}\right)$ sites, manganese the B $\left(\frac{1}{2}\frac{1}{2}\frac{1}{2}\right)$ sites and the Y atoms the D(000) sites. The ordered structure gives rise to three different types of reflections, two of which are order–dependent.

The structure factors F(hkl) are:

$$\begin{aligned}
&h, k, l \quad \text{all odd}: && F(111) = |\, 4\,[(f_a - f_c)^2 + (f_b - f_d)^2]^{\frac{1}{2}} \,| \\
&(h+k+l)/2 \quad \text{odd}: && F(200) = |\, 4\,[f_a - f_b + f_c + f_d] \,| \\
&(h+k+l)/2 \quad \text{even}: && F(220) = |\, 4\,[f_a + f_b + f_c + f_d] \,|
\end{aligned} \qquad (5.1)$$

where fa, fb, fc and fd are the average atomic scattering factors for the A, B, C and D sites respectively. F(111) and F(200) are order–dependent, but F(220) is independent of order. There are an infinite number of ways the system can disorder but there are 7 preferential ways which lead to other structures. Of particular importance in the present study is the disorder which leads to the B2 structure. In the B2 structure Mn and Y atoms occupy the B and D sites randomly.

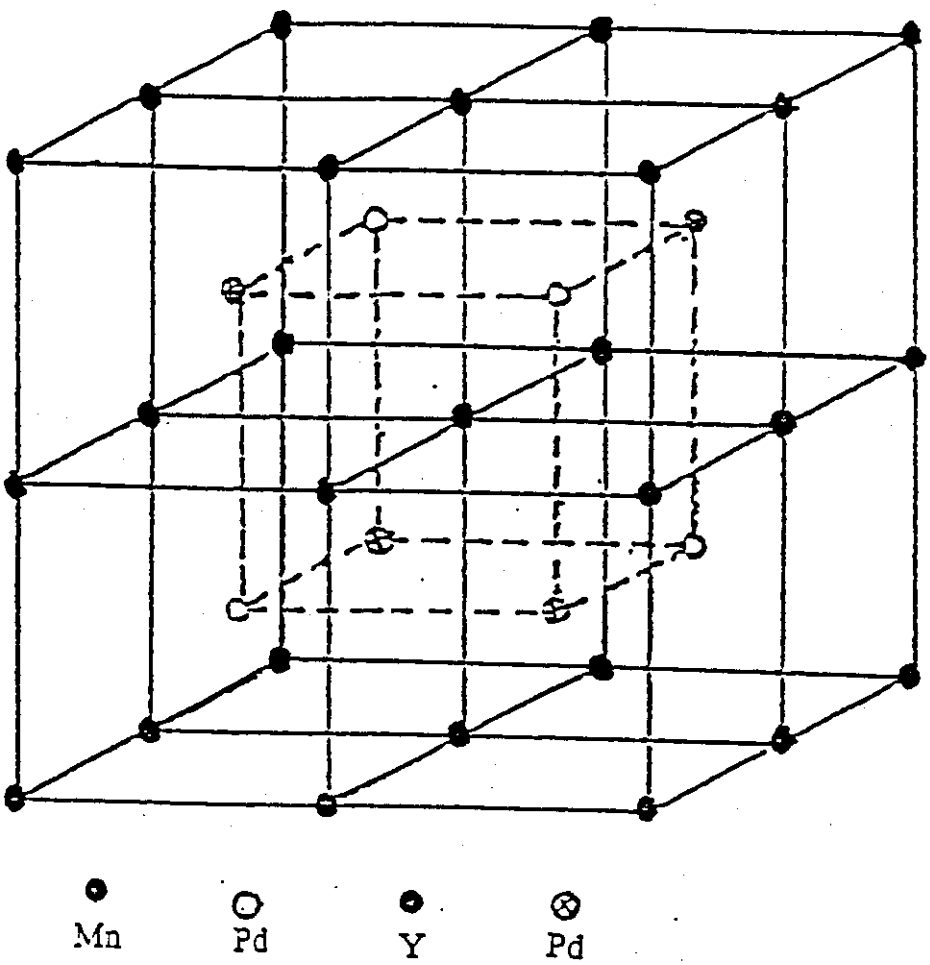

Figure (5.1) The Heusler Structure

D(Mn)	A(Pd)	B(In)	C(Pd)
0 0 0	1/4 1/4 1/4	1/2 1/2 1/2	3/4 3/4 3/4
0 1/2 1/2	1/4 3/4 3/4	1/2 0 0	3/4 1/4 1/4
1/2 0 1/2	3/4 1/4 3/4	0 1/2 0	1/4 3/4 1/4
1/2 1/2 0	3/4 3/4 1/4	0 0 1/2	1/4 1/4 3/4

5.2 THE STRUCTURE OF THE Fe_xNi_{1-x} ALLOYS

The existence of an ordered structure for the alloy Ni 75 at % Fe 25 at % has been established by many techniques (e.g. Leech and Sykes (1939), Collins et al 1964) and Liaschenko et al (1957) [76, 77]. The structure (which is of the Cu_3Au type) is an ordered face–centred cubic arrangement with iron atoms on the corners and nickel atoms on the face–centres of the cubic unit cell as shown in figure (5.2a). It may conveniently be described in terms of four inter–penetrating simple cubic lattices, three consisting of nickel atoms only, and one consisting of an iron atoms only. The space group is $Pm\bar{3}m$ with $a = 3.553\mathring{A}$ at 295°k. The basis of four atoms are [77]

$$\text{Fe at } \frac{a}{2}(000)$$

$$Ni^1 \text{ at } \frac{a}{2}(1,1,0) \qquad Ni^2 \text{ at } \frac{a}{2}(0,1,1) \qquad Ni^3 \text{ at } \frac{a}{2}(1,0,1)$$

where a is the lattice constant of the ordered structure.

For an ordered ferromagnetic alloy, the intensities of the superlattice reflections (100) and (110) are proportional to:

$$F^2_{super} = S^2[(b_A - b_B)^2 + q^2(P_A - P_B)^2] \qquad (5.2)$$

where b_A and P_A are the nuclear and magnetic scattering lengths for atoms A. S is the long range order parameter (S = 1 for perfect chemical order). For an unmagnetised sample the factor q^2 is equal to 2/3. The crystallographic ordering temperature for the LI_0 structure is ~ 618 K and the Curie temperature is 783°C. On raising the temperature, the intensity of the superlattice reflections diminishes leaving diffuse scattering characteristic of short range order (fig 5.2b). In the paramagnetic state, i.e. 805K any remanence of the superlattice reflection has disappeared.

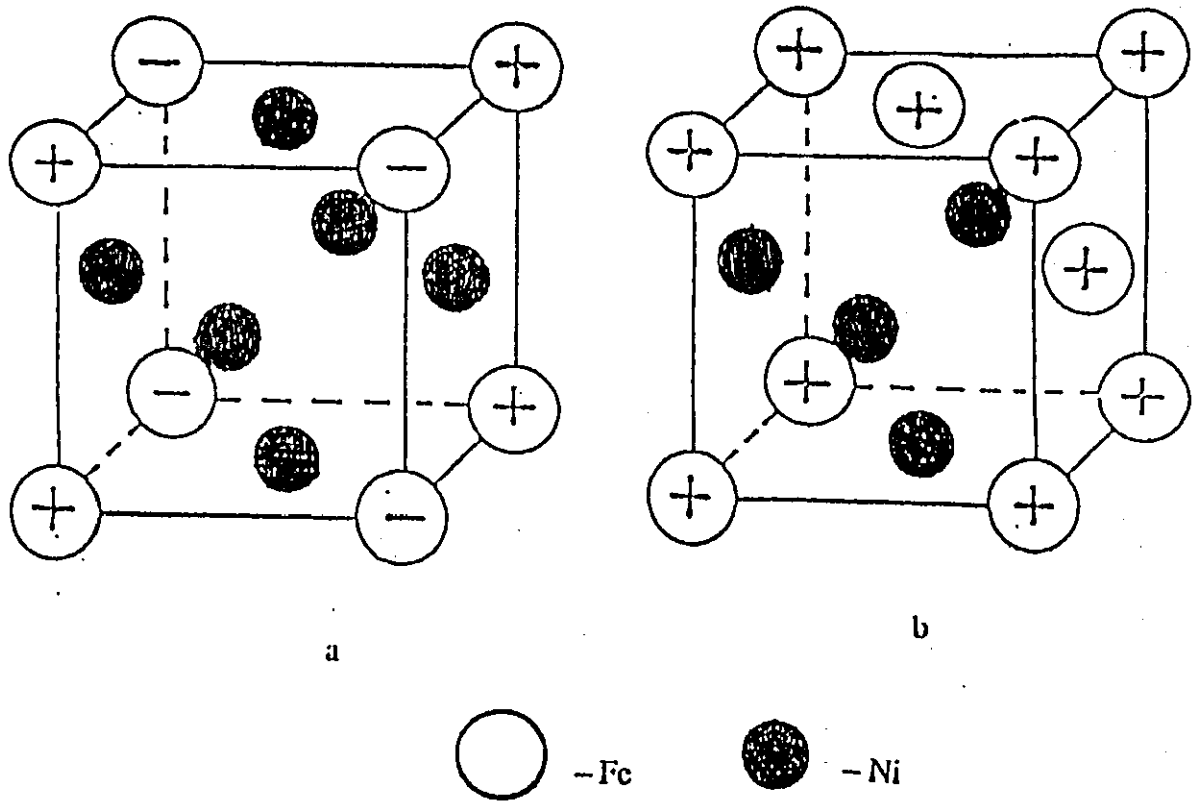

Figure (5.2) The structure of the Fe-Ni alloys

5.3 ANTIFERROMAGNETISM OF THE FCC LATTICE

At low temperature 3 different magnetic structures have been observed in the Heusler alloys consistent with antiferromagnetic order on an fcc lattice.

The Heusler alloys described in the present thesis primarily order anti ferro–magnetically with the moment confined to the manganese atoms.

The different possible types of antiferromagnetic structure for an fcc lattice are shown in figure (5.3).

In all structures the Mn atom is surrounded by 12 nearest neighbour (n.n) Mn atoms at a distance $\frac{a}{\sqrt{2}}$ and 6 next nearest neighbours (n.n.n) at distant 'a' as shown in figure (5.3).

In ordering of the first kind, two thirds of the nearest neighbours of any moment are coupled antiferromagnetically $\uparrow\downarrow$, while the other nearest neighbours are coupled ferromagnetically $\uparrow\uparrow$.

The condition for magnetic reflections occurs is when h and k are even and l odd and may be indexed as (001), (003) ... etc.

In this model, as can be seen from the diagram, the spins in the (001) plane are parallel so the propagation vector k is parallel to the tetrad axis (001) of the cubic lattice so the configurational symmetry is tetragonal.

Ordering of the second kind is characterised by having half the nearest neighbour moments parallel and half antiparallel, and all next nearest neigh–bour moments are antiparallel. The magnetic reflections are characterised by odd integral values for h, k and l and may be indexed as (111), (311), (331), ... etc, indicating that Mn atoms along the cube axes are oppositely aligned. The magnetic lattice consists of parallel (111) planes within which all the Mn atoms are coupled ferromagnetically. Neighbouring (111) planes are coupled anti–ferromagnetically. Since the postulated magnetic symmetry is rhombohedral, the orientation of the spin direction to the [111] axis can be determined.

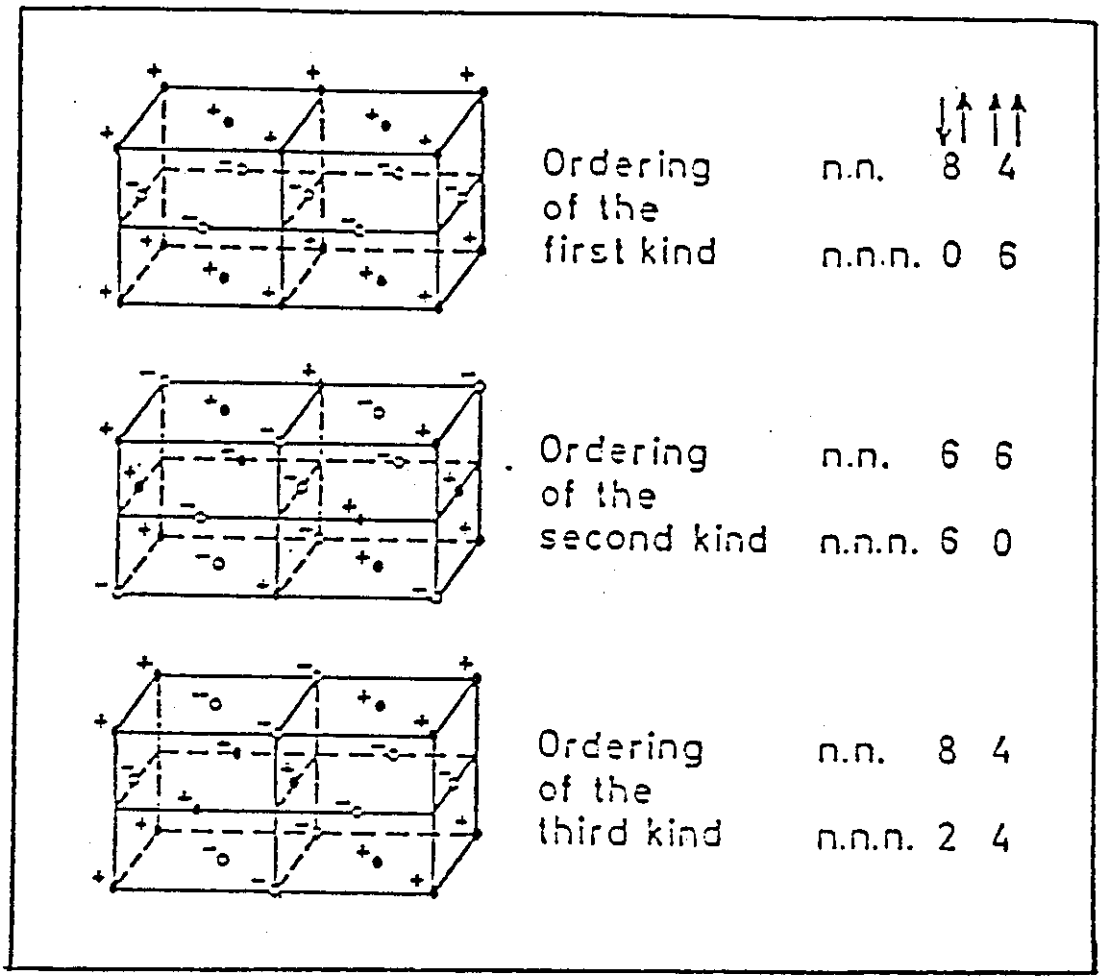

Figure (5.3) Possible antiferromagnetic ordering schemes for face centred cubic lattices

Finally, ordering of the third kind has the same nearest neighbour configuration as ordering of the first kind, but only two thirds of the next nearest neighbours are parallel. The condition for magnetic reflections to occur is characterised by even integral values for h, k and odd for l, i.e. (201), (203), ... etc. In this configuration adjacent spins along two of the cube edges are aligned parallel and along the other antiparallel, producing tetragonal magnetic symmetry.

In these magnetic structures, two types of space groups of rhombohedral ($R\bar{3}m$) and tetragonal (I4/mmm) structures are suggested to be consistent with anti–ferromagnetic structures on an fcc lattice.

5.4 MAGNETIC STRUCTURE DETERMINATION OF VARIOUS MAGNETIC MODELS

The unpaired electrons of the incomplete 3d shell in the transition metal ion give rise to a resultant magnetic moment. Interaction of atomic moments with the magnetic moment of the neutron , produces magnetic scattering which is additional to the nuclear scattering.

In ordered magnetic materials the magnetic moments are usually parallel or antiparallel and coherent Bragg reflections occur. The total scattered intensity for any reflection is obtained by calculating the total structure factor F of the unit cell. The resultant intensity is proportional to F^2 which is given by:

$$F^2 = F^2n + q^2F^2m \qquad (5.3)$$

where $\underline{q}$ is the magnetic interaction vector defined by:

$$q^2 = (1 - (\underline{\varepsilon} \cdot \underline{k})^2 = \sin^2\eta \qquad (5.4)$$

where η is the angle between the scattering and magnetisation vectors. Thus if q^2 is known for a particular reflection, the orientation of the magnetic moments may be determined. ε and k are unit vectors to the reflecting plane and direction of atomic magnetic moment respectively.

The spin direction with respect to the unique axis may be obtained from the formula derived by Shirane (1959) [78].

$$<\cos\eta^2> = [(n-r)\sin^2\theta + (n+2r)\cos^2\theta]\ \frac{a^{*2}d^2}{3}$$

and (5.5)

$$<\cos\eta^2> = [\tfrac{1}{2}(h^2+k^2)a^{*2}\sin\theta^2 + l^2c^{*2}\cos^2\theta]d^2$$

which are for rhombohedral and tetragonal configurated symmetry respectively where η is the angle between the magnetic and scattering vectors; $n = h^2 + k^2 + l^2$; $r = hk + kl + lh$ and θ is the angle between the spin direction and the unique axis.

In magnetic crystals which have cubic symmetry there is no unique axis and it is impossible to determine the moment orientations from measurements using unpolarised neutrons, since q^2 takes a mean value of 2/3 for all moment orientations.

The magnetic moment μ per magnetic atom is calculated from $p = 0.2695 \times 10^{-12}\mu.\ f_\theta$ cm, where p is the magnetic scattering amplitude and the magnetic form factor f_θ was obtained (as a function of $(\sin\theta/\lambda)$ for Mn) from Watson and Freeman [79].

5.5 APPLICATION OF MOLECULAR FIELD THEORY TO VARIOUS MAGNETIC MODELS

The Heusler alloys are a particularly useful series for investigating long–range interactions in 3d metals in that they have well separated ordered localised moments.

According to the molecular field theory, the magnetic ordering temperature θ is given by:

$$k_B\theta = \frac{2}{3}S(S+1)\sum_{i=1}^{N} G_i J_{ij} \qquad (5.6)$$

where k_B is Boltzmanns constant, S is the magnetic spin, G_i takes values +1 when ith spin is aligned parallel or −1 when they are aligned antiparallel, J_{ij} is the exchange interaction between ith neighbours, and N is the number of sets of neighbours.

Summing over all neighbours out as far as the third exchange interaction, the four possible fcc types of magnetic order ($L2_1$) can be written:

$$
\begin{aligned}
k\theta_p \approx k\theta_F &= 12J_i + 6J_2 + 24J_3 \\
k\theta_{N1} &= -4J_1 + 6J_2 + 8J_3 \\
k\theta_{N2} &= -6J_2 \\
k\theta_{N3} &= -4J_1 + 2J_2 + 8J_3
\end{aligned}
\qquad (5.7)
$$

where $k = 3K_B/2S\,(S+1)$ and θ_p, θ_{N1}, θ_{N2} and θ_{N3} represent the paramagnetic Curie temperature and the Neel temperatures for AF_1, AF_2 and AF_3 structures respectively.

Comparison of the stability of the observed structures show that the types of exchange interaction must be one that can take both positive and negative values for different neighbour distances. For AF_1 order to occur J_3 must be negative and for AF_2 J_2 must be negative and relatively large. For AF_3 J_3 must be positive. The only region in which ferromagnetism, antiferromagnetism types AF_2 and AF_3 can all exist is when J_1 and J_2 are negative and J_3 is positive.

For simplicity the phase stability diagram is shown in figure (5.4) as 3 two dimensional phase diagrams.

The details of the distance dependence of the exchange interactions in Pd_2MnSn have been derived by Noda and Ishikawa [80, 81] from measurements of the magnon dispersion curves using inelastic neutron scattering. The measurements have shown that the long range interaction (>12Å) have an oscillatory nature at large distances. The exchange constants determined from a

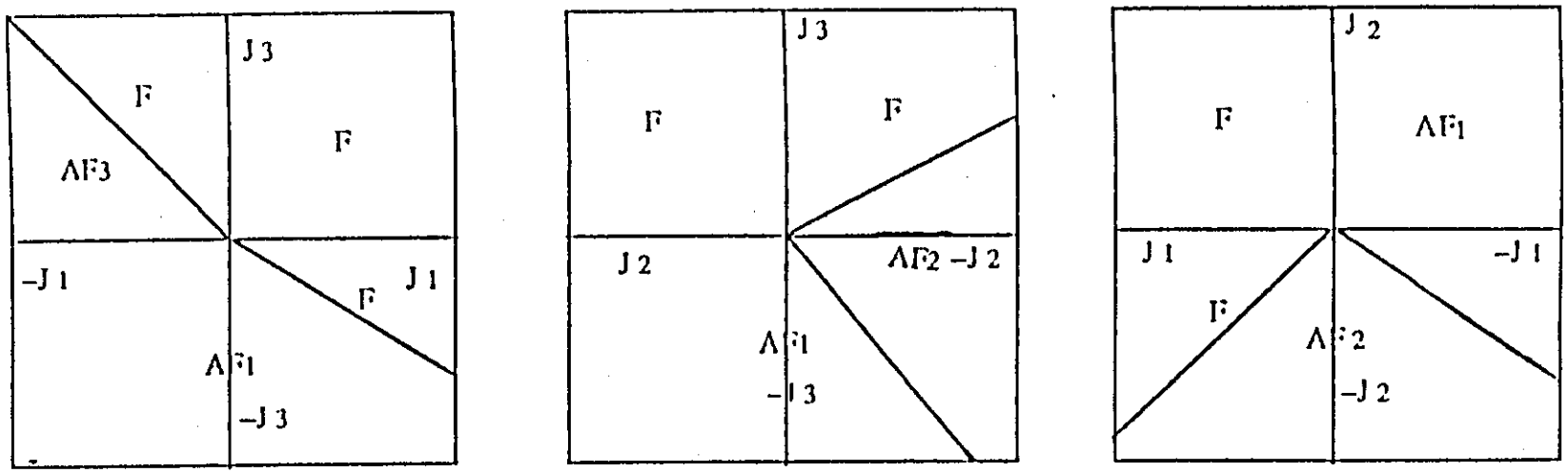

Figure (5.4) The magnetic phase stability diagrams

least square fit to the dispersion relation $\hbar w = 2S[J(0) - J(q)]$, where S is the atomic spin and $J(q) = \sum_i J_i e^{iqR_i}$ is the Fourier transform of the exchange integral.

5.6 FRUSTRATION ON ANTIFERROMAGNETIC FCC LATTICE

Antiferromagnetic interactions on a disordered lattice can produce results that are quite different from those in ordered systems. Frustration arises with antiferromagnetic interactions whenever the geometry of the lattice is such that the neighbours of a given atom are themselves neighbours of each other [83]. Figure (5.5) illustrates the idea of frustration. The + sign refers to ferro–magnetic exchange and the – sign to antiferromagnetic exchange. The three aligned spins are shown by solid circles and the frustrated spin by an open circle. The spin on its left wants to point up, but the spin above it wants to point down. This given spin cannot satisfy all of these requirements and this is refered to as frustration [75].

The spin–glass state has been found in certain disordered magnets, which undergo transitions characterised by the absence of long range order [75].

A spin–glass state can be defined as an interacting magnetic system where the magnetic atoms have positioned randomness, and is characterized by a freezing of the spin directions.

Let $< S_i >$ be the thermal average of a spin at the ith site and

$< \overline{S} > \equiv N^{-1} \Sigma < S_i >$ as the average of $< S_i >$ over all N spins. Then a spin glass is characterised as a system which is below T_c has $< \overline{S} > = 0$, but also $< \overline{S} >^2 \equiv N^{-1} \Sigma < S_i^2 > \neq 0$. Thus, in a spin glass each spin is frozen in some specific direction but this direction varies throughout the alloy so that there is no macroscopic magnetization.

A number of fascinating phenomena at temperatures below the ordering temperature are known to occur in spin glasses and they have been well documented [82].

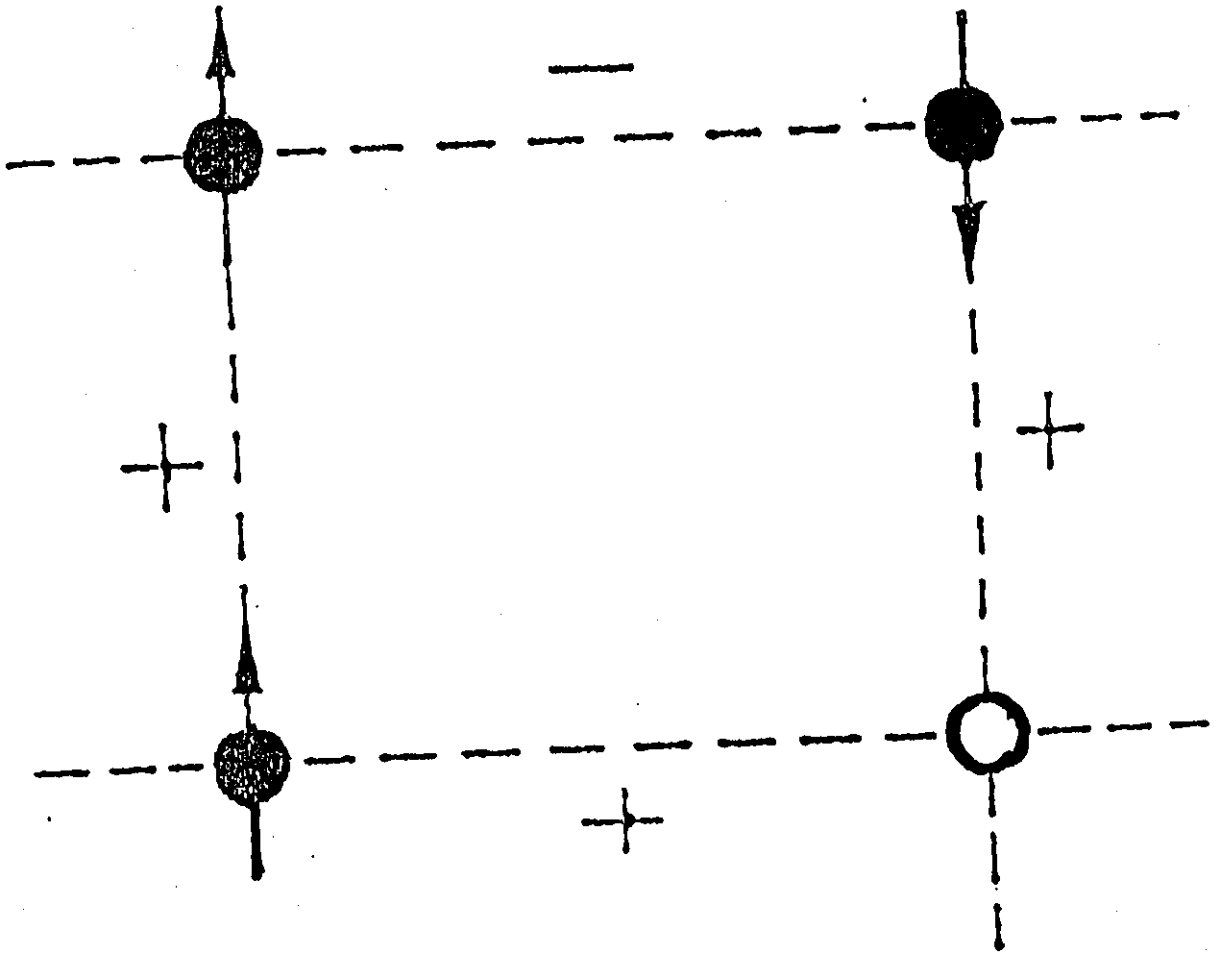

Figure (5.5) A simple example of frustration

Temperature dependence of magnetic specific heat and susceptibility measurements of CuMn alloys have been obtained by Wenger (1976) [83] and Martin (1980) [84] respectively. The results show that approximately 1/2 [83] to 2/3 [84] (of the magnetic entropy) is already frozen out at T_f (freezing temperature), indicating completing short–range antiferromagnetic interactions.

The present specific measurements of both gold and silver Heusler alloys indicates that the small magnetic entropy may be associated with the system when it is fully frustrated, i.e. in the spin glass phase.

5.7 ANTIFERROMAGNETISM IN Fe – Ni INVAR

The first suggestion of the possible presence of antiferromagnetic exchange bonds in nominally ferromagnetic first row transition metal alloys was a proposal by Carr [91] that such a mixed exchange situation might explain all deviations from the Slater–Pauling curve [92, 93]. Kondorsky and Sedov later proposed the mechanism for the case of Fe–Ni Invar and called it "Latent Antiferromagnetism" [95]. In its simplest form, latent antiferromagnetism assumes three near neighbour exchange constants: an antiferromagnetic coupling for Fe–Fe pairs and two ferromagnetic coupling constants corresponding to Fe–Ni and Ni–Ni pairs. The assumed antiferromagnetic bonds are consistent with the postulated antiferromagnetism of (fcc) γ–F_e [94]. Given such mixed exchange, one might expect some form of antiferromagnetic order to establish itself at some temperature $T_N < T_C$. There are, in fact, a number of reports that such an ordering does occur in the neighbourhood of 10–80 K in 30–40 at % Ni of Fe–Ni Invar.

The measured quantities which exhibit an anomaly or a relatively sudden change at the supposed T_N are listed in table (5.1).

Physical properties	Formula	at % Ni	TN (K)	Ref
The differential succeptibility at H = 6·7 K0e	$\Delta M/\Delta H$	36·8 43·8	15 <4·2	[85]
The field induced change in electrical resistance	$-\Delta R/Ro\Delta H$	36·8 43·8	15 15	[85, 95]
The forced linear magnetostriction coefficient	$\Delta l/lo\Delta H$	33·7	15	[96]
The small–angle neutron scattering cross section	$d\sigma/d\Omega$	16 22 26 30	100 95 90 75	[97]
The Magnetisation	M(T) at H ≈ 10 K0e	34 35·4	20 20	[98]
Ac susceptibility	χ ac	30 40 45	30 40 45	[99]
Hyperfield on ^{57}Fe	$\bar{H}_{hf}$	35	26	[100]
Transferse sound velocity	T_{sound}	34	22	[101, 102]

Table (5.1)

Measured low–temperature magnetic transitions (TN) in Fe – Ni Invar

CHAPTER SIX

EXPERIMENTAL RESULTS – $Pd_{2-x}Ag_xMnIn$

6.1 INTRODUCTION

No references were found to any previous investigations in the $Pd_{2-x}Ag_xMnIn$ system. The alloys discussed in this chapter are listed in table (6.1).

All alloys were prepared by the same technique described in Section (4.1). Each alloy was annealed at 800°C for 24 hours and then was slow cooled (sc). X–ray powder diffraction patterns were taken for all samples. The lattice parameters were determined from Nelson Riley extrapolations. The alloys discussed in this series were either antiferromagnetic or ferromagnetic at low temperatures. The majority of the alloys order in the $L2_1$ Heusler type structure, but some exhibited preferential (Mn–In) disorder, i.e. B2 disorder. In these series three types of magnetic structures are observed, antiferro–magnetic fcc type 2, AF_2, antiferromagnetic fcc type 3A, AF_3A, and ferro–magnetic.

Similar behaviour has been observed in the series $Pd_2MnSn_{1-x}Sb_x$, $Pd_2MnIn_{1-y}Sb_y$ and $Pd_2MnIn_{1-z}Sn_z$ [125, 126, 127].

The magnetic, thermal structural properties of each alloy are discussed in detail in the following sections.

Table (6.1) Lattice parameters and electron concentration of $Pd_{2-x}Ag_xMnIn$ series

Alloy	a_o(Å)	Heat Treatment	nc(e/ch. form)
Pd_2MnIn	6·369 ∓ 0·003	sc	4·0
$Pd_{1.8}Ag_{0.2}MnIn$	6·397 ∓ 0·003	sc	4·2
$Pd_{1.6}Ag_{0.4}MnIn$	6·418 ∓ 0·003	sc	4·4
$Pd_{1.4}Ag_{0.6}MnIn$	6·441 ∓ 0·003	sc	4·6
$Pd_{1.2}Ag_{0.8}MnIn$	6·470 ∓ 0·003	sc	4·8
$Pd_{0.8}Ag_{1.2}MnIn$	6·552 ∓ 0·003	sc	5·2
$Pd_{0.6}Ag_{1.4}MnIn$	6·576 ∓ 0·003	sc	5·4
$Pd_{0.4}Ag_{1.6}MnIn$	6·647 ∓ 0·003	sc	5·6

6.2 $Pd_{1.8}Ag_{0.2}MnIn$

The susceptibility and reciprocal susceptibility versus temperature curves are shown in figures (6.1) and (6.2) respectively. The specific heat versus temperature obtained by using pulse and continuous heating techniques are shown in figure (6.3).

Neutron scattering measurements have been carried out using the diffractometers D1A and D2B at the ILL. Scans were made at several temperatures between 5K and 293K. Figures (6.4) and (6.5) show the powder diffraction patterns of $Pd_{1.8}Ag_{0.2}MnIn$ obtained at a temperature of 5K and 190K using D2B and D1A respectively. At 5K, a mixture of the antiferromagnetic phase, fcc type 2, AF_2 and antiferromagnetic phase fcc type 3A, AF_3A is observed. At 190K, above the Neel temperature, all antiferromagnetic peaks have disappeared. The powder refinement was carried out using the proposed space groups of the tetragonal (I4/mmm) and rhombohedral ($R\bar{3}m$) structures, with the atoms located at positions as indicated in table (6.2). In this refinement the integrated intensity of 52 crystallographically independent Bragg reflections were determined for both structures using the Rietveld refinement program [72]. The results of the refinements show that the measured and calculated nuclear intensities for both structures are in excellent agreement, indicating the proposed structures are correct.

For simplicity, only the results of the refinement of 15 nuclear reflections for the tetragonal structures are presented in table (6.3) and shown in figure (6.6)

At room temperature, the intensities of the odd and even nuclear superlattice peaks indicate that the alloy was highly ordered in the $L2_1$ structure with a small amount of preferential B2 disorder. The odd superlattice peaks have the most intensity and are very sensitive to (Mn–In) disorder. The effect of seven types of preferential disorder on the odd and even superlattice structure factors $F^2(111)$ and $F^2(200)$ are shown in figures (6·7), and (6·8) respectively.

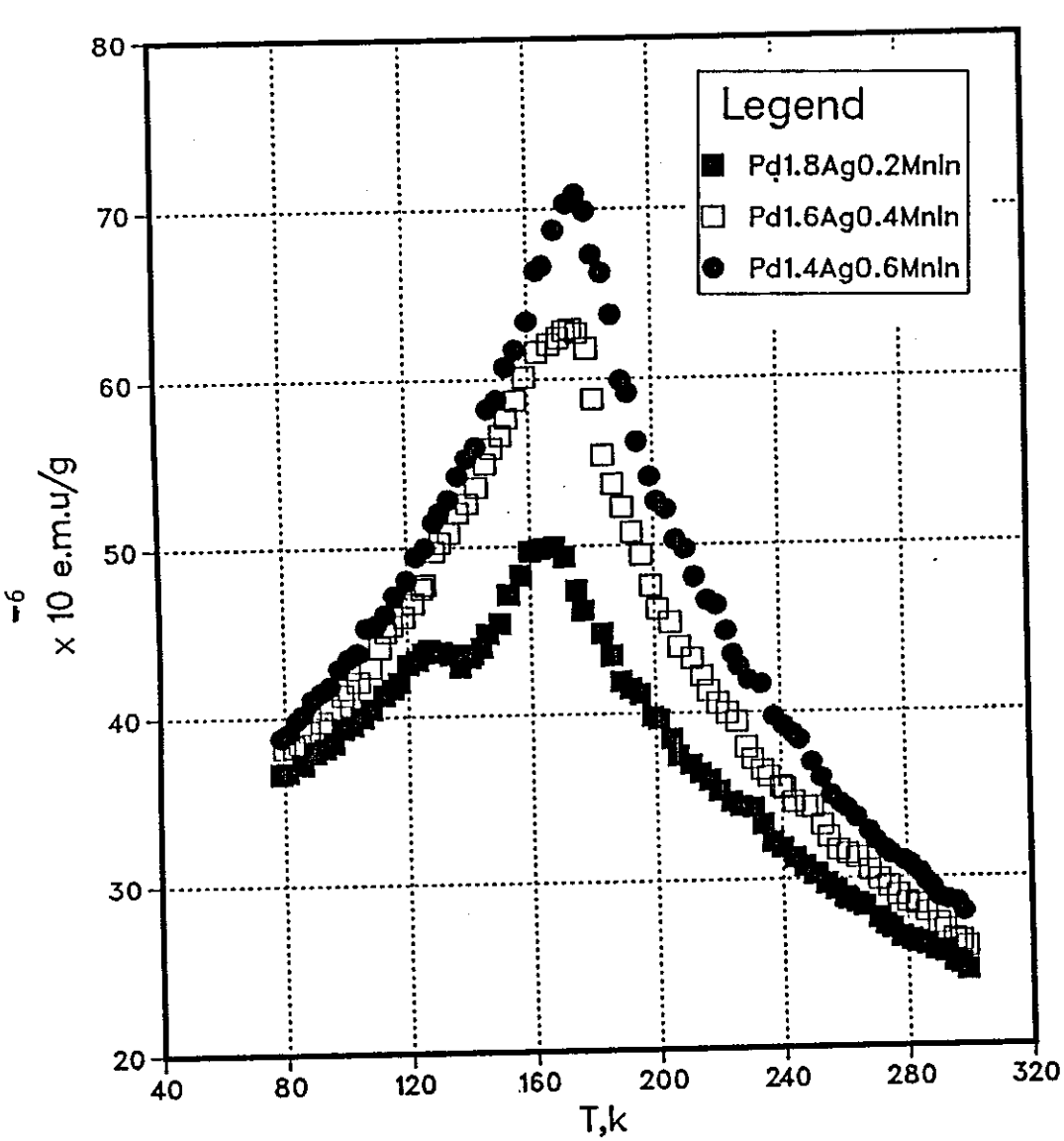

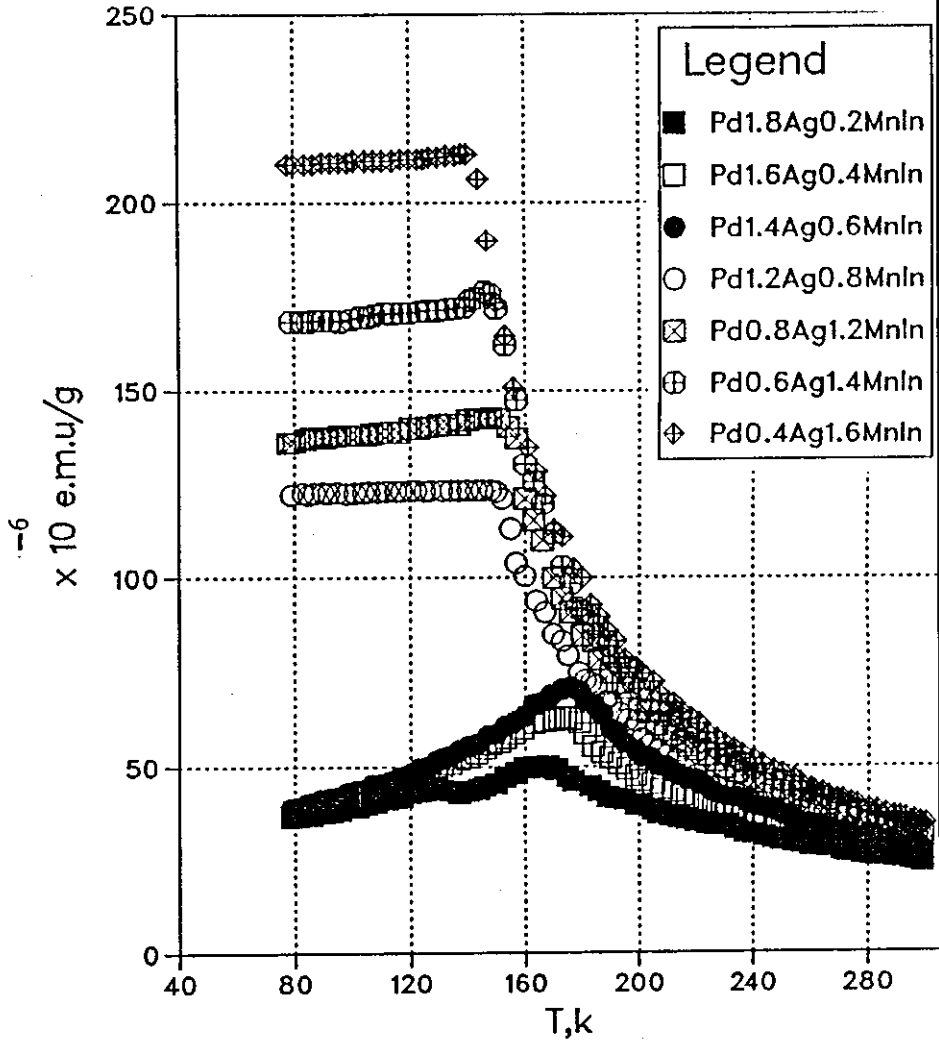

Figure (6.1) The susceptibility versus temperature curves for slow cooled alloys Pd_{2-x} Ag_x Mn In

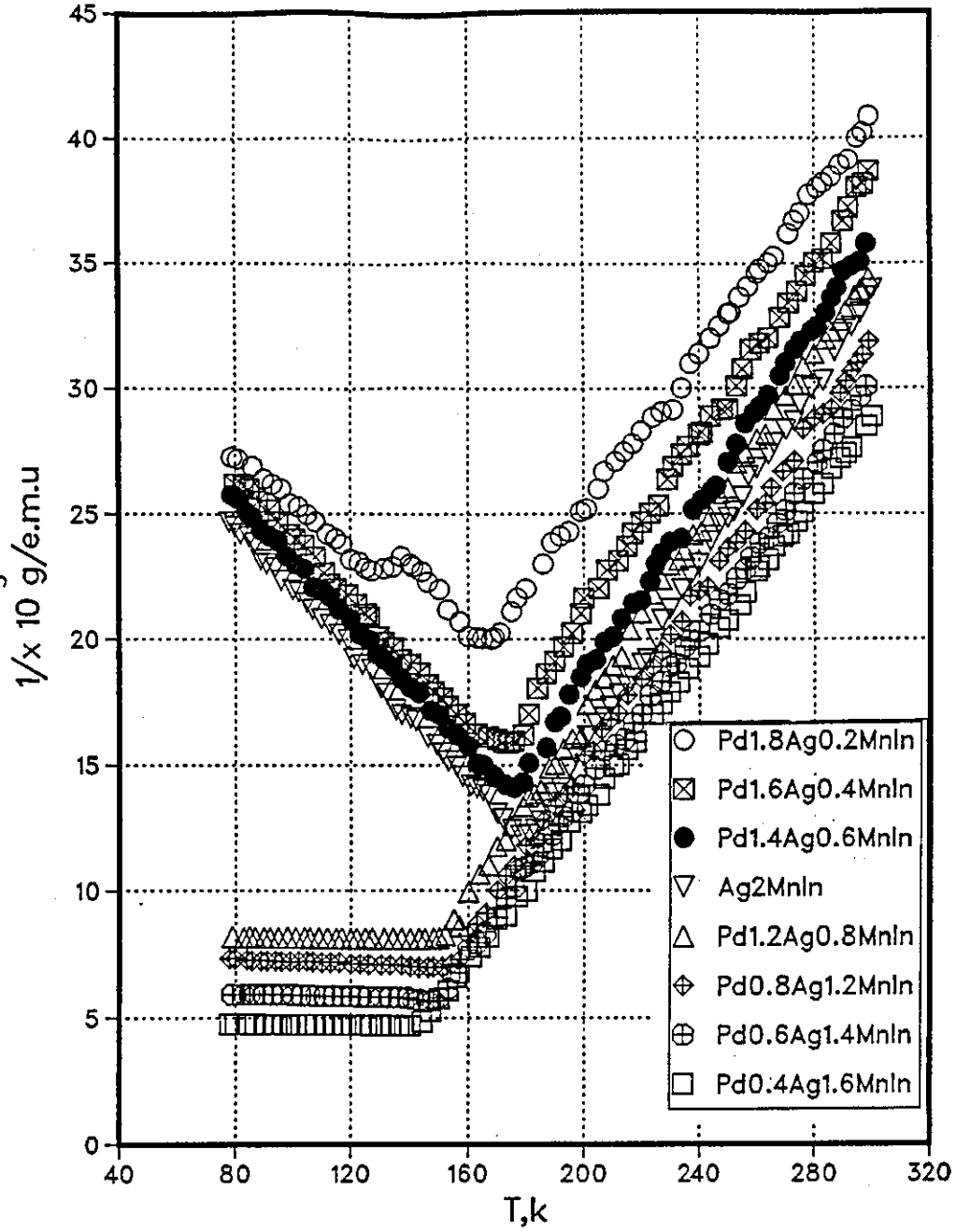

Figure (6.2) The reciprocal susceptibility versus temperature curves for slow cooled alloys Pd_{2-x} Ag_x Mn In

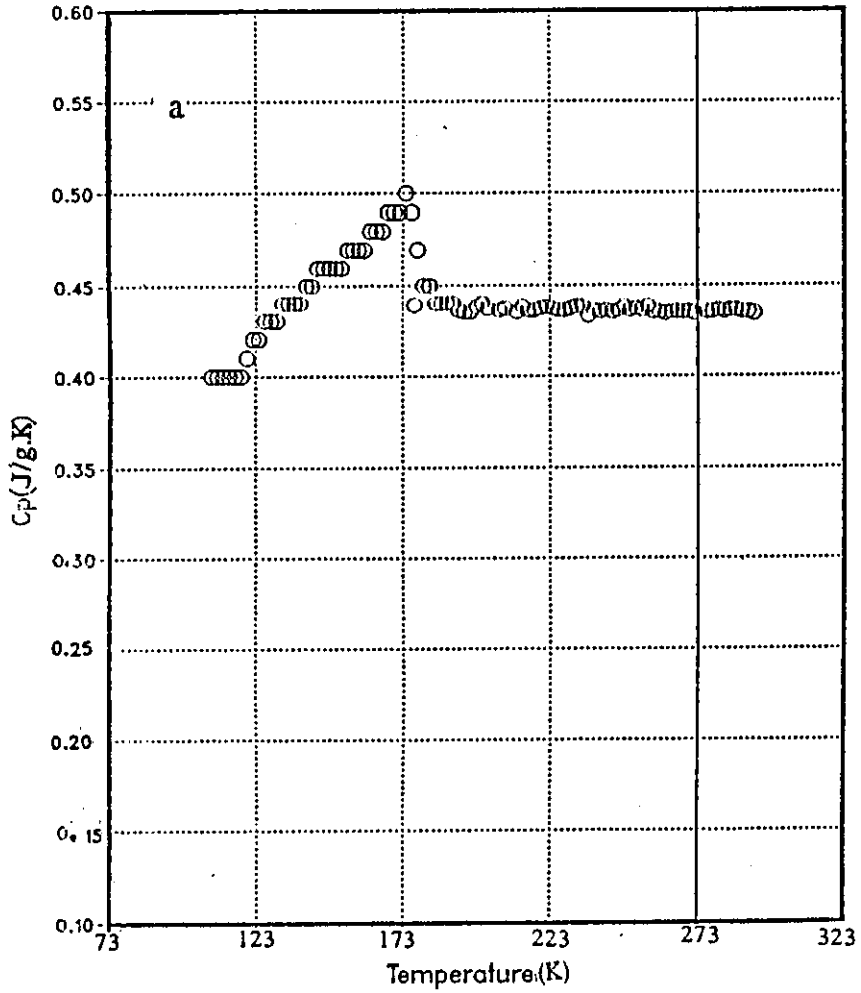

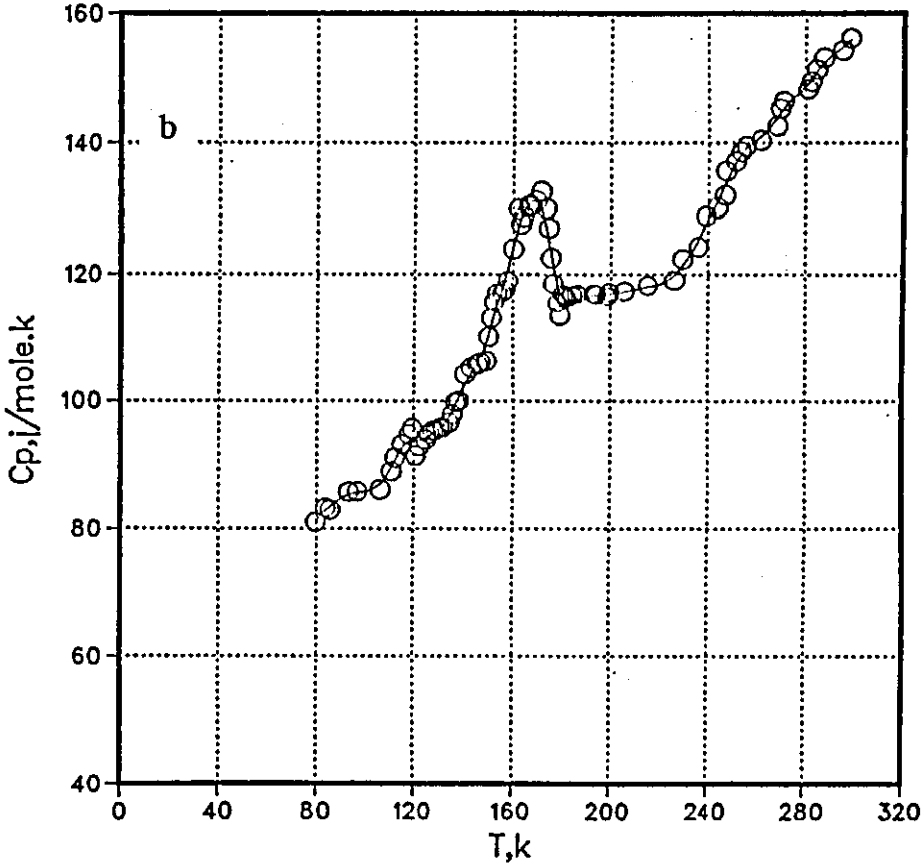

Figure (6.3) Specific heat measurements of $Pd_{1.8}$ $Ag_{0.2}$ Mn In

a - continuous heating
b - pulse heating

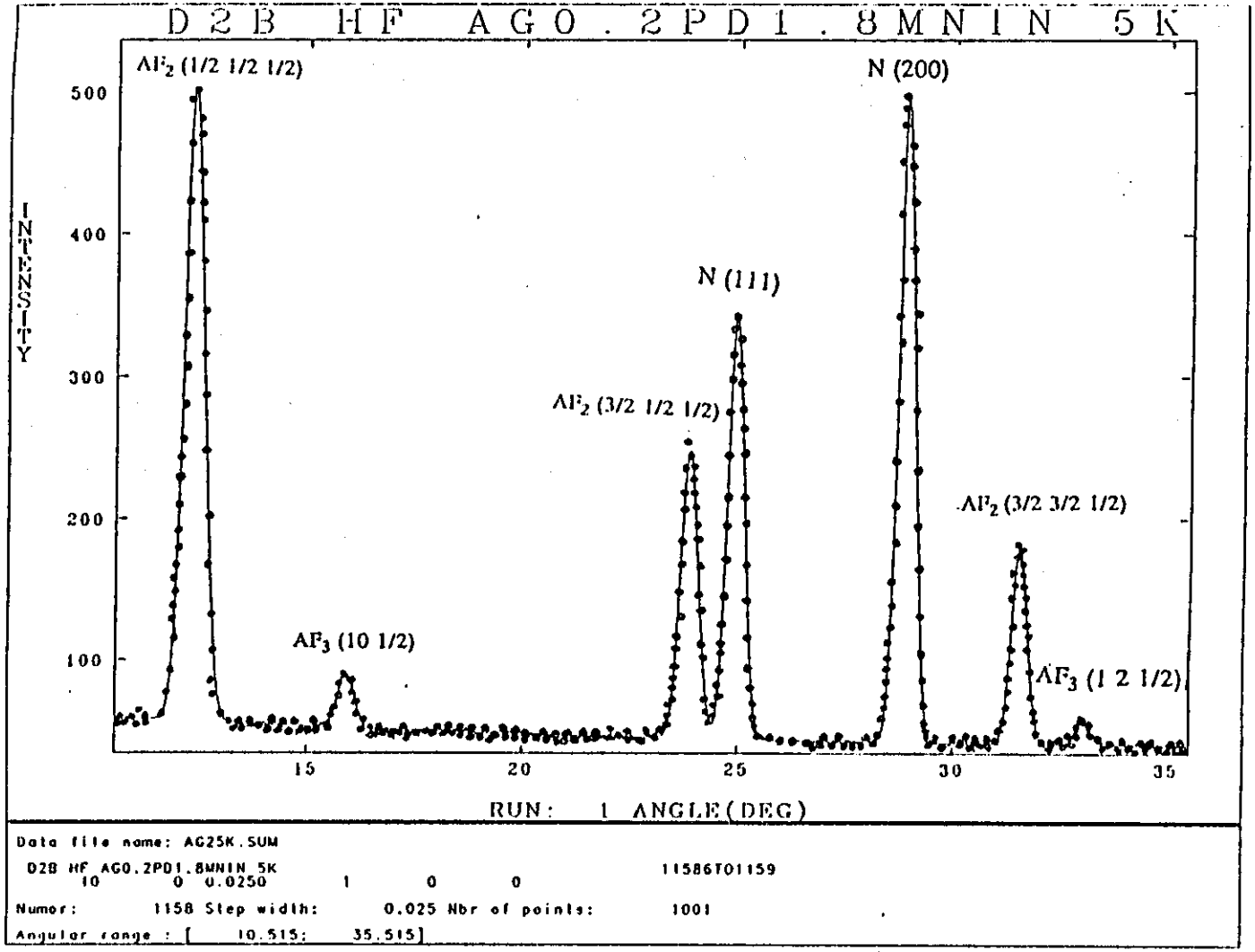

Figure (6.4) Neutron diffraction measurements at 5K

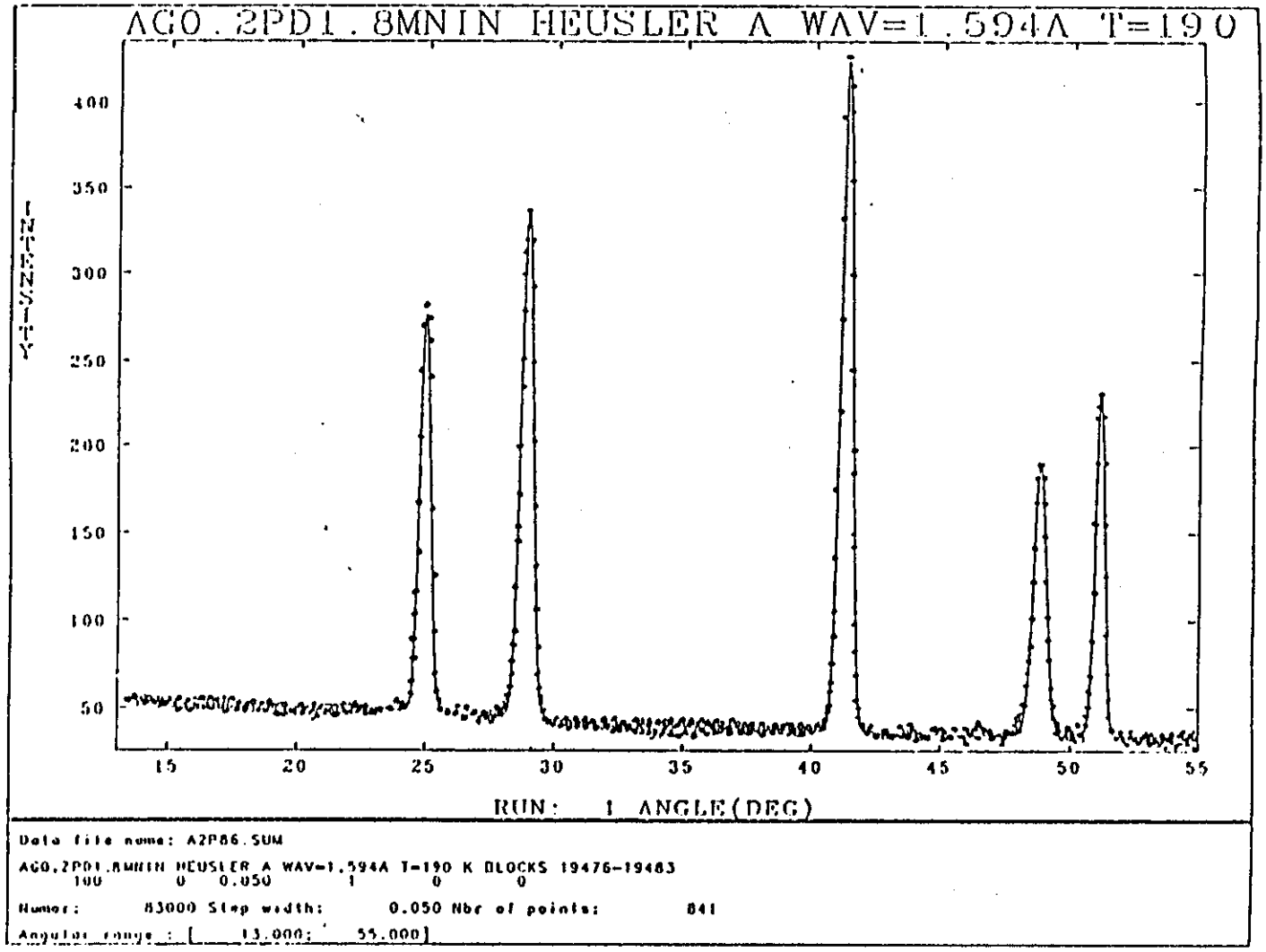

Figure (6.5) Neutron diffraction measurements at 190K

Table 6.2 Configurational Symmetry of the $Pd_{2-x}Ag_xMnIn$ alloys structure [134, 135]

Structure	Lattice parameters	Space Group	Atom	Coordinates		
fcc (R.T)	$a = b = c = 6{\cdot}4$ Å $\alpha = B = \gamma = 90°$	$Fm\bar{3}m$	Ag/Au	1/4	1/4	1/4
			Pd	1/4	1/4	1/4
			Mn	1/2	1/2	1/2
			In	0	0	0
Tetragonal (L.T)	$a = b = 4{\cdot}52$Å $c = 6{\cdot}4$ Å $\alpha = B = \gamma = 90°$	I4/mmm	Ag/Au	0	1/2	1/2
			Pd	0	1/2	1/2
			Mn	0	0	0
			In	0	0	1/2
Rhombohedral (L.T)	$a = b = c = 4{\cdot}5$Å $\alpha = B = \gamma = 60°$	$R\bar{3}m$	Ag/Au	1/4	1/4	1/4
			Pd	1/4	1/4	1/4
			Mn	0	0	0
			In	1/2	1/2	1/2

Table (6.3) The measured and calculated nuclear intensities for rhombohedral structures. The R factors are a measure of the quality of the fit, where R_n is the R factor for integrated intensities, R_p the profile R factor and R_{exp} the profile R factor expected by statistics (the definition of R_n is given in equation 4.1)

Position	h	k	l	J(mult)	I cal	I obs
24·99	1	0	0	6	2123	2139 ± 14
25·04	1	1	1	2	705	714 ± 6
28·95	0	–1	–1	6	4207	4200 ± 21
41·38	1	0	–1	6	2426	2578 ± 12
41·44	2	1	1	6	2420	2399 ± 11
48·95	1	–1	–1	6	603	674 ± 5
48·98	2	1	0	12	1205	1302 ± 9
49·03	–1	–2	–2	6	601	645 ± 6
51·29	2	0	0	6	1455	1443 ± 12
60·00	0	–2	–2	6	1275	1249 ± 15
65·98	2	0	–1	6	736	800 ± 9
66·05	3	1	1	12	367	396 ± 4
66·11	3	2	2	12	367	391 ± 6
67·93	1	–1	–2	12	1832	1910 ± 10
68·02	3	2	1	12	1829	1948 ± 11

a = b = c = 4·5050 ± 0·0002

Temp effect Mn – In = 0·3877 ± 0·075

R_n = 6·77

R_{exp} = 3·82

R_p = 17·70

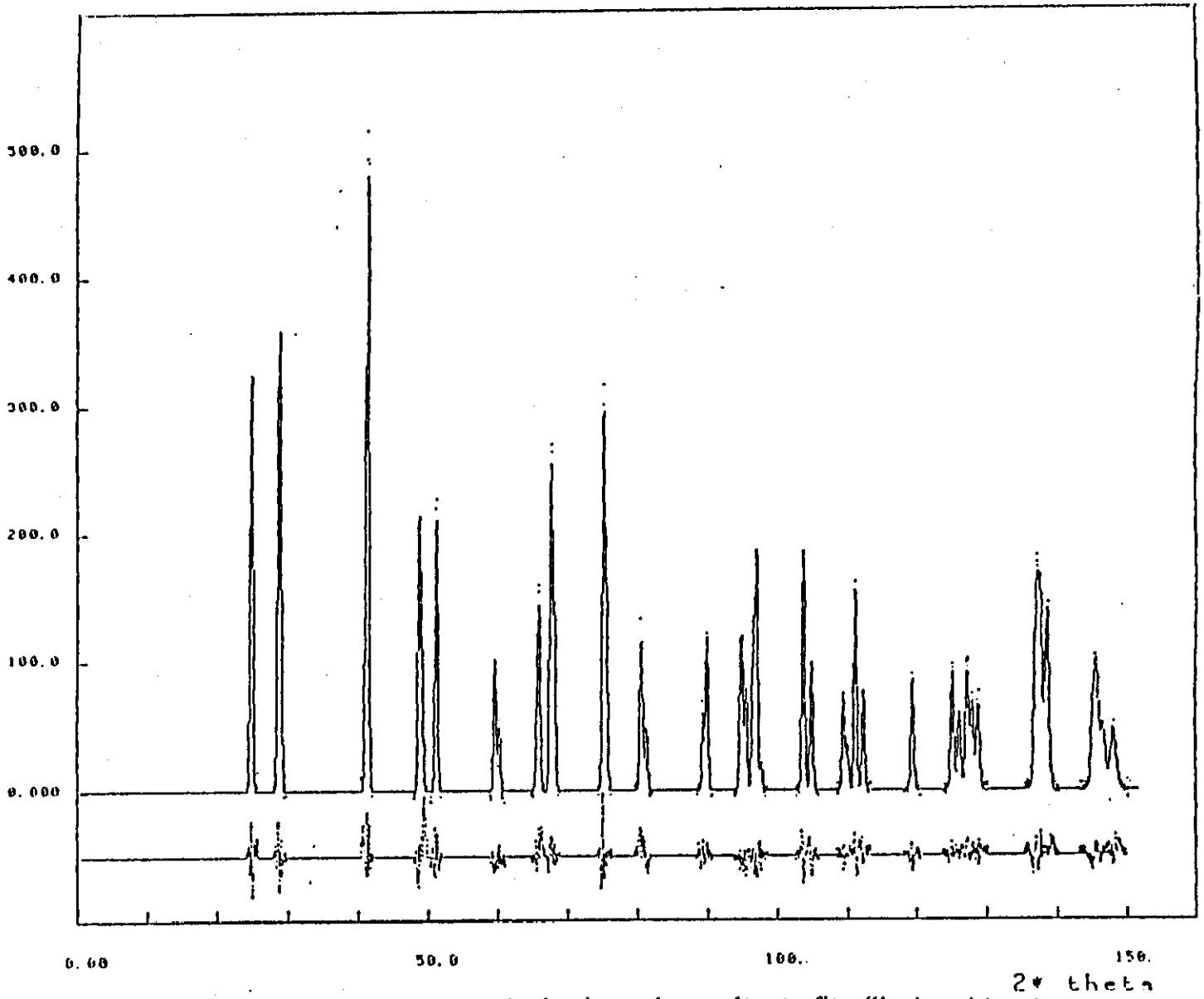

Figure (6.6) D_2B measurement (points) and resultant fit (line) with the difference (lower line below the spectrum) of $Pd_{1.8}$ $Ag_{0.2}$ Mn In at 5K. The wavelength of the neutrons was determined to be $\lambda = 1.594$ A

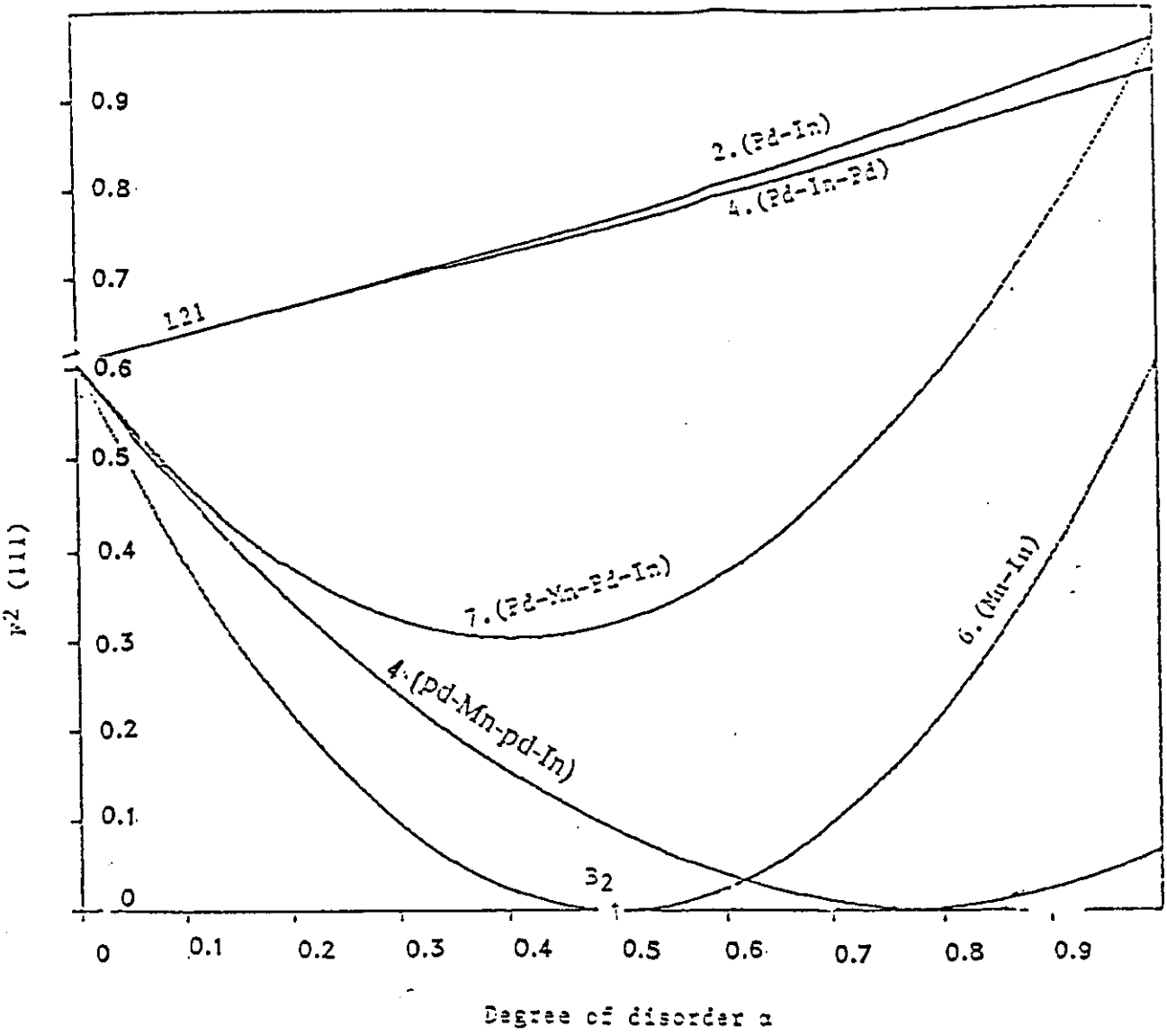

Figure (6.7) Neutron diffraction structure factor F^2 (111) versus degree of disorder α for $Pd_{1.8}$ $Ag_{0.2}$ Mn In

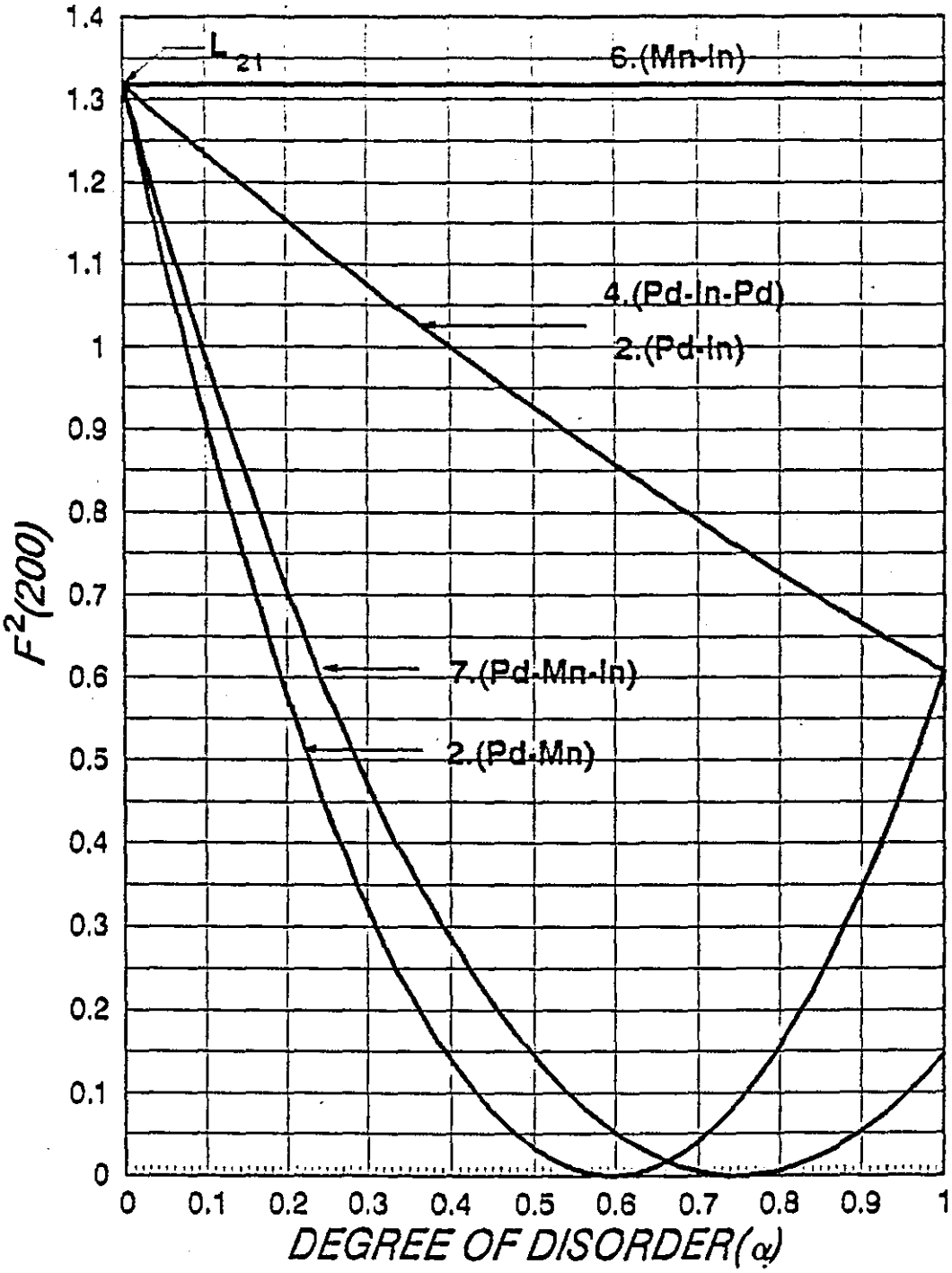

Figure (6.8) Neutron diffraction structure F^2 (200) versus degree of disorder α for $Pd_{1.8}$ $Ag_{0.2}$ Mn In

The preferential B2 disorder corresponding to α(Mn–In) was determined as 0·093.

At low temperatures the neutron diffraction pattern revealed additional antiferromagnetic peaks which could be indexed as (111), (311), (331), ... etc. using a magnetic unit cell with lattice parameter twice that of the chemical unit cell. In this structure the spins of Mn atoms along the cube axes are oppositely aligned. The proposed magnetic structure illustrated in figure (6.9a) agrees well with experimental data. The structure is similar to that suggested by Shull et al [8] (1951) for MnO. The magnetic lattice consists of parallel (111) planes within which all the Mn atoms are coupled ferromagnetically. Since the postulated magnetic symmetry is rhombohedral, the orientation of the spin direction to the unique [111] axis was determined by using the formula derived by Shirane [78] (1959) and explained in Section (5.4).

$$\cos^2\eta = [(n-r)\sin^2\theta + (n+2r)\cos^2\theta]\frac{a^{*2}d^2}{3} \qquad (6.1)$$

where η is the angle between the magnetic and scattering vectors, $n = h^2 + k^2 + l^2$ and $r = hk + kl + hl$. The value of $\sin\theta$ obtained from several reflections using the above formula are shown in table (6.4) together with the measured and calculated magnetic structures for fcc type 2A antiferromagnetism at 5K.

Table 6.4

h k l $a = 2a_o$	position	q^2 / F^2cal	$q^2 \perp F^2$cal	q^2F^2obs	sin θ
(111)	12.30	0	13·451	13·343 ± 0·3	–
(311)	33.85	7·373	11·110	10·658 ± 0·3	1·00 ± 0·01
(331)	31.55	5·210	9·982	9·500 ± 0·3	0·99 ± 0·01
(333)	37.90	0	7·314	7·510 ± 0·3	–
(511)	37.90	3·2	5·660	5·519 ± 0·3	0·99 ± 0·01

It is seen the values of $\sin\theta = 1$, $\theta = 90°$ obtained from the above formula (6.1), hence the moments are aligned at right angles to the unique [111] axis, in the (111) plane.

a

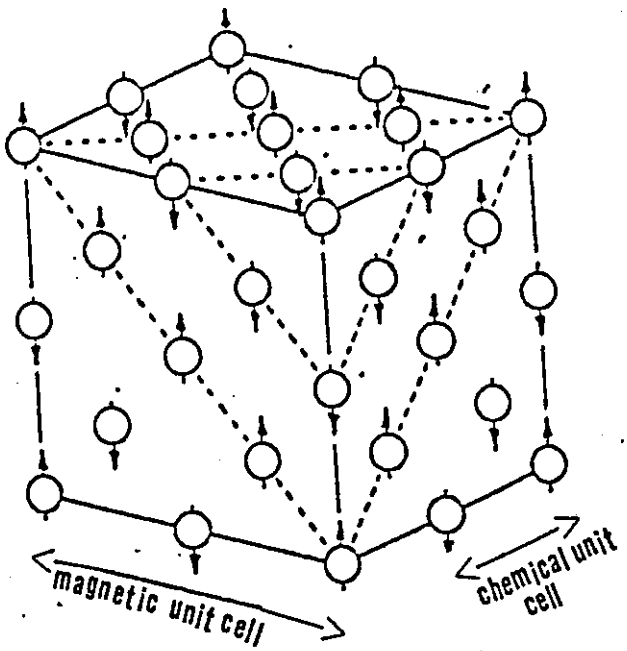

b

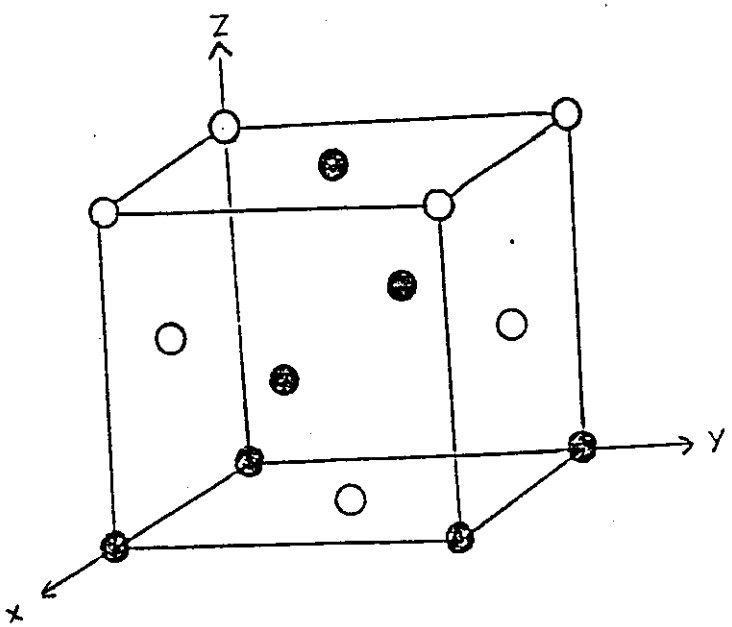

Figure (6.9) a) AF_2 Face centred cubic antiferromagnetic structure type 2

b) AF_3 Face centred cubic antiferromagnetic structure type 3A

The agreements between the measured and calculated magnetic structure factors are excellent, indicating that the postulated structure is correct. The magnetic moment of $3{\cdot}7 \mp 0{\cdot}02$ at 5K is confined to the Mn atoms. Any moment on the Pd atoms was estimated to be less that $0{\cdot}04 \mp 0{\cdot}01\mu B$. The (200) and (220) reflections are proportional to $(2P_{Pd} - P_{Mn})$ and $(2\,P_{Pd} + P_{Mn})$ respectively and are therefore sensitive to the moment distribution. There are additional reflections of antiferromagnetic origins in the low temperature diffraction pattern as shown in figure (6.4). These additional reflections are characteristic of fcc antiferromagnetism type 3A and may be indexed as (201), (203), (241), ... etc, reflections of a magnetic unit cell with lattice parameter twice that of the chemical ($L2_1$) unit cell. The proposed magnetic structure illustrated in figure (6·9b) is in excellent agreement with the experimental data. In this configuration adjacent spins along two of the cube edges are aligned parallel and along the other antiparallel, producing tetragonal magnetic symmetry.

The calculated and measured structures for fcc type 3A antiferromagnetism at 5K are compared in table (6.5).

Table (6.5)

h k l $a = 2a_o$	position	q^2F^2obs	$q^2_{\perp}F^2$cal	$q^2_{//}F^2$cal	$\mu_{Mn}(\mu_B)$
(201)	15·90	$0{\cdot}6471 \mp 0{\cdot}1$	0·578	0·221	0·80
(241)	33·05	$0{\cdot}3524 \mp 0{\cdot}1$	0·357	0·297	0·80

6.3 $Pd_{1\cdot6}Ag_{0\cdot4}MnIn$

The susceptibility and reciprocal susceptibility versus temperature curves are shown in figures (6.1) and (6.2) respectively. The specific heat measurements versus temperature are also shown in figure (6.10).

The neutron diffraction pattern obtained at several temperatures between 5K and room temperature, using D1A and D2B diffractometers. Figure (6.11) shows the nuclear powder diffraction pattern obtained at 5K using a D2B diffractometer. It shows peak splitting at high angle reflection which decreases with increasing temperature, disappearing above the Neel temperature as shown in figure (6.12). The splitting is a result of tetragonal distortion induced by the magnetic structure. The refinement for the tetragonal structure was carried out using the proposed space group (I4/mmm) with the atoms located at positions as explained in table (6.2). The measured and calculated nuclear intensities obtained using a Rietveld refinement program [72] at 5K are compared in table (6.6).

The effect of seven types of preferential disorder on the neutron structure factors have been determined as explained in the previous section. The preferential B_2 disorder in α(Mn–In) was determined as 0·10.

As in $Pd_{1\cdot8}Ag_{0\cdot2}MnIn$, the additional antiferromagnetic peaks belong to fcc type 3 antiferromagnetism and may be be indexed as (201), (203) ... etc, as shown in figure (6·13). These peaks disappear above the Neel temperature.

The calculated and measured magnetic structures at 5K are compared in table (6.7).

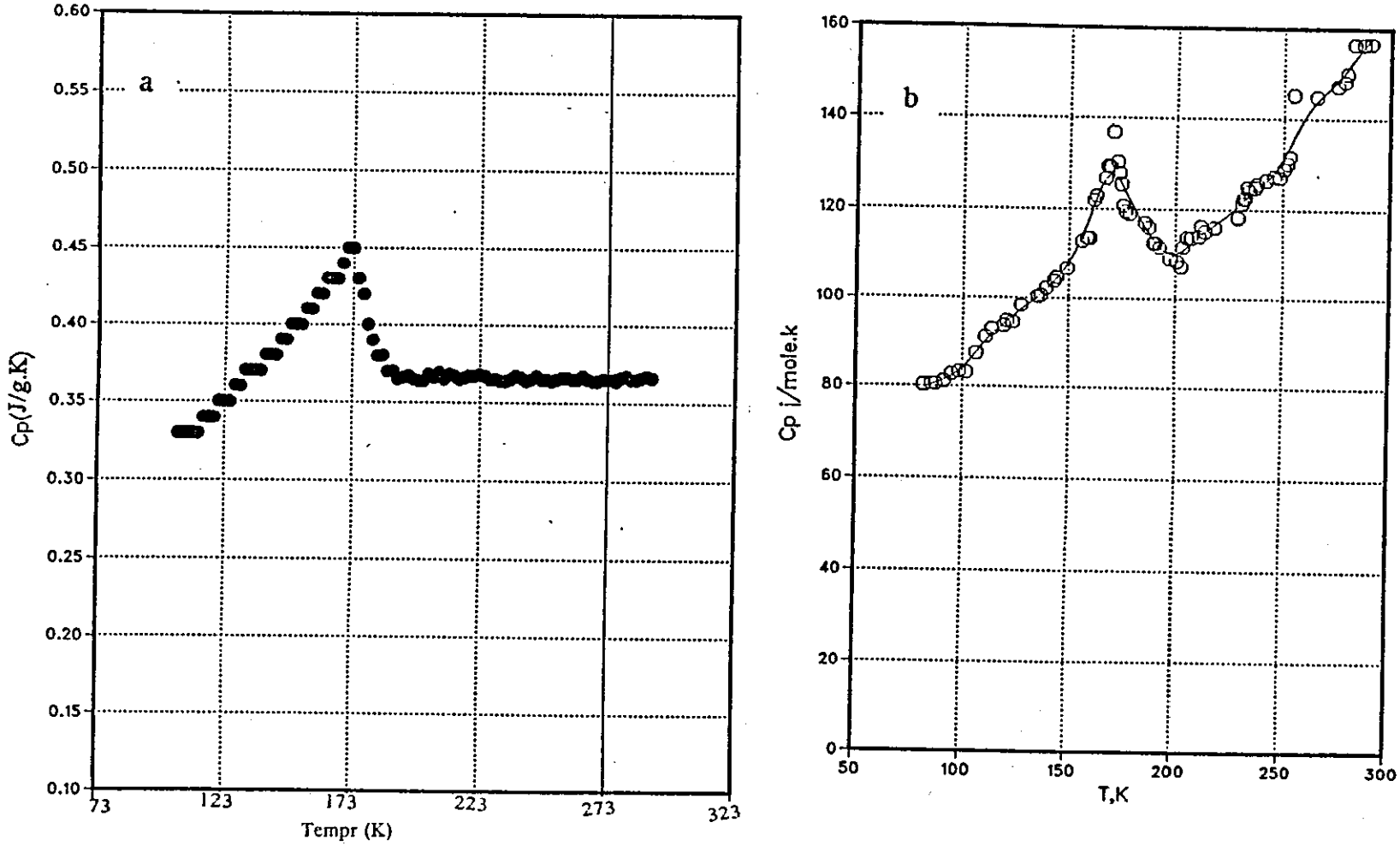

Figure (6.10) Specific heat measurement of $Pd_{1.6}$ $Ag_{0.4}$ Mn In

a - continuous heating
b - pulse heating

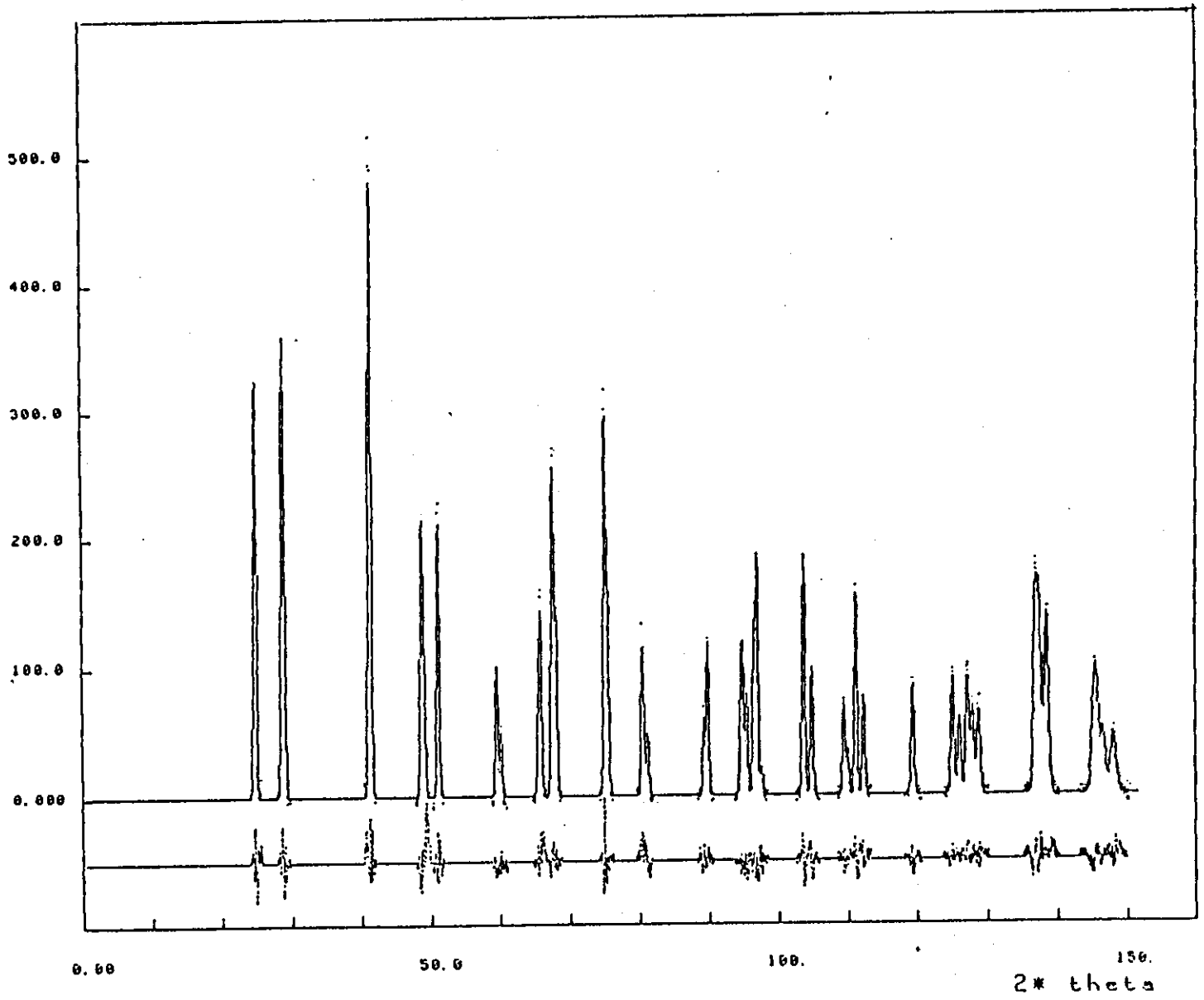

Figure (6.11) D_2B measurement (points) and resultant fit (line) with the difference (lower line below the spectrum) of $Pd_{1.6}$ $Ag_{0.4}$ Mn In at 5K. The wavelength of the neutrons was determined to be $\lambda = 1.594\text{Å}$.

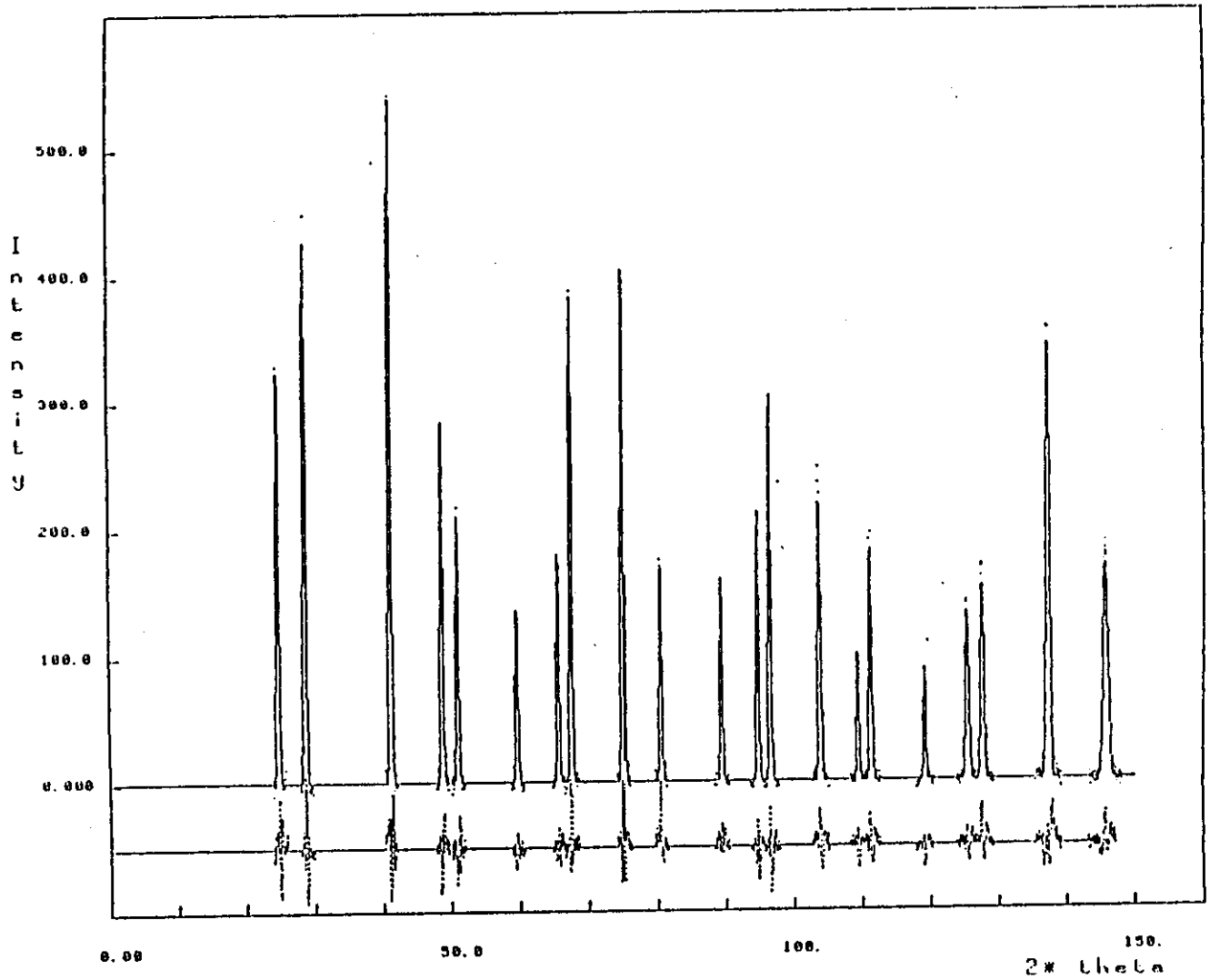

Figure (6.12) D_2B measurement (points) and resultant fit (line) with the difference (lower line below the spectrum) of $Pd_{1.6}\ Ag_{0.4}$ Mn In at 190K. The wavelength of the neutrons was determined to be $\lambda = 1.594\text{Å}$.

Table (6.6) The measured and calculated nuclear intensities for tetragonal structure. The R factors are a measure of the quality of the fit, where R_n is the R factor for integrated intensities is given in equation 4.1

Position	h k l	J(mult)	I cal	I obs
24·92	1 0 1	8	3021	3066 ∓ 34
28·76	1 1 0	4	2657	2702 ∓ 26
29·04	0 0 2	2	1304	1272 ∓ 21
41·13	2 0 0	4	1639	1784 ∓ 20
41·33	1 1 2	8	3249	3286 ∓ 27
48·69	2 1 1	16	1733	1639 ∓ 34
49·05	1 0 3	8	856	1220 ∓ 21
51·13	2 0 2	8	1841	1843 ∓ 30
59·57	2 2 0	4	859	755 ∓ 22
60·19	0 0 4	2	422	358 ∓ 20
65·59	3 0 1	8	531	514 ∓ 18
66·88	2 1 3	16	1056	1235 ∓ 22
67·48	3 1 0	8	1175	1172 ∓ 18
67·62	2 2 2	8	1172	1190 ∓ 12

a = b = 4·5378 ∓ 0·0001, c = 6·3574 ∓ 0·0002, a, b/c = 0·7137 ∓ 0·500

Temp effect Mn – In = 0·4230 ∓ 0·0221

R_n = 4·73

R_{exp} = 7·84

R_p = 11·67

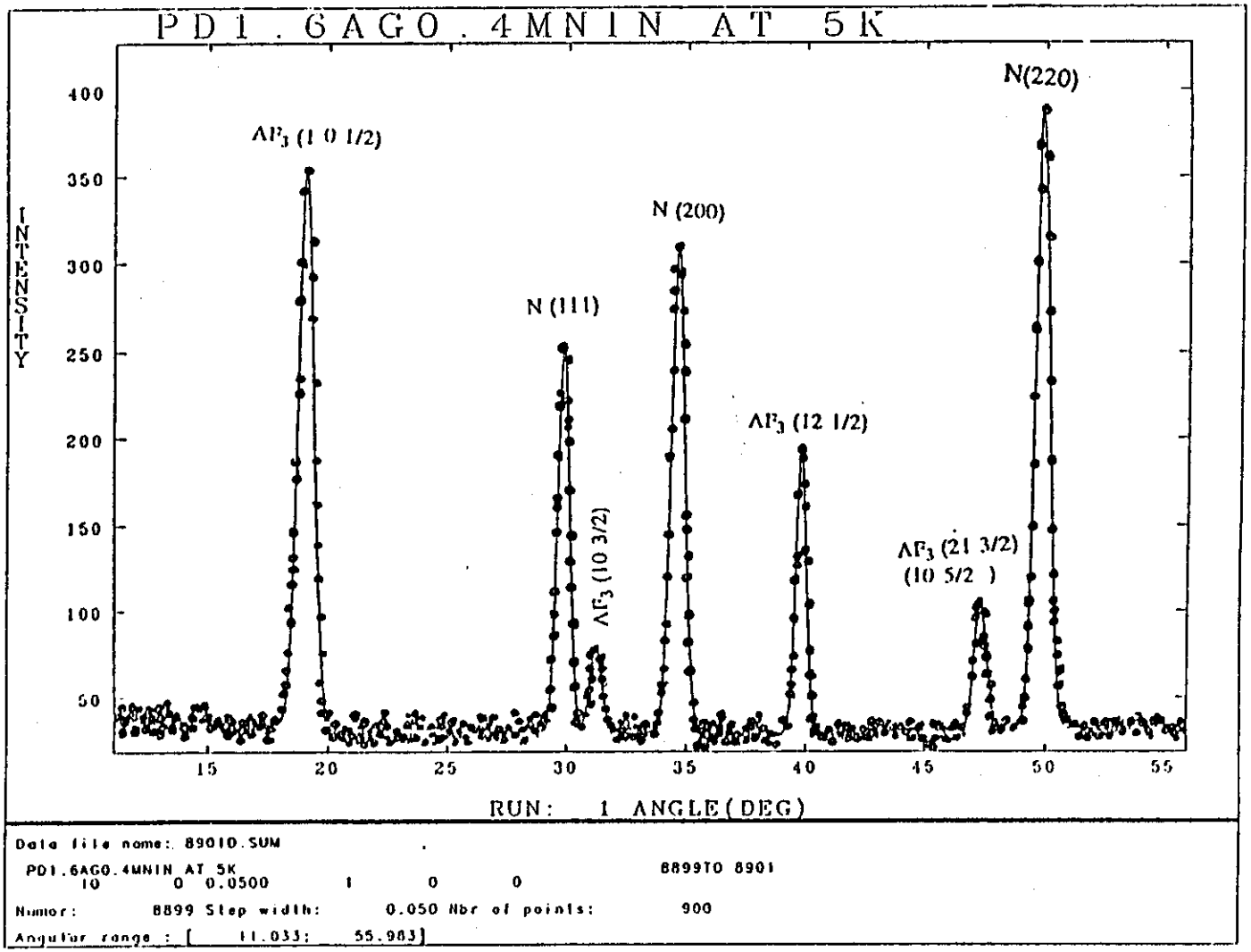

Figure (6.13) Neutron diffraction measurements at 5K.

Table (6.7)

h k l $a=2a_o$	$q^2_{//}$	$q^2_{\perp}$	$q^2_{\perp}F^2$cal	$q^2_{//}F^2$cal	q^2F^2obs	P_{Mn}	$\mu_{Mn}(\mu_B)$
(201)	0·529	0·9707	12·038	6·560	11·009 $\pm$ 0·1	0·800	3·65
(203)	0·680	0·8205	7·025	5·822	7·802 $\pm$ 0·1	0·795	3·65
(241)	0·506	0·9938	7·422	3·779	7·427 $\pm$ 0·1	0·683	3·65
(243)	0·550	0·950	8·855	3·390	8·954 $\pm$ 0·1	0·621	3·65
(205)							

The temperature dependence of the magnetic order was examined by observing the temperature dependence of the magnetic Bragg reflections. An example of such a temperature dependence for the $(1, 0, \frac{1}{2})$ magnetic Bragg reflection of $Pd_{1.6}Ag_{0.4}MnIn$ is presented in figure (6.14). The Neel temperatures suggested by magnetic susceptibility and specific heat data are also shown in figure (6.14) and are in good agreement with the value obtained by the neutron measurements. Figure (6.15) shows the observed behaviour of the reduced magnetisation with reduced temperature, compared with that predicted for the Brillouin function $J=\frac{1}{2}$, 3 and 2. From figure (6.15) it may be seen that the observed and calculated variations is in poor agreement

6.4 $Pd_{1·4}Ag_{0·6}MnIn$

The susceptibility and reciprocal susceptibility versus temperature curves are shown in figures (6.1) and (6.2) respectively. The specific heat measure–ments versus temperature are also shown in figure (6.16).

The neutron diffraction pattern was obtained at several temperatures between 5K and room temperatures, using the diffractometers D1A and D2B.

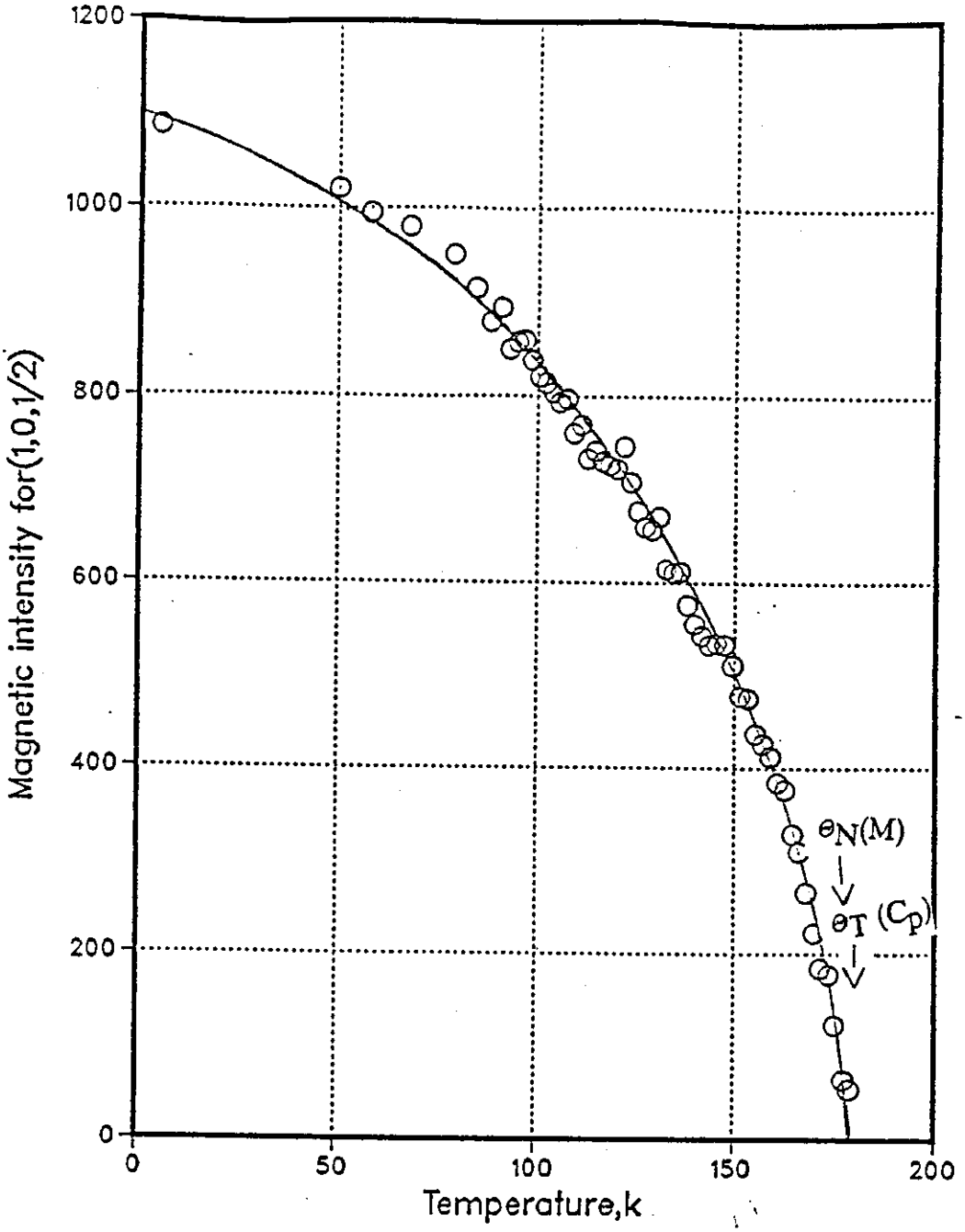

Figure (6.14) Temperature dependence of magnetic intensity for a $Pd_{1.6}$ $Ag_{0.4}$ Mn In. The Curie temperatures suggested by specific heat and magnetic susceptibility data are shown.

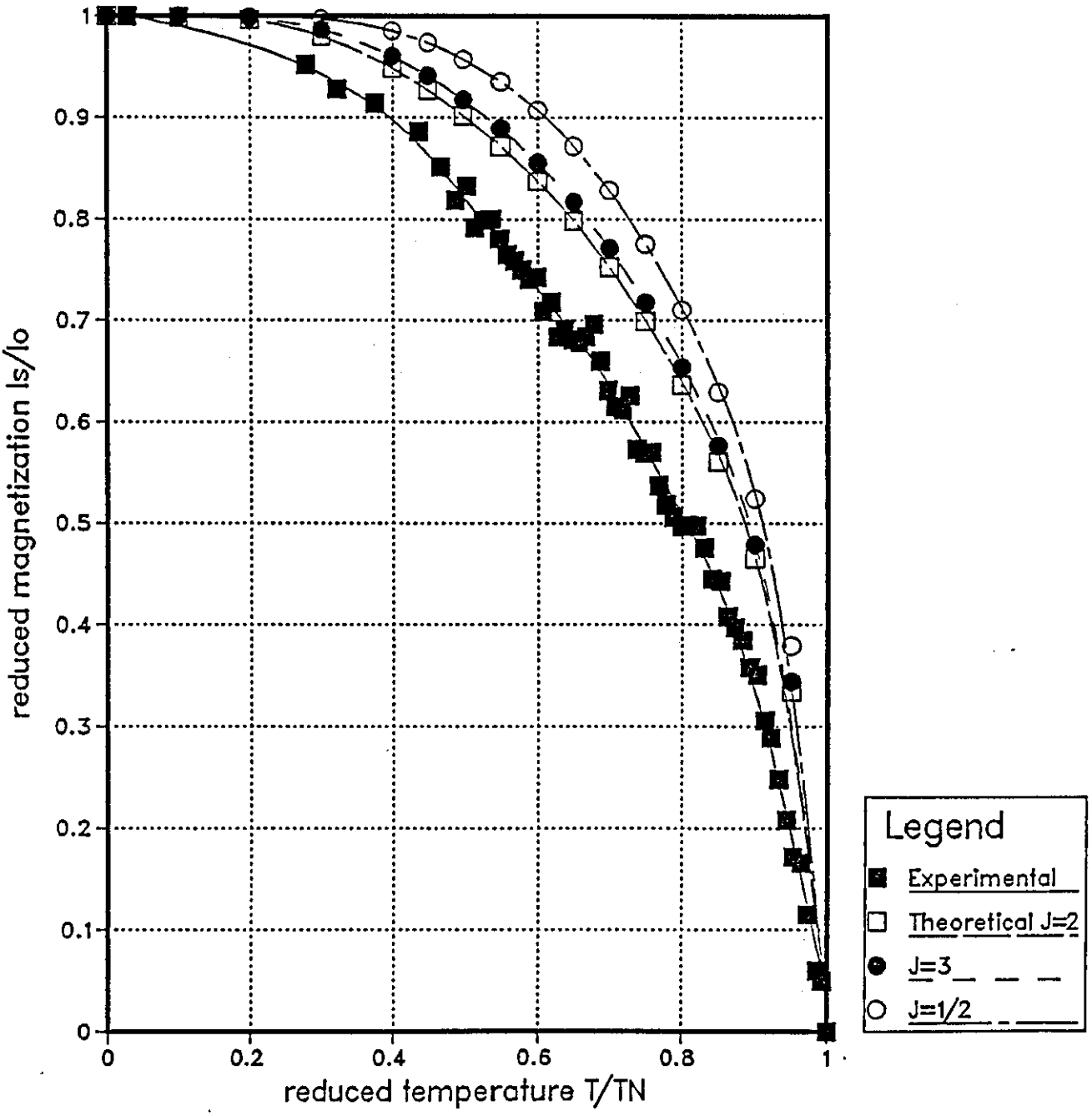

Figure (6.15) Theoretical curve of reduced magnetisation I_S/I_O against reduced temperature T/T_N, compared with experimental results for $Pd_{1.6}\,Ag_{0.4}$ Mn In.

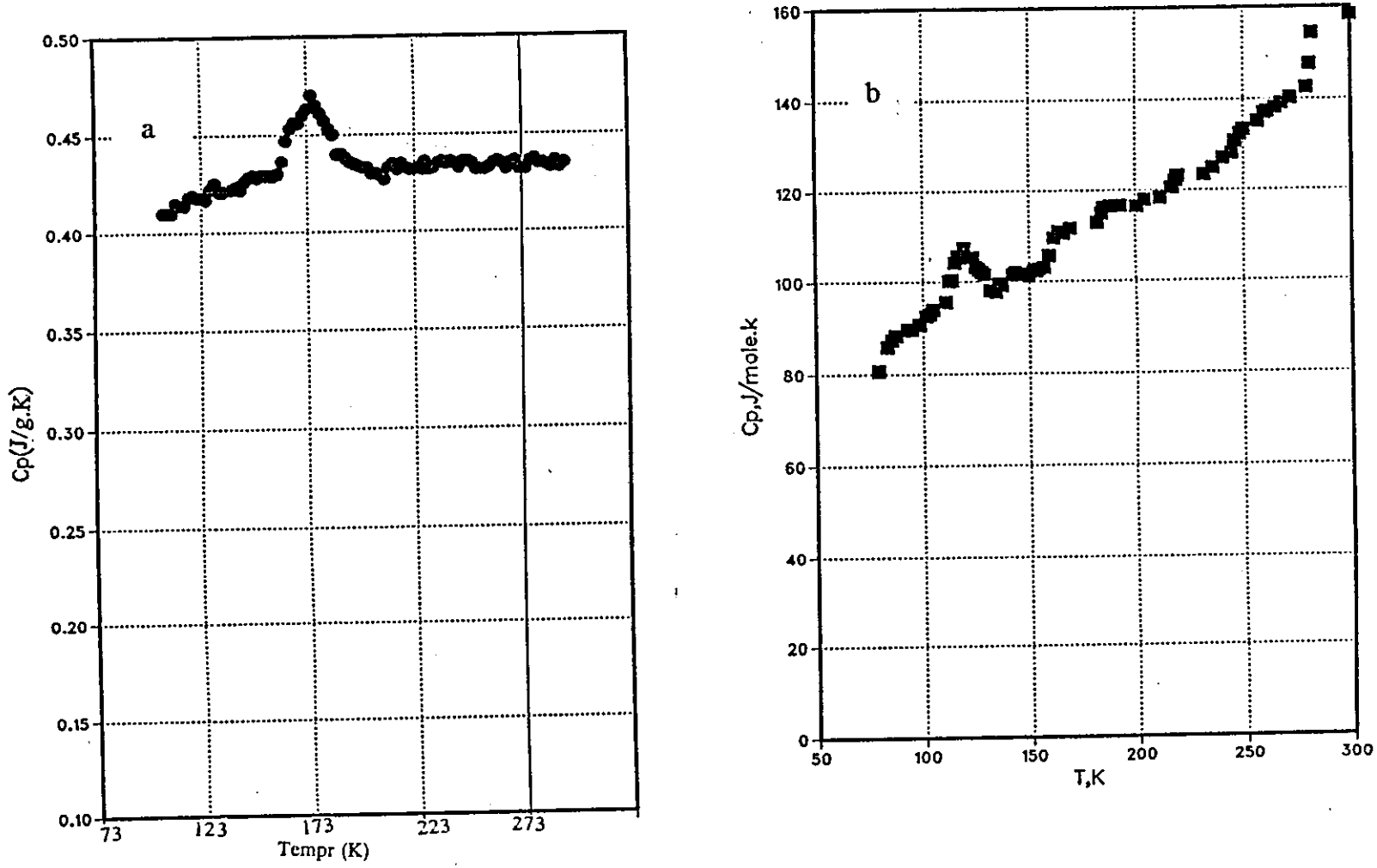

Figure (6.16) Specific heat measurements of $Pd_{1.4}$ $Ag_{0.6}$ Mn In

a - continuous heating
b - pulse heating

Figure (6.17) shows the powder diffraction patterns obtained at 5K using D2B. The high angle peaks show less splitting than that of the observed in $Pd_{1.6}Ag_{0.4}MnIn$. The splitting is a result of tetragonal distortion induced by the AF_3A magnetic structure as reported in the previous section. As expected the peak splitting decreases with increasing temperature. The refinement for the tetragonal structure was carried out using the same method as explained in previous sections. The measured and calculated nuclear intensities at 5K are compared in table (6.8). The preferential B2 disorder was also determined as before and the value α(Mn – In) was found to be 0·08.

At low temperature, theadditional antiferromagnetic peaks belong to fcc type 3 antiferromagnetism as observed for $Pd_{1.8}Ag_{0.2}MnIn$ and $Pd_{1.6}Ag_{0.4}MnIn$. This is shown in figure (6.18). The calculated and measured magnetic structures at 5K are compared in table (6.9).

Table (6.9)

h k l $a = 2a_o$	q^2F^2obs	$q^2_\perp F^2$cal	$q^2_{//} F^2$cal	$\mu_{Mn}(\mu_B)$
(201)	11·170 ∓ 0·2	13·048	7·111	3·8
(203)	7·7854 ∓ 0·2	8·614	6·310	3·8
(241)	6·633 ∓ 0·2	6·945	4·096	3·8
(243), (205)	7·676 ∓ 0·2	7·346	3·874	3·8

6.5 $Pd_{1·2}Ag_{0·8}MnIn$

The susceptibility and reciprocal susceptibility versus temperature curves are shown in figures (6.1) and (6.2) respectively. The specific heat measure–ments are shown in figure (6.19).

It may be noted from the magnetic measurements that a saturated range exists below the ordering temperature. This phenomenon is due to the onset of

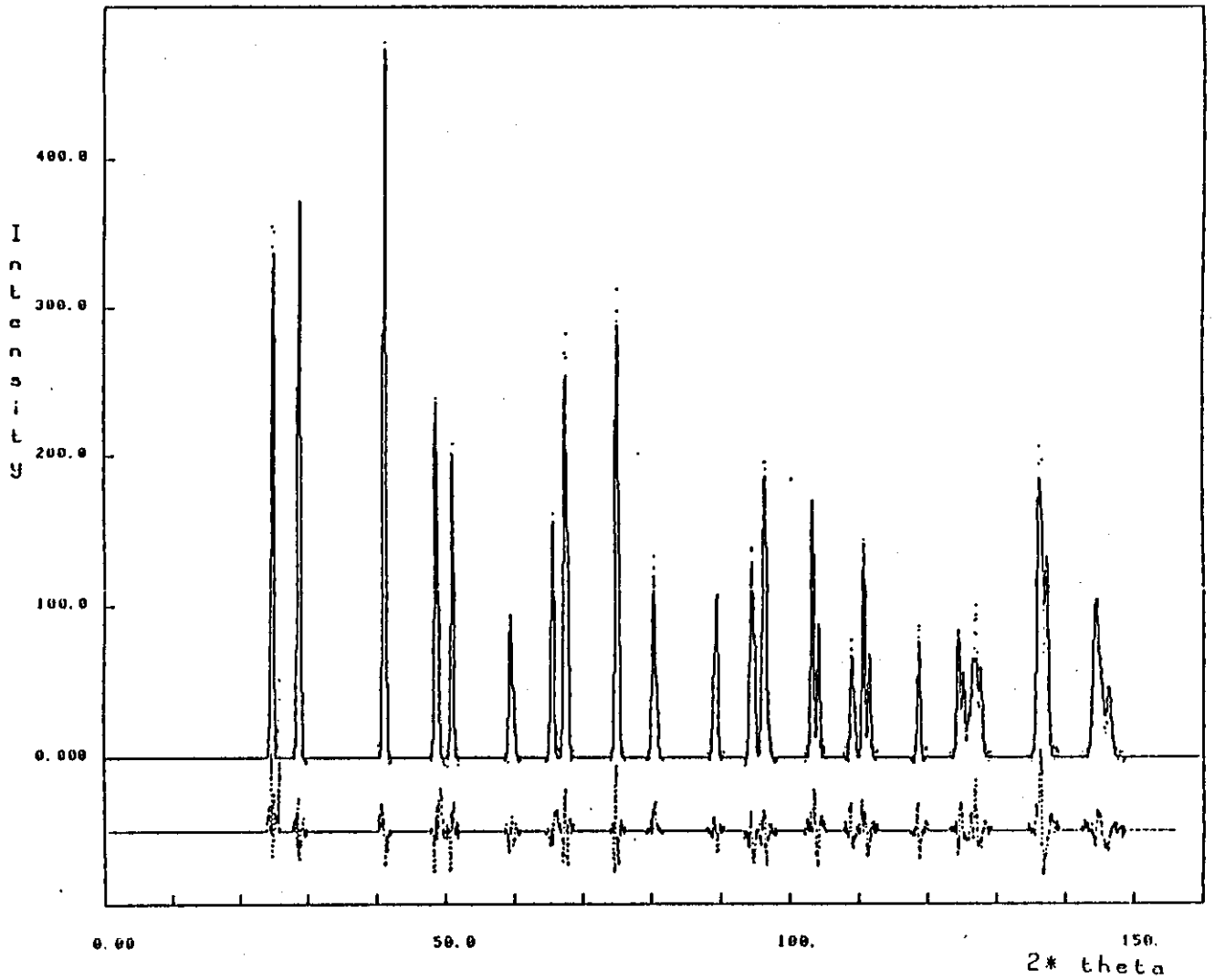

Figure (6.17) D_2B measurements (points) and resultant fit (line) with the difference (lower line below the spectrum) of $Pd_{1.4}$ $AG_{0.6}$ Mn In at 5K. The wavelength of the neutrons was determined to be λ = 1.594 A.

Table 6.8 The measured and calculated nuclear intensities for tetragonal structure

Position	h	k	l	J(mult)	I cal	I obs
24·79	1	0	1	8	3083	3460 ∓ 24
28·63	1	1	0	4	2527	2556 ∓ 18
28·84	0	0	2	2	1247	1230 ∓ 14
40·96	2	0	0	4	1522	1644 ∓ 13
41·12	1	1	2	8	3024	2924 ∓ 18
48·49	2	1	1	16	1737	1663 ∓ 17
48·76	1	0	3	8	860	1104 ∓ 15
50·90	2	0	2	8	1729	1726 ∓ 12
59·35	2	2	2	4	789	740 ∓ 16
59·82	0	0	4	2	390	365 ∓ 15
65·33	3	0	1	8	524	478 ∓ 12
65·56	2	1	3	16	1042	1149 ∓ 15
67·23	3	1	0	8	1087	1077 ∓ 12
67·34	2	2	2	8	1084	1098 ∓ 7
67·66	1	1	4	8	1076	1069 ∓ 15

$a = b = 4{\cdot}5499 \mp 0{\cdot}0001$, $c = 6{\cdot}3914 \mp 0{\cdot}0002$, $a, b/c = 0{\cdot}712 \mp 0{\cdot}500$

Temp effect Mn–In = $0{\cdot}4230 \mp 0{\cdot}221$

$R_n = 7{\cdot}66$.

$R_{exp} = 7{\cdot}16$

$R_p = 17{\cdot}94$

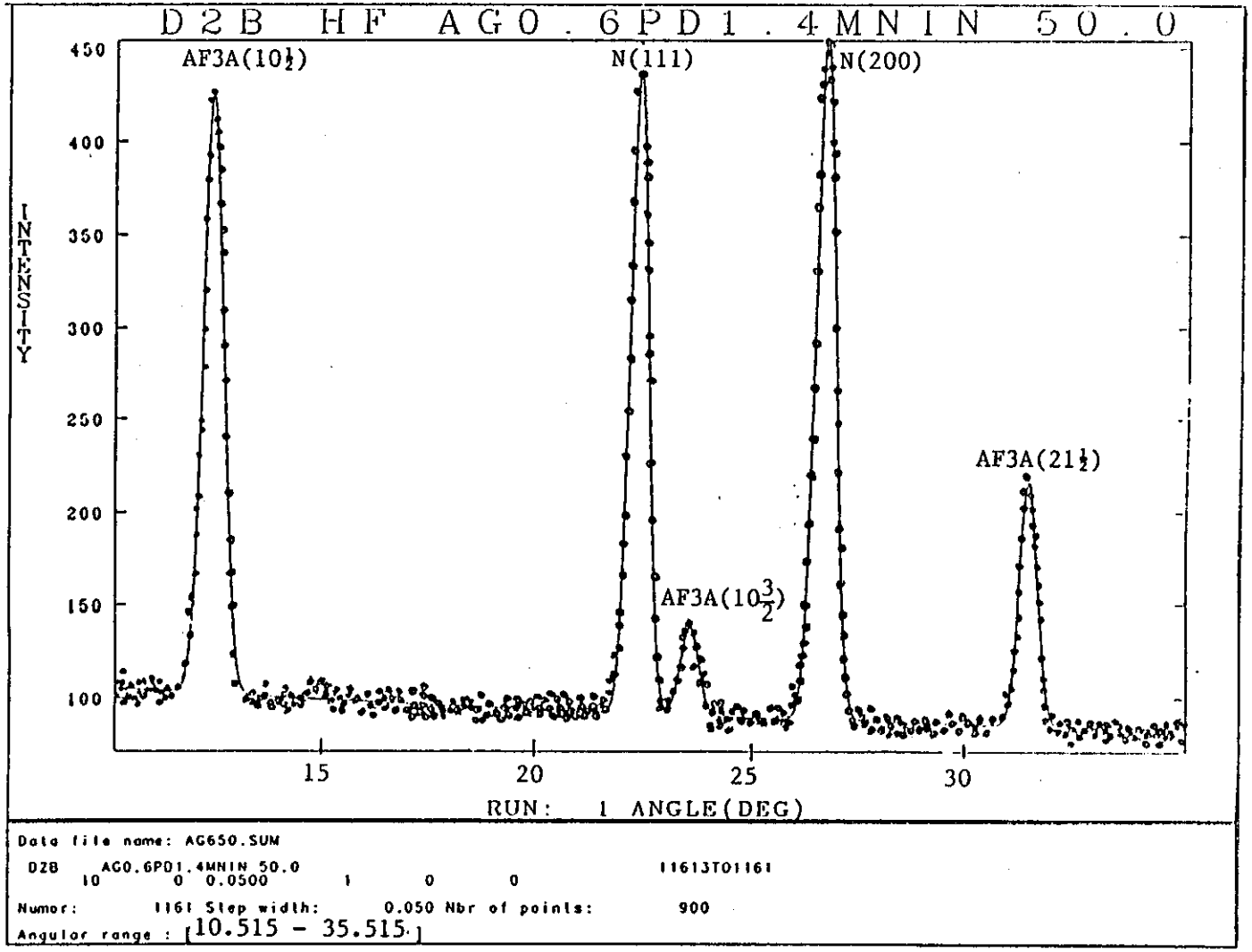

Figure (6.18) Neutron diffraction measurements at 50K.

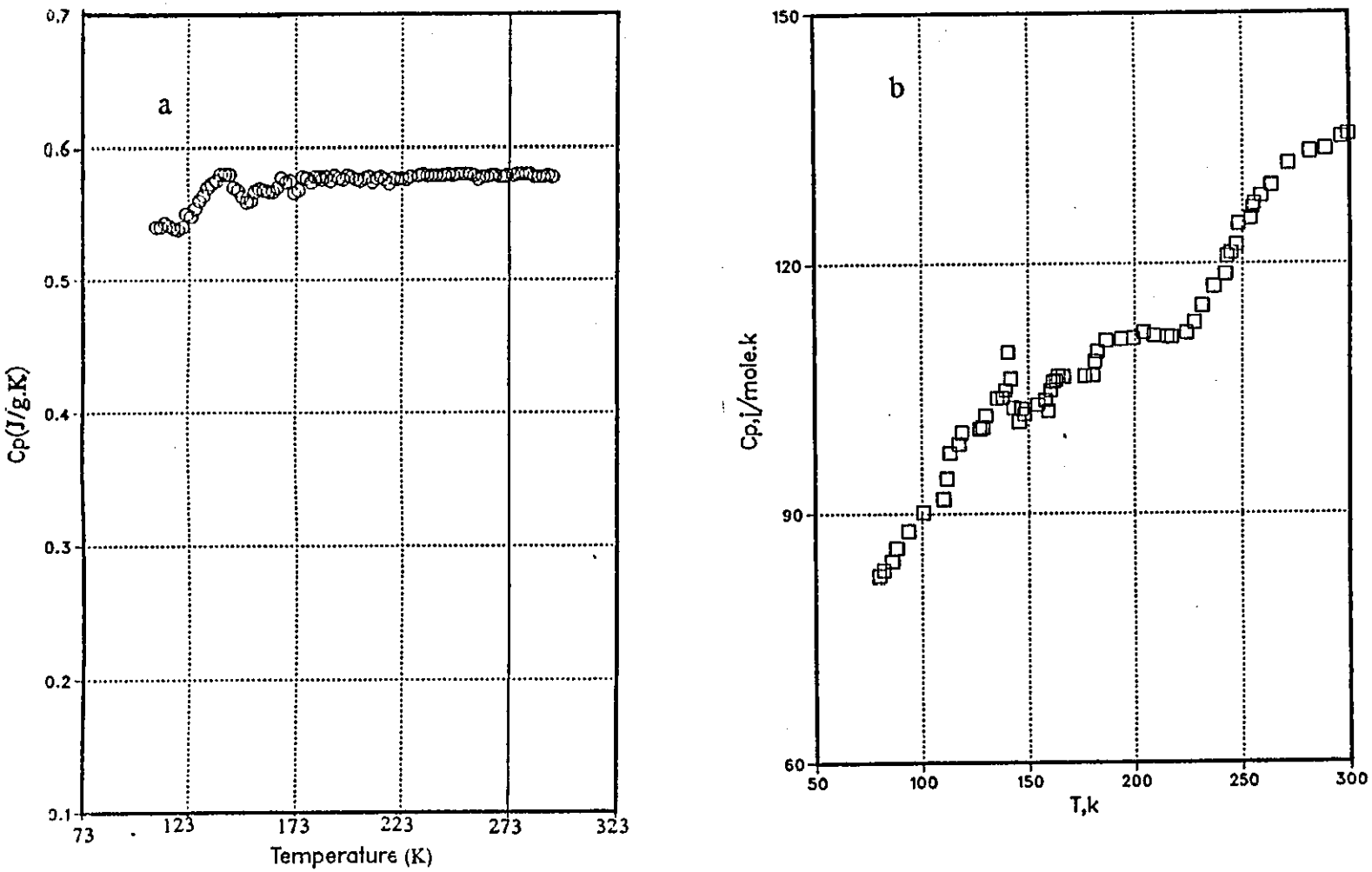

Figure (6.19) Specific heat measurements of $Pd_{1.2}$ $Ag_{0.8}$ Mn In

a - continuous heating
b - pulse heating

ferromagnetism. It is also noted from the results $Pd_{0.8}Ag_{1.2}MnIn$, $Pd_{0.6}Ag_{1.4}MnIn$ and $Pd_{0.4}Ag_{1.6}MnIn$ that when the amount of Pd is decreased to below 1.2, ferromagnetism is established as shown in figures (6.1) and (6.2).

The neutron diffraction pattern obtained at 5K using D2B at the ILL with $\lambda = 1{\cdot}594\text{Å}$ is shown in figure (6.20) for $Pd_{1.2}Ag_{0.8}MnIn$. At 5K there are no additional magnetic peaks as expected since the magnetic and chemical unit cells are the same size. Therefore the magnetic and nuclear peaks are super–imposed at the same Bragg angle θ. Since the magnetic symmetry is cubic and there is no unique axis so it was not possible to determine the moment orientation for ferromagnetics. Down to 5K there was no evidence of any type of antiferromagnetic order.

The calculated and observed magnetic structure factor are in good agree–ment as shown in table (6.10). Thus the alloy is predominantly ordered in the $L2_1$ structure. The B2 disorder corresponding to α(Mn–In) was determined as before and the value found to be close to 0·01. This means a perfect occupation of all lattice sites (i.e. no vacancies) are predicted.

It is noted from the neutron diffraction results that the ferromagnetic ordering increases considerably with increasing x composition for $x \geq 1.6$. All the alloys in this range of composition are chemically ordered in the $L2_1$ structure.

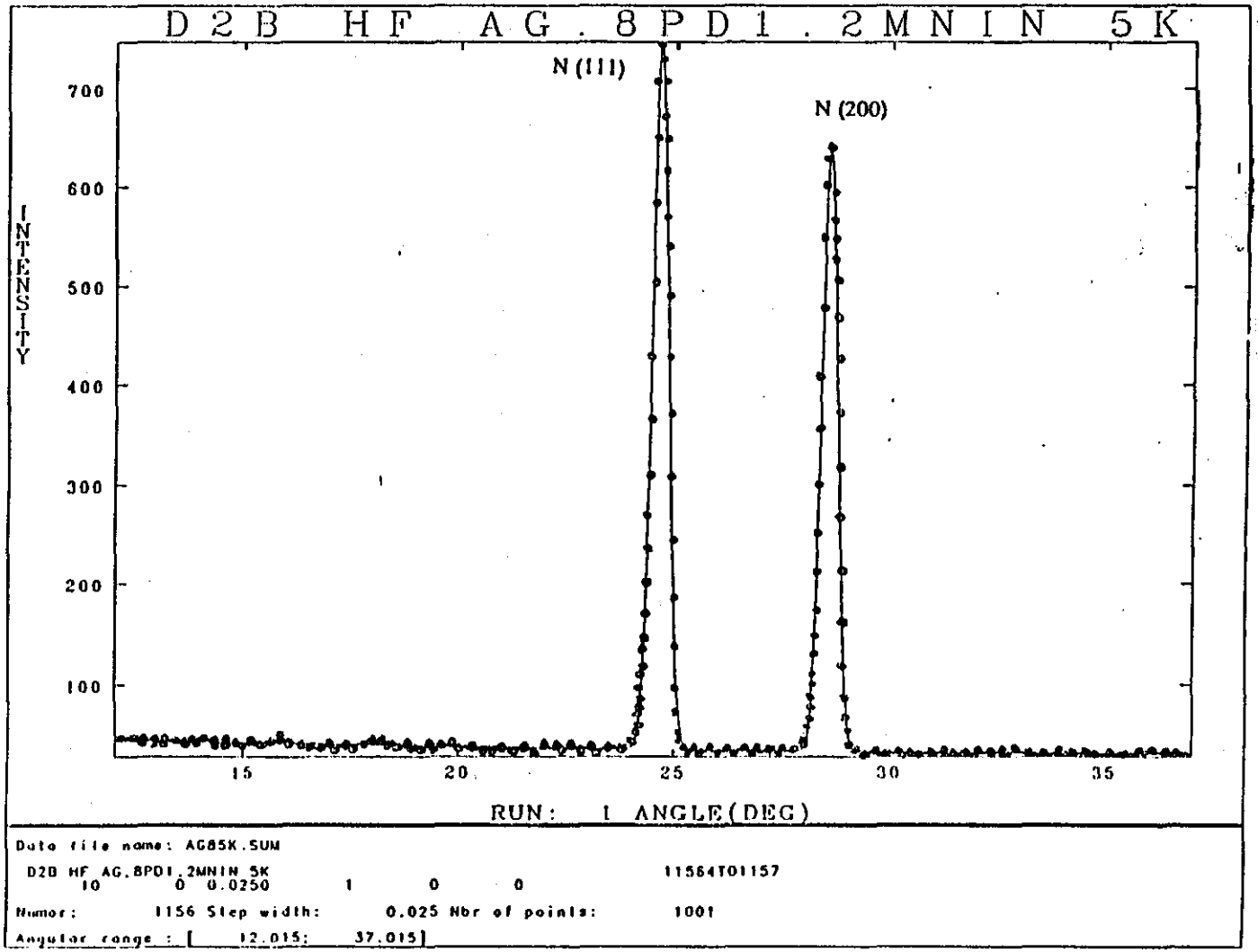

Figure (6.20) Neutron diffraction measurements at 5K

Table (6.10)

h k l	position	$q^2F^2_{N,M}$ obs	$q^2F^2_M$ cal	$q^2F^2_M$ obs
1 1 1	24·65	18·85 $\mp$ 1	9·125	9·130 $\mp$ 0·05
2 0 0	28·55	27·95 $\mp$ 1	6·987	6·840 $\mp$ 0·05
2 2 0	40·90	27·151 $\mp$ 1	3·352	3·510 $\mp$ 0·05
3 1 1	48·40	11·980 $\mp$ 1	2·145	2·259 $\mp$ 0·05
2 2 2	50·65	22·706 $\mp$ 1	1·642	1·602 $\mp$ 0·05
4 0 0	59·25	24·359 $\mp$ 1	0·709	0·720 $\mp$ 0·05
3 3 1	65·20	10·183 $\mp$ 1	0·434	0·462 $\mp$ 0·05
4 2 0	67·15	21·317 $\mp$ 1	0·263	0·265 $\mp$ 0·05
4 2 2	74·15	23·803 $\mp$ 1	0·162	0·162 $\mp$ 0·05

CHAPTER SEVEN

EXPERIMENTAL RESULTS – $Pd_{2-x}Au_xMnIn$

7.1 INTRODUCTION

The Pd–based series are particularly rich, both in the range of their magnetic properties and the variation observed in their chemical order. The basic B2 unit of the structure AuMn is itself antiferromagnetic, with sc type A order and a Neel temperature T_N = 503K. On cooling below T_N there is a slight tetragonal distortion. Neutron diffraction studies of the alloy system $Au_2Mn_{2-x}Al_x$ have established the co–existence of antiferromagnetic and ferro–magnetic structures between the compositions of AuMn and Au_2MnAl [86]. The attainment of perfect Heusler type ordering near the composition Au_2MnAl causes the appearance of a spiral spin structure for which the spiral axis is parallel to a (100) direction [86].

The alloy $Au_2Mn_{2-x}Zn_x$ was reported to be non–ferromagnetic by Morris et al (1956) and was confirmed by Bacon and Plant (1971) to be of the CsCl type [112, 87]. The absence of the odd superlattice reflection in neutron diffraction data suggests that the Mn and Zn atoms are completely disordered [87].

In an attempt to obtain details of the effects of continuous, discrete changes in electron concentration, a series of new alloys were investigated with the compositions $Pd_{2-x}Au_xMnIn$. No references were found to any earlier investigations of these alloys. All the alloys were prepared by the technique described in Chapter (4.1). X–ray powder diffraction patterns were taken for slow cooled alloys and single phase alloys were found to form for all compositions of $0 \leq x \leq 2$.

The lattice parameters were also determined. In this series four types of magnetic structures are observed, at low temperature, namely antiferromagnetic fcc type 1, AF_1, antiferromagnetic fcc type 3A, AF_3A, antiferromagnetic fcc type 2, AF_2 and ferromagnetic.

Most of the alloys were highly ordered in the Heusler ($L2_1$) structure with some B_2 disorder.

The alloys discussed in this chapter are listed in table (7.1). The magnetic, thermal and structural properties of each alloy are discussed in detail in the following sections.

Table (7.1)

Alloy	a_o(Å)	Heat Treatment	nc(e/ch. form)
Pd_2MnIn	6·369 ∓ 0·003	sc	4·0
$Pd_{1·8}Au_{0·2}MnIn$	6·341 ∓ 0·003	sc	4·2
$Pd_{1·6}Au_{0·4}MnIn$	6·349 ∓ 0·003	sc	4·4
$Pd_{1·4}Au_{0·6}MnIn$	6·413 ∓ 0·003	sc	4·6
$Pd_{1·2}Au_{0·8}MnIn$	6·448 ∓ 0·003	sc	4·8
PdAuMnIn	6·463 ∓ 0·003	sc	5·0
$Pd_{0·8}Au_{1·2}MnIn$	6·522 ∓ 0·003	sc	5·2
$Pd_{0·6}Au_{1·4}MnIn$	6·544 ∓ 0·003	sc	5·4
$Pd_{0·4}Au_{1·6}MnIn$	6·566 ∓ 0·003	sc	5·6
$Pd_{0·2}Au_{1·8}MnIn$	6·599 ∓ 0·003	sc	5.8
Au_2MnIn	6·644 ∓ 0·003	sc	6.0

7.2 $Pd_{1·8}Au_{0·2}MnIn$

The susceptibility and reciprocal susceptibility versus temperature curves are shown in figures (7.1) and (7.2) respectively. The specific heat measure–ments versus temperature obtained by using continuous and pulse heating methods are shown in figure (7.3) Neutron scattering measurements have been carried out at the ILL using the diffractometers D2B and D1A. The neutron diffraction patterns obtained at 40K and 290K using the D1A diffractometer with 1·909 A are shown in figures (7.4) and (7.5) respectively. Figure (7.4)

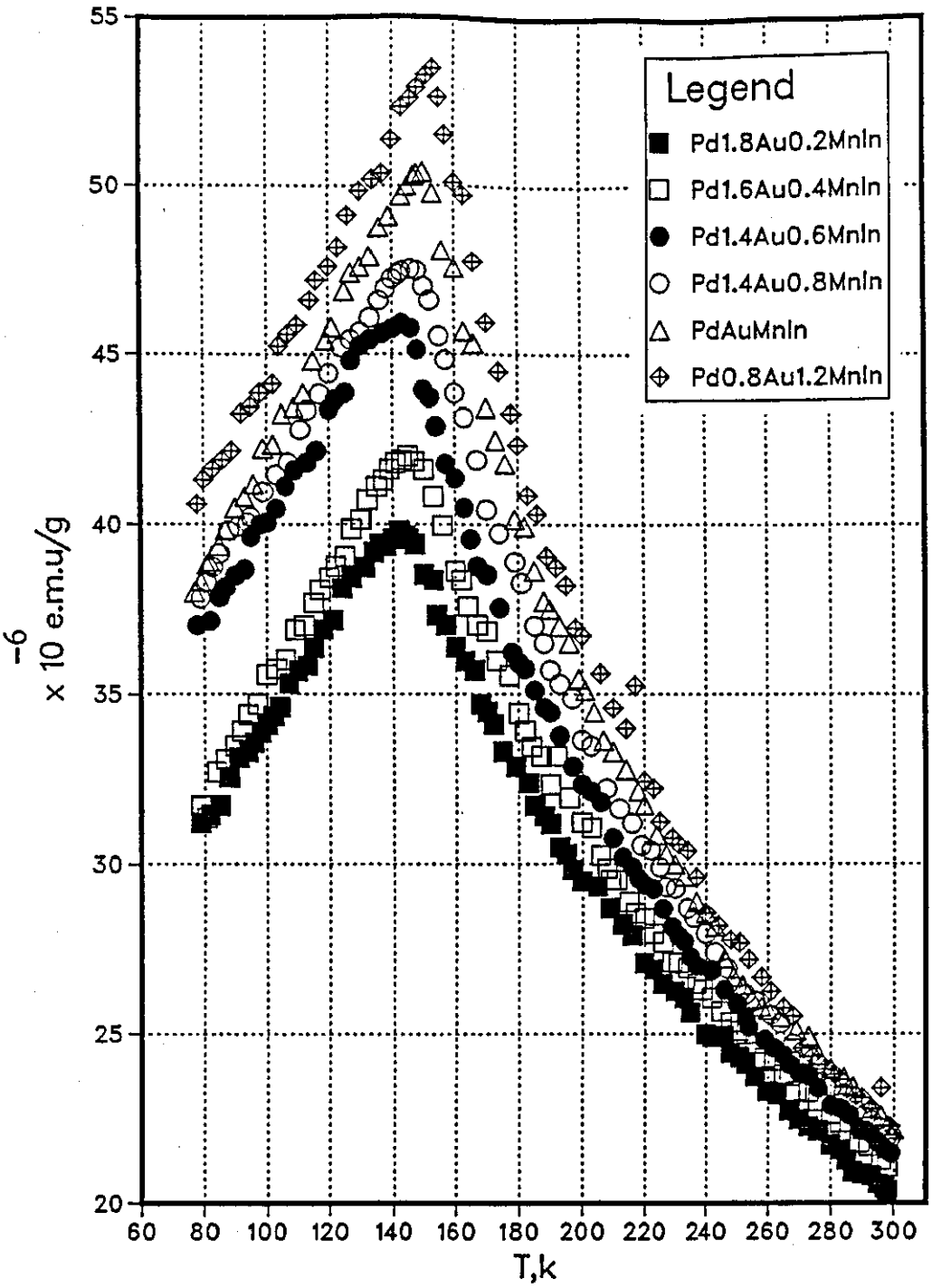

Figure (7.1) The susceptibility versus temperature curves for slow cooled alloys Pd_{2-x} Au_x Mn In

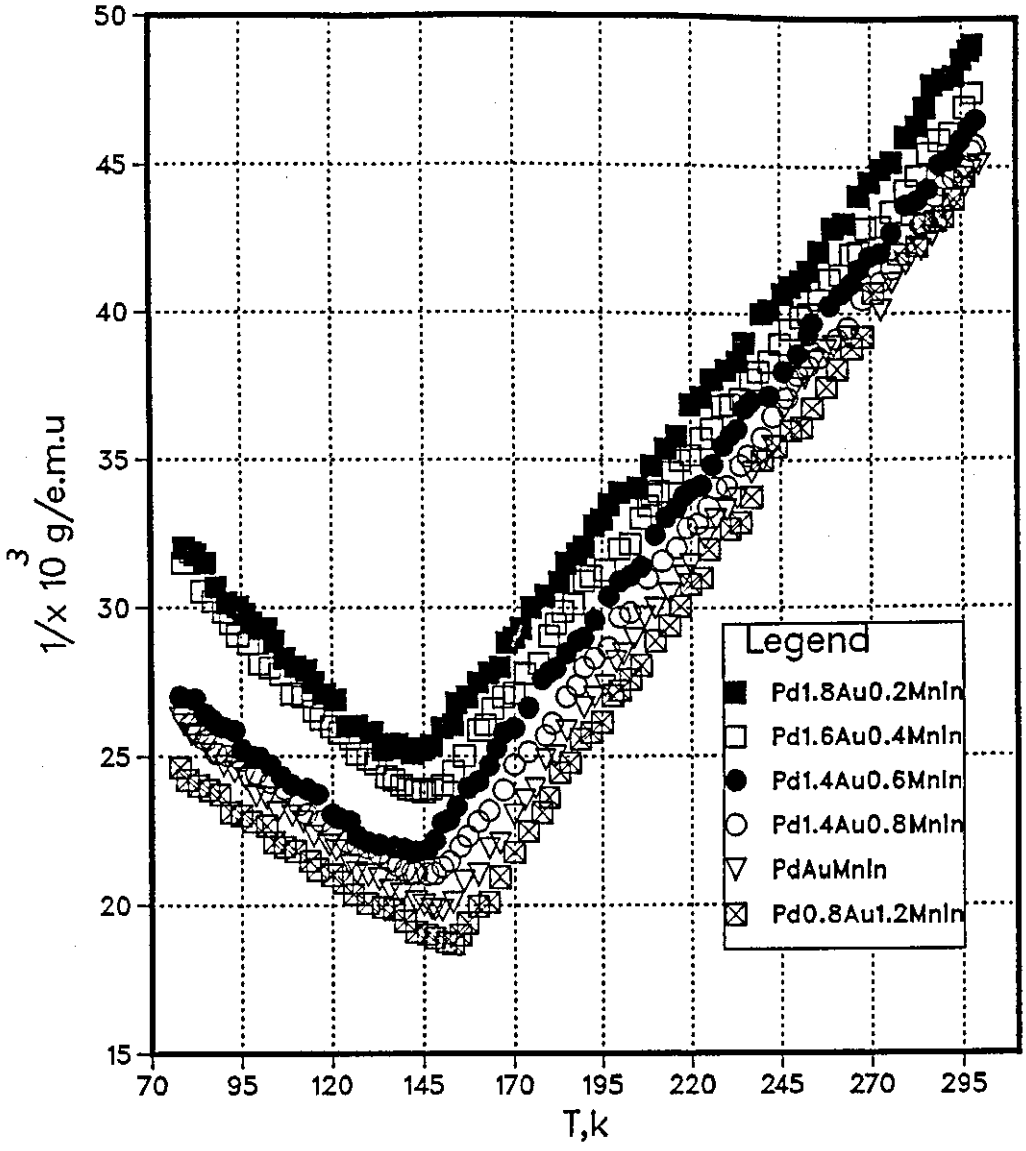

Figure (7.2) The reciprocal susceptibility versus temperature curves for slow cooled alloys Pd_{2-x} Au_x Mn In

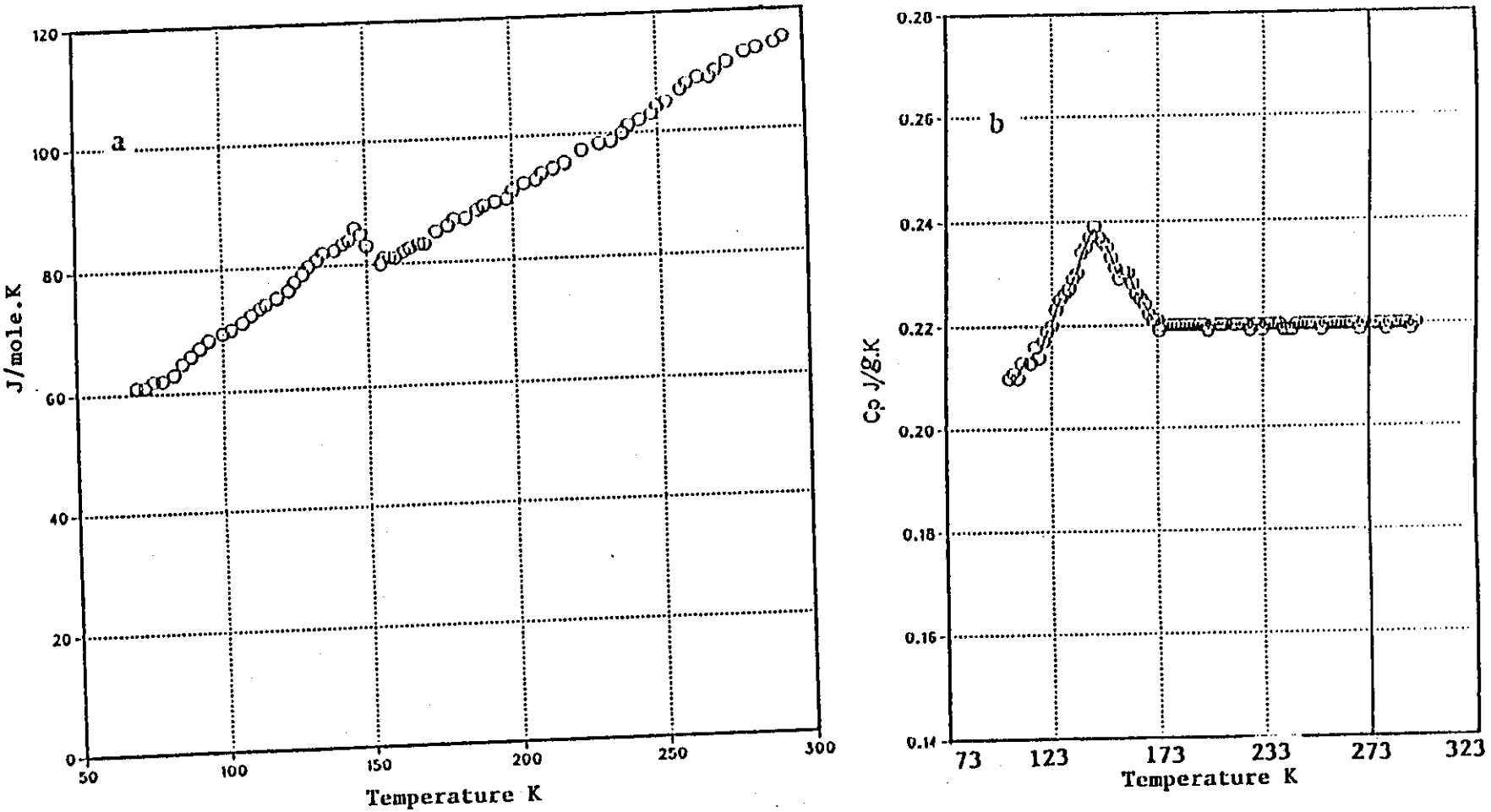

Figure (7.3) Specific heat measurements of $Pd_{1.8}Au_{0.2}MnIn$

a - pulse heating

b - continuous heating

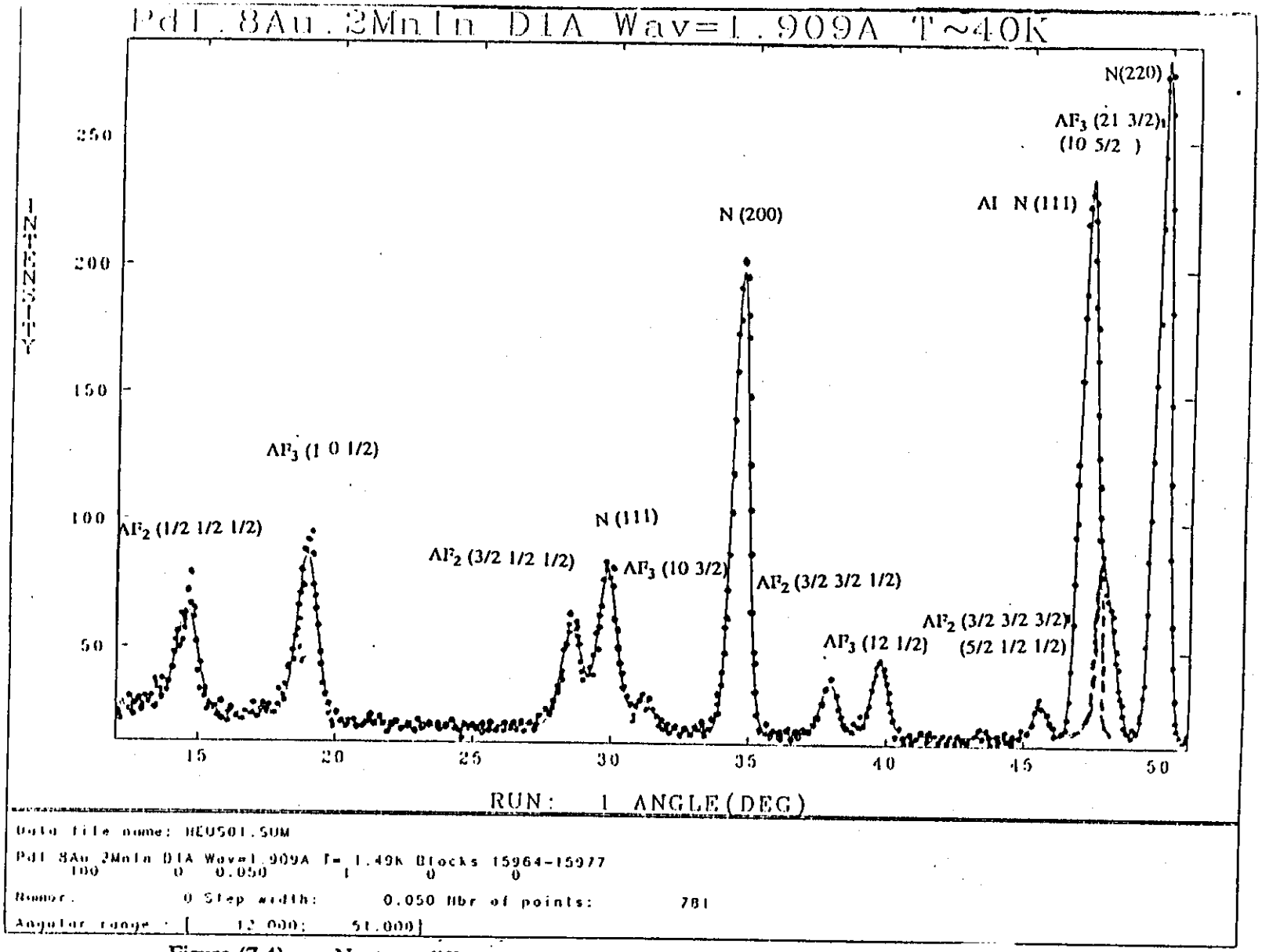

Figure (7.4) Neutron diffraction measurements at 40K showing the reflections from the nuclear and antiferromagnetic peaks.

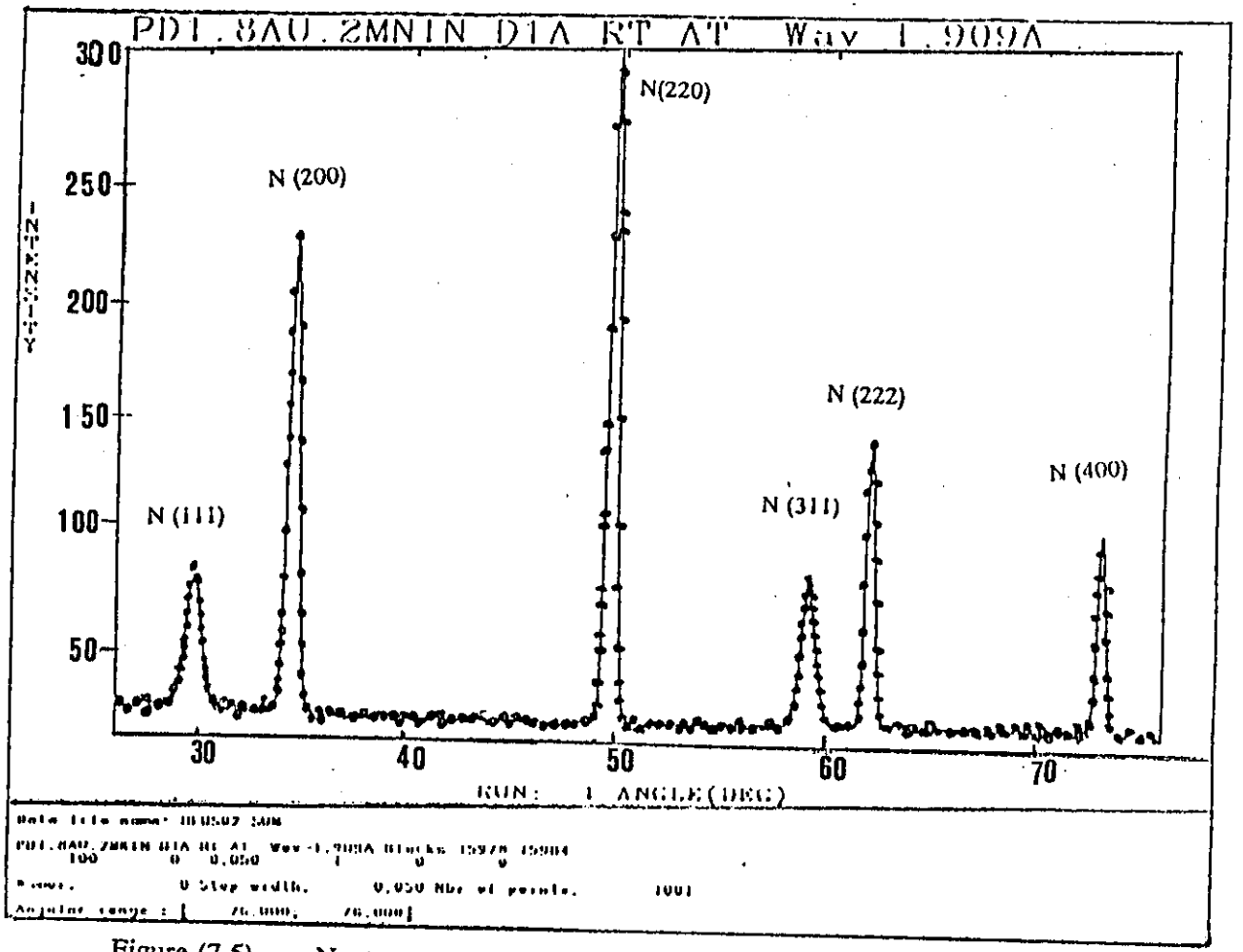

Figure (7.5) Neutron measurements at RT showing the reflections from the nuclear and antiferromagnetic peaks.

shows in addition to the nuclear reflections, magnetic reflections associated with two types of antiferromagnetic structures. The magnetic reflections may be indexed as (111), (311), (331), etc and (201), (203), (241), etc. using an enlarged magnetic unit cell with lattice parameters twice that of the chemical unit cell. These peaks are characteristics of the antiferromagnetic fcc type 2 and AF_3A structures respectively. Both magnetic structures were described in the last chapter.

Above the Neel temperature, all antiferromagnetic peaks have disappeared from the neutron diffraction patterns. The calculated and measured magnetic structure factors for both types of order, AF_2 and AF_3A are compared in tables (7.2) and (7.3) respectively.

Table(7.2)

h k l $a=2a_o$	position	$q^2 // F^2$cal	$q^2 \perp F^2$cal	q^2F^2obs	sin θ
(111)	14.644	0	11·118	11·210 ∓ 0·3	–
(311)	28.531	4·311	6·412	5·913 ∓ 0·3	0·99 ∓ 0·01
(331)	37.881	3·152	5·988	4·871 ∓ 0·3	0·98 ∓ 0·01
(333),	45·658	0	4·124	3·178 ∓ 0·3	–
(511)		2·171	3·961	3·178 ∓ 0·3	1·00 ∓ 0·01

Table (7.3)

h k l $a=2a_o$	position	$q^2 // F^2$calc	$q^2 \perp F^2$calc	q^2F^2obs
(210)	18·975	1·171	2·671	2·551 ∓ 0·2
(303)	30·837	0·901	2·441	2·20 ∓ 0·2
(241)	39·806	0·752	1·852	1·817 ∓ 0·2
(243),	47·231	1·133	2·415	2·315 ∓ 0·2
(205)				

The calculated $q^2F^2_{mag}$ values are based on the assumption that all the measured moments reside on the Mn atoms, and the magnetic form factor for Mn is that derived by Waston and Freeman [79].

The results indicate that the moment per Mn site at 40K are $2{\cdot}9\mu_B$ and $1{\cdot}5\ \mu_B$ for the AF_2 and AF_3A phases respectively. The maximum moment associated with the Pd site estimated to be $0{\cdot}06 \mp 0{\cdot}01\ \mu_B$.

The large peak at a 2θ position 47·2° (figure 7.4) consists of a contribution from the Al holder and the $AF_3(243)$ reflection. According to P W G Wyckoff [113], Al has a fcc structure at 25°C, with $a_o = 4{\cdot}0493$ Å. The program GETSFZ was used to determine the expected reflection for Al with space group $Fm\bar{3}m$ and the (111), (200) reflections were to be expected at the position above. This Al peak is very prominent in the nuclear structure refinement program because the program is carried out for one phase only. However the 2θ region of the Al reflection has been excluded to avoid producing large errors in the R–factors.

The powder refinement was carried out by the "Rietveld Profile technique" using space groups of tetragonal (I4/mmm) or rhombohedral ($R\bar{3}m$) symmetry, with atomic positions as indicated in the last chapter (Table 6.2). The program GETSFZ was used to generate a listing of reflections expected for these space groups using the Cambridge crystallographics suroutine library. The calculated and measured nuclear intensities for both structures are in good agreement, indicating the proposed structures are correct. The intensity of 15 nuclear reflections for the tetragonal structure were chosen from a total of 52 values for simplicity and are compared in the table (7.4) with calculated values obtained from figure (7.6).

The preferential B2 disorder (Mn–In) was also determined and the value of α found to be 0·07.

Table (7.4) The measured and calculated nuclear intensities for tetragonal structure

Position	h	k	l	I cal c	I obs
30·01	1	0	1	872	1173 $\pm$ 28
34·78	1	1	0	1715	1785 $\pm$ 20
34·80	0	0	2	857	887 $\pm$ 10
50·01	2	0	0	1058	1082 $\pm$ 9
50·02	1	1	2	2115	2160 $\pm$ 18
59·43	2	1	1	529	701 $\pm$ 13
59·45	1	0	3	265	354 $\pm$ 7
62·37	2	0	2	1275	1293 $\pm$ 20
73·43	2	2	0	598	595 $\pm$ 14
73·47	0	0	4	299	290 $\pm$ 7
81.31	3	0	1	175	254 $\pm$ 8
81·33	2	1	3	351	504 $\pm$ 15
83·89	3	1	0	880	893 $\pm$ 11
83.90	2	2	2	880	889 $\pm$ 11
83·93	1	1	4	880	882 $\pm$ 11

$a = b = 4{\cdot}515 \pm 0{\cdot}0002$, $c = 6{\cdot}383 \pm 0{\cdot}0007$

Temp effect Mn–In = $0{\cdot}4231 \pm 0{\cdot}0221$

$R_n = 4{\cdot}83$

$R_{exp} = 7{\cdot}85$

$R_p = 12{\cdot}67$

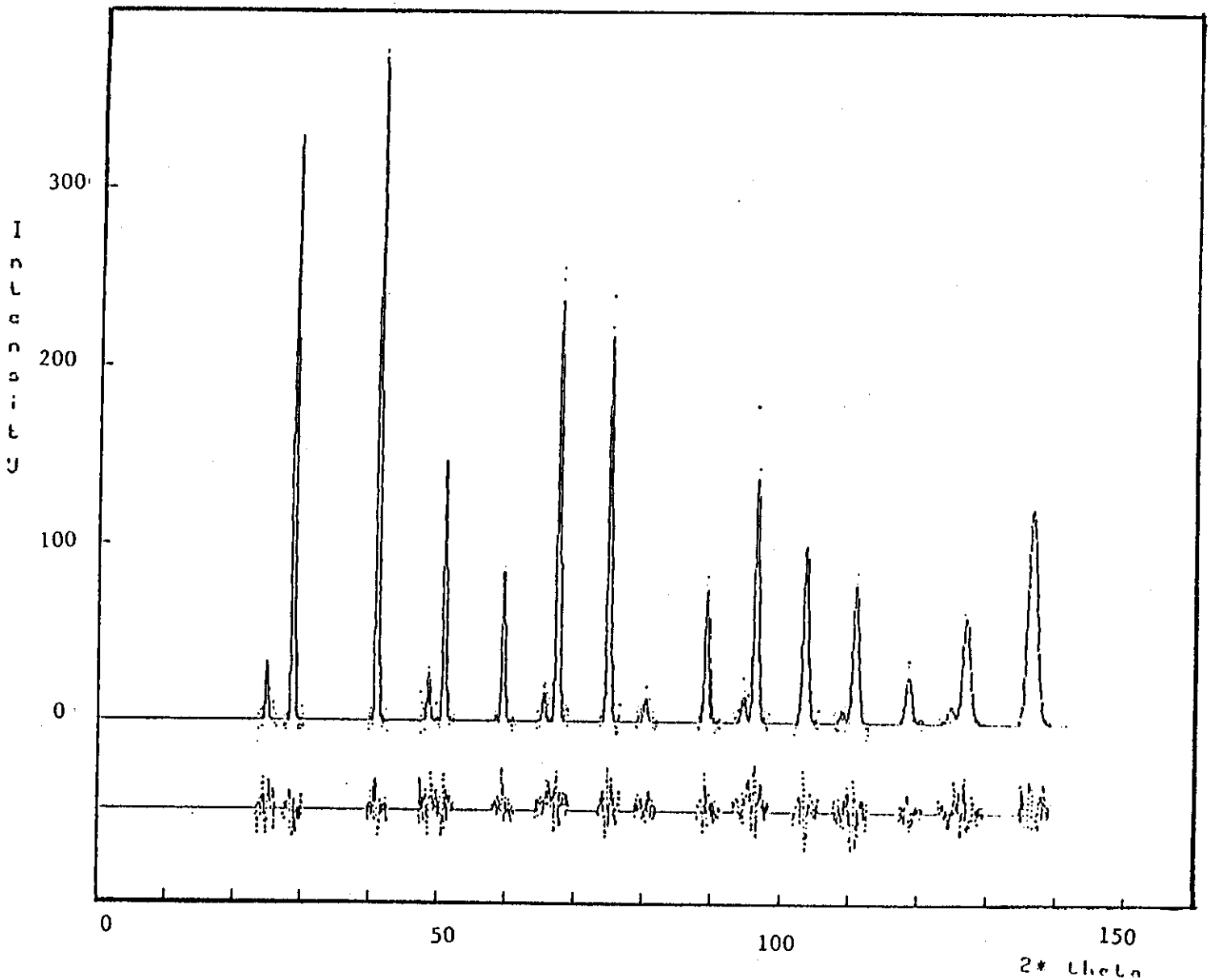

Figure (7.6) D_2B measurement (points) and results fit (line) with the difference (low line) below the spctrum) of $Pd_{1.8}$ $Au_{0.2}$ Mn In at 40 k. The wavelength of the neutrons was determined to be $\lambda = 1.549$ Å

7.3 $Pd_{1\cdot6}\ Au_{0\cdot4}MnIn$

The susceptibility and reciprocal susceptibility versus temperature curves are shown in figures (7.1) and (7.2) respectively. The specific heat as a function of temperature, obtained by using continuous heating and pulse techniques, is shown in figure (7.7).

Neutron diffraction patterns were obtained at several temperature using D1A and figure (7.8) shows the powder diffraction patterns obtained at 40K. From figure (7.8) it is noted that all AF_2 reflections are absent except the AF_2 (333) reflection, but the AF_3A reflections are still present. The measured and calculated antiferromagentic structures are compared in table (7.5). The magnetic moment per Mn site is found to be $3\cdot827 \mp 0\cdot2\ \mu_\beta$ and $1\cdot201 \mp 0\cdot01\ \mu_\beta$ for AF_3A and AF_2 at 40k, with a very small magnetic moment confined to the Pd sites to be $0\cdot037 \mp 0\cdot001\ \mu_\beta$.

The configurational symmetry indicated by the magnetic structure is tetragonal. Thus the refinement of the crystallographic structure was carried out using the Rietveld technique and tetragonal symmetry of the space group I4/mmm. The measured and calculated nuclear intensities at 40K are compared in table (7.6) and the calculated and observed profiles are shown in figure (7.9). The preferential B2 disorder in α(Mn–In) was determined to be $\alpha = 0\cdot075$.

At 270K above the Neel temperature, all powder antiferromagnetic peaks have disappeared and the crystallographic structure is cubic.

Table (7.5)

h k l $a = 2a_0$	position	$q^2_{//}F^2$calc	$q^2_{\perp}F^2$cal	q^2F^2obs
(201)	18·906	1·222	2·257	$2\cdot411 \mp 0\cdot2$
(203)	30·619	0·179	2·196	$2\cdot257 \mp 0\cdot2$
(241),	39·806	0·917	1·317	$1\cdot219 \mp 0\cdot2$
(243) (205)	47·241	0·881	1·07	$0\cdot988 \mp 0\cdot2$
(333) (511) AF_2	45·751	0·965	2·271	$2\cdot176 \mp 0\cdot2$

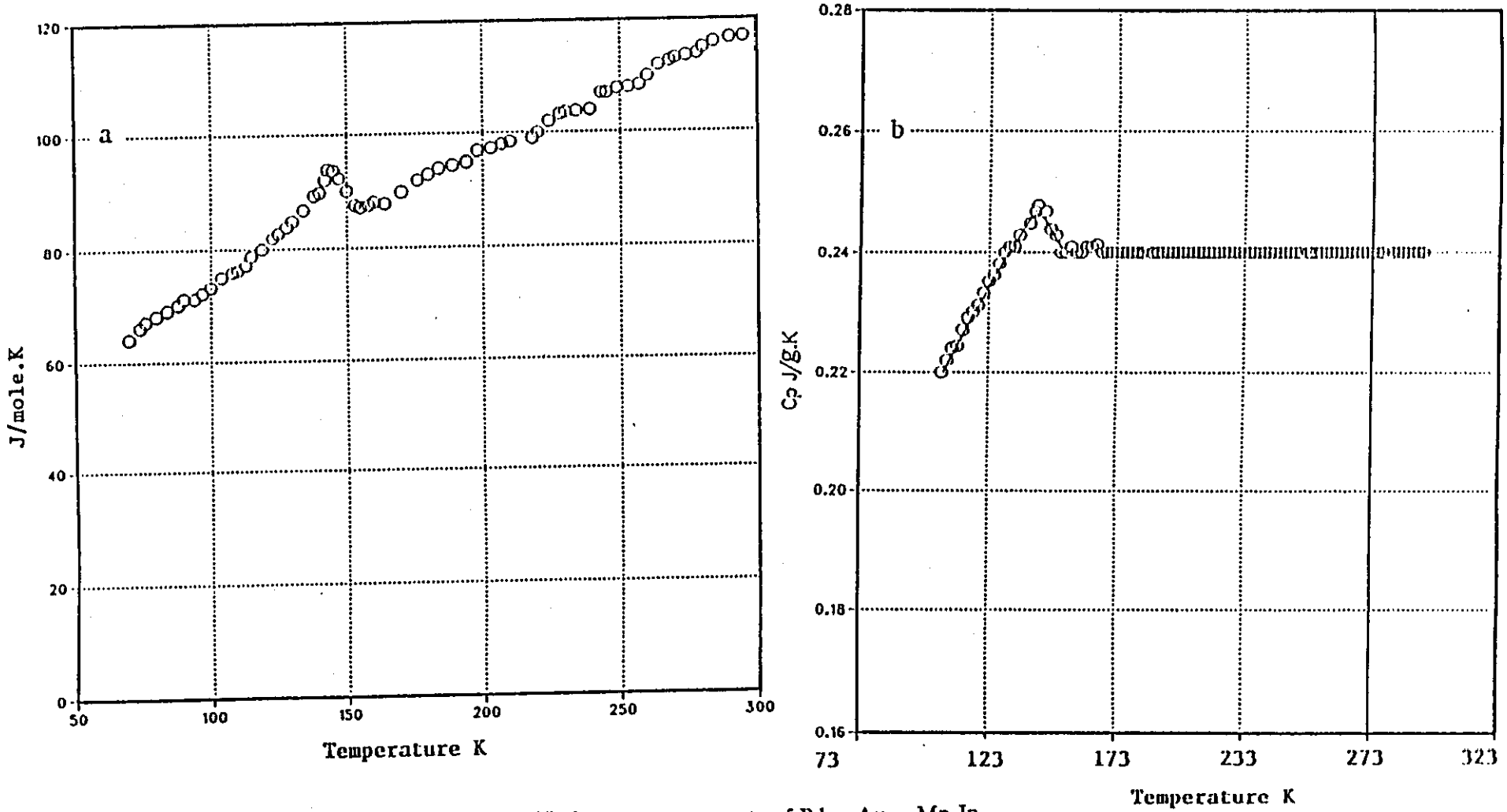

Figure (7.7) Specific heat measurements of $Pd_{1.6}$ $Au_{0.4}$ Mn In

a - pulse heating
b - continuous heating

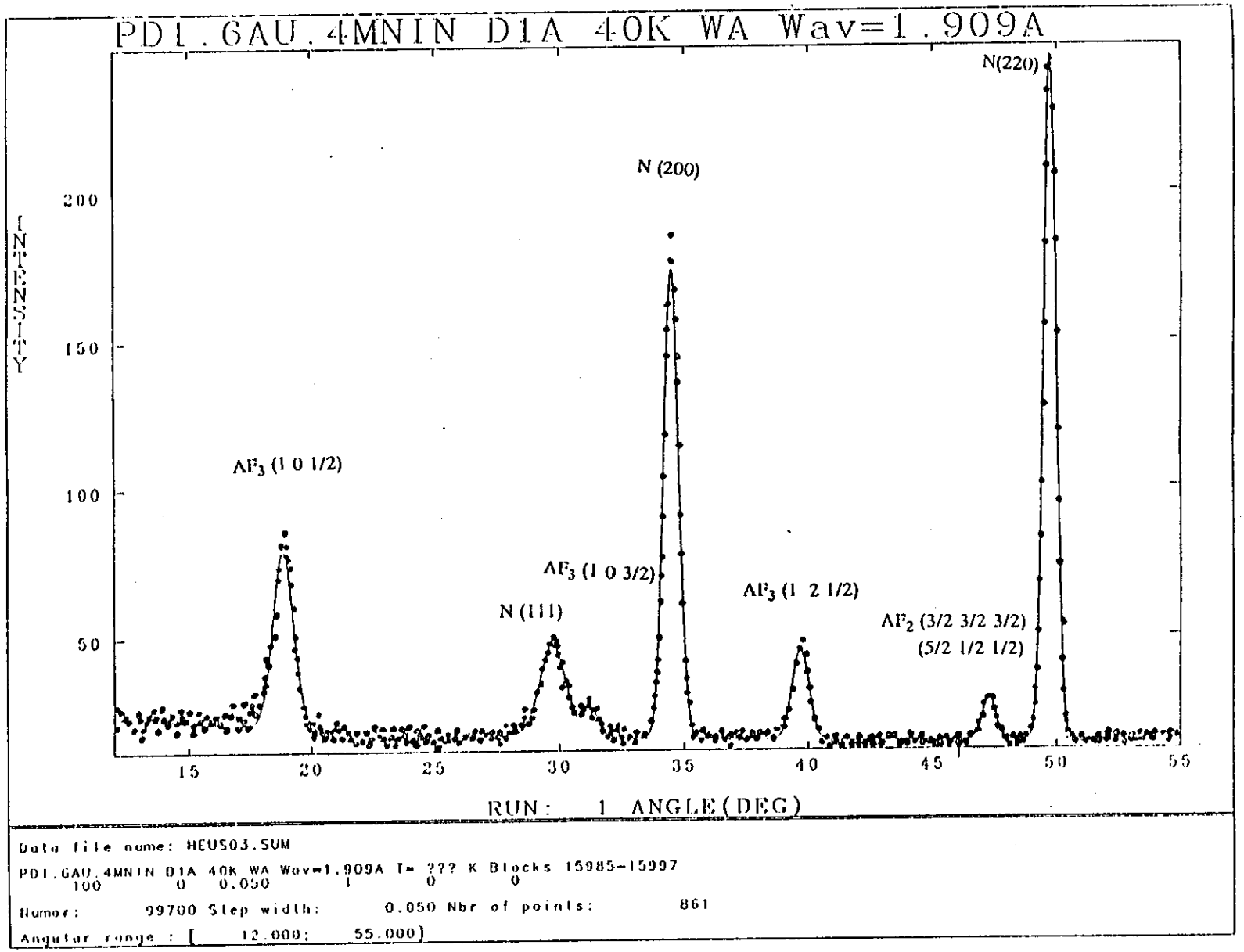

Figure (7.8) Neutron diffraction measurement at 40 K showing the reflections from the nuclear and antiferromagnetic peaks.

Table (7.6) The measured and calculated nuclear intensities for tetragonal structure

Position	h	k	l	I cal c	I obs
30·00	1	0	1	630	872 ∓ 21
34·78	1	1	0	1650	1608 ∓ 17
34·79	0	0	2	825	801 ∓ 8
50·00	2	0	0	1019	1003 ∓ 7
50·01	1	1	2	2037	2006 ∓ 14
59·42	2	1	1	382	507 ∓ 10
59·43	1	0	3	191	259 ∓ 5
62·35	2	0	2	1227	1215 ∓ 16
73·42	2	2	0	576	579 ∓ 10
73·44	0	0	4	288	291 ∓ 5
81.29	3	0	1	127	195 ∓ 5
81·30	2	1	3	253	396 ∓ 9
83·87	3	1	0	847	413 ∓ 7
83.88	2	2	2	847	907 ∓ 7
83·89	1	1	4	847	908 ∓ 7

$a = b = 4{\cdot}516 \mp 0{\cdot}0003$, $c = 6{\cdot}3855 \mp 0{\cdot}0008$

Temp effect Mn–In $= 0{\cdot}449 \mp 0{\cdot}022$

$R_n = 8{\cdot}06$

$R_{exp} = 7{\cdot}12$

$R_p = 16{\cdot}55$

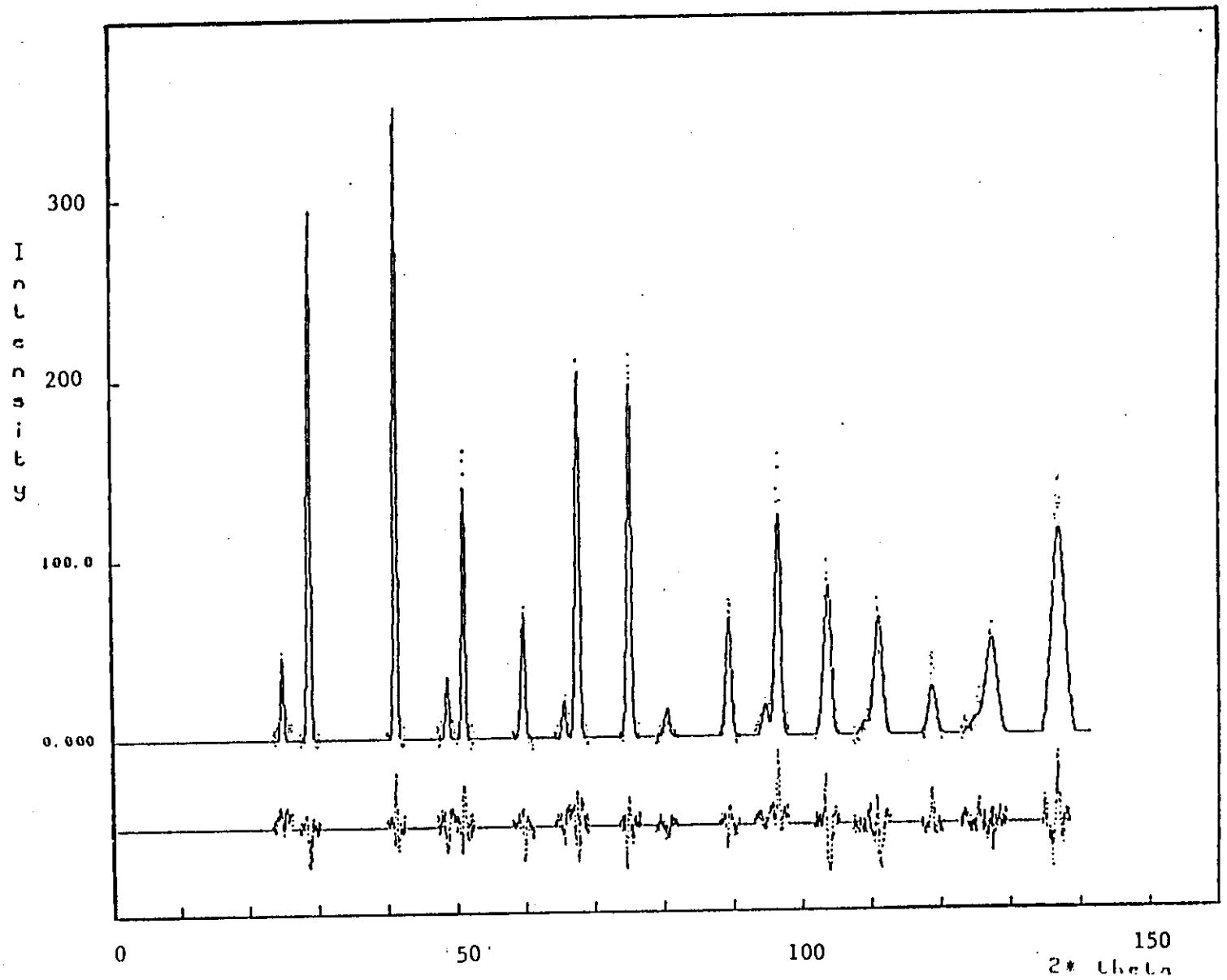

Figure (7.9) D_2B measurement (points) and results fit (line) with the difference (low line) below the spectrum of $Pd_{1.6}$ $Au_{0.4}$ Mn In at 40 K. The wavelength of the neutrons was determined to be λ = 1.549 A.

7.4 $Pd_{1\cdot4}\ Au_{0\cdot6}MnIn$

The susceptibility and reciprocal susceptibility versus temperature curves are shown in figure (7.1) and (7.2) respectively. The specific heat measurements versus temperature are shown in figure (7.10).

Figure (7.11) shows the nuclear and magnetic powder diffraction patterns obtained at 7K using the D2B diffractometer. As in $Pd_{1\cdot8}\ Au_{0\cdot2}MnIn$, $Pd_{1\cdot6}\ Aug_{0\cdot4}MnIn$, the additional antiferromagnetic peaks belong to the fcc type 3 antiferromagnetic structure and are well established, whereas AF_2 peaks have disappeared. The calculated and measured magnetic structures at 7K are compared in table (7.7).

Table (7.7)

h k l $a = 2a_o$	position	q^2F^2obs	$q^2_{\perp}F^2$calc	$q^2_{//}F^2$calc
(210)	15·95	2·861 $\mp$ 0·3	2·877	1·130
(421)	33·05	1·223 $\mp$ 0·3	1·201	0·817
(423), (205)	38·80	1·761 $\mp$ 0·3	1·861	1·417

However, from figure (7.11) it may be seen that additional peaks occur in the low temperature diffraction pattern. These peaks may be indexed as (001), (003) ... (310), (510) ..which are characteristic the fcc type $L2_1$ antiferromagnetism with a magnetic unit cell equal to that of the chemical ($L2_1$) unit cell. In this structure, the magnetic configuration consists of ferromagnetic sheets of atoms on (001) planes, adjacent planes being antiferromagnetically coupled. The configurational symmetry is the same as AF_3A which is a tetragonal and there are three different configurational domains each of which gives rise to a separate group of reflections. There are 3 equivalent [100] directions in the cubic lattice hence 3 different configuration domains. Their K–vectors are (100), (010) and (001). Therefore the conditions for magnetic reflections are [128]:

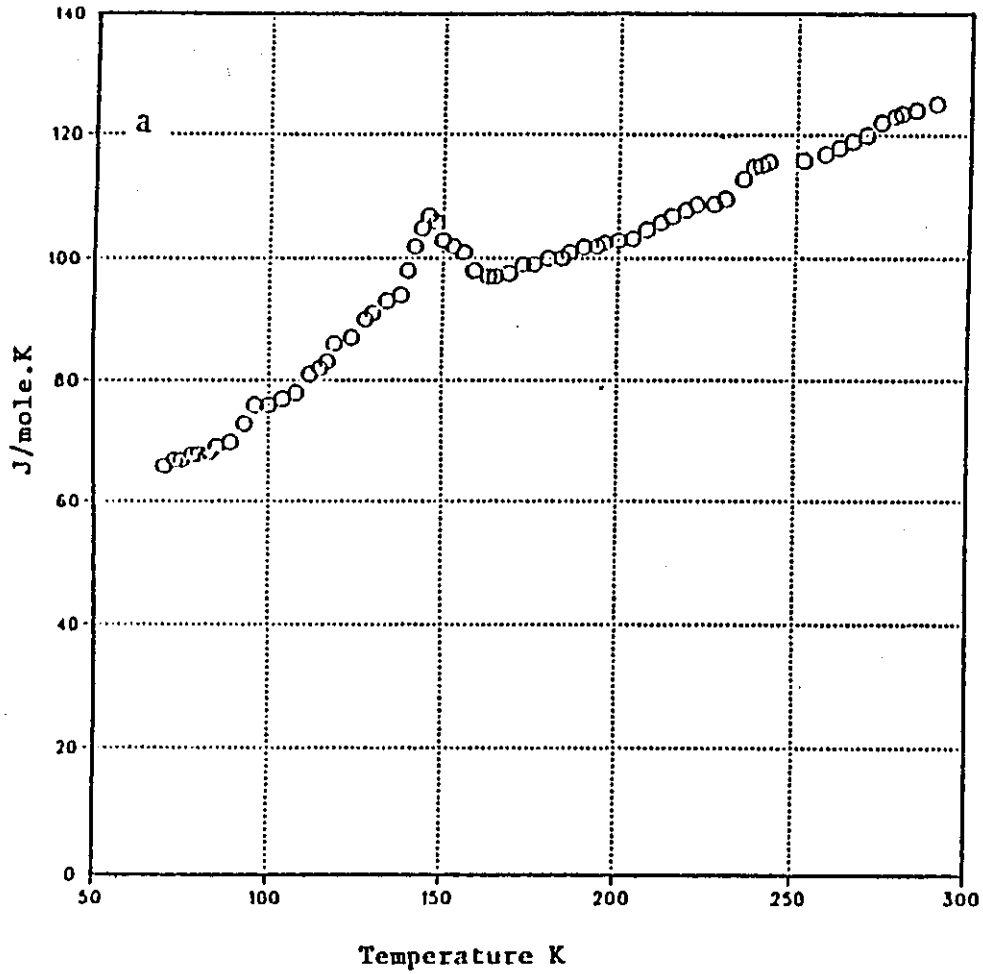

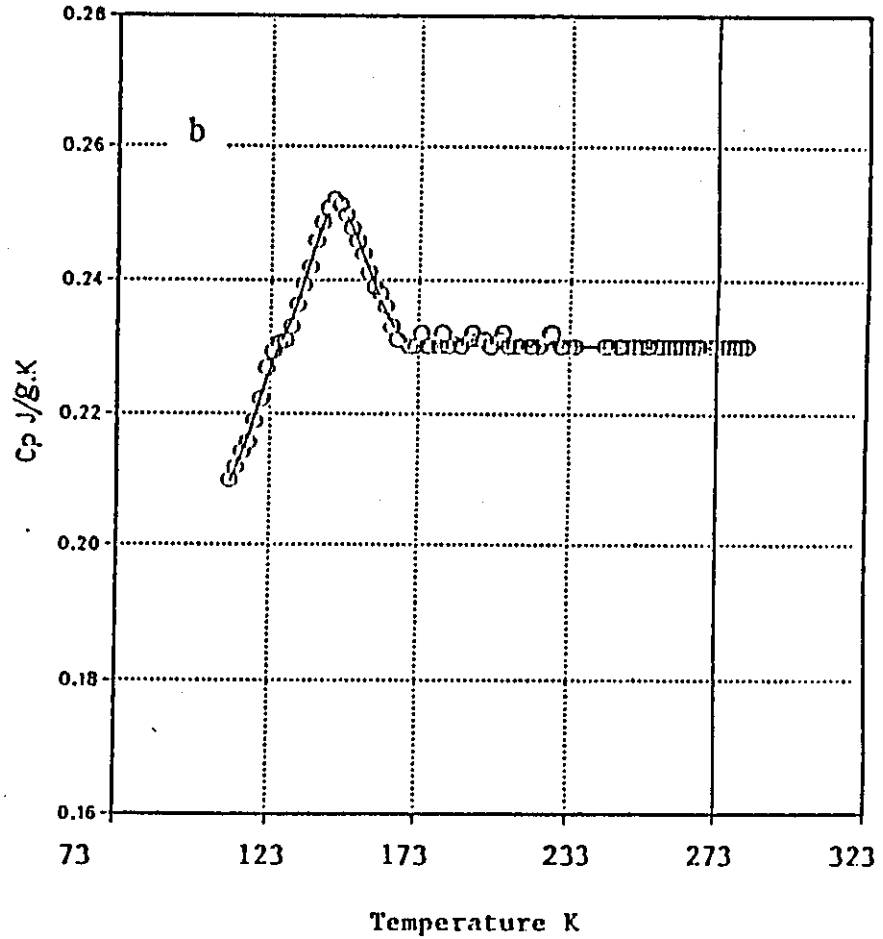

Figure (7.10) Specific heat measurements of $Pd_{1.4}$ $Au_{0.6}$ Mn In

a - pulse heating
b - continuous heating

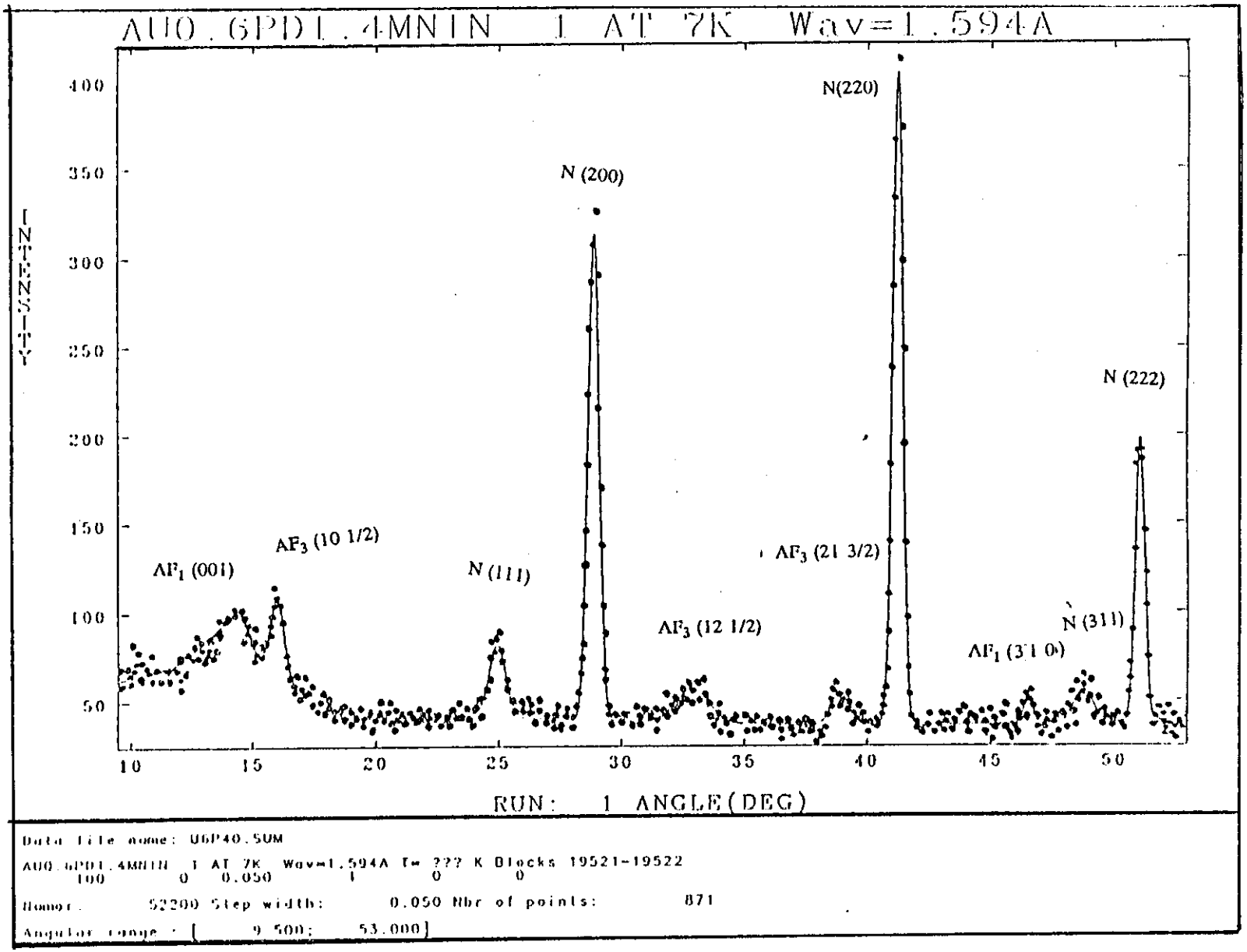

Figure (7.11) Neutron diffraction measurements at 7K showing the reflections from the nuclear and antiferromagnetic peaks.

(100)	domain	k and l even	h odd
		k and l odd	h even
(010)	domain	h and l even	k odd
		h and l odd	k even
(001)	domain	h and k even	l odd
		h and k odd	l even

The results are identical with the conditions h, k are even and l odd or h and k are odd and l even from (001) domain. The calculated and measured magnetic structures are compared in table (7.8).

Table (7.8)

h k l	position	$q^2F^2_{obs}$	$q^2_{\perp}F^2_{calc}$	$q^2_{//}F^2_{calc}$
(001)	14·50	2·217 $\mp$ 0·2	2·327	1·171
(310)	46·50	1·297 $\mp$ 0·2	1·573	0·971

The results indicate that the moment per Mn site are 2·811 μ_B and 1·481 at 7K for AF_3A and AF_1 respectively, with a small moment on the Pd sites approximated to be 0·07 $\mp$ 0·01 μ_B at 7K. The measured and calculated nuclear intensities at 7K are compared in table (7.9) and the calculated profiles are shown in figure (7.12). The powder refinement was carried out using a tetragonal space group with the atoms located at positions as explained in the last chapter. It is noted that, the peaks at high angle reflection at 7K sho w a little peak splitting due to a result of tetragonal distortion which disappears above the Neel temperature. Figure (7.12) also shows that the intensity of the odd superlattice peaks (111), (311), etc is very small, indicating the disorder between Mn–In does exist. The effect of the various types of disorder or the nuclear superlattice peak intensities of $Pd_{1\cdot4}Au_{0\cdot6}MnIn$ are shown in figures (7.13) and (7.14). It can be seen from figures (7.13) and (7.14), in general one of above types of disorder predominate in alloys at the Heusler composition. The type of order that predominates, if any, is usually clear from graphs of F^2 versus α. In

particular, disorder of type α(Mn–In) which often occurs in alloys containing In, Al, Ga is easily recognised as it only effects the odd superlattice peaks. The preferential B2 disorder in α(Mn–In) was determined as 0·139.

In the least square refinement, it was assumed that palladium remained highly ordered on the B and D sites, and an occupation of 0·8557 $\mp$ 0·0087 Mn and 0·8107 $\mp$ 0·000735 In lattice sites were detected. The following effective scattering amplitudes were obtained for A and C atomic sites:

$$b_A = -0{\cdot}336 \mp 0{\cdot}01 \times 10^{-12}\text{cm}$$
$$b_C = 0{\cdot}420 \mp 0{\cdot}02 \times 10^{-12}\text{cm}$$

These values can be compared with the well established values [129]:

$$b_{Mn} = -0{\cdot}373 \times 10^{-12}\text{cm}$$
$$b_{In} = 0{\cdot}406 \times 10^{-12}\text{cm}$$

Table (7.9) The measured and calculated nuclear intensities for tetragonal structure

Position	h	k	l	I cal c	I obs
24·81	1	0	1	317	447 $\pm$ 47
28·67	0	0	2	1041	1010 $\pm$ 25
28·75	1	1	0	2066	1938 $\pm$ 40
41·05	1	1	2	2355	2412 $\pm$ 40
41·11	2	0	0	1172	1168 $\pm$ 23
48·52	1	0	3	93	145 $\pm$ 21
48·61	2	1	1	185	259 $\pm$ 29
50·89	2	0	2	1422	1352 $\pm$ 49
59·38	0	0	4	307	376 $\pm$ 25
59·54	2	2	0	608	679 $\pm$ 32
65·43	2	1	3	116	195 $\pm$ 27
65.51	3	0	1	58	138 $\pm$ 14
67·29	1	1	4	892	989 $\pm$ 23
67·41	2	2	2	888	958 $\pm$ 27
67.44	3	1	0	887	955 $\pm$ 22

$a = b = 4{\cdot}5395 \pm 0{\cdot}0006$, $c = 6{\cdot}436 \pm 0{\cdot}00015$

Temp effect Mn–In $= 0{\cdot}463 \pm 0{\cdot}022$

$R_n = 6{\cdot}931$

$R_{exp} = 7{\cdot}162$

$R_p = 17{\cdot}94$

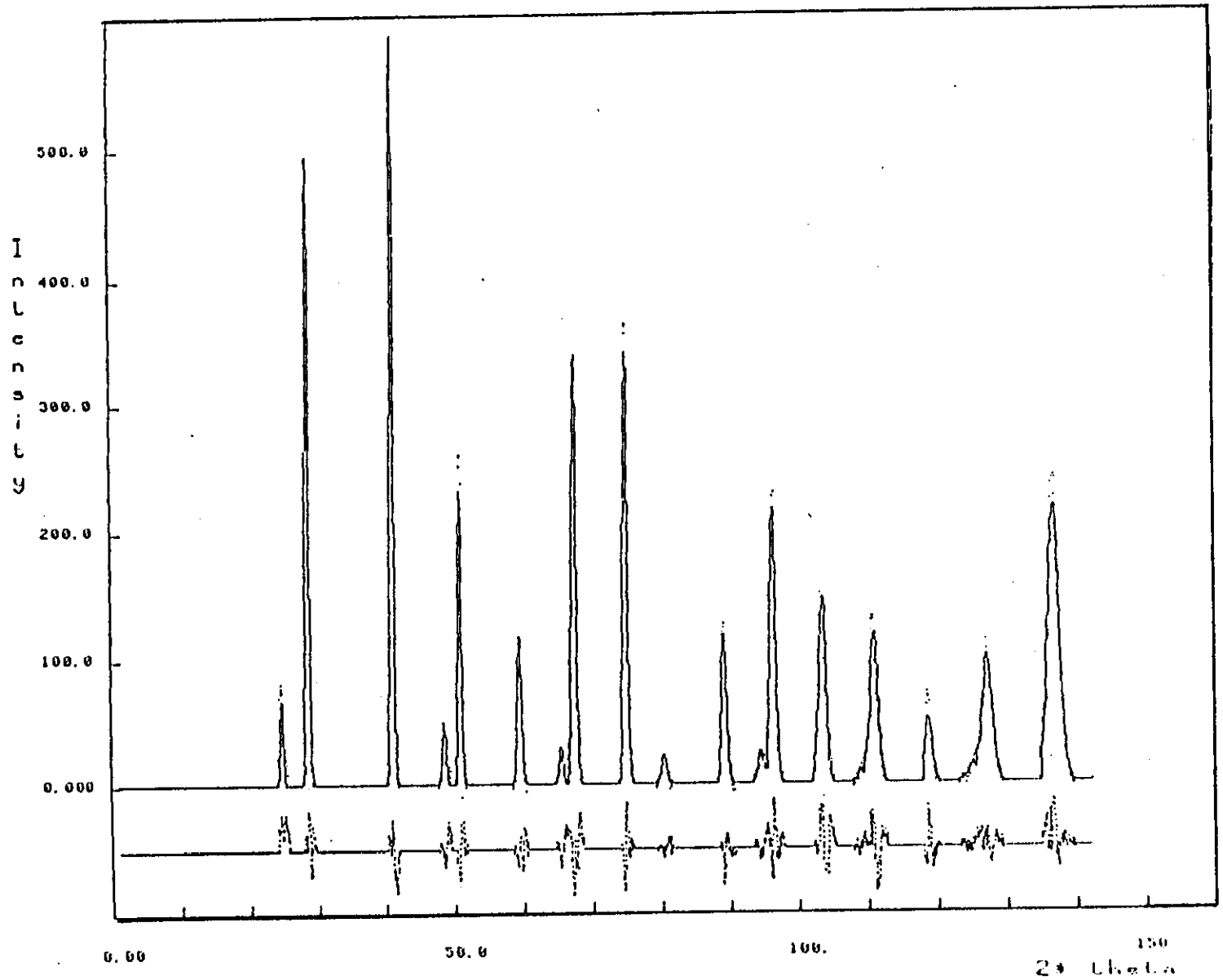

Figure (7.12) D_2B measurements (points) and results fit (line) with the difference (low line) below the spectrum of $Pd_{1.4}$ $Au_{0.6}$ Mn In at 40 K. The wavelength of the neutrons was determined to be λ = 1.549 A.

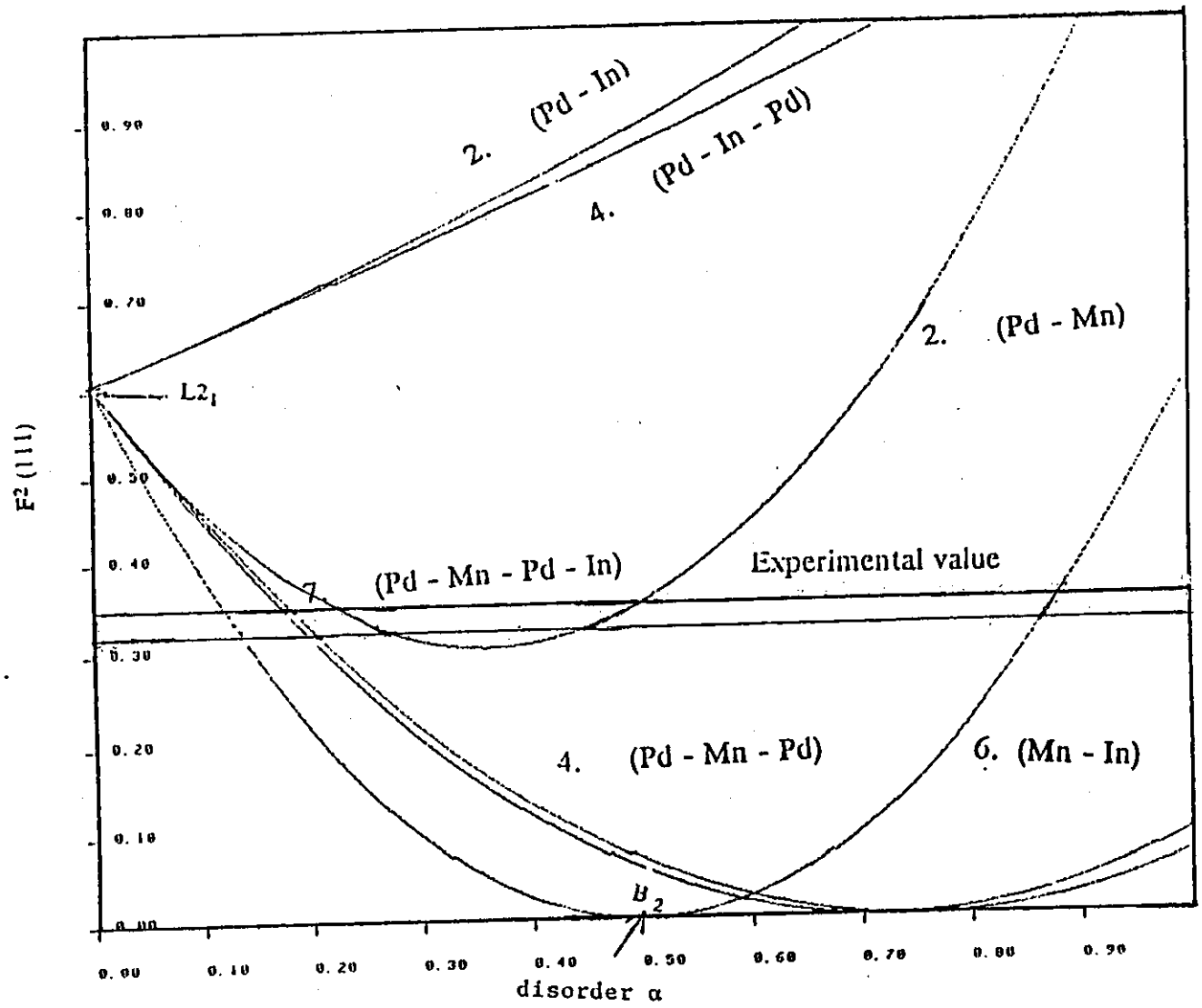

Figure (7.13) Neutron diffraction structure factor F^2 (111) versus degree of disorder α for $Pd_{1.4}$ $Au_{0.6}$ Mn In

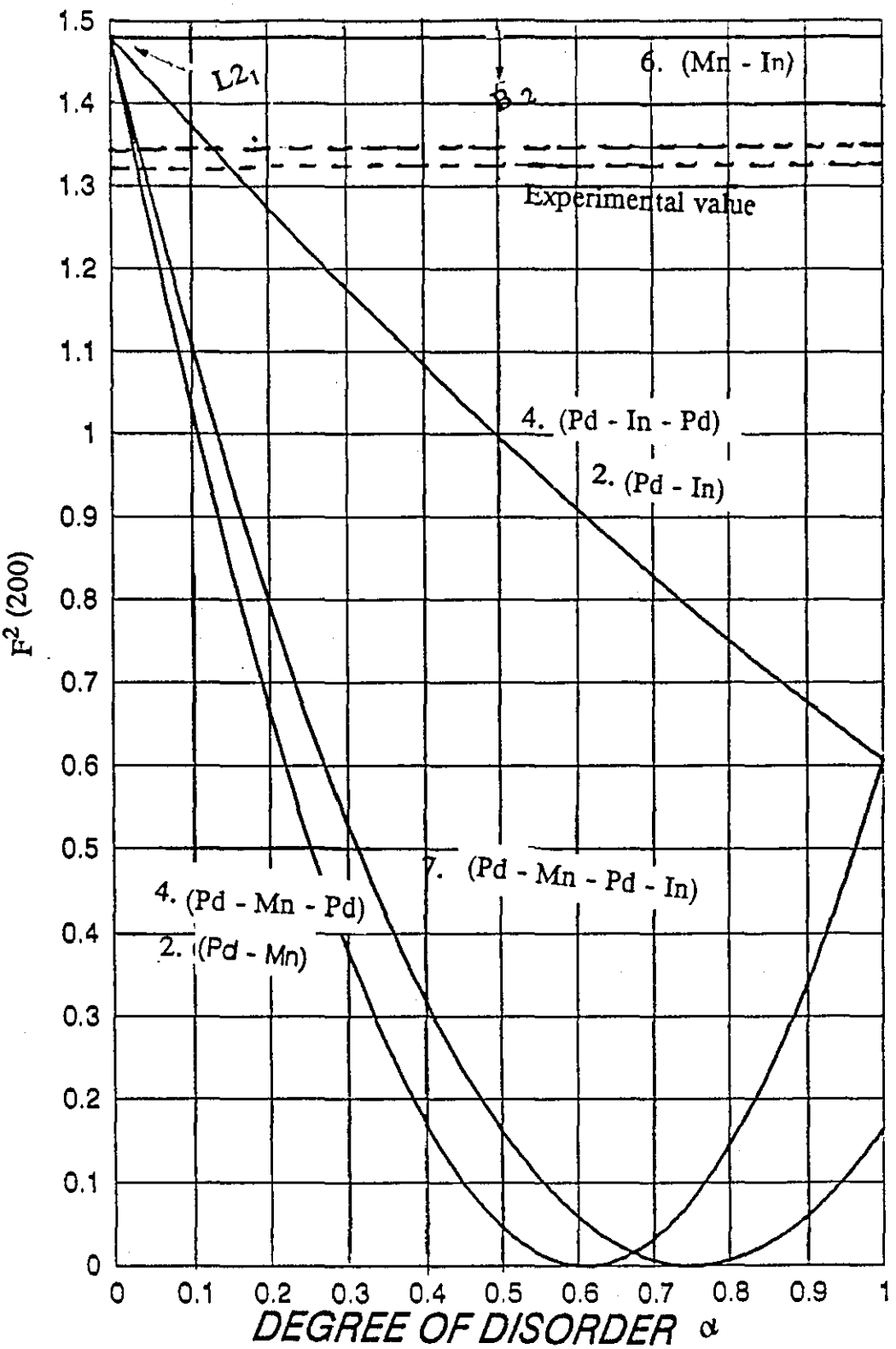

Figure 7.14 Neutron diffraction structure F^2 (200) versus degree of disorder α for $Pd_{1.4}\ Au_{0.6}\ Mn\ In$

7.5 $Pd_{1\cdot2}\ Au_{0\cdot8}MnIn$

The susceptibility and reciprocal susceptibility versus temperature curves are shown in figures (7.1) and (7.2) respectively. The specific heat versus temperature obtained by using continuous heating and pulse techniques are shown in figure (7.15).

The neutron diffraction patterns were obtained at several temperatures using the diffractometers D1A or D2B. Figure (7.16) shows the nuclear powder diffraction patterns obtained at 40K using D2B.

Peak splitting is observed for the high angle reflections due to tetragonal distortion induced by the AF_3A structure. The splitting decreases with increasing temperature and disappears above the Neel temperature as shown in figure (7.17). The refinement of the tetragonal structure was carried out as explained in the last chapter. The measured nuclear intensities obtained at 7K and those calculated using a Rietveld refinement program are compared in table (7.10). It is noted from the neutron diffraction measurements, as shown in figure (7.18), that the fcc type 3A antiferromagnetism co–exists with fcc type 1 antiferromagnetism.

The broad peak at the position $\simeq 14{\cdot}46$ consists of a contribution from (001) AF_1 and (201) AF_3A peaks as shown in figure (7.18). The calculated and measured magnetic structures for both types of antiferromagnetic AF_3A, AF_1 are compared in tables (7.11) and (7.12) respectively.

It can be seen also from figure (7.18) that the intensity of the odd nuclear reflections is very small indicating the existence of disorder between Mn–In ($\alpha = 0{\cdot}211$)

The magnetic moments per Mn site at 7K are $3{\cdot}1 \mp 0{\cdot}02\ \mu_B$ and $1{\cdot}007\ \mu_B$ for AF_3A and AF_1 respectively. The moment on the Pd atom was estimated to be $0{\cdot}04 \mp 0{\cdot}01\mu_B$.

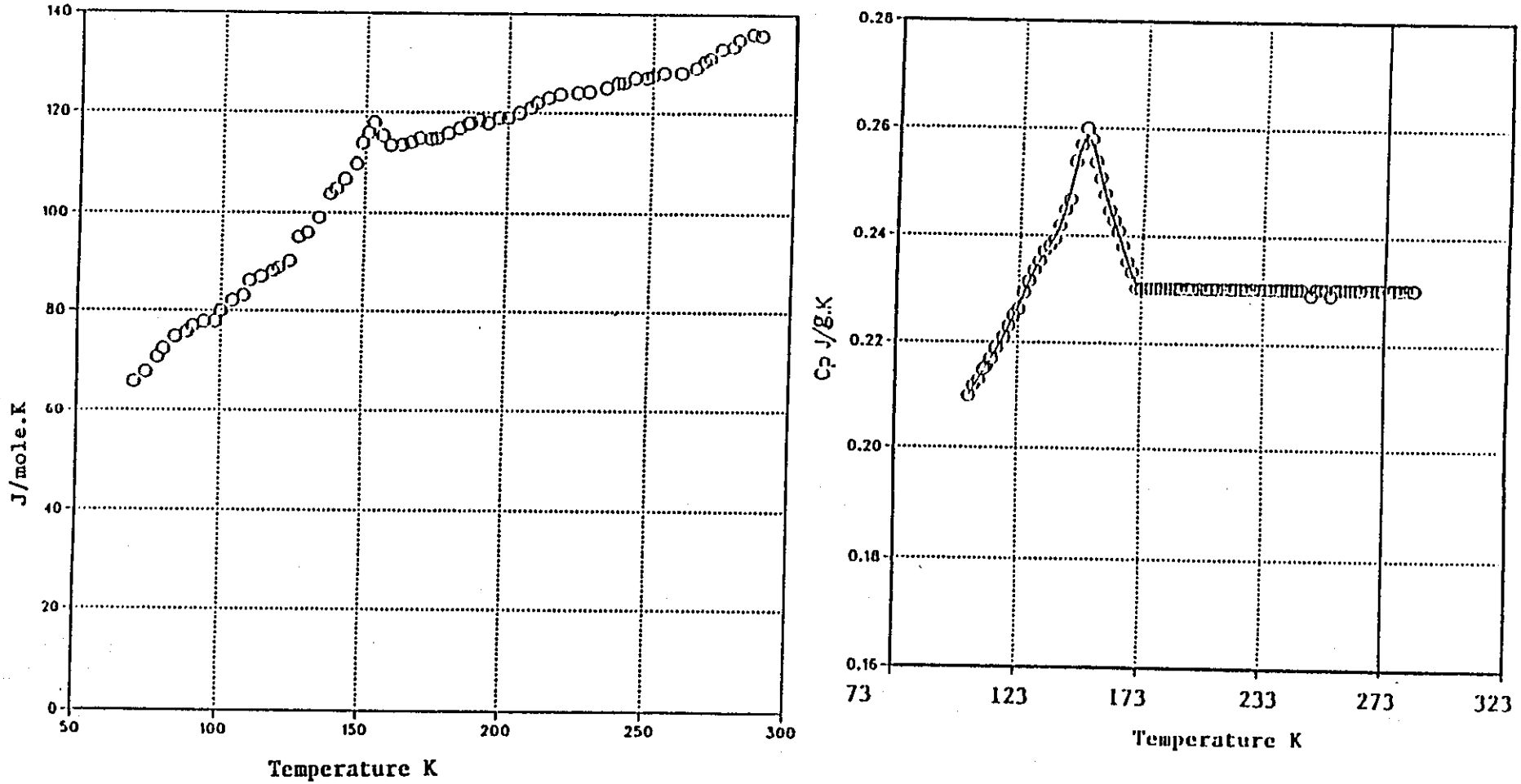

Figure (7.15) Specific heat measurements of $Pd_{1.2}$ $Au_{0.8}$ Mn In

a - pulse heating
b - continuous heating

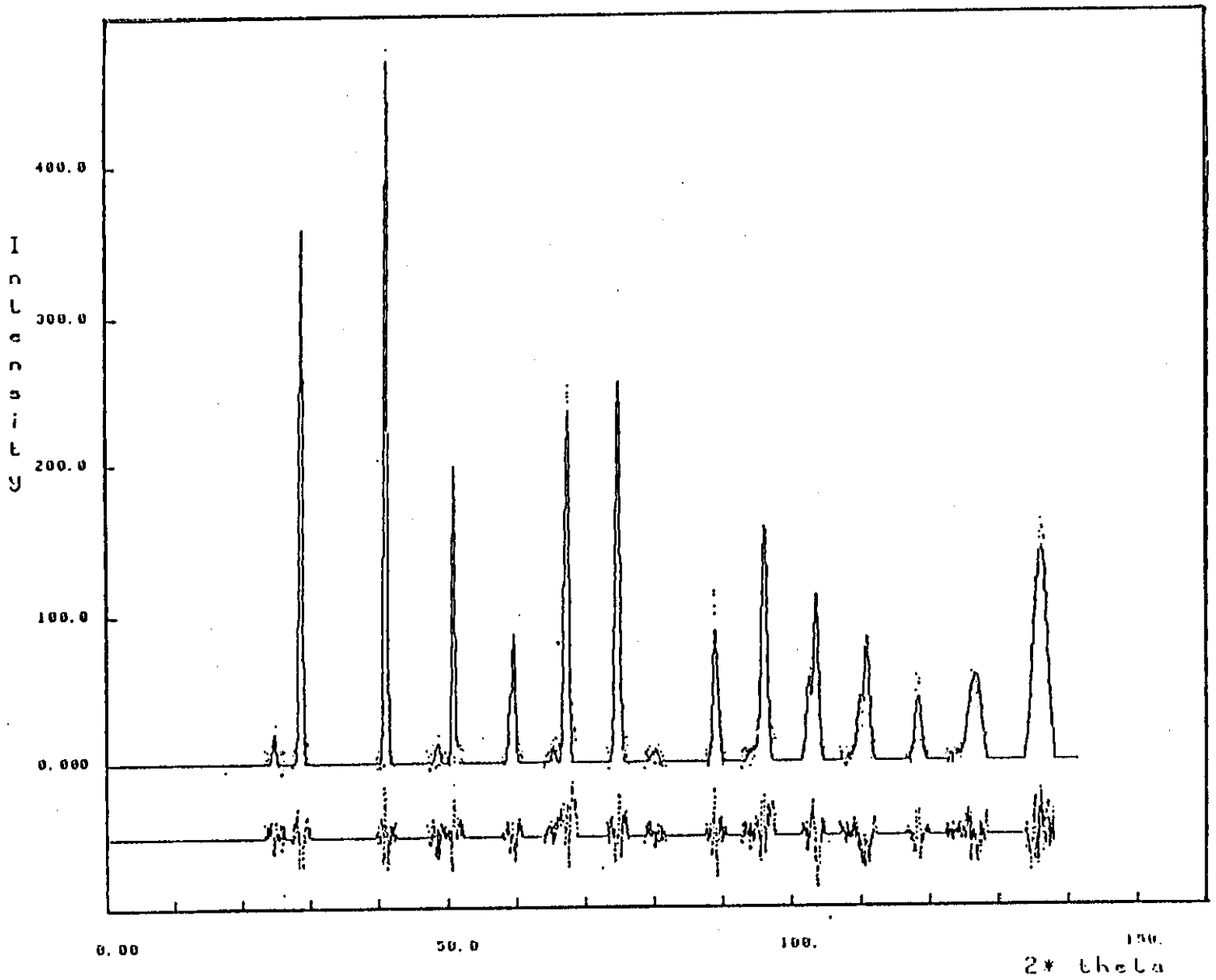

Figure (7.16) D_2B measurements (points) and results fit (line) with the difference (lower line) below the spectrum of $Pd_{1.2}$ $Au_{0.8}$ Mn In at 40 K. The wavelength of the neutrons was determined to be λ = 1.594A

Table (7.10) The measured and calculated nuclear intensities for tetragonal structure

Position	h	k	l	I cal c	I obs
24·78	1	0	1	193	289 ∓ 43
28·52	0	0	2	1403	1429 ∓ 38
28·78	1	1	0	2793	2671 ∓ 43
40·96	1	1	2	3369	3473 ∓ 46
41·15	2	0	0	1681	1719 ∓ 32
48·30	1	0	3	56	55 ∓ 28
48·63	2	1	1	112	128 ∓ 29
50·83	2	0	2	1966	2275 ∓ 53
59·03	0	0	4	448	468 ∓ 32
59·60	2	2	0	892	921 ∓ 37
65·54	2	1	3	71	162 ∓ 29
65.98	3	0	1	35	118 ∓ 17
66·98	1	1	4	1261	1464 ∓ 32
67·37	2	2	2	1257	1343 ∓ 19
67.50	3	1	0	1256	1655 ∓ 32

a = b = 4·536 ∓ 0·0003, c = 6·4714 ∓ 0·0006

Temp effect Mn–In = 0·471 ∓ 0·271

R_n = 7·98

R_{exp} = 6·917

R_p = 15·41

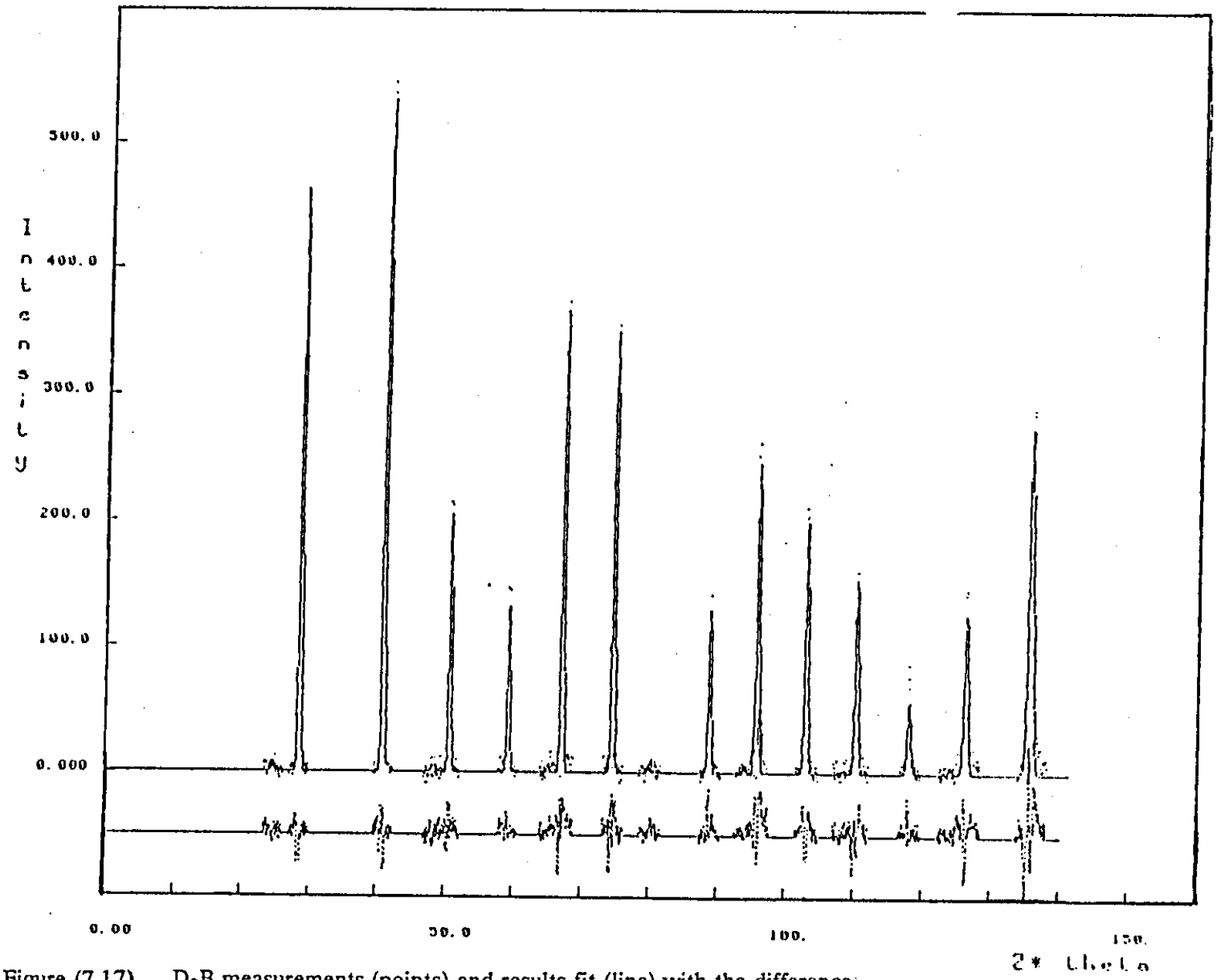

Figure (7.17) D_2B measurements (points) and results fit (line) with the difference (low line) below the spectrum of $Pd_{1.2}$ $Au_{0.8}$ Mn In at 17^0 K. The wavelength of the neutrons was determined to be λ = 1.594A.

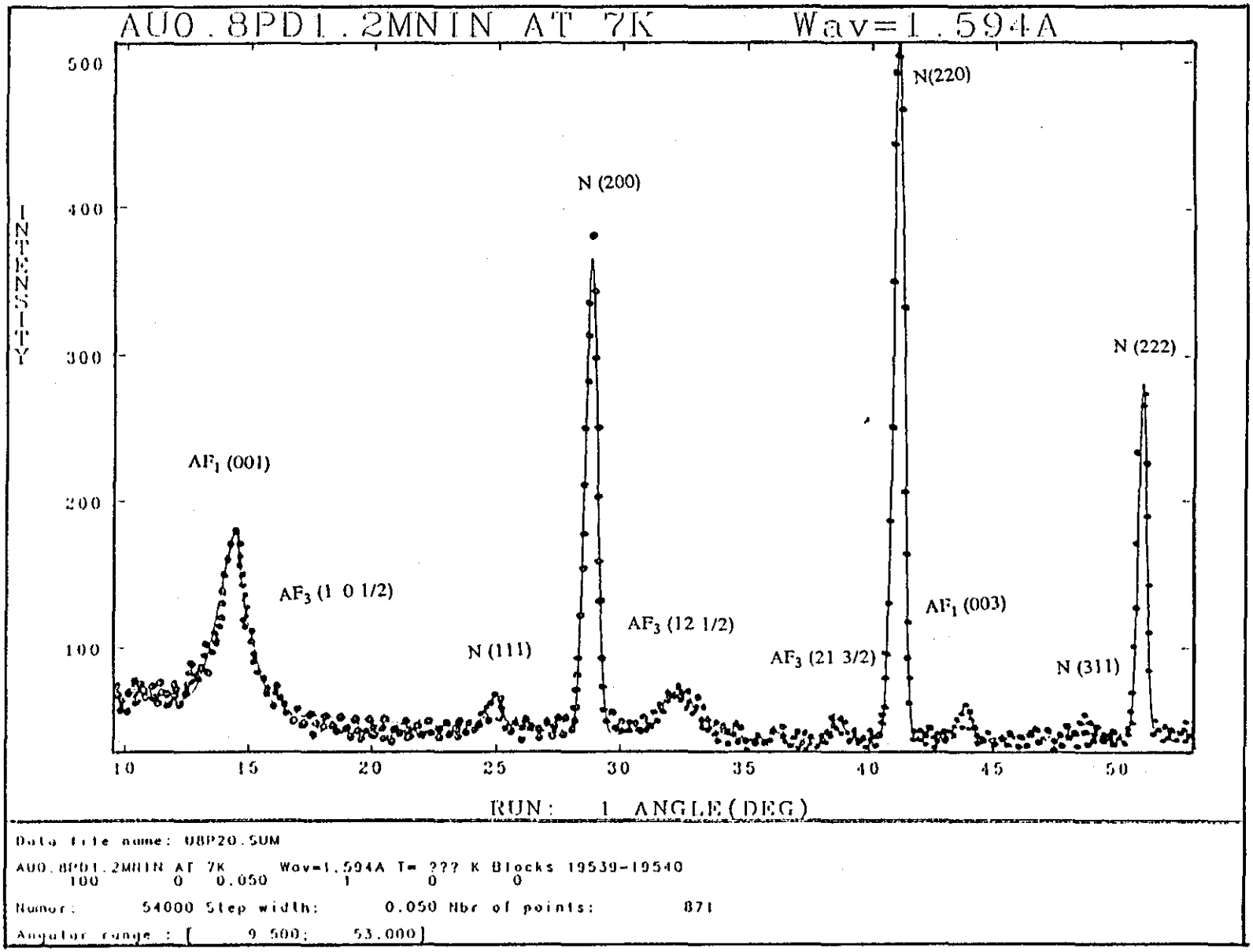

Figure (7.18) Neutron diffraction measurements at 7K showing the reflections from the nuclear and antiferromagnetic peaks.

Table (7.11)

h k l $a = 2a_o$	position	q^2F^2obs	$q^2_{\perp}F^2$cal	$q^2_{//}F^2$cal
(201)	14·96	3·375 $\mp$ 0·3	3·575	1·175
(421)	32·35	1·763 $\mp$ 0·3	1·558	0·963
(423), (205)	38·85	2·301 $\mp$ 0·3	2·317	0·915

Table (7.12)

h k l	position	q^2F^2obs	$q^2_{\perp}F^2$calc	$q^2_{//}F^2$calc
(001)	14·40	1·932 $\mp$ 0·2	1·531	0·732
(003)	43·80	0·841 $\mp$ 0·2	0·705	0·441

7.6 PdAuMnIn

The susceptibility and reciprocal susceptibility versus temperature curves are shown in figures (7.1) and (7.2) respectively. The specific heat versus temperature obtained by using continuous heating and pulse techniques are shown in figure (7.19).

Neutron scattering measurements were carried out at several temperatures using D2B and D1A. Figures (7.20) shows the powder diffraction patterns obtained at 7K indicating that both antiferromagnetic AF_1 and AF_3A structures are still present. The calculated and measured magnetic structure factors for both AF_3A and AF_1 are compared in tables (7.13) and (7.14) respectively. The magnetic moments are 3·3 $\mp$ 0·02 and 1·023 μ_B $\mp$ 0·02 per Mn site at 7K for the AF_3 and AF_1 phase respectively.

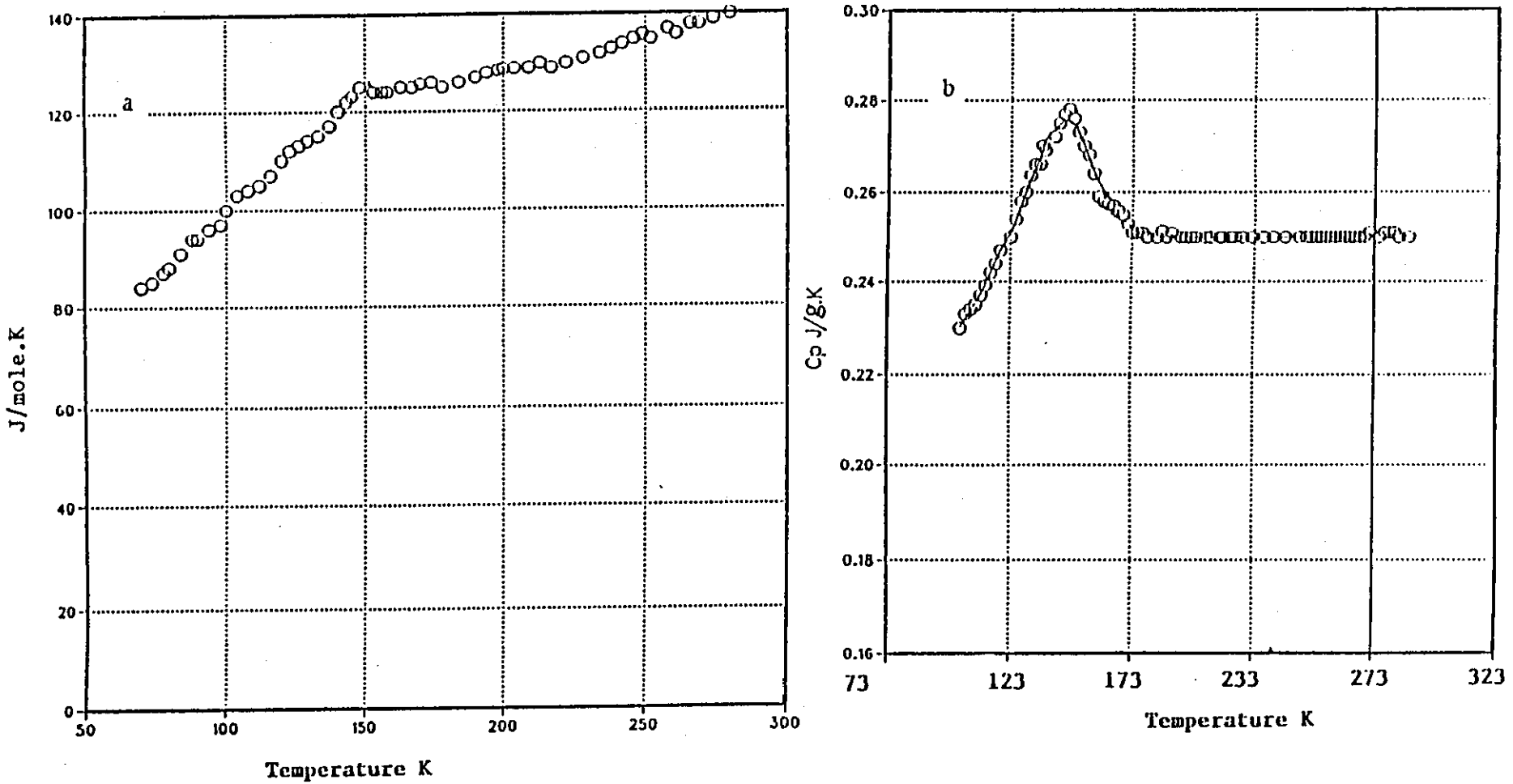

Figure (7.19) Specific heat measurements of Pd Au Mn In

a - pulse heating
b - continuous heating

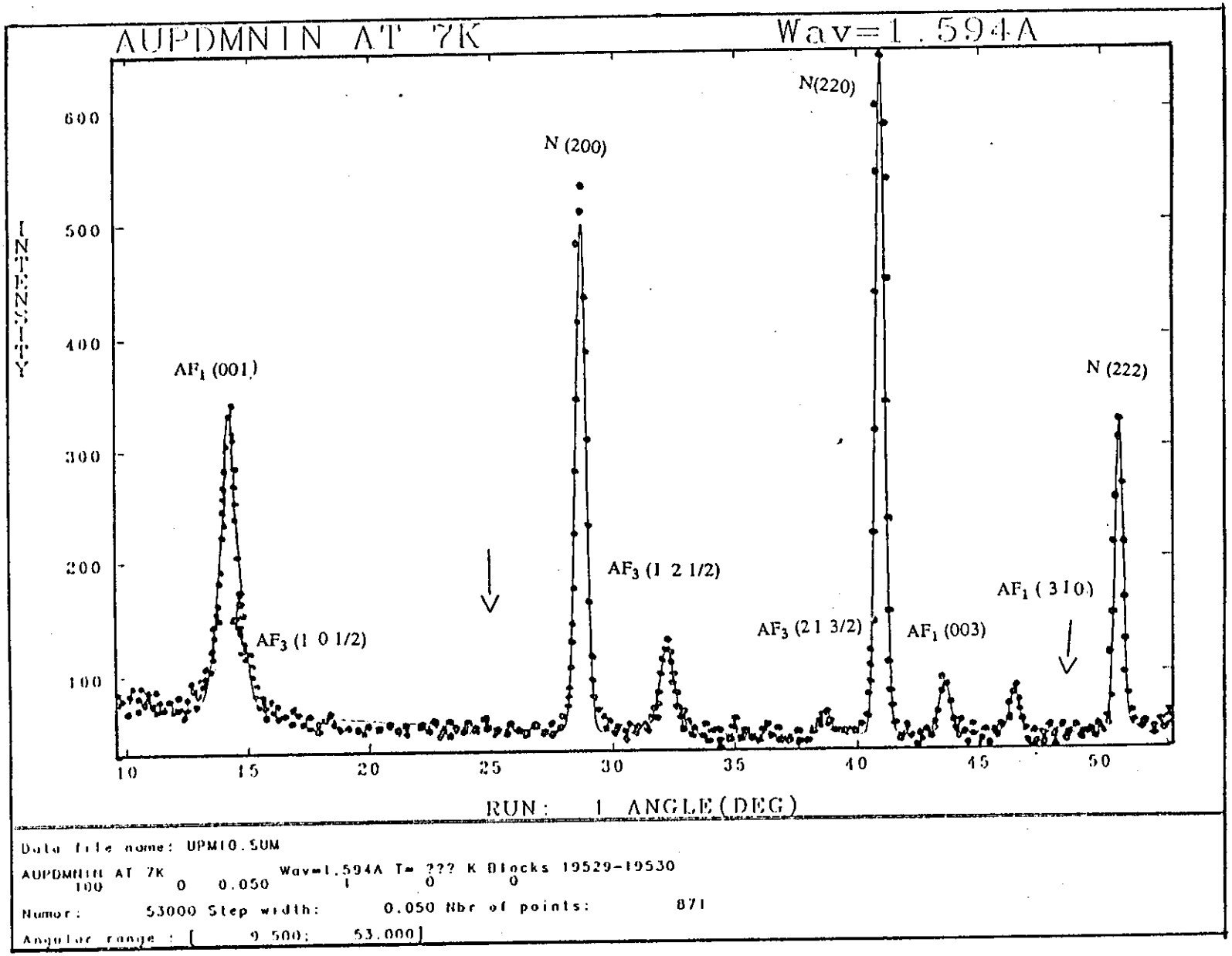

Figure (7.20) Neutron diffraction measurements at 7K showing the reflections from the nuclear and antiferromagnetic peaks.

It is noted also, that odd nuclear peaks (111), (311) are absent, indicating that the alloy is completely disorder into the B2 structure.

Table (7.13)

h k l a = 2a	position	q^2F^2obs	$q^2_{\perp}F^2$calc	$q^2_{//}F^2$calc
(201)	15·21	2·953 $\mp$ 0·2	3·654	2·765
(421)	32·15	2·430 $\mp$ 0·2	2·637	1·665
(423), (205)	38·70	2·965 $\mp$ 0·2	3·213	1·379

Table (7.14)

h k l	position	q^2F^2obs	$q^2_{\perp}F^2$calc	$q^2_{//}F^2$calc
(001)	14·250	1·543 $\mp$ 0·1	1·651	0·610
(003)	43·60	0·962 $\mp$ 0·1	0·931	0·513
(310)	46·45	0·651 0·1	0·710	0·295

7.7 $Pd_{0·8}Au_{1·2}MnIn$

The susceptibility and reciprocal susceptibility versus temperature curves are shown in figures (7.1) and (7.2) respectively

Neutron powder diffraction patterns were obtained at several temperatures using D2B and D1A at the ILL. Figure (7.21) shows the nuclear powder diffraction patterns obtained at 7K using the diffractometer D2B. It may be noted that the peaks are split at high angles due to the result of tetragonal distortion induced by the AF_3 structure. The splitting decreases with increasing temperature and disappears above the Neel temperature. The measured and calculated nuclear intensities for tetragonal structure at 7K are compared in table (7.15).

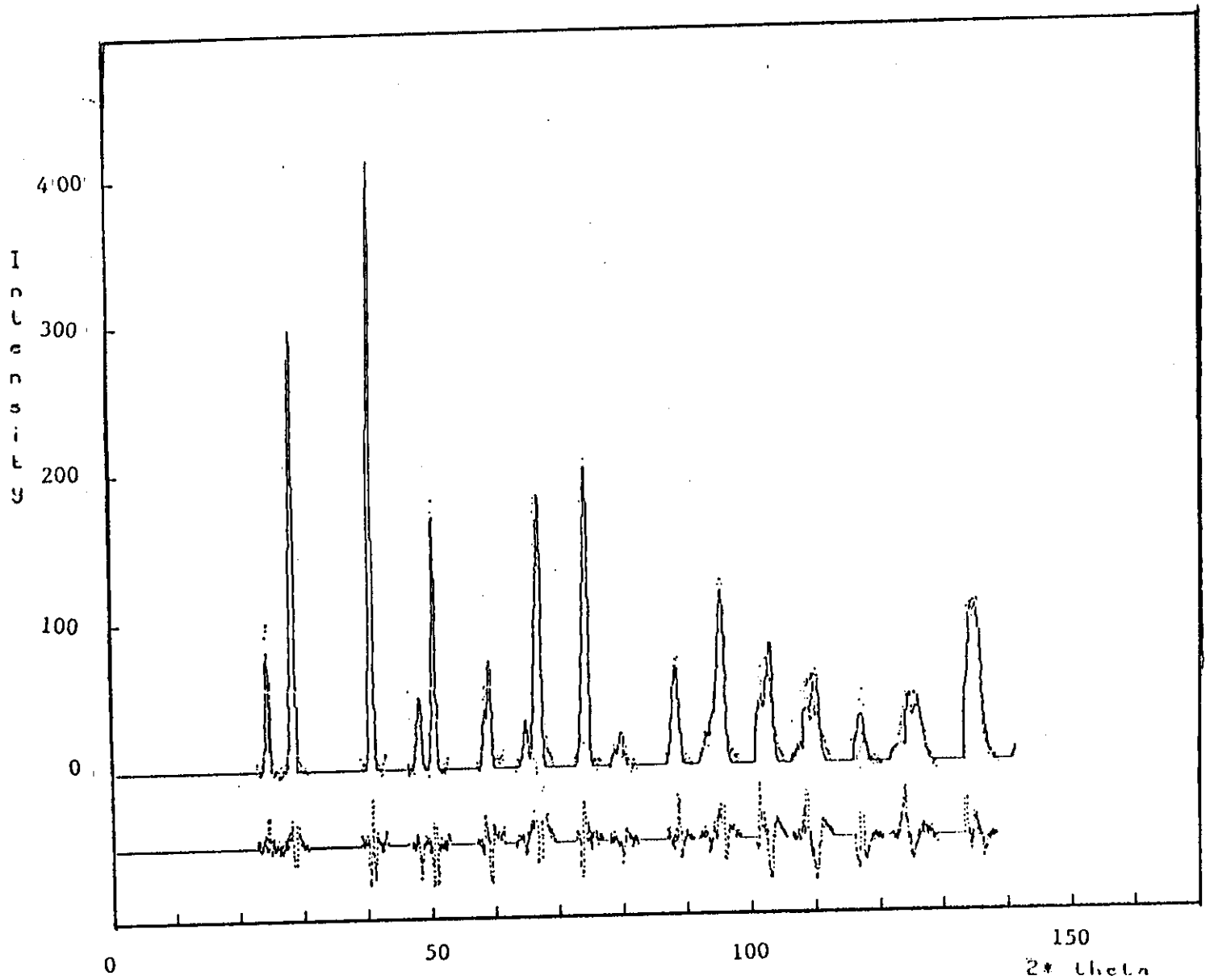

Figure (7.21) D_2B measurements (point) and results fit (line) with the difference (low line) below the spectrum of $Pd_{0.8}$ $Au_{1.2}$ Mn In at 7K. The wavelength of the neutrons was determined to be λ = 1.594 A.

Figure (7.22) shows that the antiferromagnetic AF_3 and AF_1 phase co–exist at low temperatures. It can be seen also from figure (7.22)) that the intensity of the nuclear odd reflection are larger than in the other alloys indicating that the ordering in the $L2_1$ structure increases with the composition of gold. The preferential B2 disorder was also determined as before and the value found to be 0·09.

The measured and calculated magnetic structures for both types of anti–ferromagnetic structures AF_3A, AF_1 are compared in tables (7.16) and (7.17) respectively. The results indicate that the moments per Mn site are $2{\cdot}93 \mp 0{\cdot}2\mu_B$ and $0{\cdot}981 \mp 0{\cdot}1\mu_B$ at 7k for AF_3 and AF_1 respectively, with a small moment on the Pd sites of approximately $0{\cdot}05 \mp 0{\cdot}01\mu_B$

Table (7.15) The measured and calculated nuclear intensities for tetragonal structure

Position	h	k	l	I cal c	I obs
24·71	1	0	1	74	46 ∓ 43
28·57	0	0	2	1660	1669 ∓ 27
28·62	1	1	0	3310	3344 ∓ 45
40·89	1	1	2	3546	3896 ∓ 47
40·92	2	0	0	1920	1898 ∓ 25
48·32	1	0	3	22	38 ∓ 19
48·39	2	1	1	43	71 ∓ 28
50·67	2	0	2	2272	2769 ∓ 57
59·14	0	0	4	499	559 ∓ 26
59·26	2	2	0	995	1000 ∓ 35
65·14	2	1	3	27	105 ∓ 78
65·19	3	0	1	13	77 ∓ 14
67·00	1	1	4	1420	1685 ∓ 26
67·09	2	2	2	1418	1761 ∓ 21
67·11	3	1	0	1417	1924 ∓ 26

$a = b = 4{\cdot}5679 \mp 0{\cdot}0006$, $c = 6{\cdot}4675 \mp 0{\cdot}0017$

Temp effect Mn–In $= 0{\cdot}4471 \mp 0{\cdot}0311$

$R_n = 7{\cdot}961$

$R_{exp} = 5{\cdot}312$

$R_p = 16{\cdot}951$

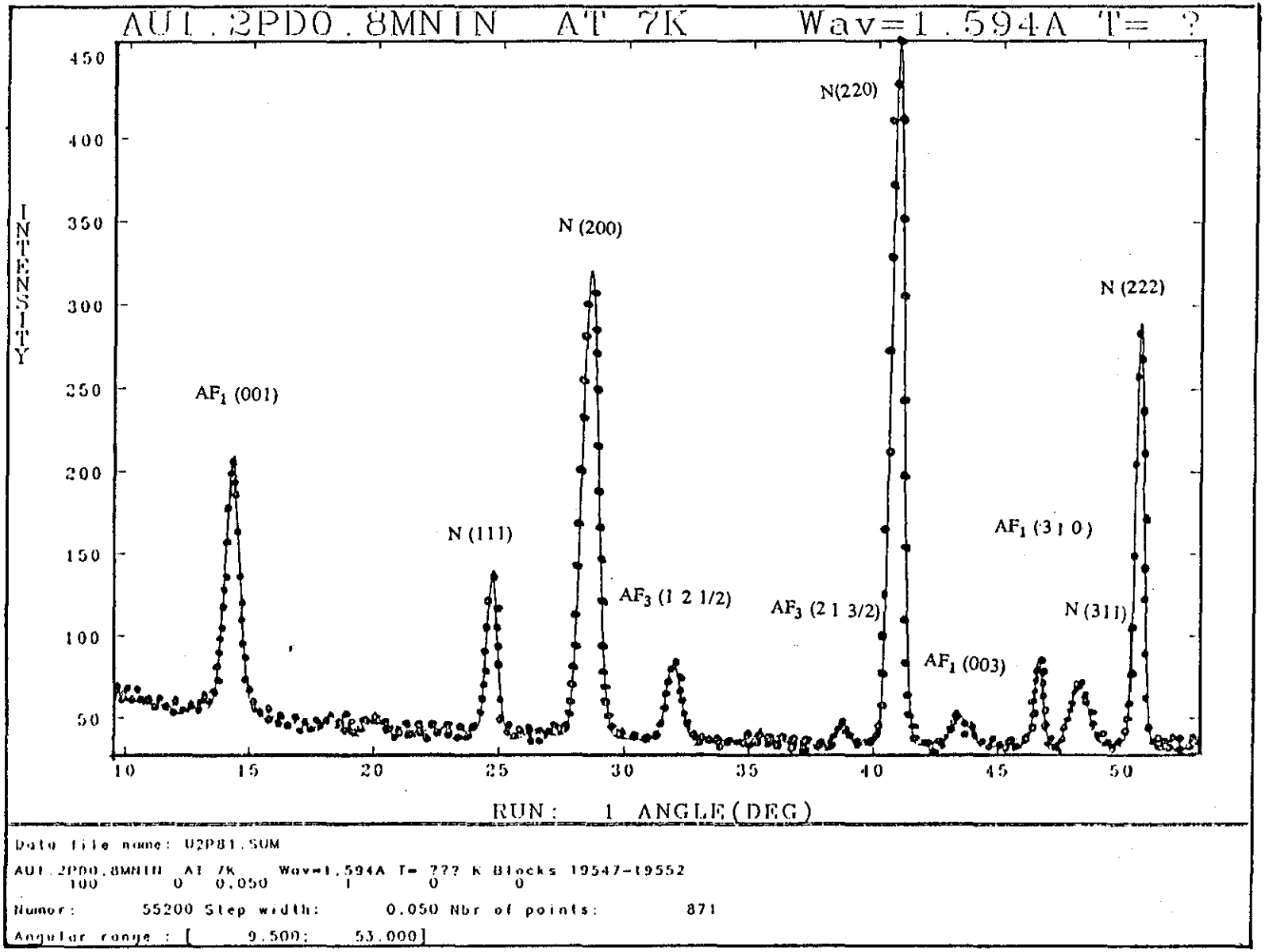

Figure (7.22) Neutron diffraction measurements at 7K showing the reflections from the nuclear and antiferromagnetic peaks.

Table (7.16)

h k l $a = 2a_o$	position	q^2F^2obs	$q^2_\perp F^2$calc	$q^2_{//} F^2$calc
(421)	32·70	2·771 $\mp$ 0·2	2·907	1·217
(423), (205)	39·63	1·930 $\mp$ 0·2	1·917	1·021

Table (7.17)

h k l	position	q^2F^2obs	$q^2_\perp F^2$calc	$q^2_{//} F^2$calc
(001)	14·40	1·631 $\mp$ 0·2	1·791	0·953
(003)	43·80	0·892 $\mp$ 0·2	0·791	0·631
(310)	46·80	0·765 $\mp$ 0·2	0·862	0·451

7.8 $Pd_{2-x}Au_xMnIn$ $(1{\cdot}4 \leq x \leq 2)$

The susceptibility and reciprocal susceptibility versus temperature curves are shown in figures (7.23) and (7.24) respectively. It is noted that when the amount of Pd is decreased to below 0·6, ferromagnetism is established.

The neutron diffraction pattern was obtained at several temperatures using D2B at the ILL. The neutron diffraction pattern obtained at 7K for $Pd_{0.6}Au_{1.4}MnIn$, is shown in figure (7.25). It is noted that both antiferro–magnetic structures AF_3A and AF_1 co–exist with the ferromagnetic phase. Above the magnetic ordering temperature, the intensity of the odd nuclear peaks was very high, indicating that the ferromagnetic alloys are predominantly ordered in the $L2_1$ structure. At 170K, which is close to the Neel temperature ($\theta_N \simeq 152 \mp 3K$), there is still a clear trace of type 1 anti–ferromagnetism with the ferromagnetic structures shown in figure (7·26).

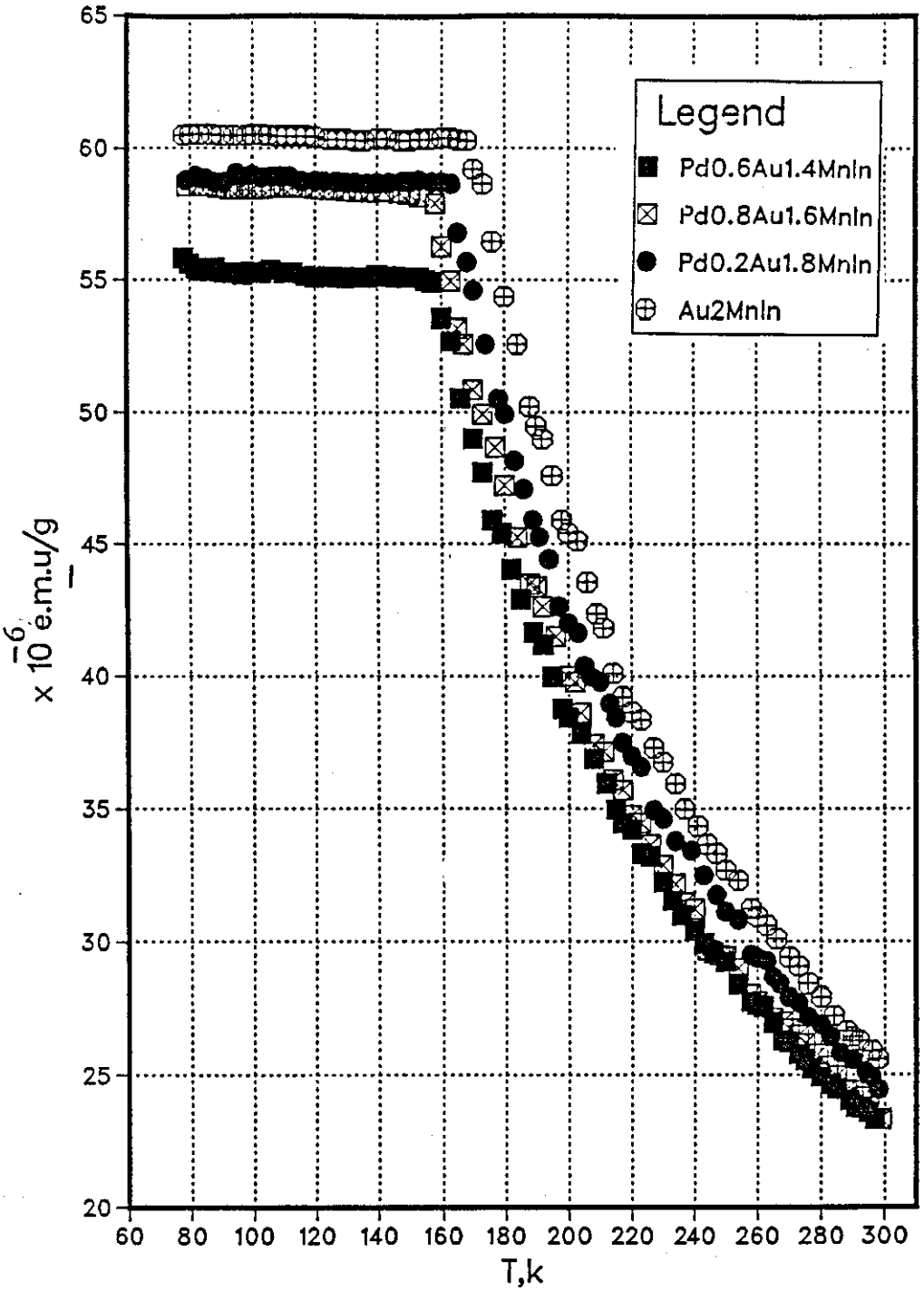

Figure (7.23) The susceptibility versus temperature curves for slow cooled alloys Pd_{2-x} Au_x Mn In.

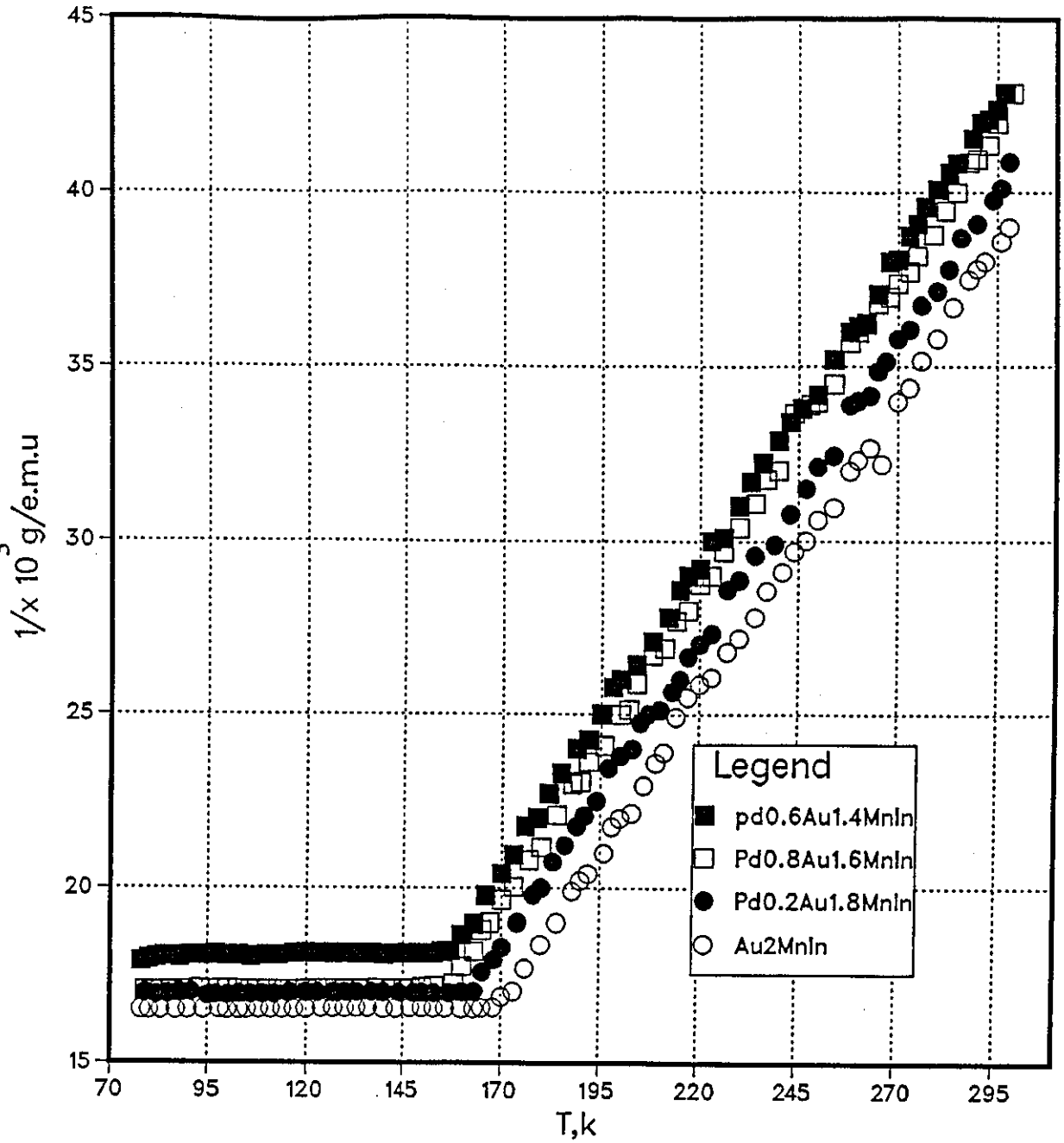

Figure (7.24) The reciprocal susceptibility versus temperature curves for slow cooled alloys Pd_{2-x} Au_x Mn In.

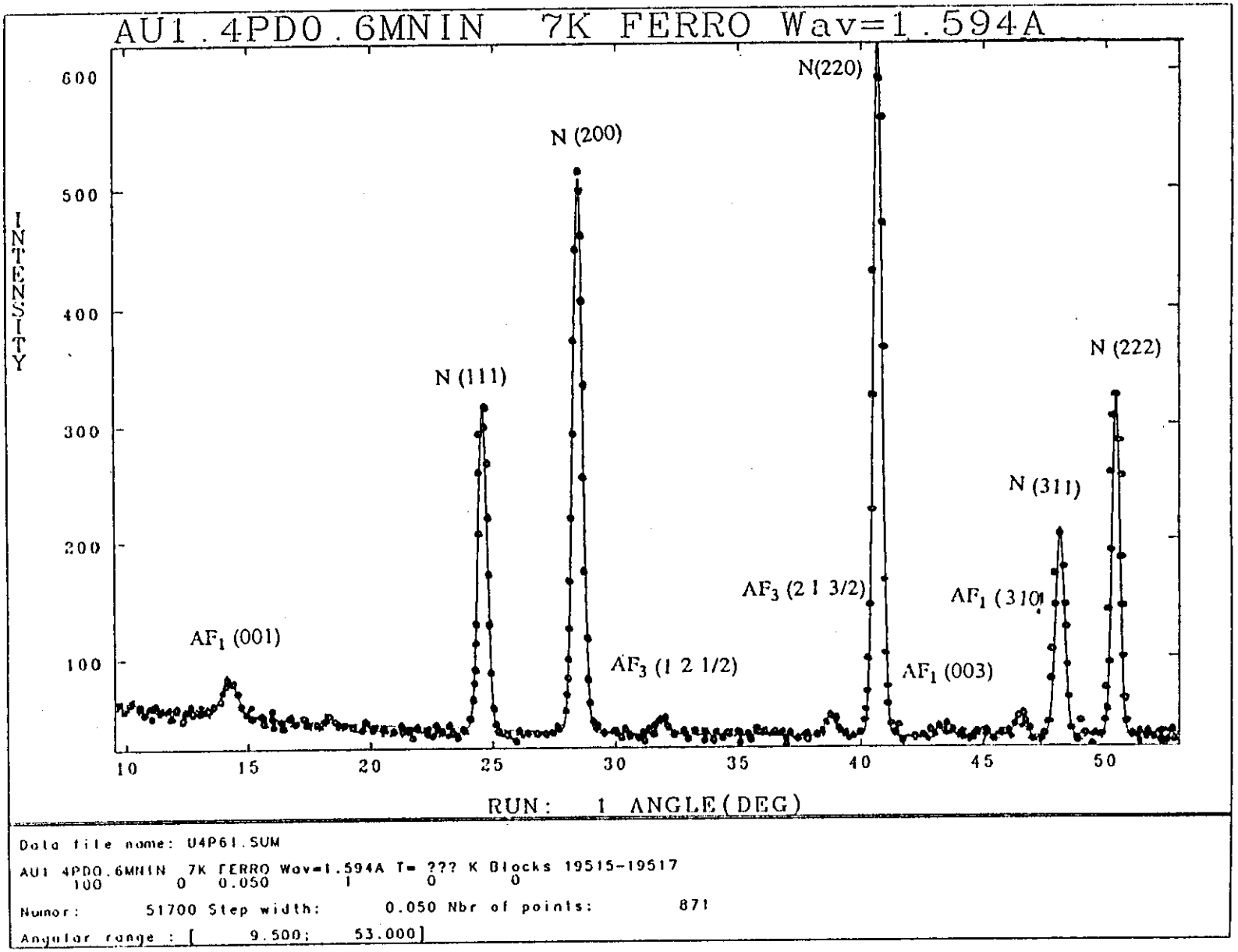

Figure (7.25) Neutron diffraction measurements at 7K showing the reflections from the nuclear and antiferromagnetic peaks.

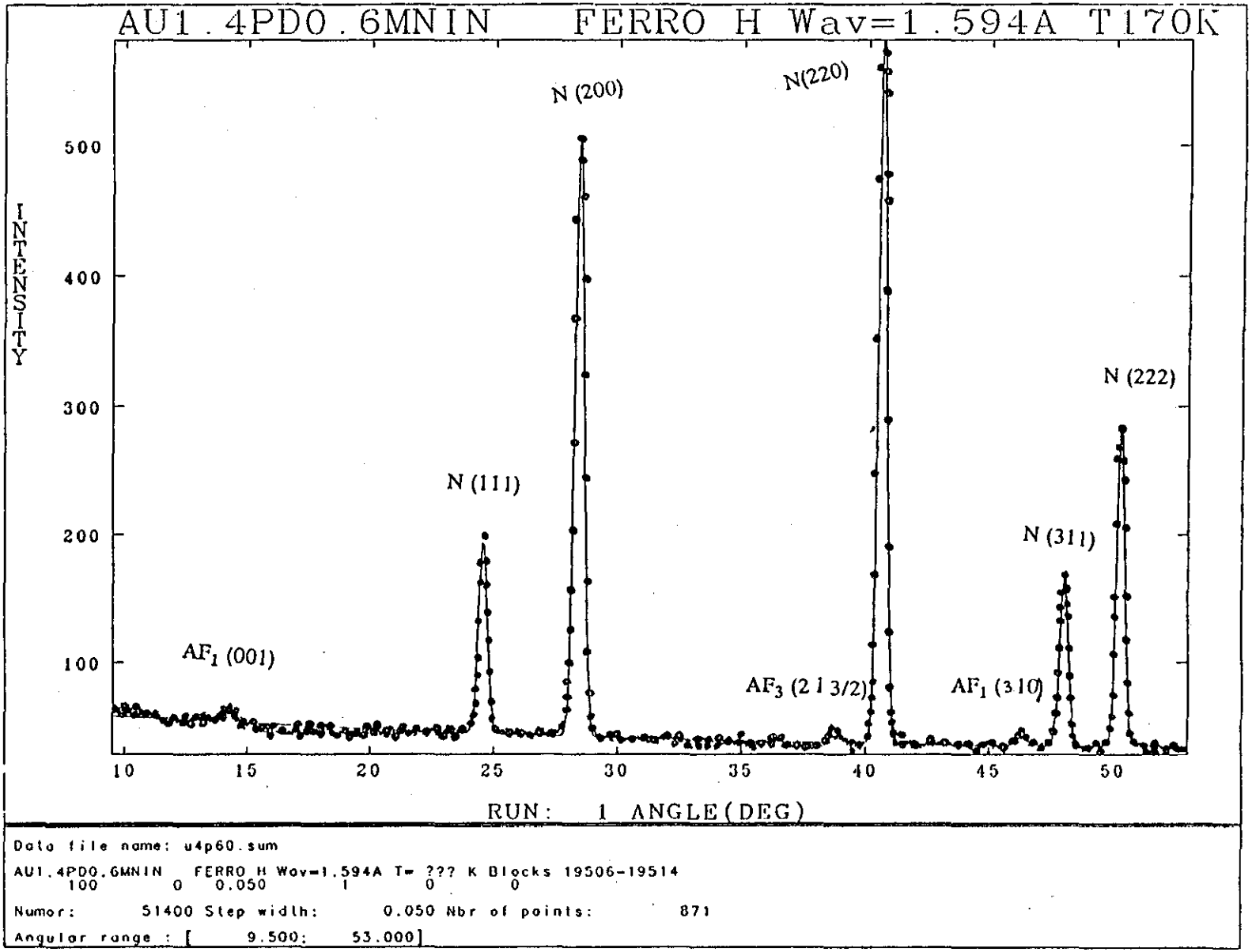

Figure (7.26) Neutron diffraction measurements at 170 K showing the reflections from the nuclear and antiferromagnetic peaks.

The neutron diffraction results show that all alloys with $x > 1{\cdot}4$ are ferromagnetic consequently the nuclear and magnetic Bragg scattering is superimposed.

The ferromagnetic magnetic moment per Mn atom remains essentially constant at approximately $4{\cdot}1 \mp 0{\cdot}01\ \mu_B$. Since the magnetic symmetry of the ferromagnetic structure is cubic and there is no unique axis, it was not possible to determine the moment orientation.

CHAPTER EIGHT

DISCUSSION AND CONCLUSION

8.1 INTRODUCTION

The main carriers of the magnetic moment in both series described in the last two chapters are Mn atoms. In the $L2_1$ structure the Mn atoms are arranged on a fcc lattice and are widely separated by non–magnetic Pd and Y atoms. Therefore, the Mn atoms have been considered to have a well defined localised moment and they are coupled via the conduction electrons, either by the double resonance type interaction proposed by Caroli and Blandin [2] or by the s–d interaction of the RKKY type.

Kasuya [121] (1974) considered a simple picture using the free electron model for the s–p electrons assuming zero conduction electrons are supplied by the Pd atoms, one from the Mn atom, and 3, 4 and 5 from IIIb, IVb and Vb sub–group elements respectively. He pointed out that all the alloys with $n_c = 5$ and 6 are ferromagnetic but for $n_c = 4$ antiferromagnetism is predominant.

8.2 DISCUSSION

The work presented in the last two chapters was concerned with establishing the structure, magnetic and thermal properties of two series of intermetallic compounds formed at the composition $Pd_{2-x}Ag_xMnIn$ and $Pd_{2-x}Au_xMnIn$ with $0 \leq x \leq 2$.

By mixing group 1B elements represented by $Ag^{47}(4d^{10}5s^1)$, $Au^{79}(4f^{14}5d^{10}6s^1)$, with a group VIII element $Pd^{46}(4d^{10})$ gives rise to a gradual change of the number of electrons per chemical formula unit (n_c from 4 to 5 to 6).

Thus, it was possible to determine the relationship between the continuous change in n_c and the change between the different types of antiferromagnetic and ferromagnetic structures.

All the alloys in the $Pd_{2-x}Ag_xMnIn$ and $Pd_{2-x}Au_xMnIn$ series have a complicated magnetic phase diagram in which the existence of the different types of antiferromagnetic structures consistent with an fcc lattice are observed at low temperatures.

A summary of the structural, thermal and magnetic features for both series are given in tables (8.1) and (8.2). The results obtained provide additional evidence for the importance of the electron concentration in determining the type of magnetic ordering. Alloys in both series with $n_c = 4{\cdot}2 (x = 0{\cdot}2)$ e/chem. form are antiferromagnetic and both fcc type 2, AF_2 and AF_3A structures are well established at low temperatures. In the silver series with $4{\cdot}4 \leq n_c \leq 4{\cdot}6$, the AF_3A structure is stable and the AF_2 peaks have disappeared, whereas in the gold series at $n_c = 4{\cdot}4$ both AF_3A and AF_2 structures are still present. At $n_c = 4{\cdot}8$ and above, all the alloys in the silver series are ferromagnetic. Thus in the silver series, magnetic order changes from a mixed ($AF_2 + AF_3A$) region to AF_3A and then to F as the electron concentration is increased. In the $Pd_{2-x}Au_xMnIn$ series, at $n_c = 4{\cdot}6$ ($x = 0{\cdot}6$) a new antiferromagnetic phase AF_1 appears and the AF_3A structure is still present. The alloys with $n_c \geq 5{\cdot}6$ are all ferromagnetic. The sequence of magnetic structures found in this series is ($AF_2 + AF_3A$), ($AF_1 + AF_3A$), ($AF_1 + AF_3A + F$) and then F, ferromagnetism.

At room temperature, the symmetry of all Heusler alloys is cubic with space group Fm3m. The variation of the lattice parameters, 'a', at room temperature, as a function of n_c for both series is shown in figure (8.1). It is noted that the lattice parameters increased slightly in proportion to n_c with a gradient of da/dn_c 0·174 and 0·168 Å/e/che.form for the silver and gold alloys respectively. This increase may be due to the different atomic radius of Au, Ag($\simeq$ 144 Pm) and Pd($\simeq$ 137 Pm).

At low temperatures there is a small crystallographic change in the structure to either tetragonal or rhombohedral structure dependent upon the antiferromagnetic structure as shown in figure (8.2 b,c).

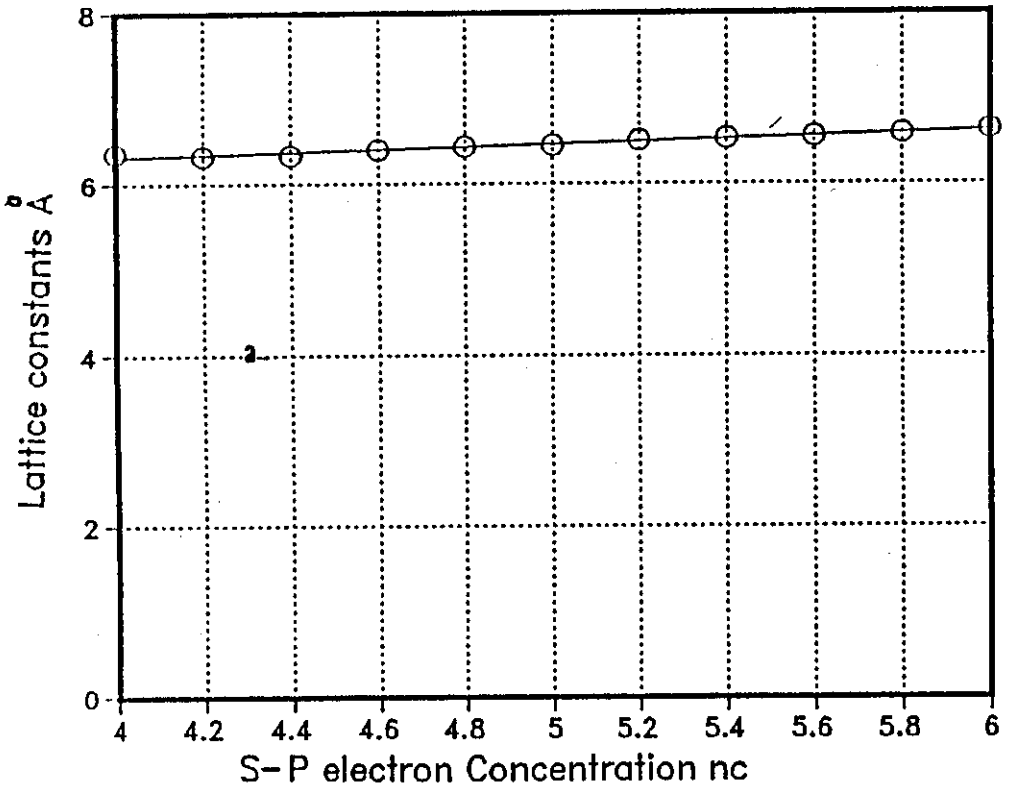

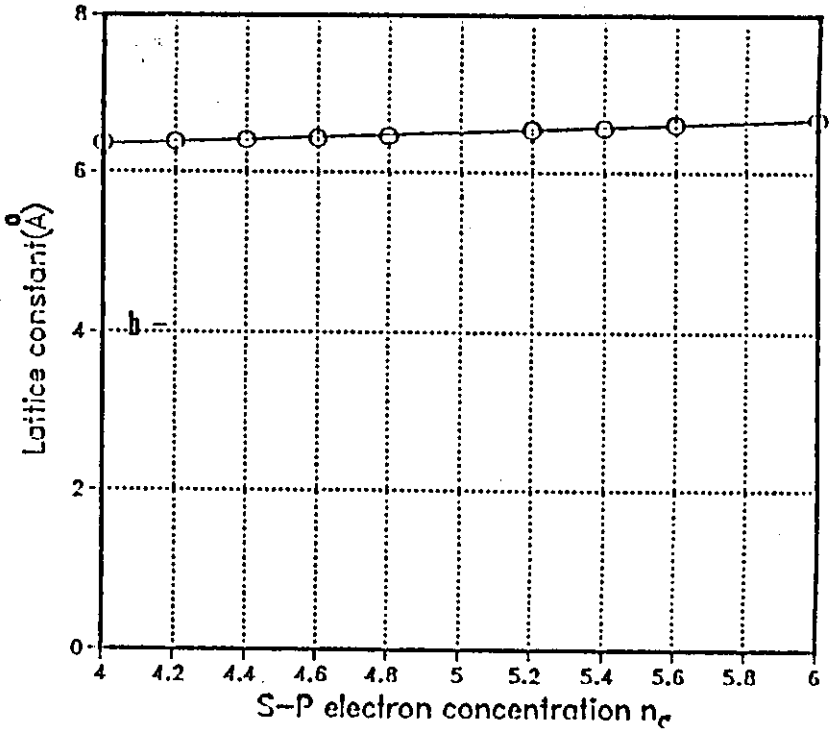

Figure (8.1) Lattice parameters, a_o, versus electron concentration n_c at room temperature for:

(a) $Pd_{2-x}\ Au_x\ Mn\ In$
(b) $Pd_{2-x}\ Ag_x\ Mn\ In$

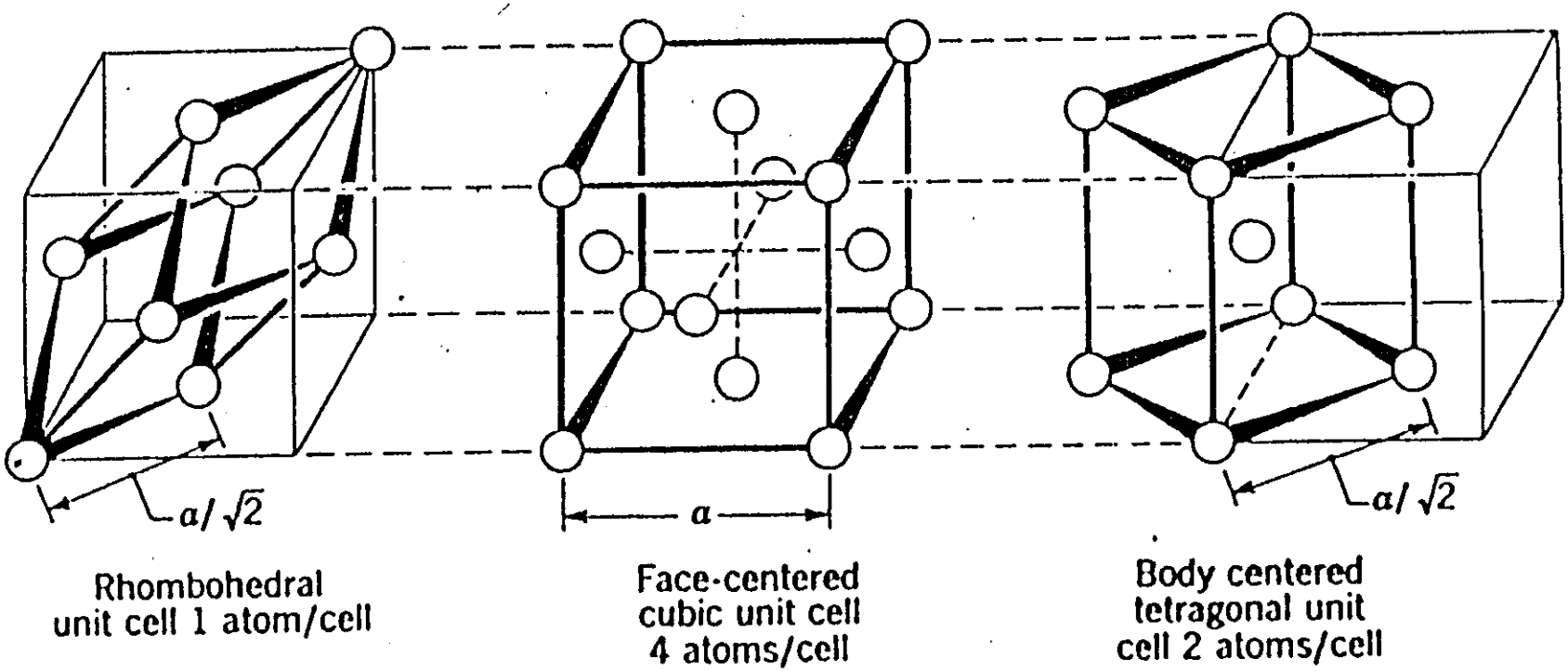

Figure (8.2) Possible unit cells of the fcc structure

For the tetragonal structure a small change due to the distortion caused splitting of the cubic nuclear reflections at high Bragg angles. Below the Neel temperature, the splitting increased with decreasing temperature as shown in figures (6.10) and (6.17) for $Pd_{1.6}Ag_{0.4}MnIn$ and $Pd_{1.4}Ag_{0.6}MnIn$ respectively and figures (7.17) and (7.21) for $Pd_{1.2}Au_{0.8}MnIn$ and $Pd_{0.8}Au_{1.2}MnIn$ respectively. Figure (8.3) shows the high angle nuclear peak of $Pd_{1.6}Au_{0.4}MnIn$ versus temperatures. It shows that the splitting increases below the Neel temperature.

This splitting is a result of tetragonal distortion induced by the AF_3A structure. However, AF_2 structure does not show any rhombohedral deformation below Neel temperature and the profile of the nuclear peaks remain essentially unaltered.

The temperature dependence of the magnetic reflection AF_3A $(10\frac{1}{2})$ of $Pd_{1.6}Ag_{0.4}MnIn$ is shown in figure (6.13). It may be seen that the Neel temperature is in good agreement with that suggested by magnetic susceptibility and specific heat data.

The lattice constants ($a = b \neq c$) for the tetragonal structure of $Pd_{2-x}Ag_xMnIn$ have been refined from high resolution neutron diffraction data. Figure (8.4) shows the variation of the lattice constants a, b with temperature. A significant anomaly around the Neel temperatures may be seen. The lattice constant c does not show any anomaly at Neel temperature but it changes slightly with increasing temperature. The unit cell volume also does not show any anomaly but it increases slightly with increasing temperature.

The anomaly in a and b could arise from the magnetostriction due to the coupling between the atomic moments and the crystalline lattice. This effect occurs because the magnetocrystalline energy depends on the strain in such a way that a stable state is obtained by deformation of the original lattice.

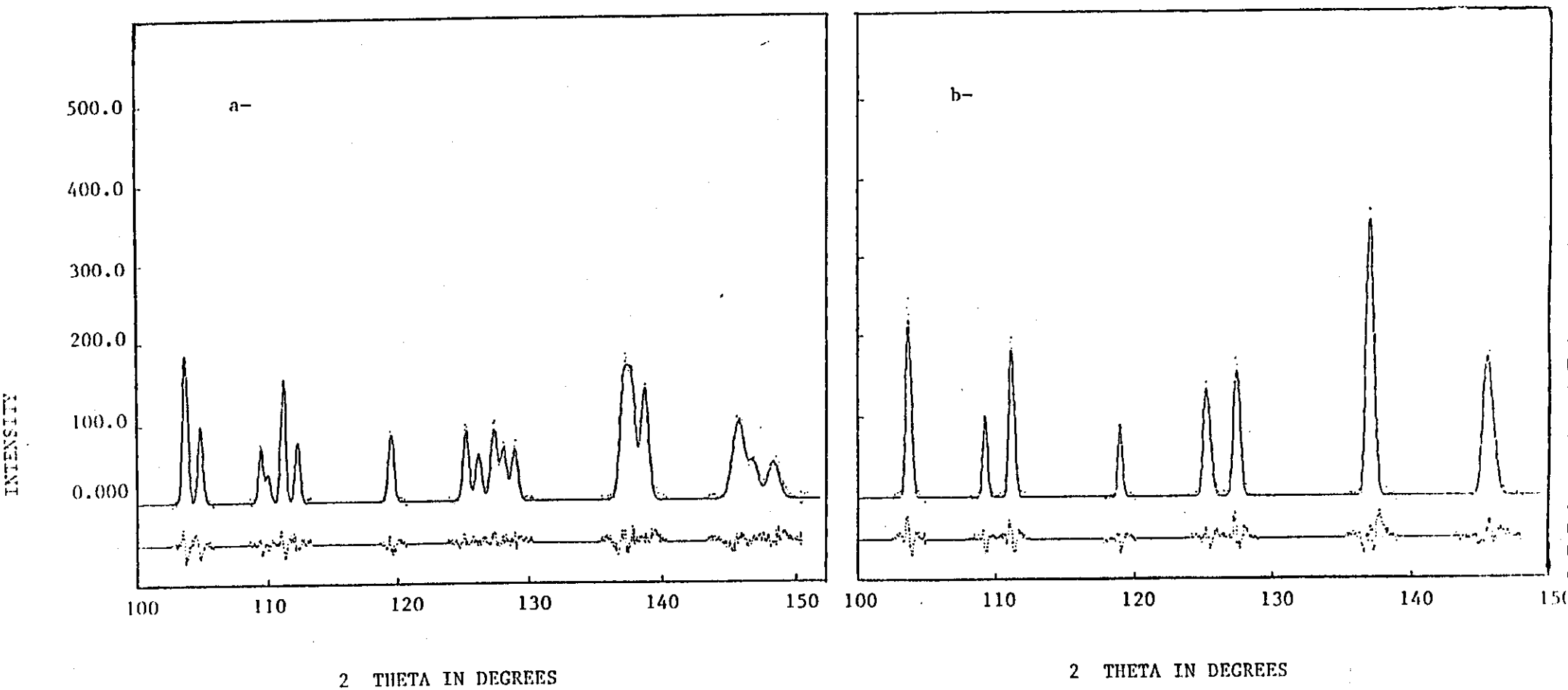

Figure (8.3) The high angle nuclear peaks of $Pd_{1.6}$ $Ag_{0.4}$ Mn In of

(a) 5K
(b) 170K

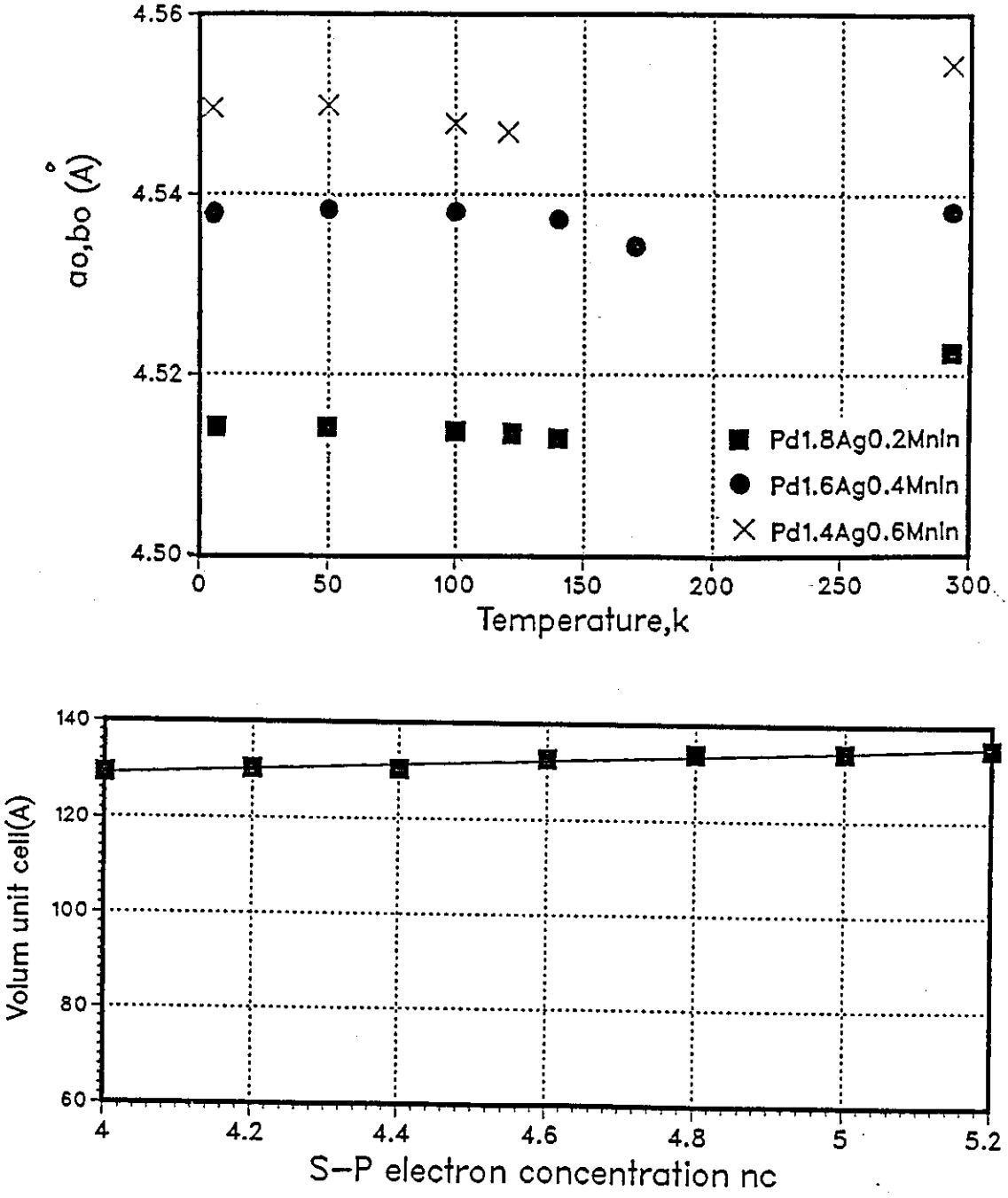

Figure (8.4) (a) Lattice constants a_o, b_o obtained from refinement for different neutron experiments.

(b) Volume unit cell versus concentration n_c at 7K obtained from powder diffraction refinement

Above the ordering temperatures of all the alloys in both series show Curie–Weiss behaviour. The extrapolated paramagnetic Curie temperature θ_P are shown in figures (8.5) and (8.6) for $Pd_{2-x}Ag_xMnIn$ and $Pd_{2-x}Au_xMnIn$ respectively. Paramagnetic and ferromagnetic Curie temperatures θ_P, θ_F and Neel temperatures θ_N for both series are shown in figures (8.7) and (8.8). It can be seen that there is a very slight increase in θ_P with increasing n_c. At $n_c \geq 4{\cdot}8$ and $n_c \geq 5{\cdot}4$ for the silver and gold series respectively, ferromagnetic ordering is observed with increasing n_c.

The measured susceptibility of both series with $x \geq 0{\cdot}8$ and $x \geq 1{\cdot}4$ for $Pd_{2-x}Ag_xMnIn$ and $Pd_{2-x}Au_xMnIn$ are shown in figures (6.1) and (7.25) respectively. It is noted that a saturation magnetisation below the ordering temperature occurs. The Faraday balance technique is not appropriate for such materials since the forced exerted becomes too large. The effective magnetic moments per atom P_{eff} versus composition x for both alloy series are shown in figures (8.9) and (8.10). P_{eff} changes slightly with increasing n_c but generally takes a mean value of $4{\cdot}4\ \mu_B \mp 0{\cdot}2\ \mu_B$ and $4{\cdot}49 \mp 0{\cdot}2\ \mu_B$ for the silver and gold alloys respectively. There is no evidence in all the alloys investigated throughout this work that the magnetic moment resides on any atom other than Mn. Neutron diffraction measurements set in upper limit of close to $0{\cdot}04 \mp 0{\cdot}001\ \mu_B$ for a moment on the Pd atoms.

Ishikawa and Noda [4] (1974), Johnson et al [123] (1982), using polarised neutron techniques, have shown that the magnetic moment in Pd_2MnSn and Pd_2MnSb are well localised on the Mn atoms, with no observable moment on the Pd sites.

All the phase transitions determined from specific heat measurements are in good agreement with neutron diffraction and magnetisation measurements, as

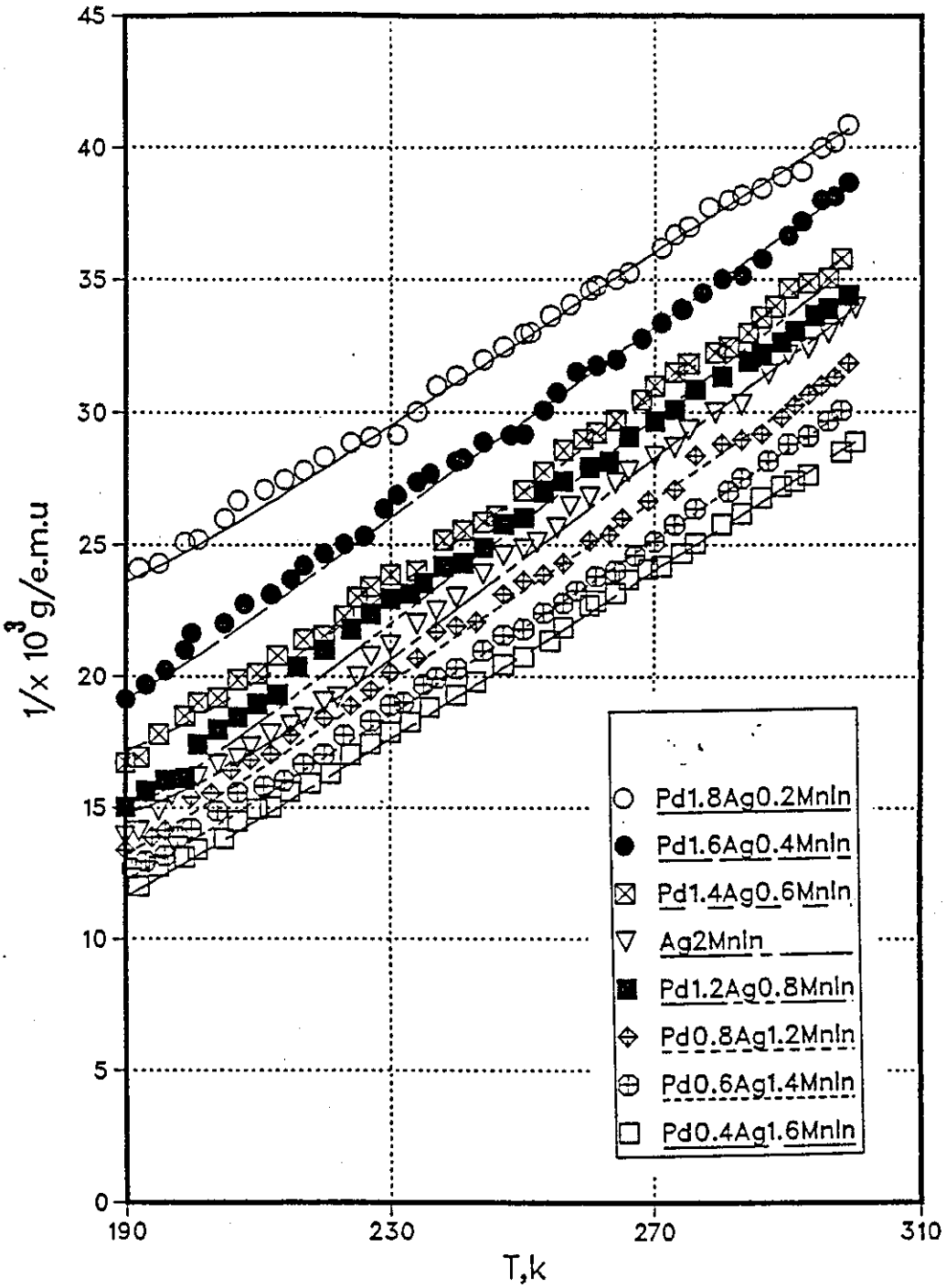

Figure (8.5) The reciprocal susceptibility versus temperature curves for Pd_{2-x} Ag_x Mn In alloys

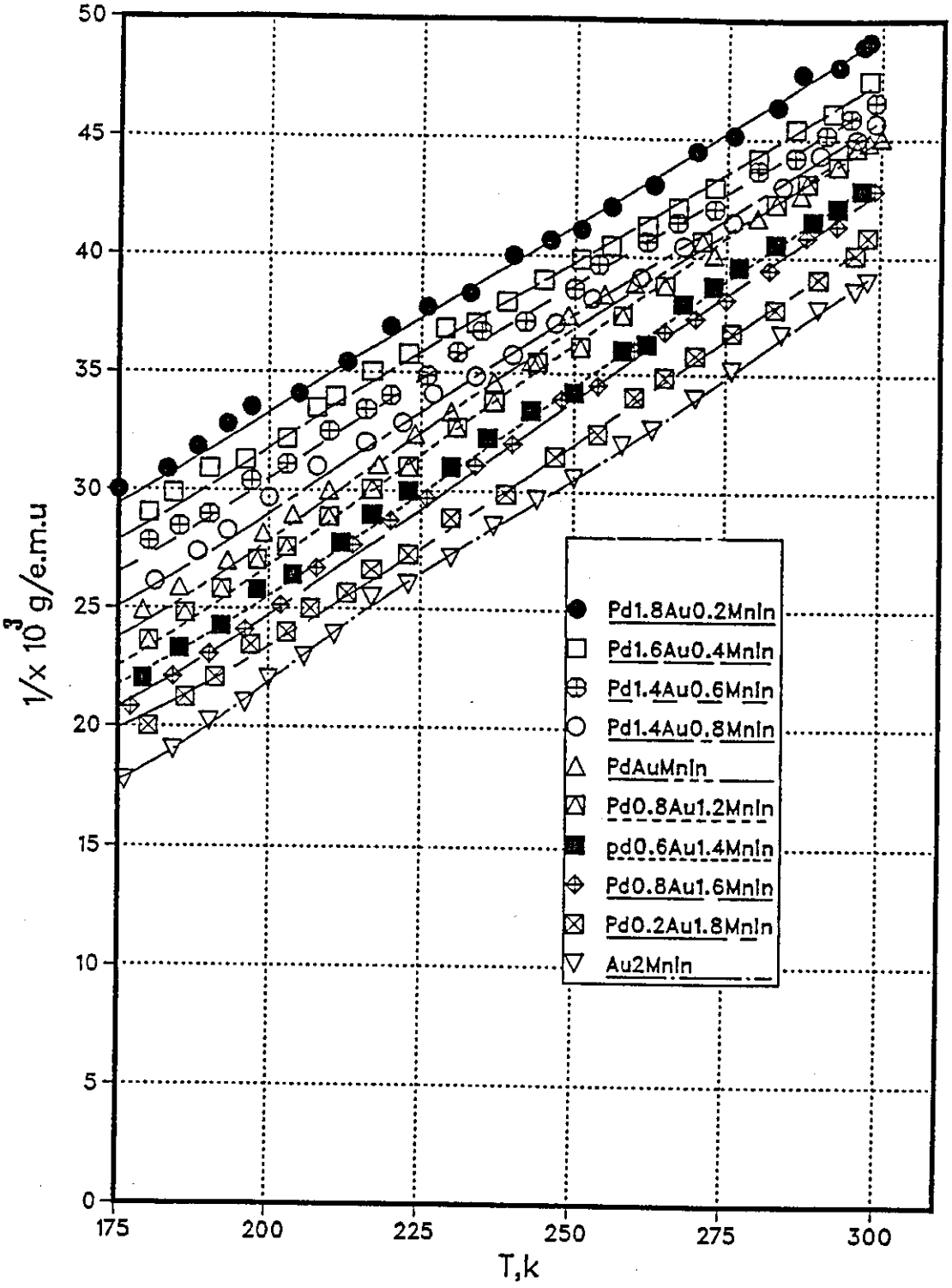

Figure (8.6) The reciprocal susceptibility versus temperature curves for Pd_{2-x} Au_x Mn In alloys

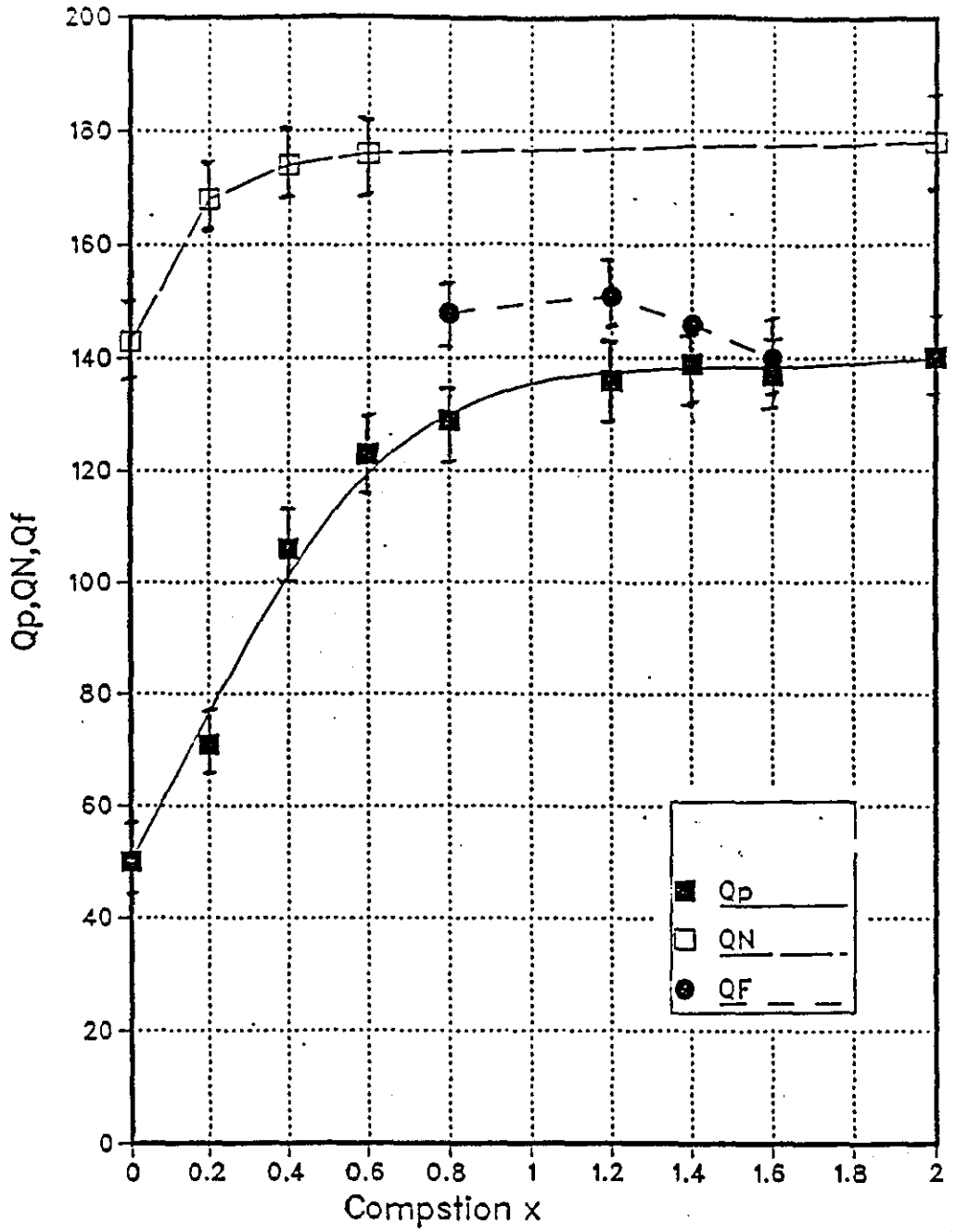

Figure (8.7) Paramagnetic and Ferromagnetic Curie temperatures θ_P and θ_F and Neel temperatures θ_N versus atomic composition x for $Pd_{2-x}\ Ag_x$ Mn In

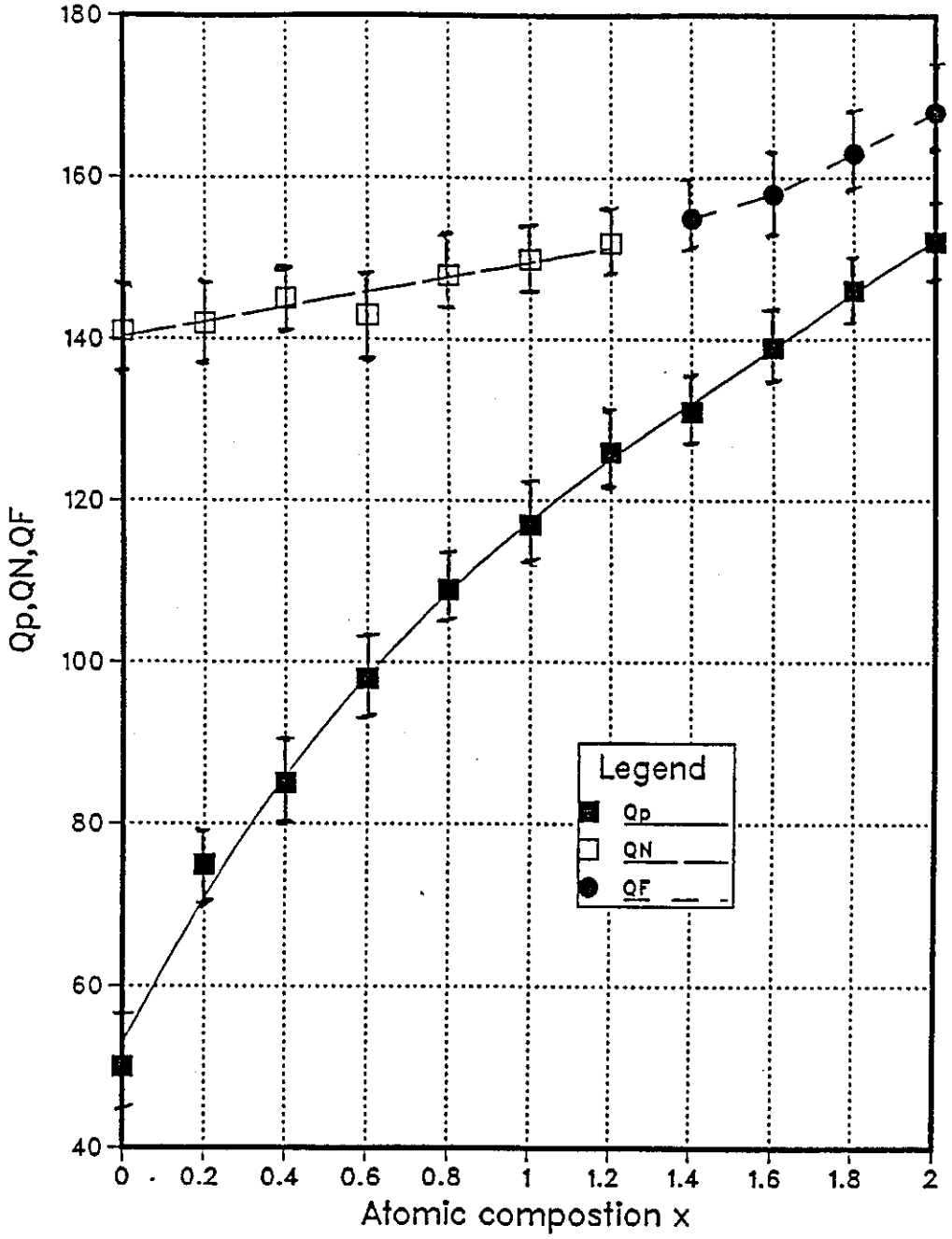

Figure (8.8) Paramagnetic and Ferromagnetic Curie temperatures θ_P and θ_F and Neel temperatures θ_N versus atomic composition x for Pd_{2-x} Au_x Mn In

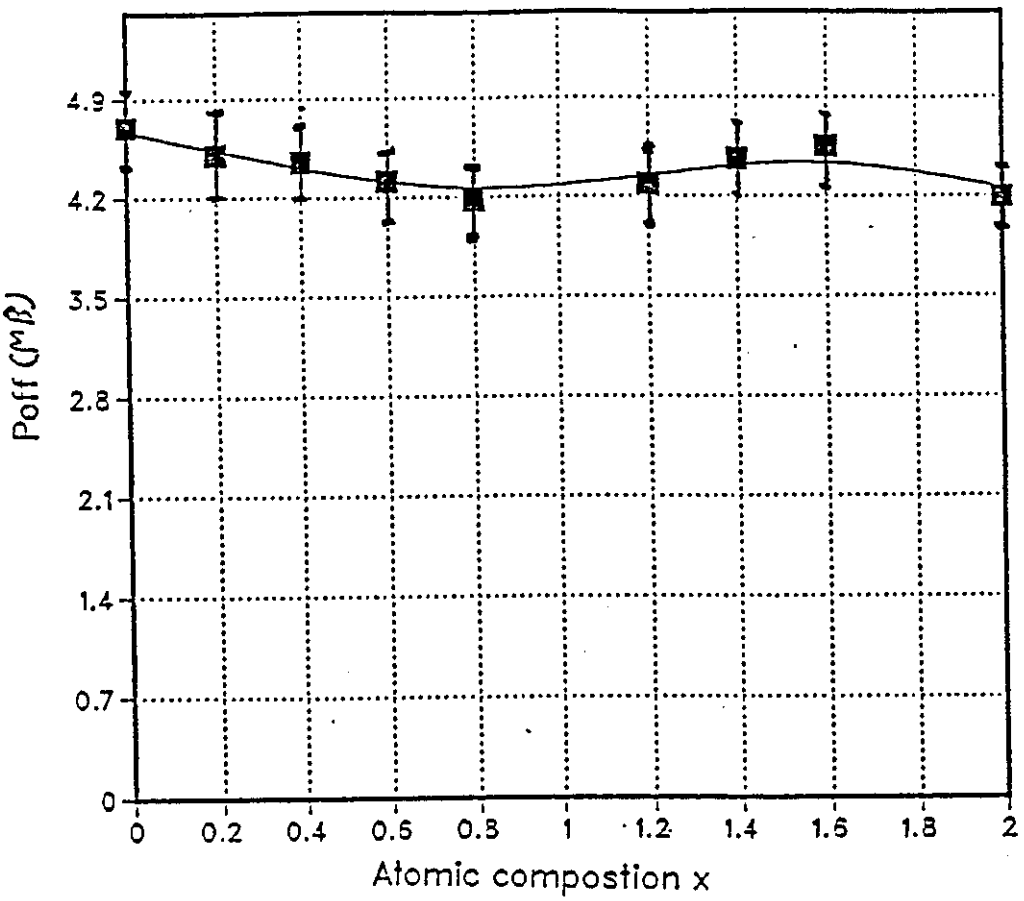

Figure (8.9) The effective magnetic moments versus compositions for Pd_{2-x} Ag_x Mn In

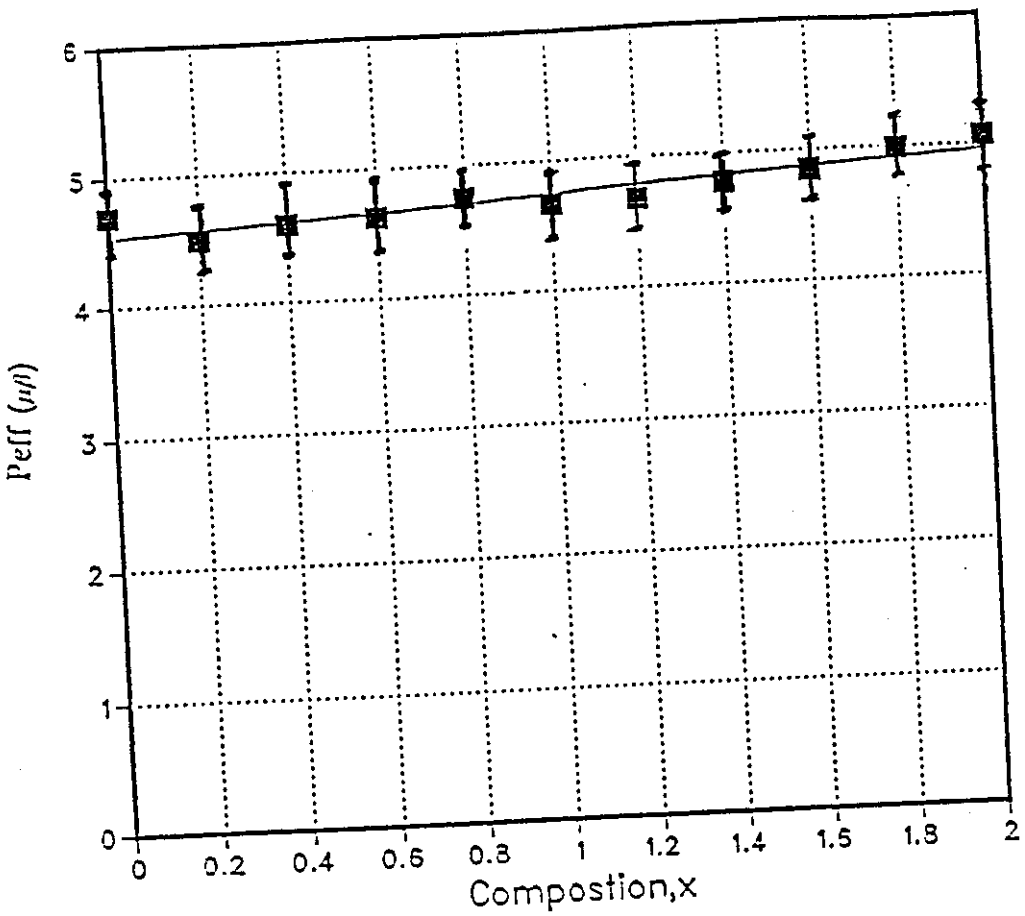

Figure (8.10) The effective magnetic moments versus compositions for Pd_{2-x} Au_x Mn In

shown in figure (6.14) and tables (8.1) and (8.2) respectively. There is significant difference between the spin entropy S_M of the magnetic Mn atoms compared with the value of the spin quantum number s obtained from susceptibility measurements. The difference is thought to be due to the fact that the magnetic entropy is already frozen out at T_N, indicating competing short–range interactions or possibly from frustration associated with fcc antiferromagnetism . This phenomenon was reported by Wenger [83] (1976) and Martin[84] (1980), who found that the magnetic entropy of CuMn alloys is already frozen out at the freezing temperature. An alternative explanation may be that the entropy comes out over a wide range of temperature. The variation of spin entropy with composition for silver alloys is shown in figure (8.11). It is noted that for alloys with $x \leq 0{\cdot}8$ the compounds have a degree of B2 disorder. The greater the chemical disordered the higher the entropy. Consequently, the nearest neighbour Mn distances are changed some will be a/2 and others $a/\sqrt{2}$.

All the specific heat curves, obtained by a continuous heating method (DSC), show almost constant reading above the ordering temperature. This constant reading is at variance with the Debye theory of specific heat which approaches the classical value of 3R at high temperatures. However, the specific heat measured using the pulse method agrees with Debye's theory as shown in figure (8.12) for $Pd_{2-x}Au_xMnIn$ alloys.

It is noted from the neutron diffraction powder data that all alloys in both series, have the Heusler $L2_1$ type chemical structure but with some B2(Mn–In) disorder.

It is seen from figures (7.11) and (7.18) for $Pd_{1\cdot2}Au_{0\cdot8}MnIn$ and $Pd_{1\cdot4}Au_{0\cdot6}MnIn$ that at $2\theta \simeq 14{\cdot}64$, the magnetic contributions appear significantly broader than the nuclear peaks at low temperatures. It may arise from spin glass behaviour where the occurrence of localised freezing gives rise to a broad peak due to the effect of short range magnetic order. This broadening consists of the two mixed magnetic (001) peak, AF_1 and (201), peak AF_3A. The width and the intensity of the (001) AF_1 peak decreases with increasing

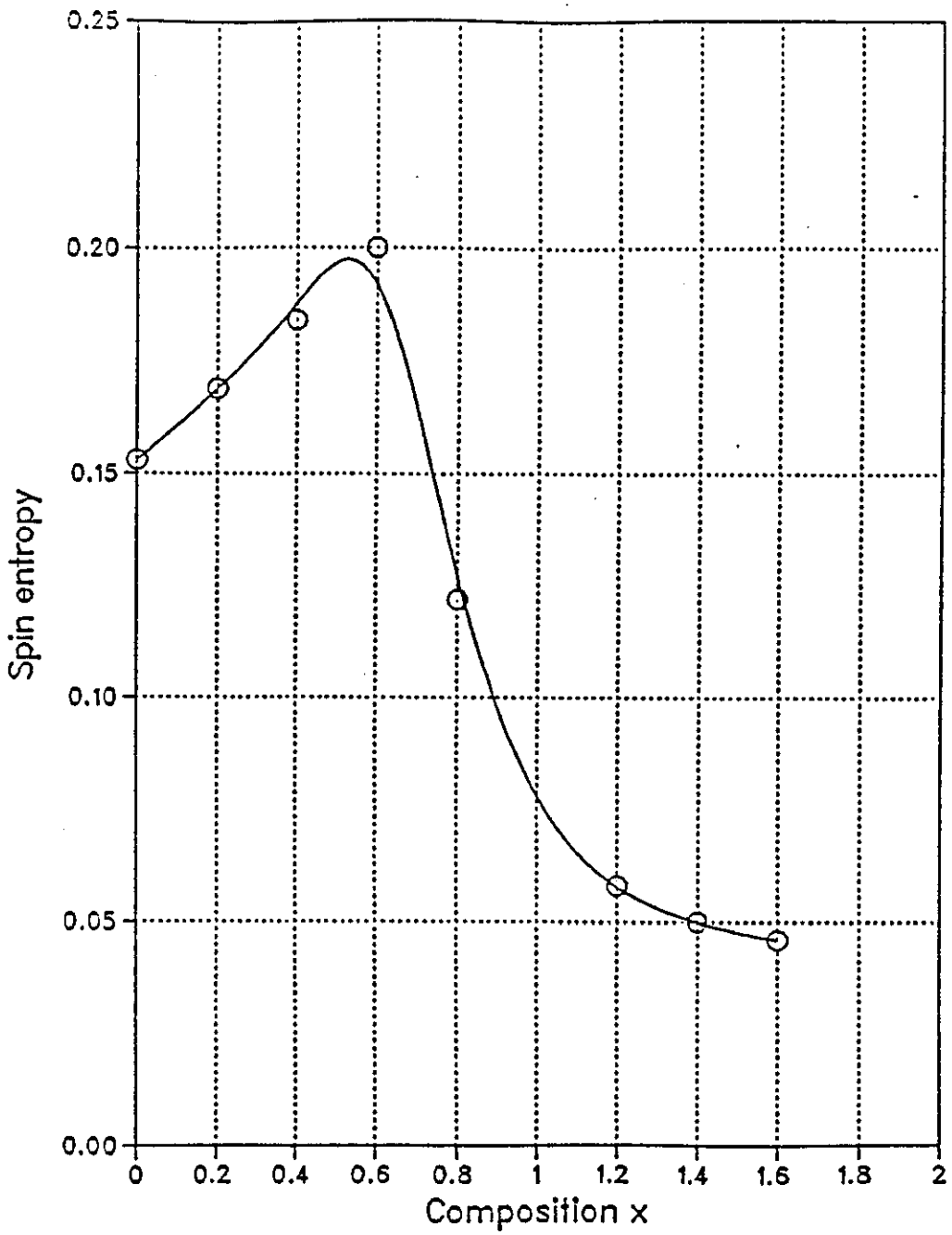

Figure (8.11) Spin magnetic entropy versus composition for $Pd_{2-x}\ Ag_x\ Mn\ In$

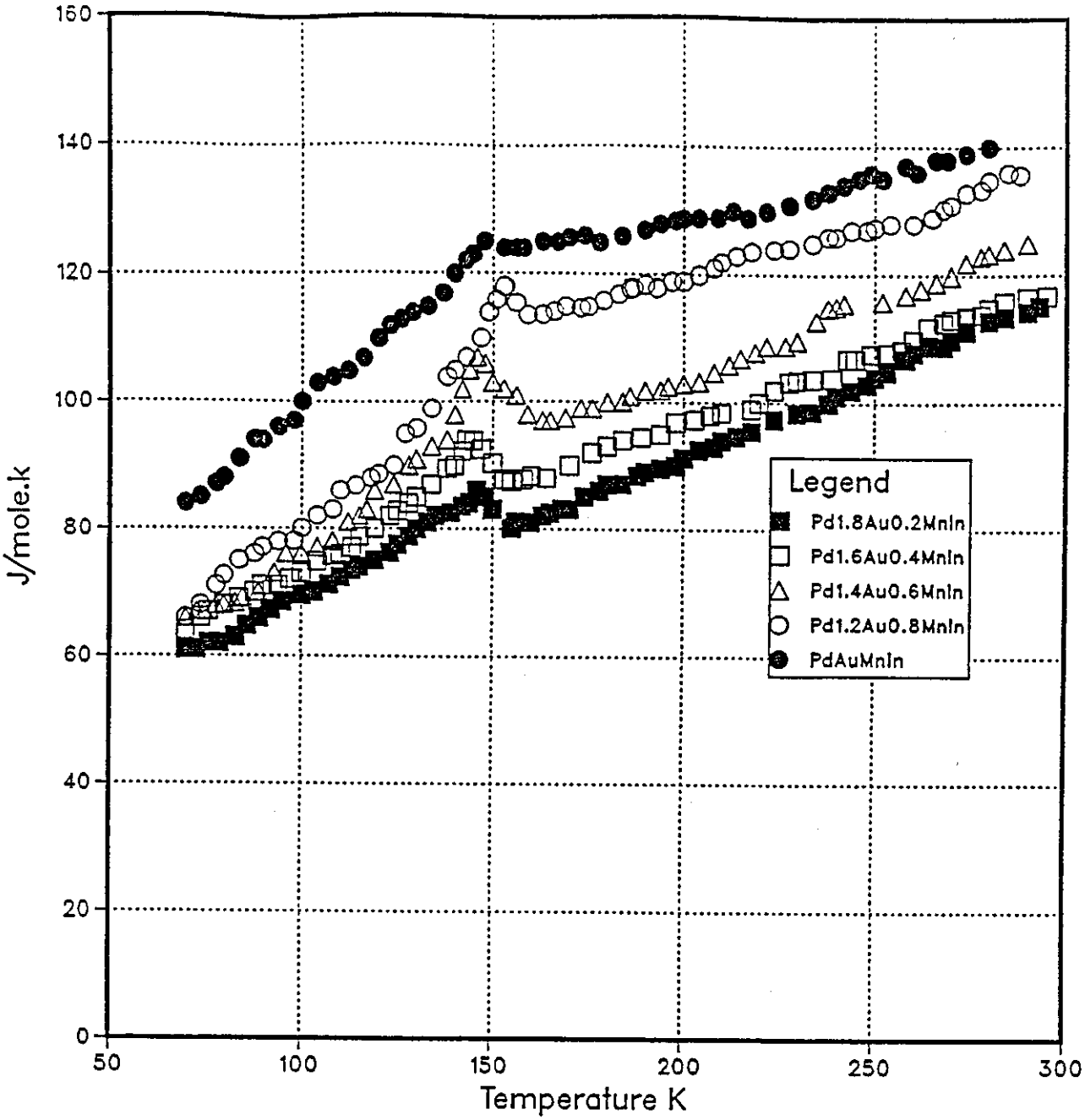

Figure (8.12) The specific heat curves versus temperature for slow cooled alloys Pd_{2-x} Au_x Mn In

The width and the intensity of the (001) AF_1 peak decreases with increasing composition x. For x = 0·6, two magnetic peaks which correspond to two different magnetic structures are clearly seen.

The neutron diffraction and specific heat measurements did not show any evidence for the existence of more than one transition temperature. However, it is noted from $1/\chi$ versus T curve for $Pd_{1.8}Ag_{0.2}MnIn$ (figure 6.2), where the fcc type 2 and 3A structures exist, that there is a small hump around $\simeq$ 143K. This may be due to the existence of separate ordering for the AF_2 or AF_3A structures. This is not confirmed by neutron diffraction.

In the ordered Heusler structure the Mn atoms are located on an fcc sub-lattice with a lattice parameter ~ 6Å and nearest Mn–Mn distances ~ 4·2Å. This is normally considered to be too large for direct exchange and so several indirect s–d exchange mechanism of a RKKY type or of the double resonance type have been postulated as possible exchange mechanisms [80]. Spin wave measurements [81] have shown that the long range magnetic interactions (r > 12 Å) in Heusler alloys have an oscillatory nature at long distances which can be well accounted for by s–d interactions.

It was shown that both $Pd_{2-x}Ag_xMnIn$ and $Pd_{2-x}Au_xMnIn$ alloys were ordered in $L2_1$ structure in which the Mn atoms form a fcc lattice or were partially disordered in the B2 structure. In the B2 phase the magnetic order has been shown to be simple cubic antiferromagnetic [124]. In the $L2_1$ structure, the nearest neighbour Mn–Mn distance is larger than 4·6Å and therefore, the localised model should be a good approximation for these materials.

According to the molecular field theory, the magnetic ordering temperature θ is given by the equation (see 5.6 Chapter 5):

$$K_B\theta = 2/3\, S(S+1) \sum_{i=1}^{N} \varepsilon_i J_{ij} \qquad (8.1)$$

where J_{ij} is the exchange interaction between a magnetic atom j and one of its Nth neighbours. ε_i takes account of the spin orientation and has the value +1 or –1 depending upon whether the moments on atom i and j are parallel or antiparallel.

For simplicity to solve equation (8.1), we assume here that the exchange interactions extends only up to the third neighbours. We assumed also that the moment exhibited by each Mn atom is the same whether the alloy is ordered in the $L2_1$ or B_2 structure. By substituting the values from tables (8.1) and (8.2) in the equation (8.1) and summing up to the third neighbour interactions, the exchange integrals for $L2_1$ structure can be determined for four possible types of magnetic order. The exchange integrals calculated from the measured data are tabulated in tables (8.3) and (8.4) for the $Pd_{2-x}Ag_xMnIn$ and $Pd_{2-x}Au_xMnIn$ series respectively.

From the results it can be concluded that ferromagnetism prevails when J_2 and J_3 and J_1 are all positive, for AF_3A, J_3 must be positive and J_1 negative, for AF3, J_2 must be negative. For AF_1, J_3 must be negative. The condition for ferromagnetism, AF_2 and AF_3A to co–exist is that J_1 and J_2 are negative and J_3 is positive.

8.3. CONCLUSION

Two series of intermetallic compounds formed at the compositions $Pd_{2-x}Ag_xMnIn$ and $Pd_{2-x}Au_xMnIn$ with $0 \leq x \leq 2$ have been investigated. X–ray, neutron diffraction measurements (used to determine chemical and magnetic ordering), specific heat and magnetic susceptibility measurements provide useful information in the analysis of the degrees and types of long–range exchange interactions in the 3d metals.

The full angular range and high resolution capacities of D2B were employed to determine simultaneously both the magnetic structures and any related lattice distortion, observed in both series as a function of temperature.

Both series are highly ordered in the $L2_1$ structure with a partial disorder into the B2 type structure.

Manganese the element common to all the alloys, carries in every case a large magnetic moment (usually about 4·3 μ_B) which is coupled via some form of neighbouring Mn atoms in an ordered magnetic structure.

In all the alloys investigated, the electron concentration appears to have an important influence on the magnetic properties. The magnetic structure for $Pd_{2-x}Ag_xMnIn$ alloys, with increasing silver concentration was observed to progress from $AF_2 + AF_3A$ to AF_3A and then to F. For $Pd_{2-x}Au_xMnIn$, with increasing gold concentration, the magnetic structure was observed to progress from $AF_2 + AF_3A$ to $AF_1 + AF_3A$ to $AF_1 + AF_3A + F$ and then to F.

In the gold series, an additional magnetic structure was identified to be fcc antiferromagnetism type 1.

A generalised molecular field theory has been employed as a first step in the theoretical analysis to describe the magnetic phase diagram. The existence of negative and positive exchange interactions suggests that both the Caroli–Blandin theory of the double resonance scattering or the RKKY theory based on the free electron model could be applicable.

In order to obtain more information related to these compounds, the following experiments are suggested for future work:

1 Specific heat and magnetic susceptibility measurements from helium temperature to 77K.

2 Due to the difficulty of using Faraday balance technique to study the ferromagnetic structure, the vibrating sample magnetometer technique could be used.

3. Neutron spin wave scattering to determine the exchange constants in these compounds further than 3 neighbours.

Table (8.1) Structures, Magnetic and thermal properties of the Alloys $Pd_{2-x}Ag_xMnIn$

Alloy	a_o (Å)	0p(K)	θ_N or θ_F Neel or Curie Temp (K)	$P_{eff}(\mu_B)$ $(1/\chi, T)$	S	Phase Transition from Cp	Spin entropy from Cp	Magnetic structure	$\mu(\mu_B)$	nc (e/ch.form)
Pd_2MnIn [127]	6·373 ± 0·003	52 ± 6	141 ± 4	4·9 ± 0·2	–	–	–	AF_2	4·8 ± 0·2	4·0
"Our research"	6·369 ± 0·003	51 ± 2	143 ± 3	4·7 ± 0·2	1·95	143 ± 2	0·153 ± 0·1	–	–	–
$Pd_{1·8}Ag_{0·2}MnIn$	6·397 ± 0·003	71 ± 3	168 ± 3	4·5 ± 0·3	1·803	173 ± 2	0·169 ± 0·1	AF_2, AF_3	4·82 ± 0·2	4·2
$Pd_{1·6}Ag_{0·4}MnIn$	6·418 ± 0·003	106 ± 3	174 ± 2	4·48 ± 0·2	1·781	172 ± 2	0·184 ± 0·1	AF_3	4·74 ± 0·2	4·4
$Pd_{1·4}Ag_{0·6}MnIn$	6·441 ± 0·003	123 ± 2	176 ± 3	4·31 ± 0·2	1·715	173 ± 3	0·200 ± 0·1	AF_3	3·8 ± 0·2	4·6
$Pd_{1·2}Ag_{0·8}MnIn$	6·470 ± 0·003	129 ± 3	148 ± 3	4·24 ± 0·2	1·648	139 ± 2	0·122 ± 0·1	F	4·16 ± 0·2	4·8
$Pd_{0·8}Ag_{1·2}MnIn$	6·552 ± 0·003	136 ± 2	151 ± 3	4·27 ± 0·3	1·701	153 ± 3	0·058 ± 0·03	F	4·13 ± 0·2	5·2
$Pd_{0·6}Ag_{1·4}MnIn$	6·576 ± 0·003	139 ± 2	146 ± 3	4·48 ± 0·2	1·788	144 ± 2	0·050 ± 0·03	F	–	5·4
$Pd_{o·4}Ag_{1·6}MnIn$	6·647 ± 0·003	137 ± 3	140 ± 3	4·51 ± 0·2	1·829	138 ± 2	0·046 ± 0·03	F	–	5·6

Table (8.2) Structures, Magnetic and thermal properties of the Alloys $Pd_{2-x}Au_xMnIn$

Alloy	a_o (Å)	0p(K)	θ_N or θ_F Neel or Curie Temp (K)	$P_{eff}(\mu_B)$ (1/χ,T)	S	Phase Transition from Cp	Spin entropy from Cp	Magnetic structure	$\mu(\mu_B)$	nc (e/ch.form)
$Pd_{1.8}Au_{0.2}MnIn$	6·341 ± 0·003	75 ± 3	142 ± 3	4·50 ± 0·02	1·804	145 ± 2	0·269 ± 0·02	AF_2, AF_3	5·40 ± 0·2	4·2
$Pd_{1.6}Au_{04}MnIn$	6·349 ± 0·003	85 ± 2	145 ± 3	4·60 ± 0·02	1·853	143 ± 3	0·257 ± 0·02	AF_3, AF_2	3·921 ± 0·2	4·4
$Pd_{1.4}Au_{0.6}MnIn$	6·413 ± 0·003	98 ± 2	143 ± 3	4·52 ± 0·02	1·816	146 ± 2	0·317 ± 0·02	AF_1, AF_3	4·98 ± 0·2	4·6
$Pd_{1.2}Au_{0.8}MnIn$	6·448 ± 0·003	109 ± 3	148 ± 2	4·75 ± 0·03	1·928	150 ± 2	0·279 ± 0·02	AF_1, AF_3	4·11 ± 0·2	4·8
PdAuMnIn	6·463 ± 0·003	117 ± 3	150 ± 3	4·67 ± 0·02	1·889	151 ± 3	0·333 ± 0·02	AF_1, AF_3	4·32 ± 0·2	5·0
$Pd_{0.8}Au_{1.2}MnIn$	6·522 ± 0·003	126 ± 3	152 ± 2	4·68 ± 0·03	1·895	153 ± 2	0·367 ± 0·02	AF_1, AF_3,	3·91 ± 0·2	5·2
$Pd_{0.6}Au_{1.4}MnIn$	6·544 ± 0·003	131 ± 3	155 ± 2	4·78 ± 0·02	1·943	159 ± 3	0·371 ± 0·02	AF_1, AF_3, F	4·73 ± 0·2	5·4
$Pd_{0.4}Au_{1.6}MnIn$	6·566 ± 0·003	139 ± 3	158 ± 2	4·85 ± 0·02	1·977	163 ± 3	0·332 ± 0·02	F	4·1 ± 0·2	5·6
$Pd_{0.2}Au_{1.8}MnIn$	6·599 ± 0·003	146 ± 2	146 ± 2	4·99 ± 0·03	2·047	161 ± 3	0·291 ± 0·02	F	4·12 ± 0·2	5·8
Au_2MnIn	6·644 ± 0·003	152 ± 2	168 ± 2	5·04 ± 0·03	2·070	164 ± 2	0·317 ± 0·02	F	–	6·0

Table (8.3) The Exchange Integrals calculated from measured data for the series $Pd_{2-x}Ag_xMnIn$

Alloy	S	$\frac{J_1}{\rho}$	$\frac{J_2}{\rho}$	$\frac{J_3}{\rho}$	$\frac{1}{\rho}\left(\frac{J_1}{2}+\frac{J_2}{4}+J_3\right)$	$\rho=\frac{3}{2s(s+1)}$	θp(K)	θ_N(K) or θ_F(K)	nc c/ch.form	Magnetic order
Pd_2MnIn	1·95	16·0833	–23·833	0·0417	–	0·2608	51 ± 2	143 ± 3	4·0	AF_2
$Pd_{1·8}Ag_{0·2}MnIn$	1·803	–18·042	–28·000	18·9792	–	0·2968	71 ± 3	168 ± 3	4·2	AF_2, AF_3
$Pd_{1·6}Ag_{0·4}MnIn$	1·781	–17·333	0·0000	13·0833	–	0·3029	106 ± 3	174 ± 2	4·4	AF_3
$Pd_{1·4}Ag_{0·6}MnIn$	1·715	–16·875	0·0000	13·5625	–	0·3222	123 ± 2	176 ± 3	4·6	AF_3
$Pd_{1·2}Ag_{0·8}MnIn$	1·648	–	–	–	6·1667	0·3437	129 ± 3	148 ± 3	4·8	F
$Pd_{0·8}Ag_{1·2}MnIn$	1·701	–	–	–	6·2927	0·3265	136 ± 2	151 ± 3	5·2	F
$Pd_{0·6}Ag_{1·4}MnIn$	1·788	–	–	–	6·0833	0·3009	139 ± 2	146 ± 3	5·4	F
$Pd_{0·4}Ag_{1·6}MnIn$	1·829	–	–	–	5·8333	0·2899	137 ± 3	140 ± 3	5·6	F

Table (8.4) The Exchange Integrals calculated from measured data for the series $Pd_{2-x}Au_xMnIn$ series

Alloy	Magnetic order	nc	S	θ_P (K)	θ_N (K)	θ_F (K)	$\frac{J_1}{\rho}$	$\frac{J_2}{\rho}$	$\frac{J_3}{\rho}$	$\frac{1}{\rho}\left(\frac{J_1}{2}+\frac{J_2}{4}+J_3\right)$
$Pd_{1.8}Au_{0.2}MnIn$	AF_2, AF_3	4·2	1·804	75 ± 3	142 ± 3	–	–15·38	–23·67	15·98	–
$Pd_{1.6}Au_{0.4}MnIn$	AF_2, AF_3	4·4	1·853	85 ± 2	145 ± 3	–	–14·58	–24·17	16·88	–
$Pd_{1.4}Au_{0.6}MnIn$	AF_1, AF_3	4·6	2·816	98 ± 2	143 ± 3	–	–13·79	–23·83	–28·85	–
$Pd_{1.2}Au_{0.8}MnIn$	AF_1, AF_3	4·8	1·928	109 ± 3	148 ± 3	–	–13·96	–24·67	–30·02	–
$PdAuMnIn$	AF_1, AF_3	5·0	1·889	117 ± 3	150 ± 3	–	–13·88	–25·00	–30·31	–
$Pd_{0.8}Au_{1.2}MnIn$	AF_1, AF_3	5·2	1·895	126 ± 3	152 ± 2	–	–13·75	–25·33	–31·12	–
$Pd_{0.6}Au_{1.4}MnIn$	AF_1, AF_3, F	5·4	1·943	131 ± 3	–	155 ± 2	–13·92	–21·83	–18·88	–
$Pd_{0.4}Au_{1.6}MnIn$	F	5·6	1·977	139 ± 3	–	158 ± 2	–	–	–	6·58
$Pd_{0.2}Au_{1.8}MnIn$	F	5·8	2·047	146 ± 2	–	163 ± 3	–	–	–	6·79
Au_2MnIn	F	6·0	2·070	152 ± 2	–	168 ± 2	–	–	–	7·00

CHAPTER NINE

DYNAMIC FORM FACTOR IN THE INVAR ALLOY $Fe_{65}Ni_{35}$

9.1 INTRODUCTION

Alloys which exhibit Invar behaviour have a small thermal expansion coefficient below the Curie temperature, a large forced volume magneto–striction and show a substantial pressure dependence of the magnetisation and Curie temperature, etc. For alloys in the Fe–Ni system, local fluctuations in composition resulting in heterogenous magnetisations are believed essential for the Invar effect, which shows a maximum at the composition $Fe_{65}Ni_{35}$. This is not the case for Fe_3Pt, which orders in the $L1_2$ structure and exhibits a more pronounced Invar effect than in $Fe_{65}Ni_{35}$ Both alloys are iron rich with an fcc structure. Iron rich alloys in the Fe–Ni series which have a bcc structure do not exhibit Invar behaviour.

In recent years attempts have been made using ultrasonic [51], neutron scattering [88,98] and other techniques to elucidate the microscopic origin of the Invar effect, but as yet no clear understanding has been reached. Neverthe–less, in all models of the Invar effect it is recognised that the relationship between magnetic moment and the atomic volume or interatomic distance plays a crucial role, and hence the interactions between the vibrational and magnetic degrees of freedom are of great importance. One very sensitive way to study such interactions is through the polarisation dependence of the magneto–vibrational neutron scattering. The polarised neutron technique was first used by Steinsvoll et al [65] to study magneto–vibrational scattering in metallic iron and nickel. They were able to show that whereas for nickel the magnetic density giving rise to magneto–vibrational scattering was indistinguishable from that giving rise to elastic scattering, for iron there was a small but significant difference. We have now used this same technique to study magneto–vibrational scattering on Fe–Ni alloys, for which it is expected that the magnetic moment is strongly coupled to the atomic vibrations.

$Fe_{65}Ni_{35}$ alloy which shows the largest Invar anomaly among the iron and nickel alloy systems was chosen for the first experiment. At this composition the sample can be cooled down to 5K without the risk of a martensitic transformation from a fcc to a bcc structure.

In addition to the $Fe_{65}Ni_{35}$ alloy, two other samples, $Fe_{50}Ni_{50}$ and $Fe_{78}Ni_{22}$ have been studied. The relevant properties of the three samples are listed in table (9.1).

9.2 INELASTIC NEUTRON MEASUREMENTS

The experiments were carried out on a single crystal of $Fe_{65}Ni_{35}$ in the form of a cube 12 x 12 x 12mm with edges parallel to [1–10], [001] and [110]. The $Fe_{65}Ni_{35}$ crystal was held at 100K in a vertical field of 2T (sufficient to saturate the sample) provided by a pair of superconducting coils mounted on the IN20 polarised triple axis spectrometer at ILL reactor, Grenoble.

Measurements were made with K_f fixed at either 2·662 or 4·1 $\mathring{A}^{-1}$. Experimental details and uses of the instrument are presented in Chapter 4.

Dispersion curves for the major symmetry directions for which complete measurements were made are taken from Endoh (1979) [88] and Onodera, ..., etc (1981)[89] as shown in figure (9.1).

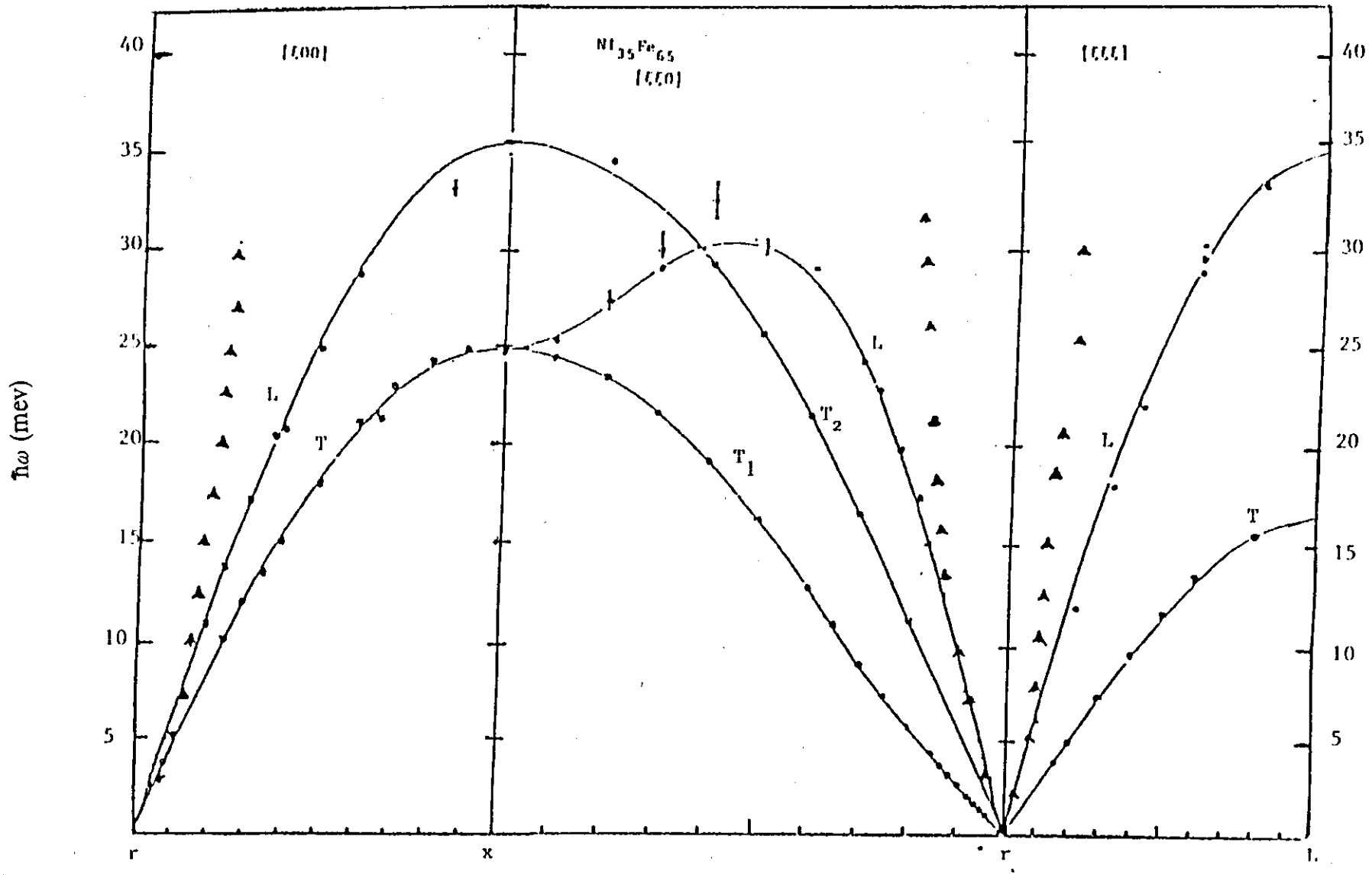

Figure (9.1) Dispersion curves for face centered cubic $Fe_{65}Ni_{35}$ alloy. The dots represent phonon and triangles represent magnon. The slopes of the straight lines through the origin represent the ultrasonic velocities of sound for the alloy.

Table (9.1) Properties of the fcc alloys at 296K

Properties	$Fe_{0.65}Ni_{35}$	$Fe_{50}Ni_{50}$	$Fe_{78}Ni_{22}$	Ref
Average atomic mass (amu)	56°90	57·28	56·31	–
Lattice constant (Å)	3·596	3·586	3·586	[103, 104]
Melting temperature (K)	1740	1710	1750	[105]
Saturation magnetic moment (μ_B/atom)	1·85	1·68	1·25	[31]
Curie temperatuure (K)	538	790	340	[104, 106]
Debye temperature (K)	346·63	407·8	315	[104, 106]
Elastic constants (10^{12}dyn/cm^2)				
c_{11}	1·432 ± 0·4	1·90	1·463	[107, 108]
c_{12}	1·000 ± 0·3	1·34	0·881	
c_{14}	0·994 ± 0·14	1·08	1·132	
Structure	fcc γ–phase	fcc γ–phase	bcc α–phase	[103, 104]

A series of constant energy scans were carried out. In each scan the scattered intensity was measured at each point with the flipper on, and then with it off, to obtain the polarisation dependence of the scattered intensity. The scattered intensity for both polarisation states measured in the scans was fitted to a sum of Gaussian peaks superposed on a linear background. The fits were constrained so that the centres and widths of the peaks for both polarisation states were the same, and the centres of peaks in scans at the same energy for $\tau + \underline{q}$ and $\tau - \underline{q}$ (where τ is a reciprocal lattice vector) were also at the same value of $\underline{q}$. When one of the peaks in a scan was identified with a magnon, it was constrained to have the same intensity for both polarisation states. This fitting for a series of constant energy scans at the three principle symmetry directions have been made.

The spin wave dispersion relation was calculated in all the symmetry directions for the $Fe_{65}Ni_{35}$ alloy, using a dispersion relation $E = D\,\underline{q}^2$ as shown by triangles in figure (9.1).

9.2.1 The [111] and [001] directions.

The polarisation dependence of the intensity of neutron scattering by the LA111 and LA100 magneto–acoustic excitations at 100K have been measured. A series of constant E scans which were made in these directions are shown in figures (9.2), (9.3), (9.4) and (9.5) for LA111 and LA100 respectively.

The ratio of the scattered peak intensities for the two polarisation states, after correction for incomplete polarisation of the beam, were used to calculate the ratio γ of magnetic to nuclear scattering in the phonon peaks. The results are given in tables (9.2) and (9.3) for both directions.

The centres of the fitted peaks in the [001] and [111] directions are shown at the dispersion curves as squares (phonon) and triangle (magnon) in figure (9.6). They show that LA111 branch is displayed in the positive Q direction and the LA001 branch in the negative one. Figure (9.6) also shows that the magnon mode crossing the LA[111] phonon mode at $\simeq$ 12 mev and the LA [100] and the LA[100] phonon mode at $\simeq$ 7 mev.

Table (9.2) LA 100 phonon

E mev	K_f Å^{-1}	q	Fm	R	Q_{100}	sinθ/λ
4	2·662	1·94 2·06	0·89 0·85	2·60 2·47	3·40 3·60	0·269 0·287
6	2·662	1·832 2·102	0·71 0·71	2·14 1	3·20 3·863	0·255 0·293
9	2·662	1·84 2·16	0·63 0·52	1·96 1·74	3·22 3·78	0·258 0·300
9	4·1	2·15 1·85	0·20 0·62	1·46 1·93	3·77 3·24	0·300 0·26
15	4·1	2·27 1·73	0·49 0·53	1·96 1·75	3·98 3·03	0·32 0·24

Table (9.3) LA 111phonon

E mev	K_f Å^{-1}	q	Fm	R	Q_{111}	sinθ/λ
4	2·662	0·97 1·03	1·18 1·04	3·57 3·05	2·94 3·12	0·23 0·25
9	2·662	0·92 1·08	0·49 0·56	1·83 1·73	2·79 3·28	0·22 0·26
15	4·1	0·876 1·124	0·38 0·64	1·50 1·98	2·65 3·40	0·21 0·27
20	4·1	0·82 1·18	0·65 0·66	2·00 2·02	2·49 3·58	0·20 0·28

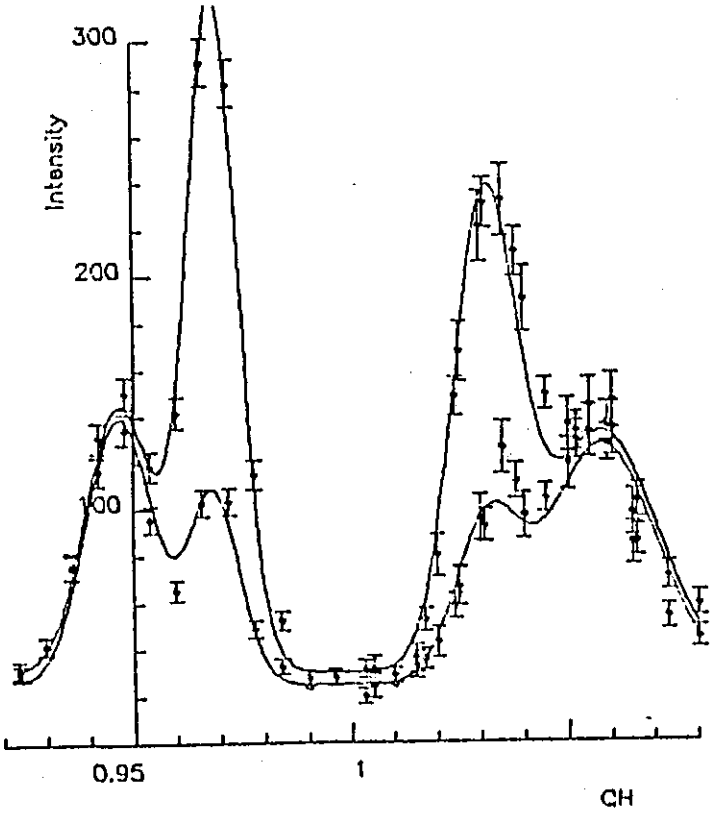

Peak No	Hgt Up	Hgt Down	Width	Centre
1	114(6)	114(6)	0.01102(70)	0.94704(47)
2	81(7)	289(14)	0.00821(37)	0.96863(26)
3	65(7)	193(11)	0.01055(52)	1.03137(26)
4	102(5)	102(5)	0.0174(12)	1.05296(47)

Scans		Background Level		Background Slope	
Up	Down	Up	Down	Up	Down
L1140F	L1140N	24(1)	29(2)	0(0)	0(0)

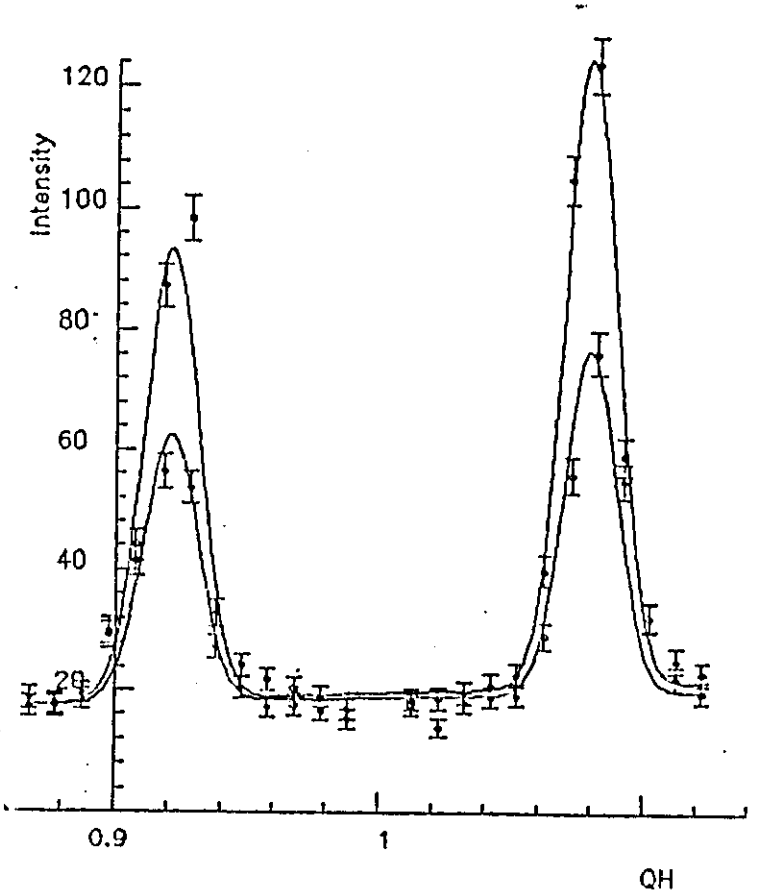

Peak No	Hgt Up	Hgt Down	Width	Centre
1	74(6)	44(4)	0.01447(94)	0.92080(44)
2	103(7)	57(5)	0.01396(81)	1.07920(44)

Scans		Background Level		Background Slope	
Up	Down	Up	Down	Up	Down
L1190N	L1190F	4(12)	9(12)	15(12)	9(12)

Figure (9.2) Constant energy scans in the LA111 direction

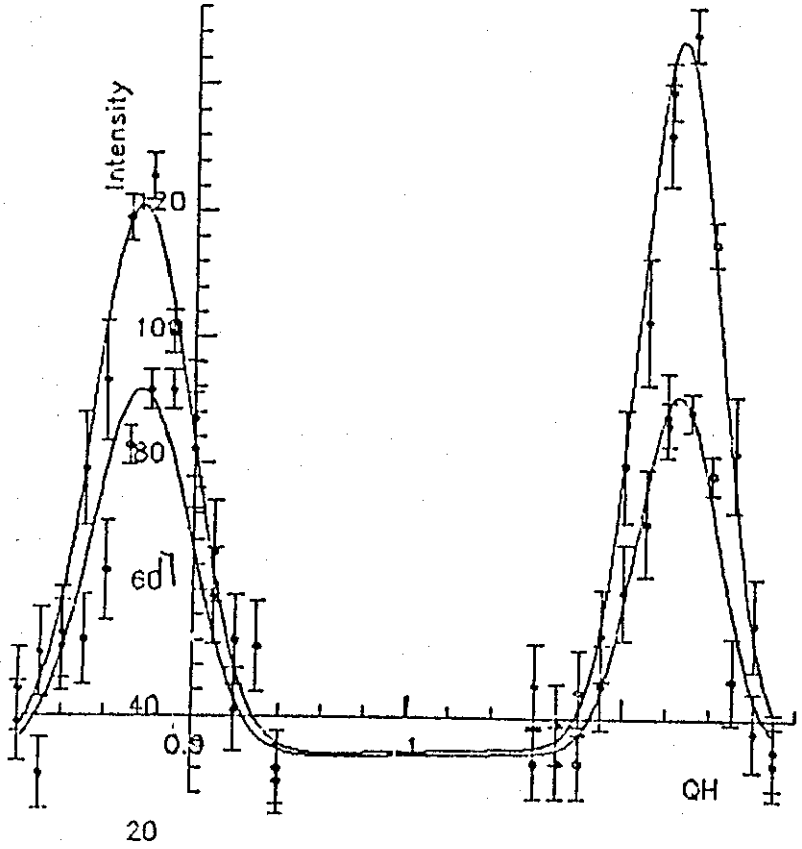

Peak No	Hgt Up	Hgt Down	Width	Centre
1	87(4)	58(3)	0.0325(23)	0.87563(71)
2	111(4)	56(4)	0.0259(17)	1.12437(71)

Scans		Background Level		Background Slope	
Up	Down	Up	Down	Up	Down
L4115N	L4115F	26(3)	28(2)	8(0)	5(0)

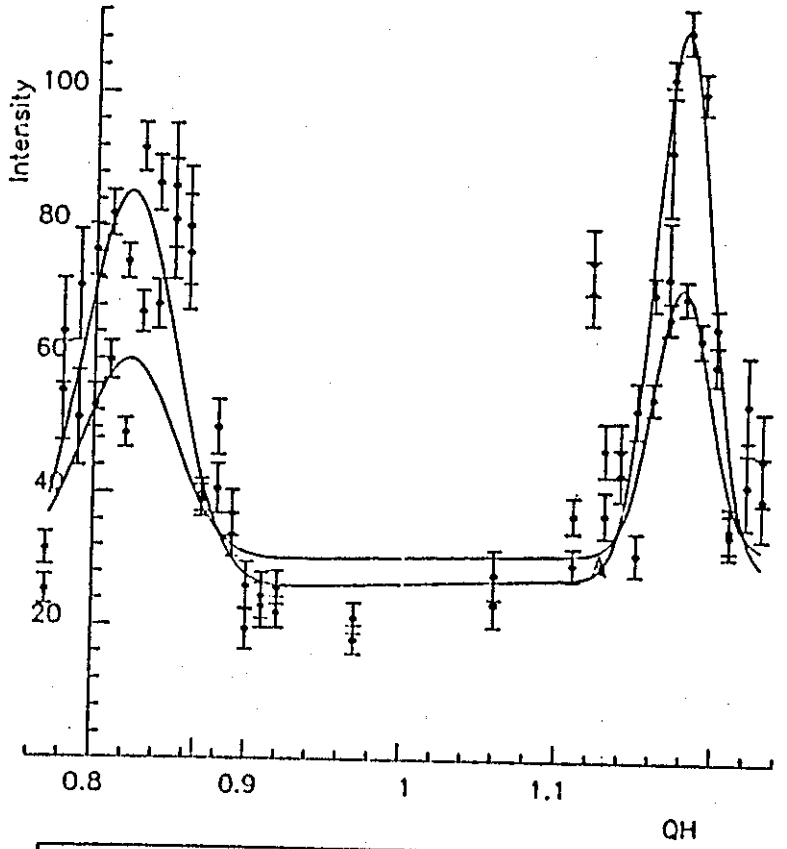

Peak No	Hgt Up	Hgt Down	Width	Centre
1	60(5)	30(5)	0.0422(49)	0.8221(12)
2	81(6)	40(5)	0.0253(24)	1.1779(12)

Scans		Background Level		Background Slope	
Up	Down	Up	Down	Up	Down
L4120N	L4120F	18(3)	25(2)	8(0)	5(0)

Figure (9.3) Constant energy scans in the LA111 direction

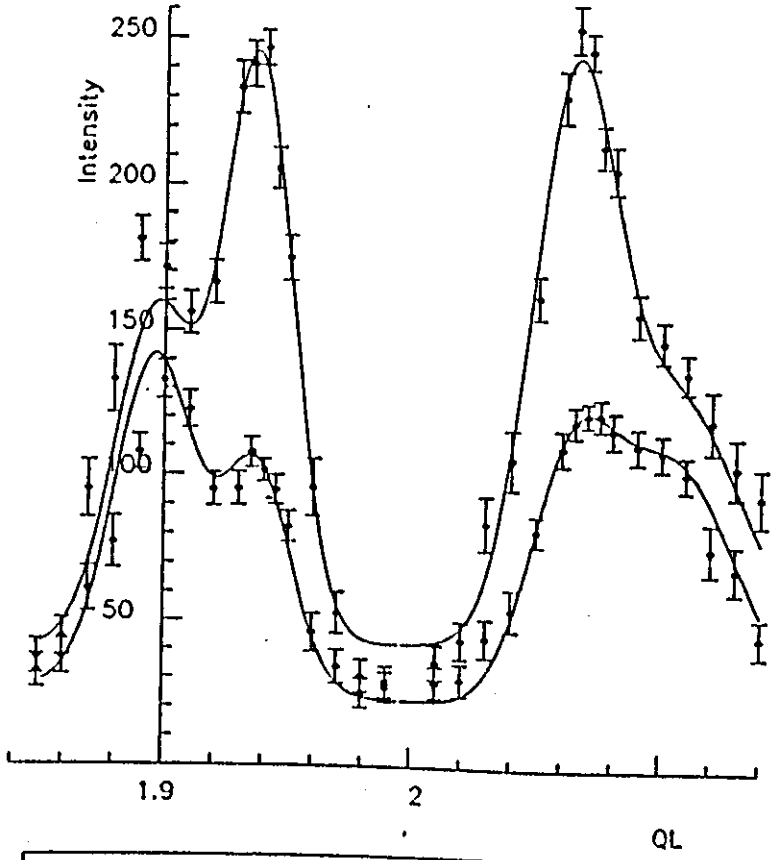

Peak No	Hgt Up	Hgt Down	Width	Centre
1	115(6)	115(6)	0.0224(19)	1.8960(14)
2	200(7)	77(5)	0.0201(12)	1.93707(74)
3	173(12)	70(10)	0.0230(14)	2.06293(74)
4	87(7)	87(7)	-0.0380(59)	2.1040(14)

Scans		Background Level		Background Slope	
Up	Down	Up	Down	Up	Down
L2204N	L2204F	15(94)	80(94)	13(48)	-28(47)

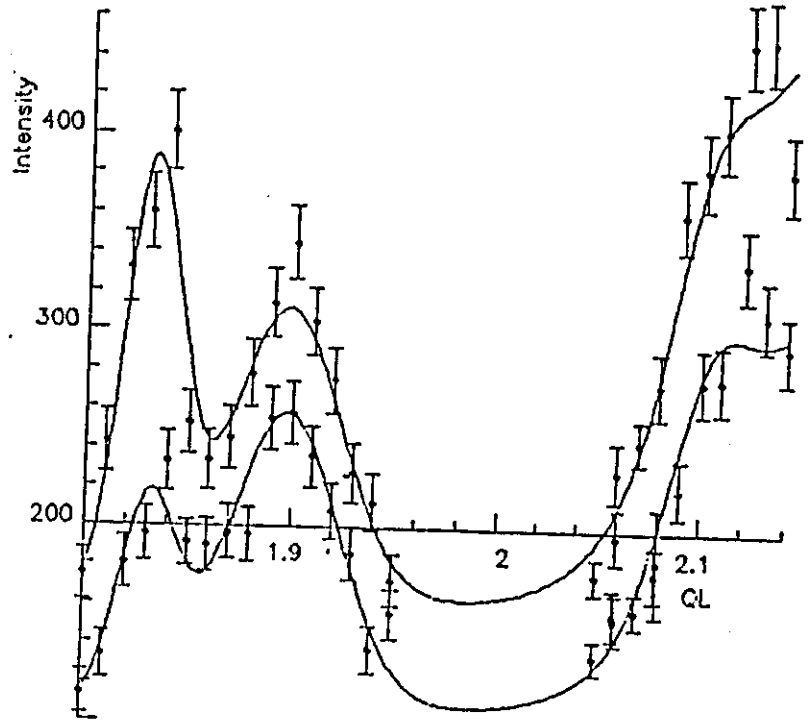

Peak No	Hgt Up	Hgt Down	Width	Centre
1	220(20)	103(15)	0.0198(20)	1.8317(14)
2	150(14)	150(14)	0.0376(39)	1.8976(18)
3	75(23)	75(23)	0.0259(76)	2.1024(18)
4	304(30)	205(32)	0.078(10)	2.1683(14)

Scans		Background Level		Background Slope	
Up	Down	Up	Down	Up	Down
L2206N	L2206F	161(14)	107(11)	0(0)	0(0)

Figure (9.4) Constant energy scans in the LA100 direction

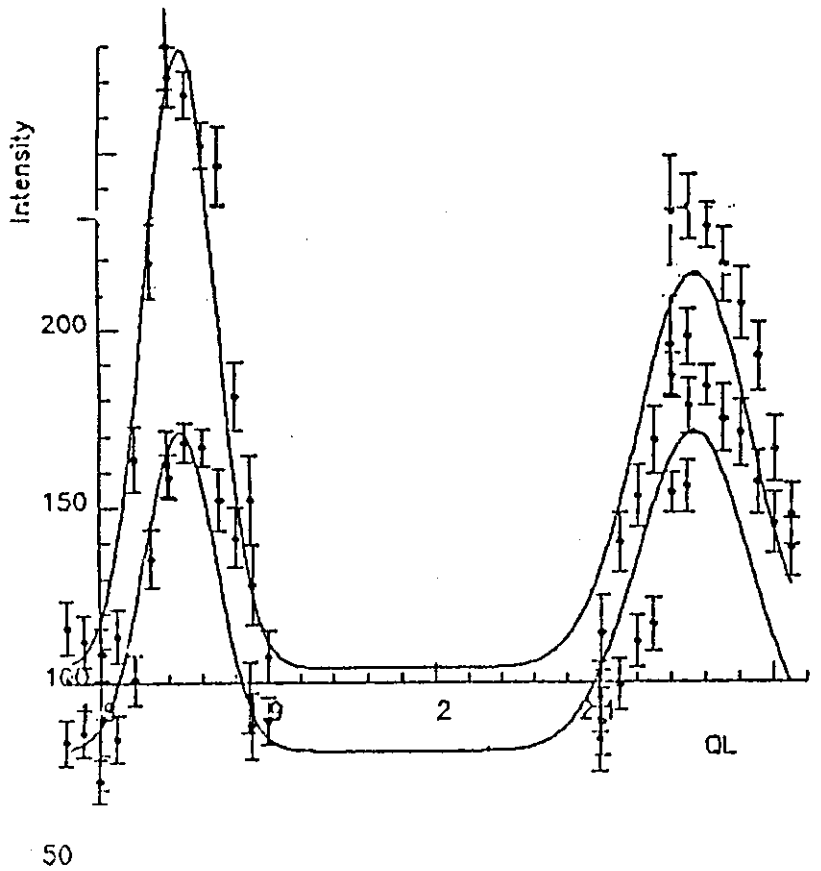

Peak No	Hgt Up	Hgt Down	Width	Centre
1	111(13)	90(10)	0.0461(54)	2.1529(13)
2	174(14)	90(11)	0.0295(33)	1.8471(13)

Scans		Background Level		Background Slope	
Up	Down	Up	Down	Up	Down
L4209N	L4209F	104(10)	80(7)	0(0)	0(0)

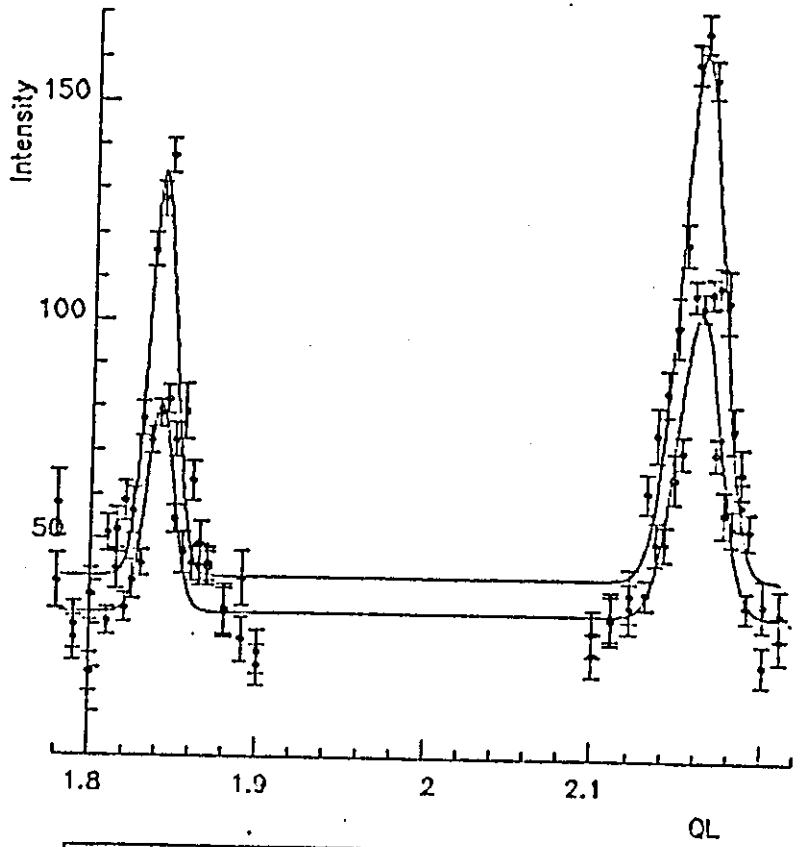

Peak No	Hgt Up	Hgt Down	Width	Centre
1	92(6)	47(4)	0.01150(93)	1.84077(42)
2	120(5)	69(4)	0.0179(10)	2.15923(42)

Scans		Background Level		Background Slope	
Up	Down	Up	Down	Up	Down
L2209N	L2209F	41(2)	33(2)	0(0)	0(0)

Figure (9.5) Constant energy scans in the LA100 direction

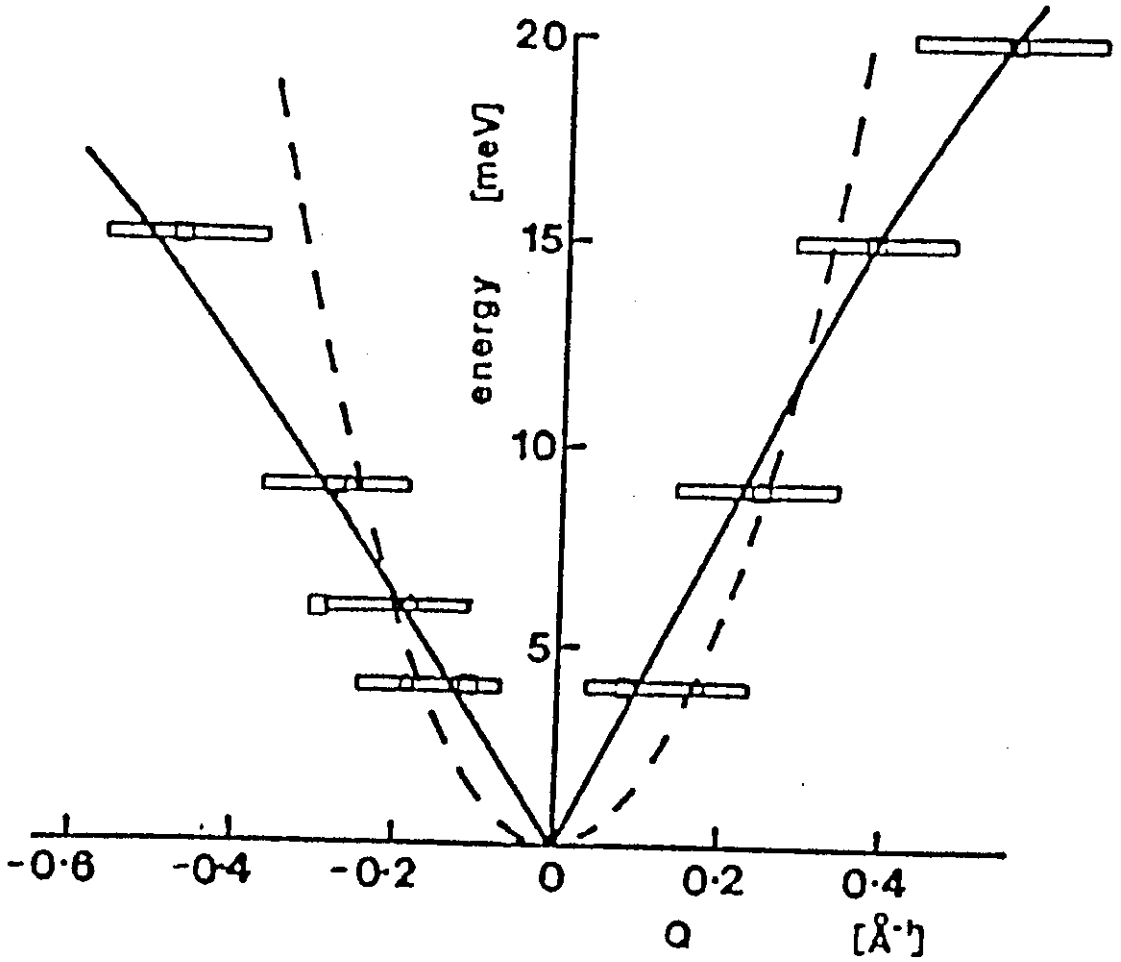

Figure (9.6) Dispersion curves for the magnon (dashed curve) and LA111 and LA001 phons (full curves) in $Fe_{65}Ni_{35}$. The squares and triangles within the oblongs show the positions determined for the phonon and magnon peaks respectively

These results indicate a deviation in the form of the dispersion curves from their ideal forms around the magnon phonon crossover, which may indicate anti–crossing behaviour due to interaction between them.

Measurements were also made for the LA001 phonon and TA110 phonon in the 002 zone using a series of constants energy scans as shown in figures (9.7), (9.8) and (9.9) for the LA001 and TA110 modes respectively. The main energy scans for both directions are listed in tables (9.4) and (9.5).

9.2.2 The [100] direction

A series of constant energy scans were made along the [100] direction first with $[1\bar{1}1]$ and then with [001] perpendicular to the plane of scattering. In both geometries only phonon scattering from the LA100 branch should be observed, since the polarisation of the degenerate transverse modes are perpendicular to the scattering vector ($\underline{\varepsilon}\cdot\underline{\kappa}=0$) and therefore the cross–section for these modes is 0.

However, three excitations were observed which disperse as shown in figure (9.10) The curves represented by circles and triangles can be identified with the LA100 phonon and the magnon respectively. The observed dispersion of these modes is in good agreement with that published previously [107]. The third excitation (represented by crosses) has the same dispersion as the TA100 phonon which should not be visible in the scattering geometry used.

The polarisation dependence of the intensity scattered by all three excitations was measured. As expected, the magnon intensity had no polarisation dependence. The polarisation dependence in terms of an effective normalised moment μ_N defined as the fraction of the mean atomic moment which should be needed to give the observed polarisation dependence for magneto–acoustic scattering. Because of overlap with the magnon only three reliable measurements are available for the LA100 phonon as shown in figures (9.11) and (9.12). At 15 and 18 mev the whole moment effectively contributes, but at 20 mev there is evidence for a

Table (9.4) LA 100 at 100K for Mode 1 and Mode 2

E mev	K_f Å^{-1}	q	sinθ/λ	μ_N	F_M
3	2·662	1·954	0·274	0·79	0·81
	//	1·913	0·269	0·43	0·43
7	//	1·878	0·263	0·60	0·64
		1·816	0·255	0·54	0·59
8	//	1·862	0·262	0·44	0·47
		1·786	0·251	0·53	0·59
10	//	1·806	0·254	0·59	0·65
		1·717	0·241	0·50	0·57
15	//	1·719	0·242	0·95	1·09
		1·596	0·224	0·50	0·61
18	//	1·653	0·232	0·99	1·17
		1·489	0·209	0·19	0·24
20	//	1·614	0·227	0·83	1·00
		1·407	0·198	0·16	0·21

Table (9.5) TA 110 phonon off 200

E mev	K_f Å^{-1}	q	sinθ/λ	F_M	μ_N
5	2·662	0·0834	0·282	0·68	0·76
7·5	//	0·1297	0·282	0·29	0·32
10	//	0·1797	0·283	0·94	1·04

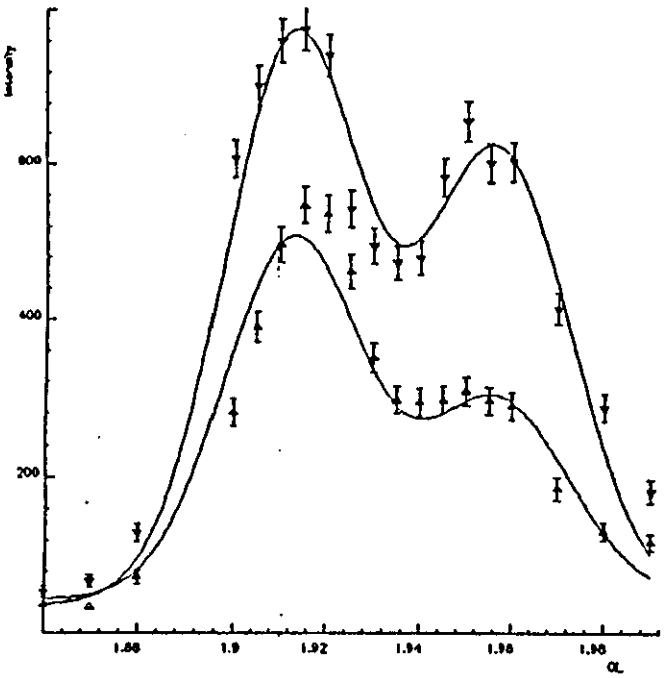

Peak No	Hgt Up	Hgt Down	Width	Centre
1	253(20)	578(31)	0.0227(21)	1.9564(15)
2	457(24)	724(32)	0.0207(15)	1.9126(10)

Scans		Background Level		Background Slope	
Up	Down	Up	Down	Up	Down
L2203N	L2203F	32(8)	25(8)	6(0)	6(0)

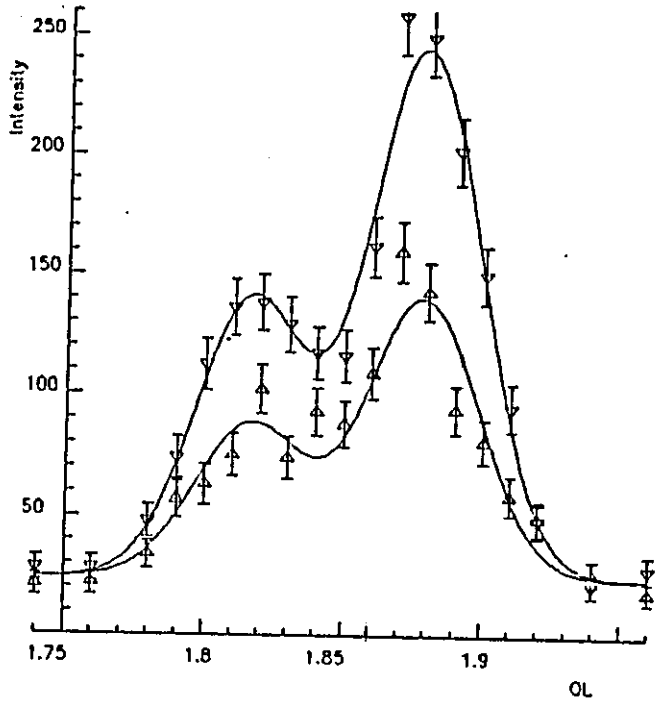

Peak No	Hgt Up	Hgt Down	Width	Centre
1	63(6)	115(8)	0.0282(28)	1.8161(21)
2	115(7)	220(10)	0.0284(16)	1.8781(12)

Scans		Background Level		Background Slope	
Up	Down	Up	Down	Up	Down
L2207N	L2207F	24(2)	24(2)	0(0)	0(0)

Figure (9.7) Constant energy scans for LA001 in the 002 zone

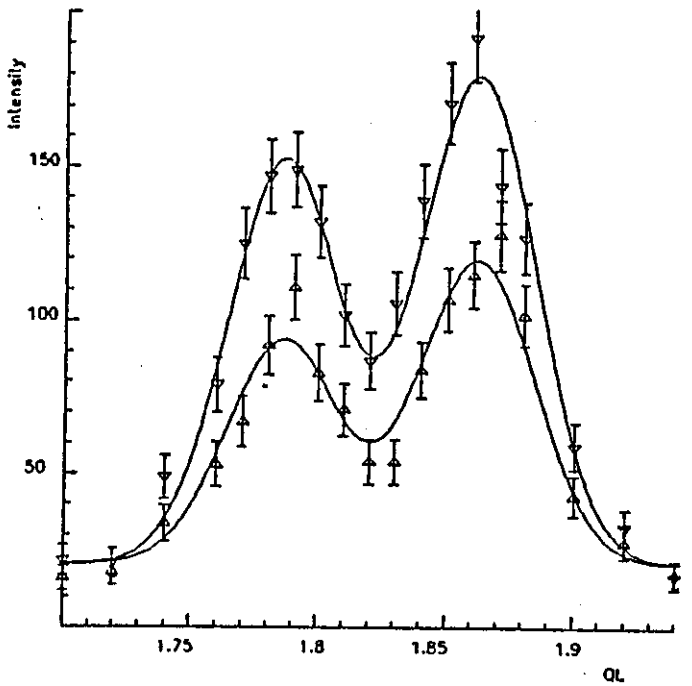

Peak No	Hgt Up	Hgt Down	Width	Centre
1	98(6)	158(7)	0.0320(17)	1.8616(12)
2	72(5)	131(7)	0.0308(21)	1.7859(13)

Scans		Background Level		Background Slope	
Up	Down	Up	Down	Up	Down
L2208N	L2208F	20(2)	20(2)	0(0)	0(0)

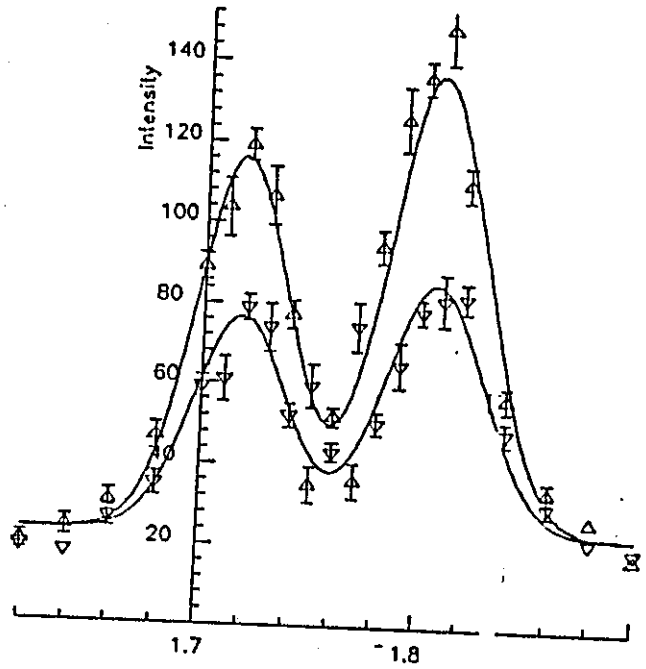

Peak No	Hgt Up	Hgt Down	Width	Centre
1	113(7)	61(5)	0.0326(19)	1.8062(13)
2	92(6)	53(5)	~0.0298(22)	1.7173(14)

Scans		Background Level		Background Slope	
Up	Down	Up	Down	Up	Down
L10N.F	L10F.F	23(1)	23(1)	0(0)	0(0)

Figure (9.8) Constant energy scans for LA001 in the 002 zone

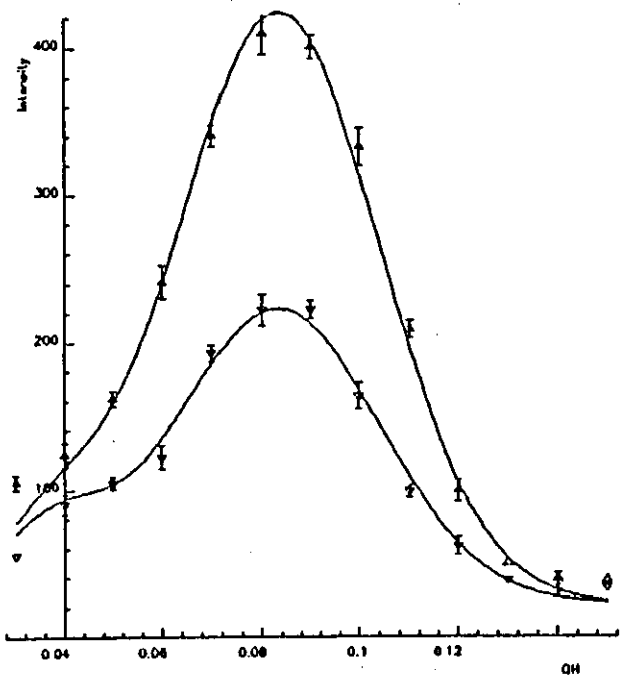

Peak No	Hgt Up	Hgt Down	Width	Centre
1	403(11)	201(7)	0.02919(74)	0.08337(61)
2	51(3)	51(0)	0.0162(13)	0.0373(23)

Scans		Background Level		Background Slope	
Up	Down	Up	Down	Up	Down
L2605N	L2605F	22(1)	22(1)	0(0)	0(0)

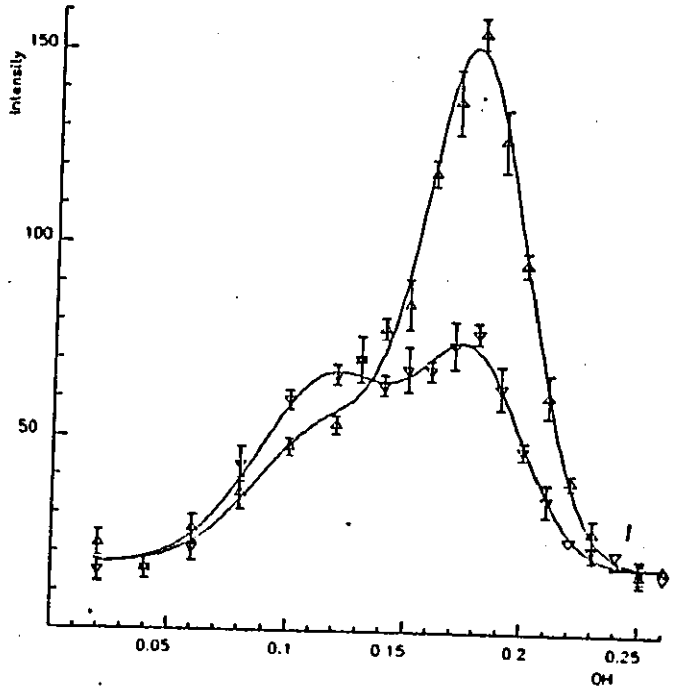

Peak No	Hgt Up	Hgt Down	Width	Centre
1	130(2)	50(1)	0.03085(68)	0.17836(60)
2	36(1)	49(1)	0.0428(15)	0.1175(17)

Scans		Background Level		Background Slope	
Up	Down	Up	Down	Up	Down
L2610N	L2610F	16.75(56)	16.75(56)	0(0)	0(0)

Figure (9.9) Constant energy scans for LA001 in the 002 zone

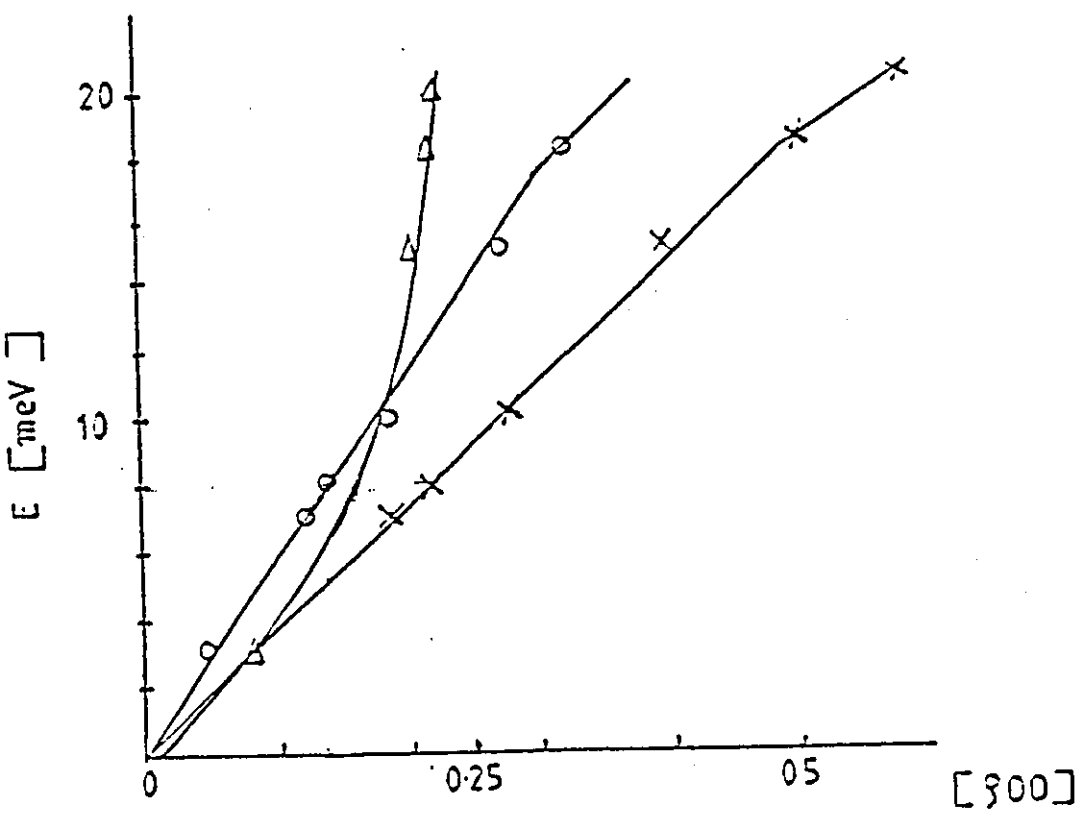

Figure (9.10) The observed dispersion in the 100 direction indicating the expected magnon (Δ) and LA100 (0) modes and "forbidden" transverse acoustic mode TA 001 (x)

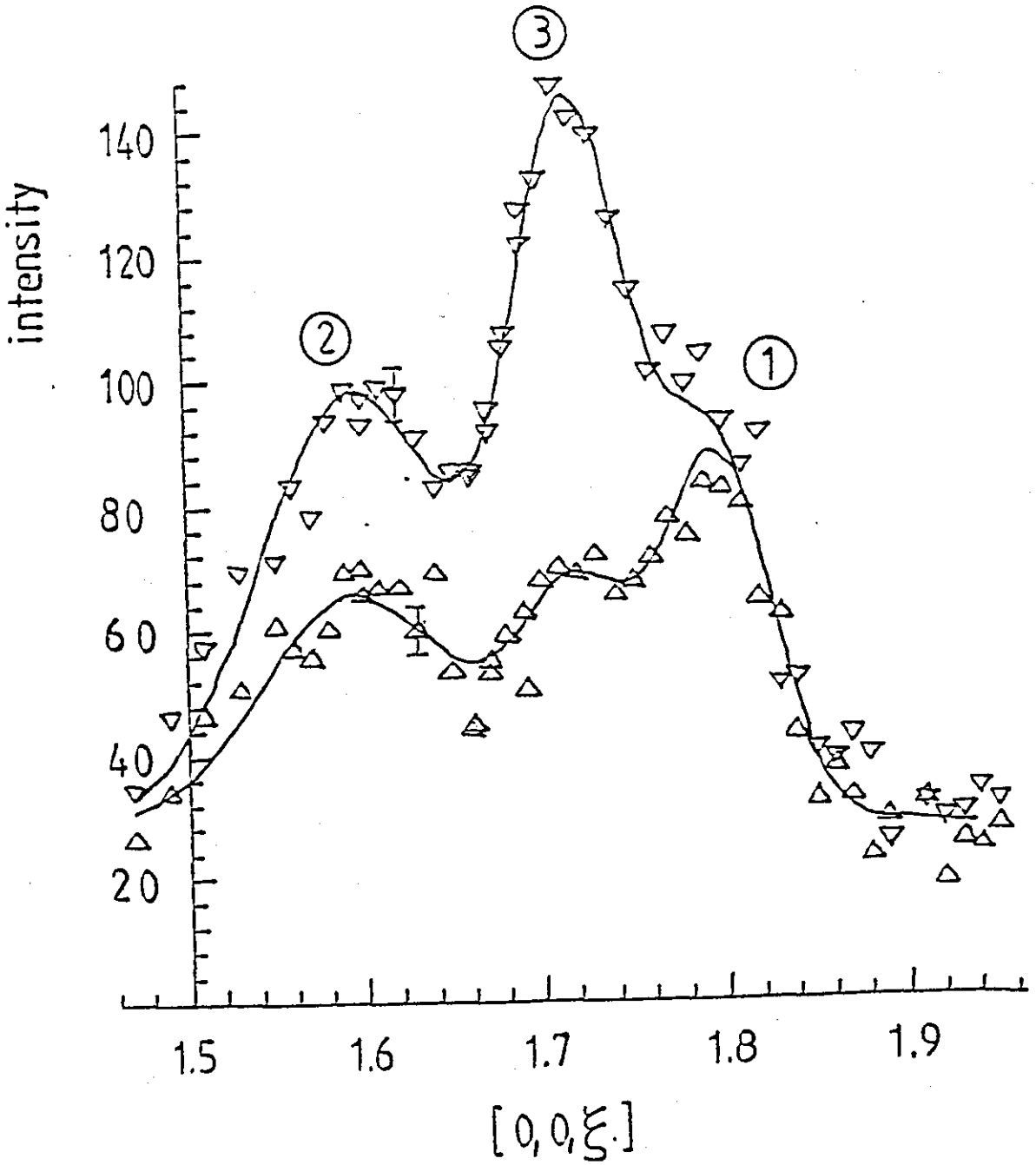

Peak No	Hgt Up	Hgt Down	Width	Centre
1	57(1)	57(1)	0.0411(16)	1.7973(17)
2	37(1)	69(1)	0.0779(20)	1.5962(24)
3	35(1)	110(2)	0.0465(12)	1.7189(13)

Scans		Background Level		Background Slope	
Up	Down	Up	Down	Up	Down
L4115N	L4115F	28.28(58)	28.28(58)	0(0)	0(0)

Figure (9.11) A constant energy scan E = 15 mev carried out along the 001 direction indicating the 3 peak structure referred to in the text. The peak identified by 1 represents the magnon and therefore does not have a flipping ratio assocated with it. Peak 3 is the LA phonon expected for the scattering geometry used in the scan. Peak 2 represents the "forbidden" TA mode

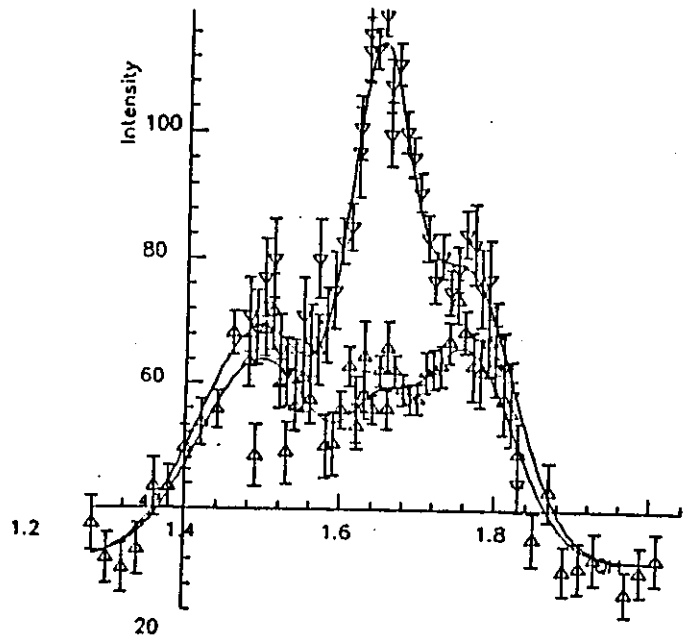

Peak No	Hgt Up	Hgt Down	Width	Centre
1	14.92(19)	67(1)	0.0544(13)	1.6458(17)
2	33(1)	45(1)	0.0899(20)	1.7591(31)
3	32(1)	37(1)	0.1115(22)	1.4959(51)

Scans		Background Level		Background Slope	
Up	Down	Up	Down	Up	Down
L4218N	L4218F	31.90(61)	31.90(61)	0(0)	0(0)

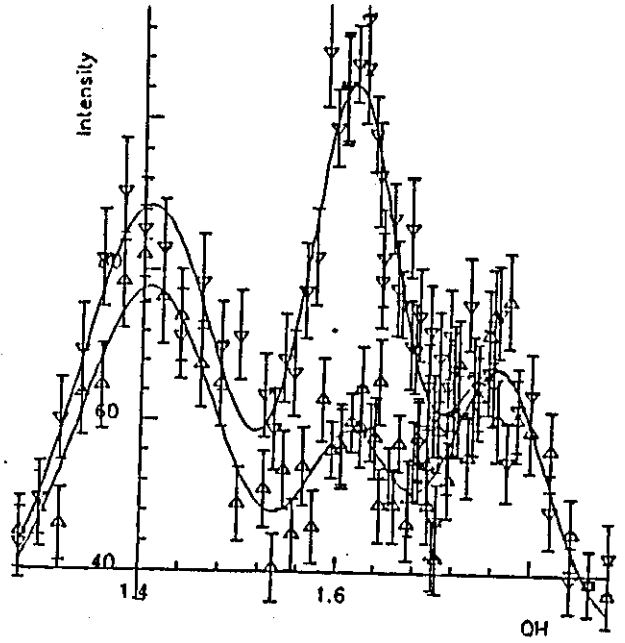

Peak No	Hgt Up	Hgt Down	Width	Centre
120	34(1)	34(1)	0.0704(23)	1.7641(32)
2	25.36(76)	71(1)	0.0681(22)	1.6142(20)
3	45(1)	56(1)	0.1003(31)	1.4073(35)

Scans		Background Level		Background Slope	
Up	Down	Up	Down	Up	Down
L4120N	L4120F	32.51(55)	32.51(55)	0(0)	0(0)

Figure (9.12) Constant energy scans in the LA100 direction

significant reduction. The "forbidden" TA100 mode (9.11) differs in that at low energy transfers, only about one half the moment is observed in the scattering; this again falls off above 15 mev. The presence of the "forbidden" magnon mode could be explained by a strong coupling of the magnetic and lattice degrees of freedom. In table (9.4) a list of the main energy scans is presented.

9.2.3 The [110] direction

The TA_2 110 mode, that with polarisation parallel to $[1\bar{1}0]$, has been shown [107] to exhibit significant softening at the Invar composition. We have investigated the polarisation dependence of neutron scattering by this mode and also of the LA110 mode. A (001) crystal orientation was used and the modes were measured from the (220) Bragg position. The energy constant scans are shown in figure (9.13).

The longitudinal mode can only be measured uncontaminated by the magnon at energies above 15 mev and the value of μ_N at 18 and 20 mev are not significantly different from unity as indicated in table (9.6). Because of its softening the TA_2 110 mode is well separated from the magnon at energies above 3 mev but no significant deviation of μ_N from unity was observed up to 15 mev as given in table (9.7) and shown in figure (9.14).

9.2.4 Temperature Dependence

Measurements at 5K were made following the observation of Shiga [109] of anomalous changes in the elastic constants below 5K. Several constant energy scans were made in the [100] direction off 200 at 10, 15, 18 and 20 mev, and in the [110] direction from 220 at 5, 10 and 15 mev as shown in figures (9.15), (9.16) and (9.17) for [100] and [110] directions respectively. The results are given in tables (9.8) and (9.9).

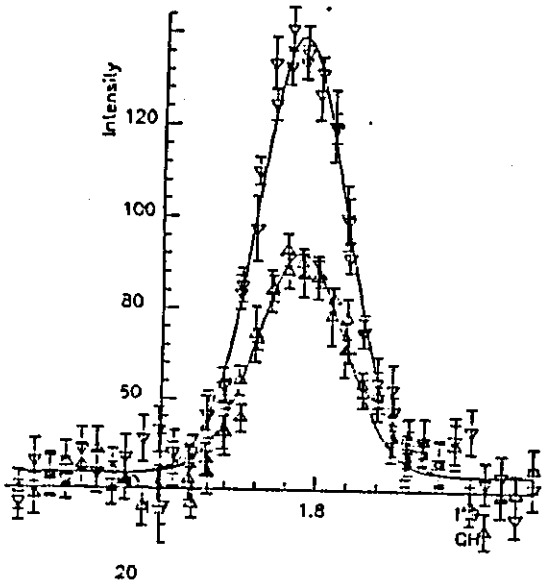

Peak No	Hgt Up	Hgt Down	Width	Centre
1	48(1)	85.93(91)	0.0412(165)	1.76824(51)

Scans		Background Level		Background Slope	
Up	Down	Up	Down	Up	Down
L4118N	L4116F	43.36(65)	43.36(65)	0(0)	0(0)

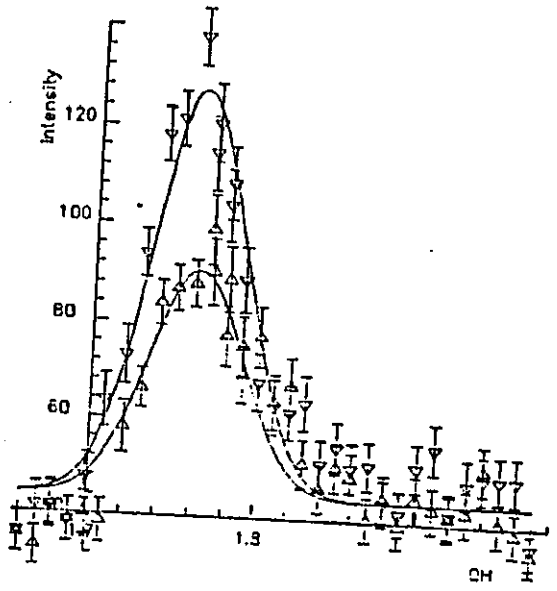

Peak No	Hgt Up	Hgt Down	Width	Centre
1	46(1)	82(3)	0.0404(23)	1.7615(14)

Scans		Background Level		Background Slope	
Up	Down	Up	Down	Up	Down
L4120N	L4120F	44.03(99)	44.03(99)	0(0)	0(0)

Figure (9.13) Constant energy scans of the LA110 mode from the 220 Bragg reflection

Table (9.6) L 110 off 200

E mev	q	$\sin\theta/\lambda$	F_M	μ_N	R	γ
18	1·788	0·355	0·65	1·03	1·939	0·179
20	1·762	0·350	0·57	0·89	1·78	0·157

Table (9.7) TA2 100 mode

E mev	q	F_M	$\sin\theta/\lambda$	μ_N
5	1·816	0·52	0·399	1·02
10	1·661	0·50	0·403	0·98
25	1·523	0·47	0·409	0·90

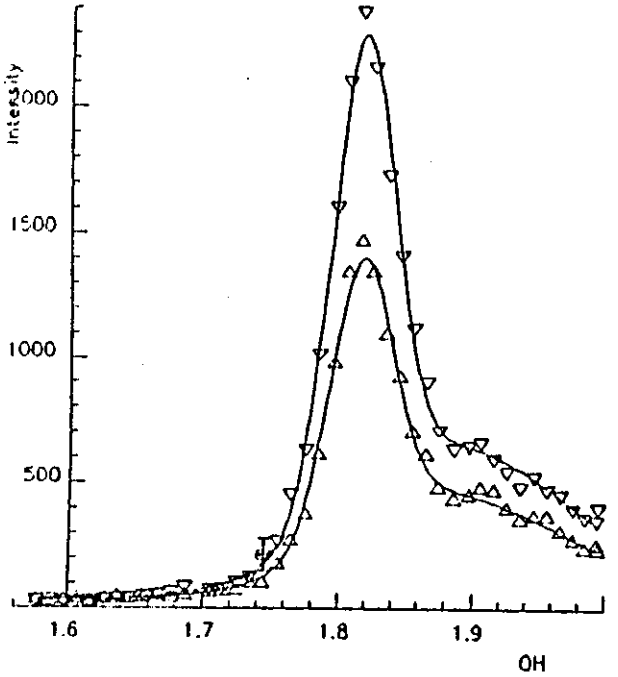

Peak No	Hgt Up	Hgt Down	Width	Centre
1	1106(28)	1878(34)	0.03356(66)	1.81568(57)
2	365(13)	551(17)	0.1252(27)	1.8982(24)
3	69(3)	71(2)	0.05300(95)	1.870(16)

Scans		Background Level		Background Slope	
Up	Down	Up	Down	Up	Down
T4105N	T4105F	32(1)	32(1)	0(0)	0(0)

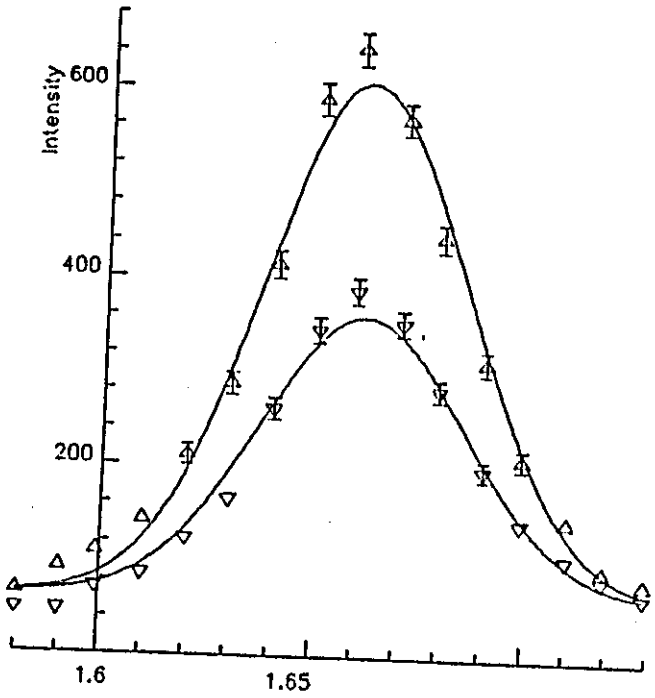

Peak No	Hgt Up	Hgt Down	Width	Centre
1	543(13)	296(12)	0.03425(87)	1.66087(71)

Scans		Background Level		Background Slope	
Up	Down	Up	Down	Up	Down
T4110N	T4110F	62(3)	62(3)	0(0)	0(0)

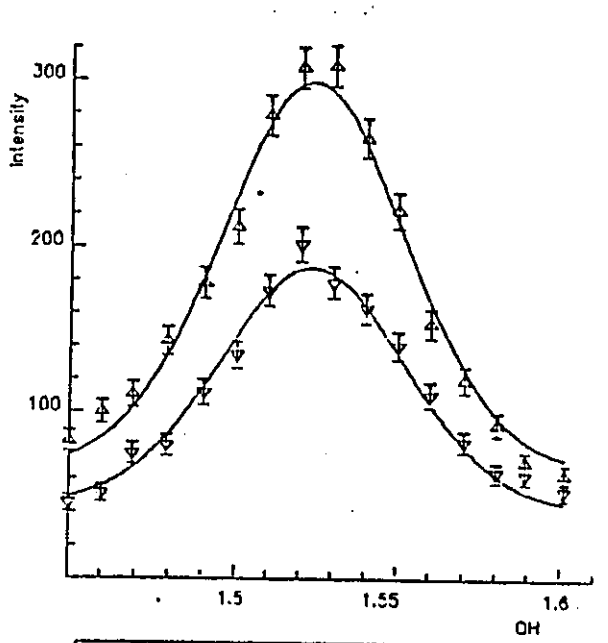

Peak No	Hgt Up	Hgt Down	Width	Centre
1	232(10)	143(6)	0.0398(11)	1.52324(76)

Scans		Background Level		Background Slope	
Up	Down	Up	Down	Up	Down
T4115N	T4115F	54(1)	53(1)	7.67(73)	−6.42(66)

Figure (9.14) Constant energy scans of the TA_2 110 mode

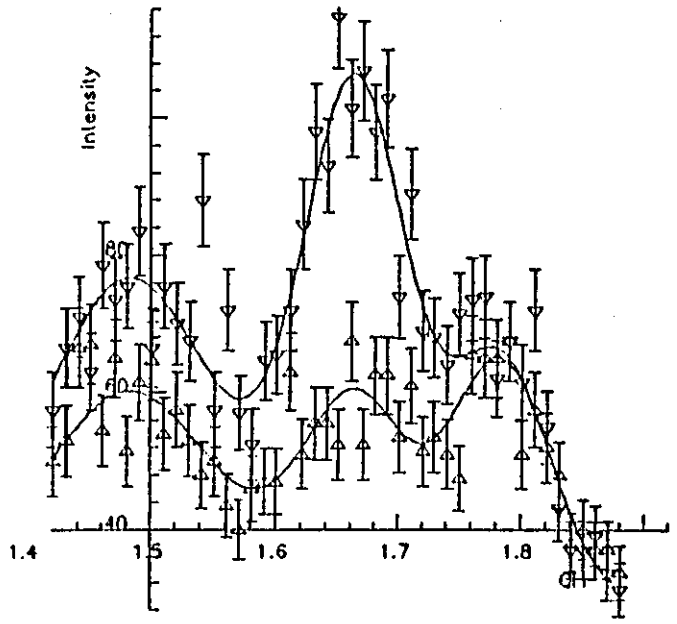

20

Peak No	Hgt Up	Hgt Down	Width	Centre
1	29(1)	75(2)	0.0624(20)	1.6642(24)
2	35(1)	35(0)	0.0571(21)	1.7841(31)
3	30(1)	47(1)	0.0999(33)	1.4626(45)

Scans		Background Level		Background Slope	
Up	Down	Up	Down	Up	Down
L4318N	L4318F	29.25(58)	29.25(58)	0(0)	0(0)

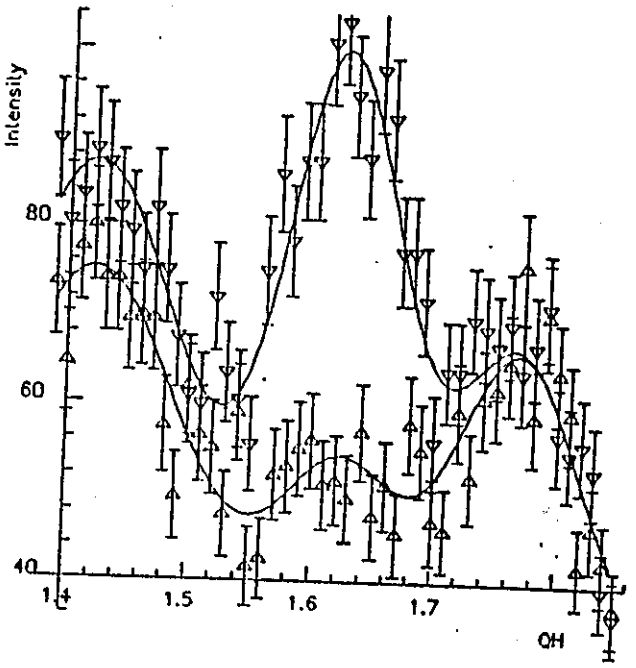

20

Peak No	Hgt Up	Hgt Down	Width	Centre
1	32.65(94)	32.65(94)	0(0)	1.7876(29)
2	19.95(81)	65(1)	0(0)	1.6226(21)
3	42(1)	54(1)	0(0)	1.4203(41)

Scans		Background Level		Background Slope	
Up	Down	Up	Down	Up	Down
L4320N	L4320F	33.18(63)	33.18(63)	0(0)	0(0)

Figure (9.15) Constant energy scans at 5K in the 100 direction off 200

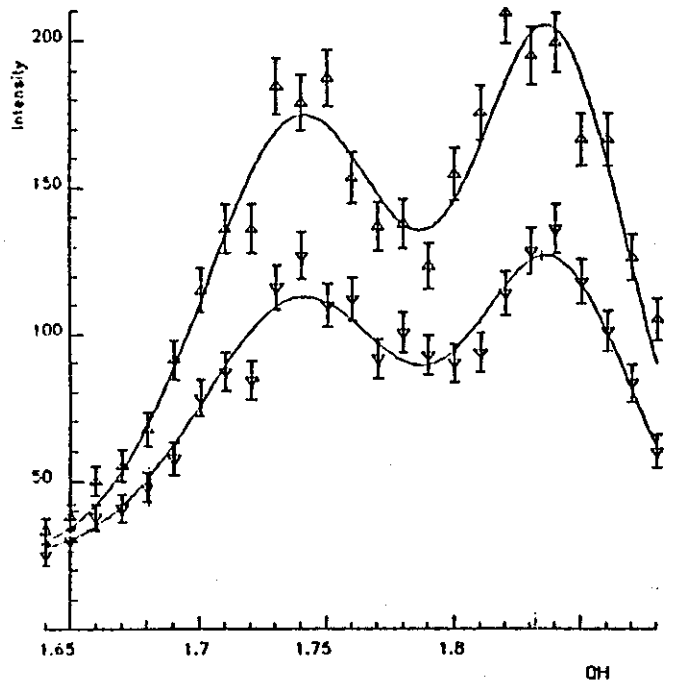

Peak No	Hgt Up	Hgt Down	Width	Centre
1	174(4)	98(2)	0.0421(10)	1.8381(13)
2	149(4)	87(2)	0.0544(13)	1.7401(13)

Scans		Background Level		Background Slope	
Up	Down	Up	Down	Up	Down
L4310F	L4310N	25(0)	25(0)	0(0)	0(0)

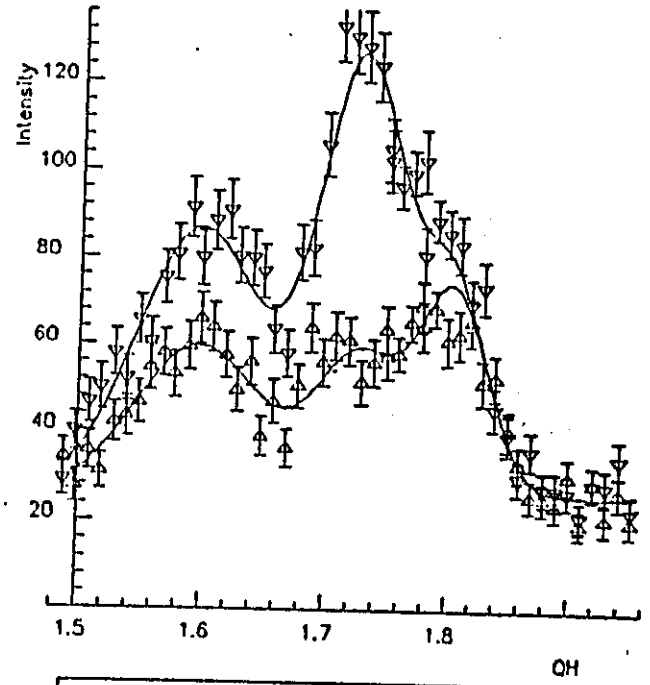

Peak No	Hgt Up	Hgt Down	Width	Centre
1	45(1)	45(1)	0.0399(14)	1.8048(20)
2	33(1)	60(1)	0.0711(21)	1.5961(28)
3	31(1)	97(2)	0.0491(12)	1.7270(18)

Scans		Background Level		Background Slope	
Up	Down	Up	Down	Up	Down
L4315N	L4315F	25.99(75)	25.99(75)	0(0)	0(0)

Figure (9.16) Constant energy scans at 5K in the 100 direction off 200

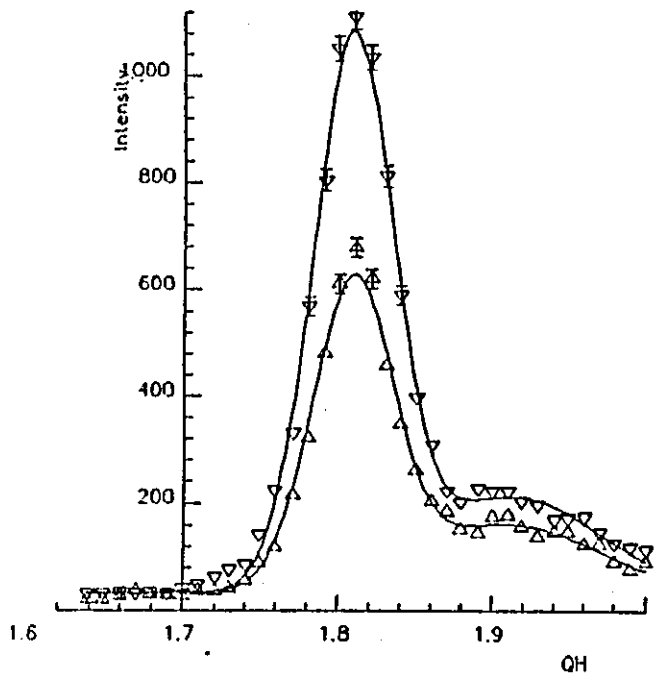

Peak No	Hgt Up	Hgt Down	Width	Centre
1	565(16)	1013(22)	0.03642(69)	1.80813(61)
2	109(4)	157(5)	0.0775(39)	1.9226(37)
3	37(1)	42(1)	0.06264(93)	1.862(14)

Scans		Background Level		Background Slope	
Up	Down	Up	Down	Up	Down
T4305N	T4305F	34(1)	34(1)	0(0)	0(0)

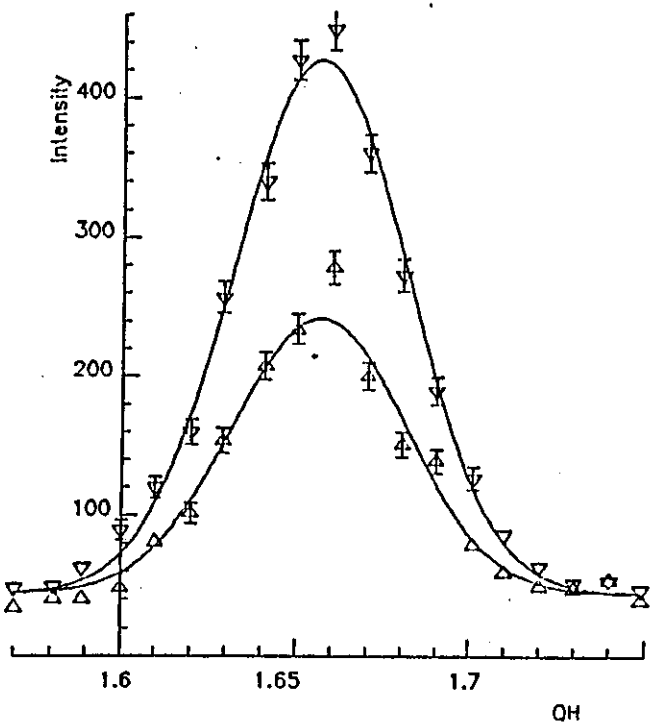

Peak No	Hgt Up	Hgt Down	Width	Centre
1	197(7)	382(10)	0.03489(70)	1.65638(59)

Scans		Background Level		Background Slope	
Up	Down	Up	Down	Up	Down
T4310N	T4310F	44(1)	44(1)	0(0)	0(0)

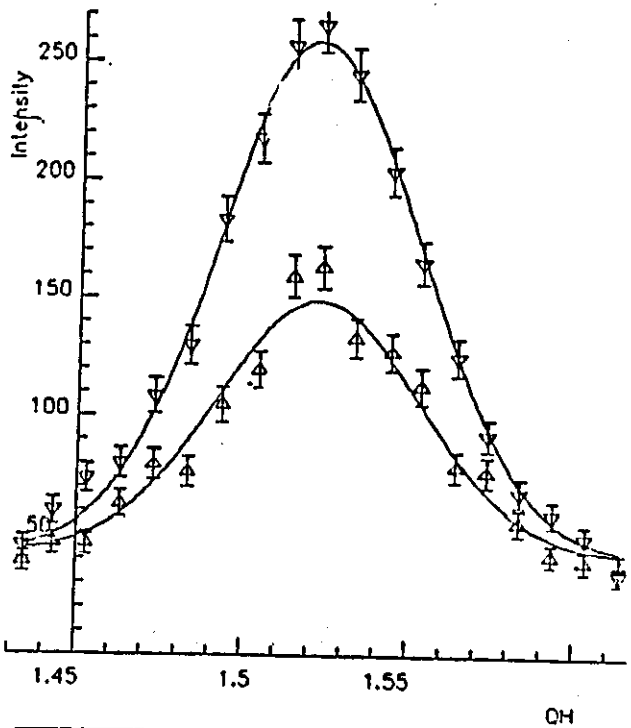

Peak No	Hgt Up	Hgt Down	Width	Centre
1	107(3)	217(4)	0.04320(76)	1.52168(71)

Scans		Background Level		Background Slope	
Up	Down	Up	Down	Up	Down
T4315N	T4315F	41(1)	41(1)	0(0)	0(0)

Figure (9.17) Constant energy scans at 5K in the 110 direction off 200

Table (9.8) L 100 at 5K

E mev	q	Fm	K_f Å^{-1}
10	1·838 1·7401	0·56 0·53	4·1
15	1·805 1·727 1·596	0 1·12 0·59	4·1
18	1·784 1·664 1·483	0 0·93 0·44	4·1
20	1·768 1·623 1·420	0 1·16 0·25	4·1

Table (9.9) T 110 at 5K

E mev	K_f Å^{-1}	q	Fm
5	4·1	1·808	0·57
10	4·1	1·656	0·65
15	4·1	1·522	0·69

9.2.5 Polarisation Dependence

Measurements of the polarisation dependence of the scattered indensity have been made for two other Fe–Ni alloys at 100K. One Invar sample with concentration below % 35Ni, $Fe_{78}Ni_{22}$ and a second non–Invar compound with 50% Ni, $Fe_{50}Ni_{50}$ were chosen. The measurements are repeated under the same conditions as for $Fe_{65}Ni_{35}$, and several constant energy scans were made in the [100] direction. The main energy scans for these alloys are shown in figures (9.18), (9.19) and (9.20) for $Fe_{50}Ni_{50}$ and $Fe_{78}Ni_{22}$ respectively. The results are summarised in tables (9.10) and (9.11).

9.3 SPECIFIC HEAT MEASUREMENTS

The specific heat Cp(T) for two $Fe_{1-x}Ni_x$ alloys (x = 35, 50) have been measured using the Differential Scanning Calorimeter (DSC) from 300 to ≃ 870K. The experimental results are shown in figures (9.21) and(9.22) for $Fe_{65}Ni_{35}$ and $Fe_{50}Ni_{50}$ respectively. The figures reveal a broad bumb in Cp(T) occuring in both alloys. Similar effects have been seen by W Benwick (1978) [90] in other Invar alloys such as $Fe_{50}(Ni_xMn_{1-x})50$. Table (9.12) summarises the thermal properties in both alloys.

9.4 ELASTIC CONSTANTS DETERMINATION

The cubic elastic constants C_{11}, C_{44}, C_{12} and $C_{11} - C_{12}/2$ were determined from the dispersion curves in the major symmetry directions using a calculated molecular weight M and the lattice parameter observed in this experiment. The lattice parameters a and the density ρ, calculated using a at room temperature are displayed in figure (9.23). It is noted that the lattice constant decrease linearly with the decrease of Ni concentration. A minimum value of the lattice constant occurs at ≃ 40%Ni. A minimum value of the lattice constant occurs at 40%Ni. It has already been mentioned that the spontaneous

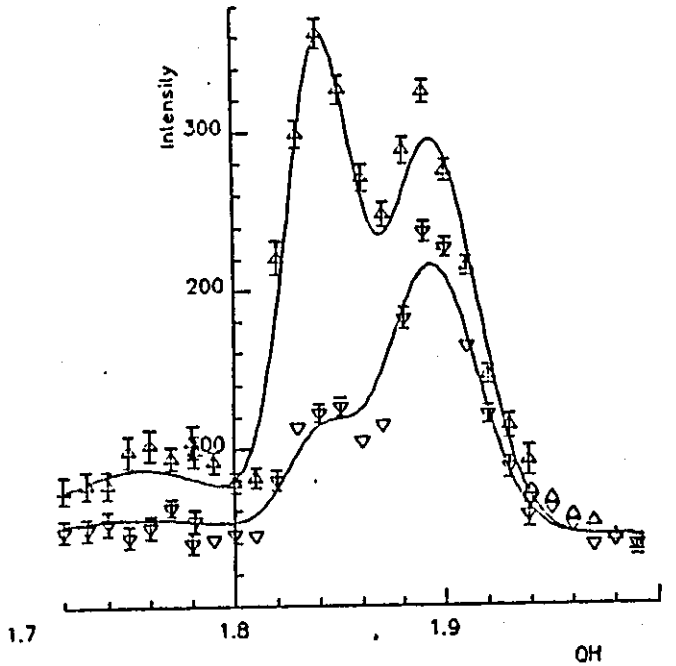

Peak No	Hgt Up	Hgt Down	Width	Centre
1	43(3)	11(1)	0.0600(10)	1.757(14)
2	296(10)	60(5)	0.0221(14)	1.8403(14)
3	250(8)	172(9)	0.0311(10)	1.8934(13)

Scans		Background Level		Background Slope	
Up	Down	Up	Down	Up	Down
L5010N	L5010F	43(2)	43(2)	0(0)	0(0)

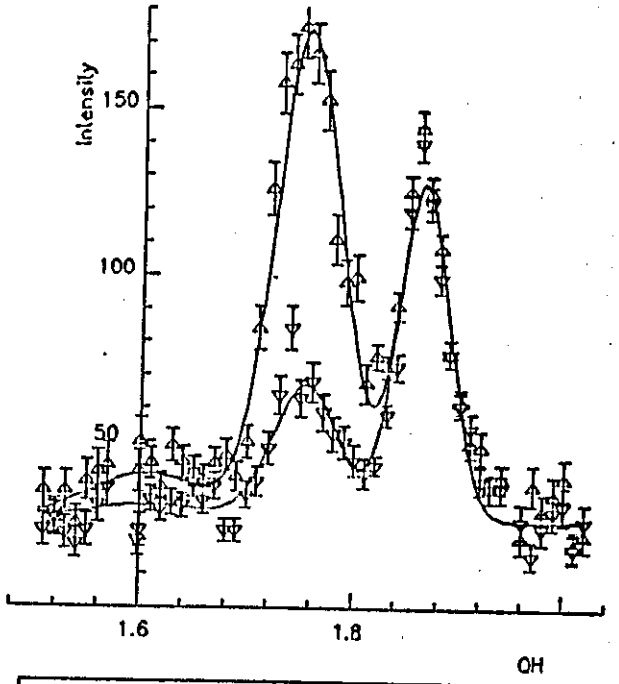

Peak No	Hgt Up	Hgt Down	Width	Centre
1	14.43(61)	4.77(13)	0.0789(33)	1.607(18)
2	146(4)	41(2)	0.0443(17)	1.7546(16)
3	101(2)	101(0)	0.0344(11)	1.86462(92)

Scans		Background Level		Background Slope	
Up	Down	Up	Down	Up	Down
L5015N	L5015F	25(1)	25(1)	0(0)	0(0)

Figure (9.18) Constant energy scans of $Fe_{50}Ni_{50}$ at 100 in the 100 direction

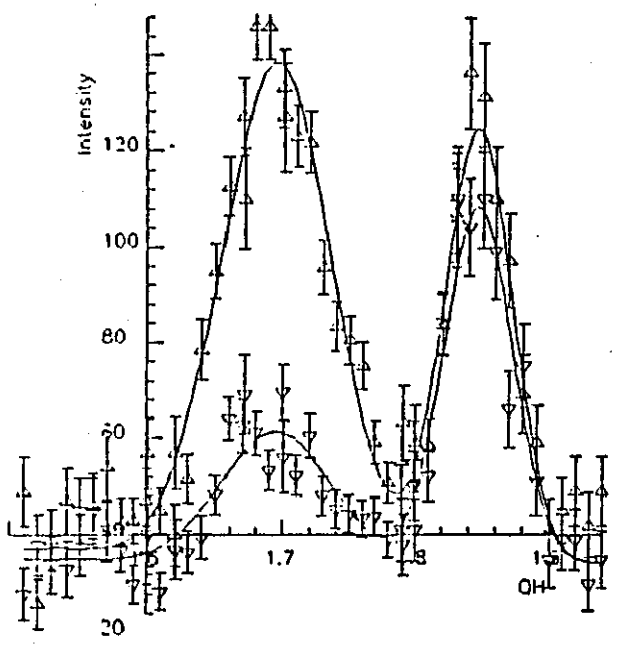

Peak No	Hgt Up	Hgt Down	Width	Centre
1	3.180(40)	1(0)	0.07821(75)	1(0)
2	104(3)	27(1)	0.0582(17)	1.6950(14)
3	90(3)	74(2)	0.0359(13)	1.5467(14)

Scans		Background Level		Background Slope	
Up	Down	Up	Down	Up	Down
L5018N	L5019F	34.15(81)	34.15(81)	0(0)	0(0)

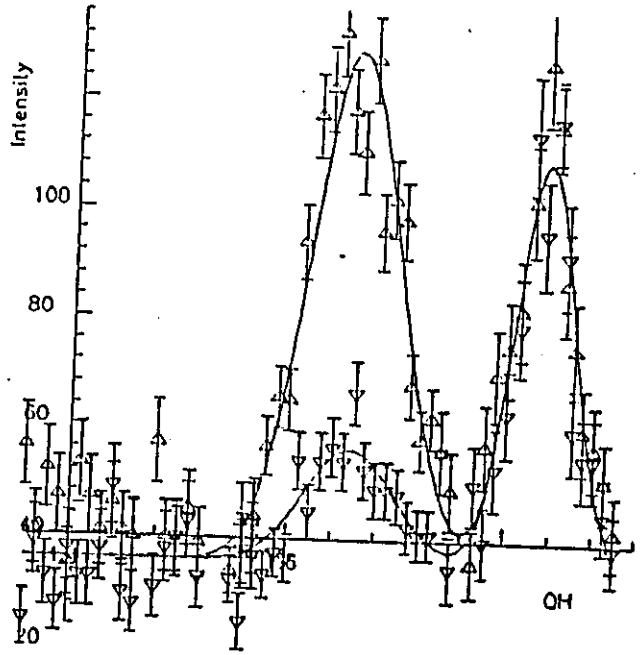

Peak No	Hgt Up	Hgt Down	Width	Centre
1	92(2)	20.11(83)	0.0579(22)	1.6555(22)
2	72(1)	72(0)	0.0379(16)	1.8318(19)

Scans		Background Level		Background Slope	
Up	Down	Up	Down	Up	Down
L5020N	L5020F	36.02(83)	36.02(83)	0(0)	0(0)

Figure (9.19) Constant energy scans of $Fe_{50}Ni_{50}$ at 100K in the 100 direction

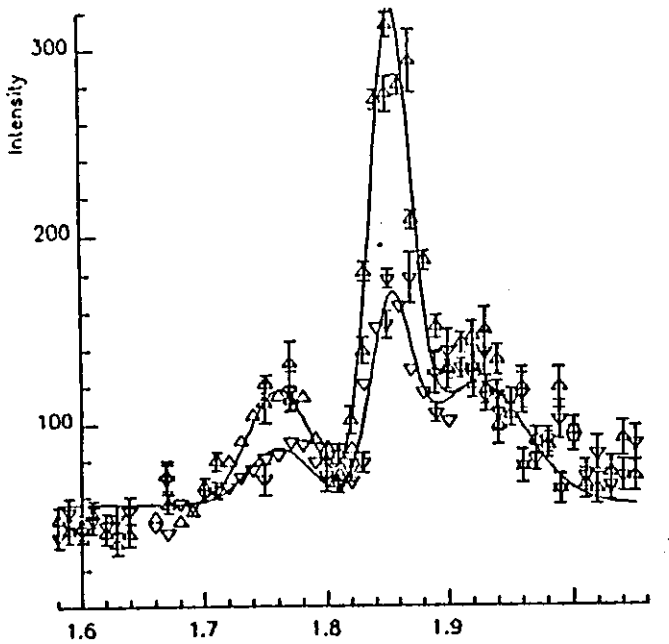

Peak No	Hgt Up	Hgt Down	Width	Centre
1	61(4)	30(2)	0.0362(26)	1.7607(24)
2	255(9)	101(5)	0.02445(79)	1.85263(79)
3	64(3)	64(0)	0.0547(37)	1.9240(38)

Scans		Background Level		Background Slope	
Up	Down	Up	Down	Up	Down
L2210N	L2210F	55(1)	55(1)	0(0)	0(0)

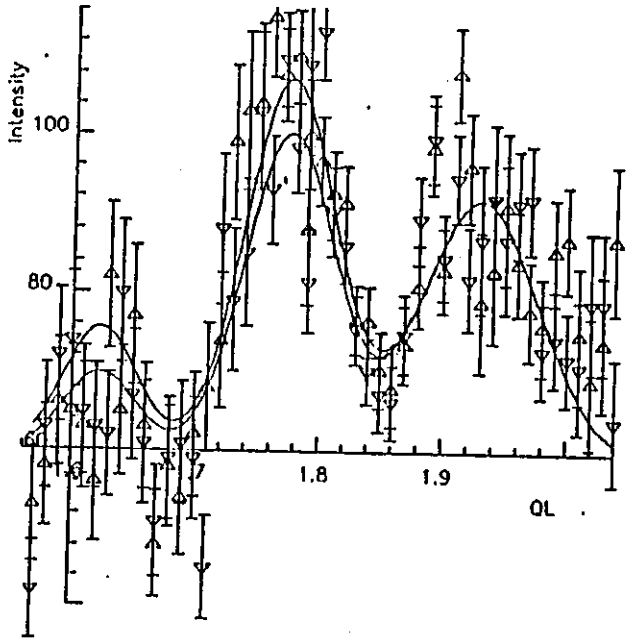

Peak No	Hgt Up	Hgt Down	Width	Centre
1	16.37(57)	10.63(25)	0.04340(70)	1.622(10)
2	47(1)	40(1)	0.0521(16)	1.7750(35)
3	32.57(93)	32(0)	0.0688(20)	1.9295(45)

Scans		Background Level		Background Slope	
Up	Down	Up	Down	Up	Down
L2215N	L2215F	59(1)	59(1)	0(0)	0(0)

Figure (9.20) Constant energy scans of $Fe_{78}Ni_{22}$ at 100K in the 100 direction

Table (9.10) L 100 at 100K for $Fe_{50}Ni_{50}$

E mev	K_f Å^{-1}	q	R	Q	sinθ/λ
10	4·1	1·8403 1·8934	4·933 1·453	3·224 3·318	0·257 0·264
15	4·1	1·7546 1·8646	3·561 1	3·047 3·267	0·245 0·260
18	4·1	1·6950 1·8467	3·852 1·2162	2·970 3·236	0·236 0·258
20	4·1	1·6555· 1·8318	4·575 1	2·901 3·210	0·231 0·255

Table (9.11) L 100 at 100K for $Fe_{78}Ni_{22}$

E mev	K_f Å^{-1}	q	R	Q_{111}	sinθ/λ
10	4·1	1·8526 1·9240	2·52 1	3·25 3·37	0·26 0·27
15	4·1	1·715 1·9295	1·18 1·02	3·11 3·38	0·25 0·27

Table (9.12)

Alloy series	Anomaly Temp (K)	Curie Temp (K)	Ref (90) Anom (K)	Ref (90) Curie (K)	e/a
$Fe_{65}Ni_{35}$	–	478	–	455	8·7
$Fe_{50}Ni_{50}$	640	760	525	790	9·0

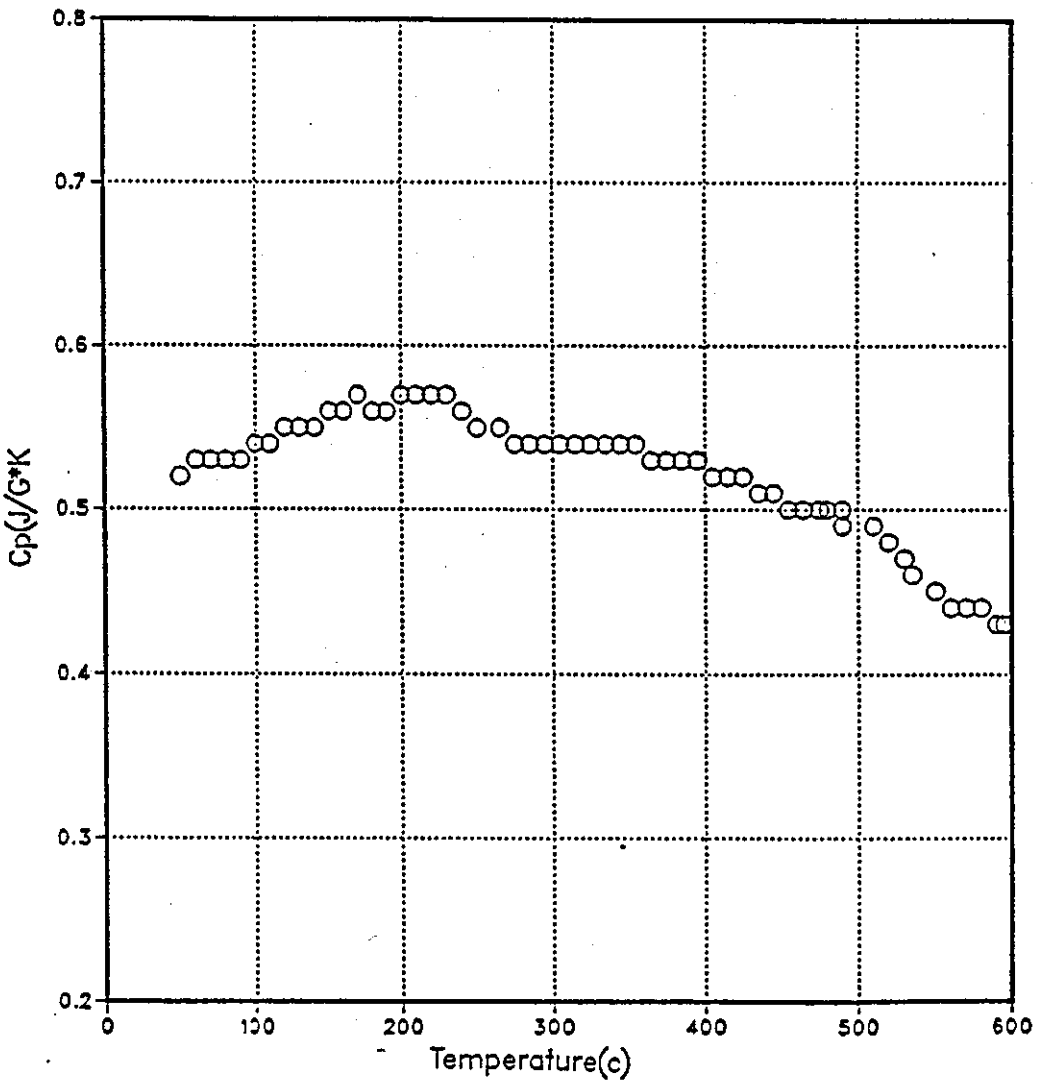

Figure (9.21) Specific heat capacity C_p as a function of temperature for $Fe_{65}Ni_{35}$

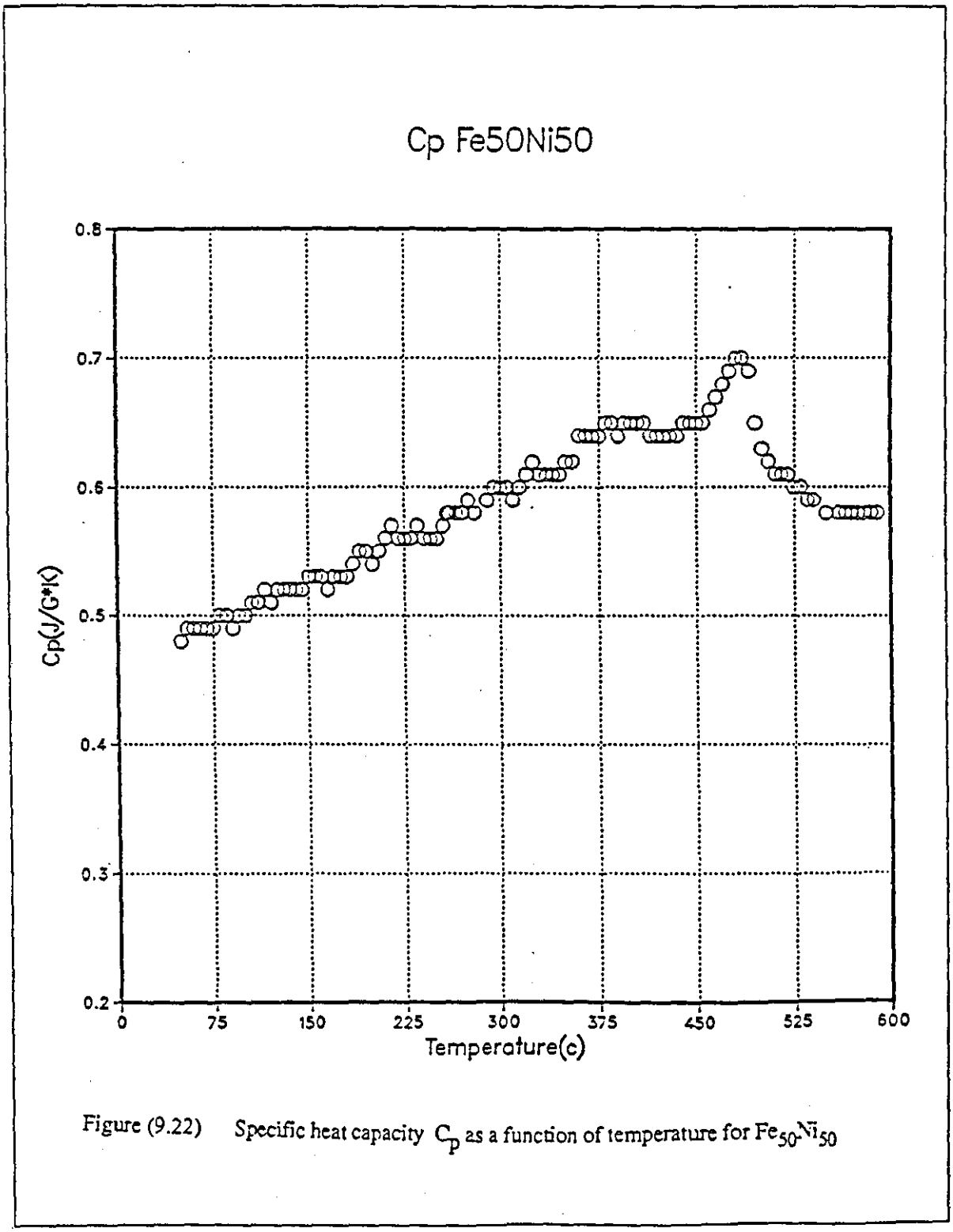

Figure (9.22) Specific heat capacity C_p as a function of temperature for $Fe_{50}Ni_{50}$

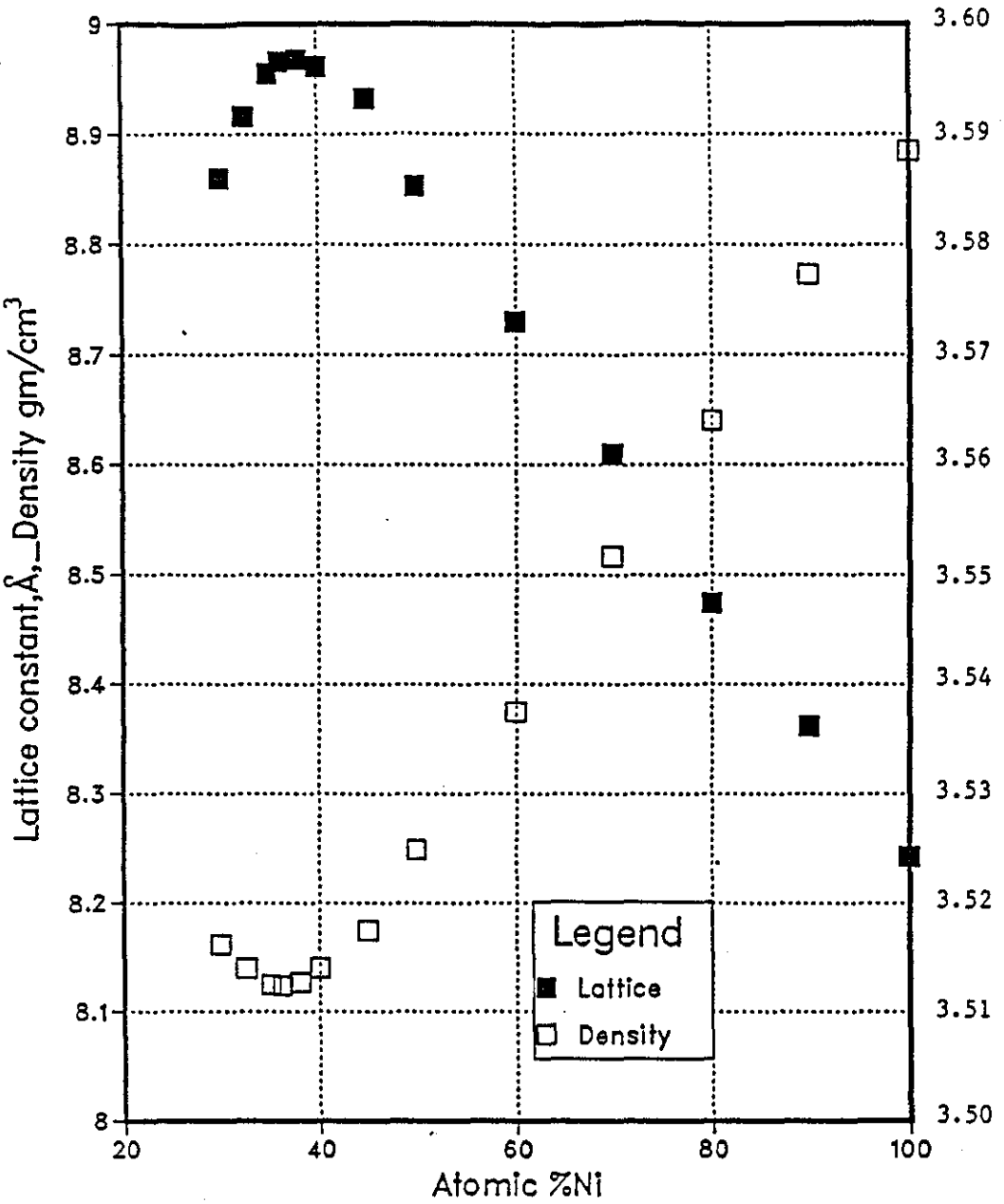

Figure (9.23) The lattice parameters a and the density versus the Ni concentration

magnetisation of the alloys deviates slightly at 60%Ni from the linear region and then falls sharply below 40% Ni [31].

The initial slopes of the phonon dispersion curves enable the velocities of sound to be determined. The values so achieved are compared from the ultrasonic data as in table (9.13).

The results are plotted in figures (9.24) and (9.25) along with curves determined by Y. Endoh (1979) [110] from ultrasonic measurements. The elastic constant of $Fe_{65}Ni_{35}$ Invar calculated from neutron measurements at 100K are listed in table (9.13).

9.5 DISCUSSION AND CONCLUSIONS

In the adiabatic approximation, and under the assumption that the magnetisation density around an atom is independent of its thermal displacement from its equilibrium position, the ratio of the magneto– vibrational to the nuclear vibration scattering is:

$$\gamma^2 = (f(Q)\,\bar{\mu}\,/\,\bar{b}\,)^2 \qquad (9.1)$$

where f(Q) is the magnetic form factor, $\bar{\mu}$ the mean magnetic moment per atom and $\bar{b}$ the mean of the nuclear scattering lengths. Using the value $\bar{b}$ =0·981 x 10^{-12} cm, the product $\bar{\mu}$ f(Q) was evaluated and is plotted against Q in figure (9.26). From this figure it may be seen that the product $\bar{\mu}$ f(Q) varies much more rapidly with Q than does the static form factor f(Q) indicated by the dotted line. It is not a monotonic function of Q but appears to decrease with increasing energy transfer as q increases on either side of the Brillouin Zone centre for both phonon batches that were measured. This behaviour suggests that the mean magnetic moment $\bar{\mu}$ contributing to the magneto–vibrational scattering at high Q and E is reduced by a factor of about two with respect to the mean periodic moment [10]. The full and dashed curves of figure (9.26) correspond to a crude model in which the moment drops to zero in that part of the phonon vibration in which the near neighbour distance is reduced from its equilibrium value by a critical fraction corresponding to about 0·01 for the curve shown. The reduction of the effective moment contributing to the magneto–

Table (9.13) The low temperature (100K) values of the Elastic Constants of Ni–Fe as measured by various investigators. The values of C_{11}, C_{12}, C_{44}, Bulk Modulus β and the Compressibility K are calculated from the qualities ρv_1^2, ρv_2^2 and ρv_3^2. All units are 10^{12} dyne cm^{-2} except for K which is 10^{-12} cm^2/dyne

References	ρv_1^2 $\frac{1}{2}(C_{11}+C_{12}+C_{44})$	ρv_2^2 C_{44}	ρv_3^2 $\frac{1}{2}(C_{11}-C_{12})$	C_{11}	C_{12}	β $\frac{1}{3}(C_{11}+2C_{12})$	K
Present research	2·179	1·079	0·161	2·610	2·288	2·395	0·417
Endoh, Noda and Ishikawa [107]	–	–	0·187 ± 3	–	–	–	–
Hausch and Warlimont [104]	2·182	1·017	0·162	–	–	–	–
Endoh [110]	2·193	–	0·162	–	–	–	–
Bower and Claridge [111]*	2·41	1·006	0·169	–	–	–	–

*The measurements were made at 4.2 K

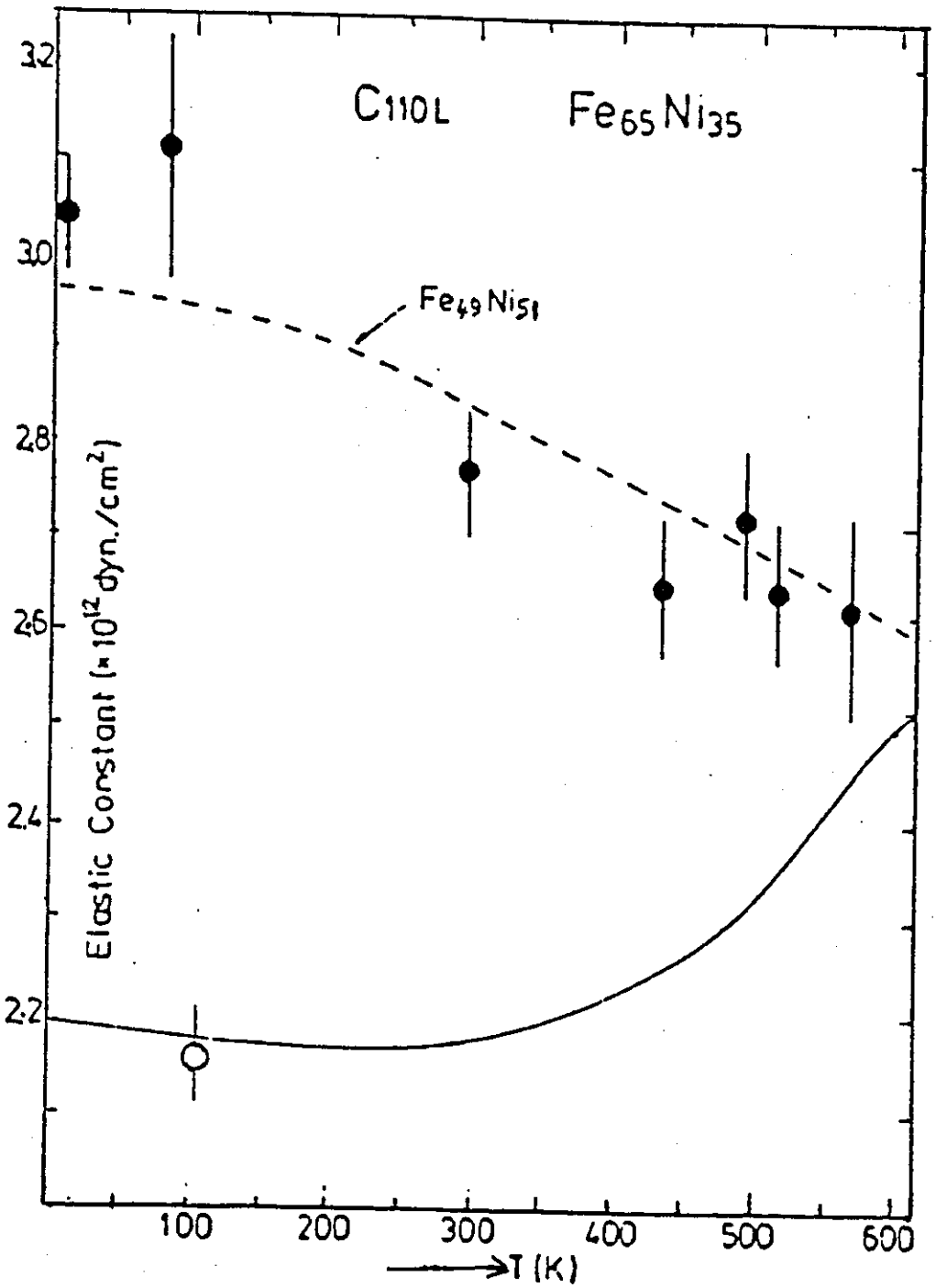

Figure (9.24) Temperature dependence of $\frac{1}{2}(C_{11} + C_{12} + 2C_{44})$ in $Fe_{65}Ni_{35}$. The solid and broken curves are the ultrasonic results for $Fe_{65}Ni_{35}$ and $Fe_{50}Ni_{50}$, respectively [104]. The filled circle is the neutron scattering results taken from Endoh [110]. The open circle is our research

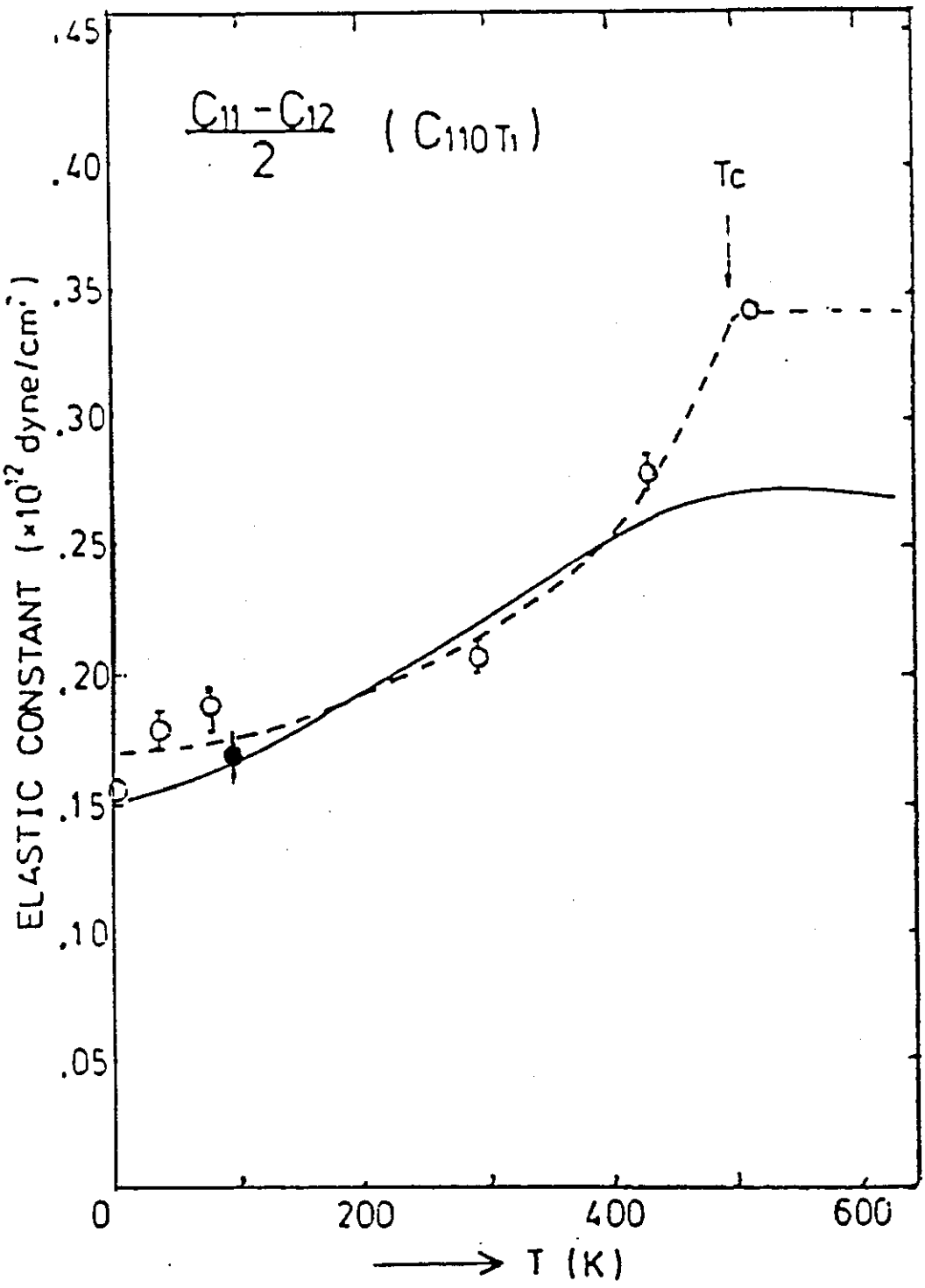

Figure (9.25) Temperature dependence of the elastic constant $\frac{1}{2}(C_{11}-C_{12})$ in $Fe_{65}Ni_{35}$. The solid curve is the ultrasonic measurement [104]. The open circle is the neutron scattering result taken from Endoh [110]. The filled circle is our reseach

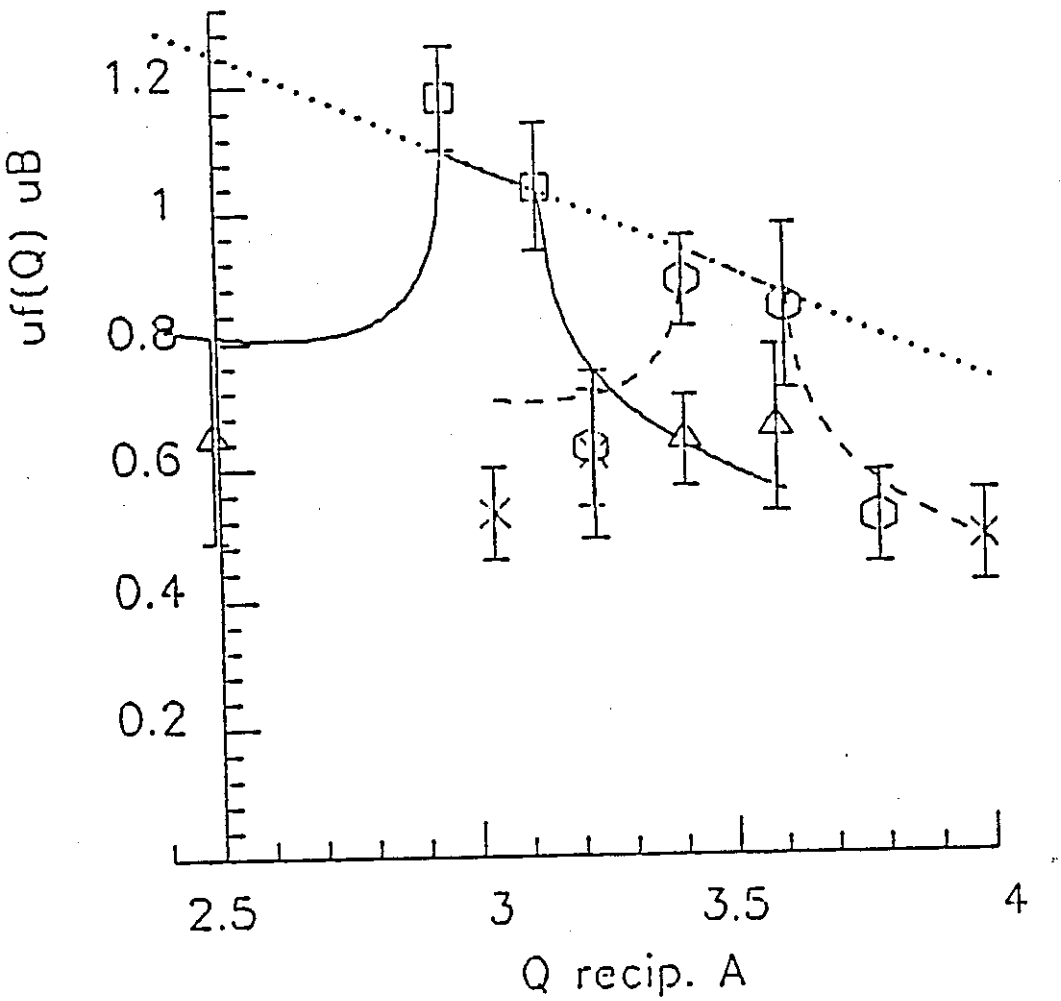

Figure (9.26) Experimental values of the product μf(Q) plotted against Q. The points marked with squares and triangles are for the LA111 phonon, measured using final wave vectors of 2.66 and 4.1 A^{-1} respectively. Those marked with circles and crosses are similarly for the LA001 phonon measured in the 002 zone. The dotted line indicated the moment variation due to the form factor obtained from static measurements.

vibrational scattering at high energy transfers may be due either to a collapse of the localised moment itself or to a reduction in the mean moment through an increased anti–parallel coupling. The former explanation would imply coupling with the stoner modes, whereas the latter may involve coupling with the magnons. The experimental evidence does suggest the existence of some magnon–phonon coupling, particularly in the [001] direction as shown in figure (9.6).

On the basis of the lattice and spin dynamics, it is clear that the Invar effect is associated with the coupling of the magnetic and lattice degrees of freedom in a dynamic process. Support for this interpretation is provided by measure–ments of the dynamic form factor, which not only reveal a deviation from the elastic form factor, but also the presence of a "forbidden" phonon mode as shown in figure (9.11), rendered observable by a strong magnon phonon interaction.

The results of the measurements, carried out at 100K, were compared with equivalent scans at 5K (Table 9.14). Very little difference was found between the [100] scans at the two temperatures but the intensities of the peaks in the [110] scans were significantly reduced and the corresponding value of the effective moment $\bar{\mu}_N$ increased at lower temperature as indicated in table (9.14C).

In order to investigate the origin of the forbidden phonon further measure ments were performed on two other Fe–Ni alloys which were x = 50 and x =22. The results show that the forbidden phonon is absent in both alloys. Table (9.15) summarises the compared intensities in these alloys. It is noted that the intensity of the $Fe_{50}Ni_{50}$ Non Invar at 100K is much bigger than alloys and this corresponding the values of the $\bar{\mu}_N$ increased at the high concentration of Ni (Non Invar range).

These experiments also indicated some anomalies in the spectrum of excitations observed at 100K for example L[100] in the Invar alloy $Fe_{65}Ni_{35}$ and non Invar $Fe_{50}Ni_{50}$ alloy at the same direction shown in table (9.15) and figures (9.11), (9.12) and (9.18), (9.19) for $Fe_{65}Ni_{35}$ and $Fe_{50}Ni_{50}$ respectively.

Table (9.14) Temperature comparison of 5K and 100K

(a) L 100

E mev	q		Fm	
	5K	100K	5K	100K
10	1·838 1·7401	1·806 1·717	0·56 0·53	0·65 0·57
15	1·805 1·727 1·596	1·797 1·719 1·596	0 1·12 0·59	0 1·09 0·61
18	1·784 1·664 1·483	1·770 1·653 1·489	0 0·93 0·44	0 1·17 0·24
20	1·768 1·623 1·420	1·764 1·614 1·407	0 1·16 0·25	0 1·01 0·21

(b) T 110

E mev	q		Fm	
	5K	100K	5K	100K
5	1·808	1·816	0·57	0·52
10	1·656	1·661	0·65	0·50
15	1·522	1·523	0·69	0·47

(c) Intensities T 110, 5K, and 100K

E mev	q	
	5K	100K
5	665 1013	1106 1878
10	197 382	296 543
15	107 217	143 232

Table (9.15)

(a) L 100 $Fe_{50}Ni_{50}$ Non Invar 100 K

Polarisation Ratios						
E mev	Phonon		Magnon		Anom	Phonon
10	296	60	250	172	43	11
15	146	41	101	101	14	5
18	104	27	90	74	3	1
20	92	20	72	72	0	0

(b) LA 100 $Fe_{65}Ni_{35}$ Invar 100 K

10	93	52	115	59	0	0
15	110	36	69	37	37	32
18	67	14·92	45	33	57	57
20	71	25·36	34	34	56	45

(c) LA 100 $Fe_{65}Ni_{35}$ Invar 5 K

10	149	87	174	98	0	0
15	97	31	45	45	60	33
18	75	29	35	35	47	30
20	65	19·95	32	32	54	42

(d) LA 100 $Fe_{78}Ni_{22}$ Invar 100 K

10	255	101	64	64	61	30
15	47	40	32·57	32	16·37	10·63

The specific heat results shown in figures (9.21) and (9.22) reveal an anomalous temperature dependence. At $Fe_{50}Ni_{50}$, C_p curve is characterised by two distinct maxima, one at about 760K and the second reveals an anomalous maximum at about 640K. The positions of this anomalous maxima is only slightly concentration–dependent, whereas a strong decrease of the Curie temperature as well as of the magnetic heat of transformation occurs with decreasing nickel content so that the alloy with 35% Ni reveals only a single maximum composed of both Curie peak and the maximum caused by the anomalous excess heat.

In conclusion, we can summarise the results and discussions as follows:

Measurements have been made of the polarisation dependence of the intensity of neutron scattering by the LA100 and LA111 magneto–acoustic excitations at 100k on the Invar alloy $Fe_{65}Ni_{35}$. The results suggested that the magnetic moment contributing to the scattering in these excitations decreases with energies above 15 mev. The results also indicated some anomalies in the spectrum of excitations observed in the 100 direction.

Measurements were repeated at 5k and the results compared with equivalent scans at 100k. The intensities of the peaks in 110 scans are significantly reduced. Polarisation dependence results show that the intensity of non–Invar alloy ($Fe_{50}Ni_{50}$) is bigger than other Invar alloys.

In both $Fe_{65}Ni_{35}$ and $Fe_{78}Ni_{28}$ the decrease in magnetisation at low temperature with increasing temperature is more rapid than that observed in Ni. Spin waves have been observed in both compounds with well defined magnon groups resolved up to 80 mev. The Stoner continuum was therefore assumed to lie above this energy. Consequently single particle excitations were not believed to be responsible for the Invar effect or for the rapid decrease in the magnetisation at low temperature. Furthermore the thermal population of spin wave was also unable to account for this rapid decrease. The present results which indicate the existence of strong magnon–phonon coupling, as evidenced by the presence of a "forbidden" phonon mode, suggests that this mechanism must be taken into account in any description of the magnetic properties. Preliminary model calculations based on the band structure of Fe_{65} Ni_{35} in

which both lattice and magnetic degrees of freedom are taken into account suggest that this mechanism will account for the properties of Invar alloys.

Furthermore, on the basis of the spin and lattice dynamics, it is clear that the Invar effect is associated with the coupling of the magnetic and lattice degrees of freedom in a dynamic process. Support for this interpretation is provided by measurements of the dynamic form factor, which not only reveals a deviation from the elastic form factor, but also the presence of a "forbidden" phonon mode, rendered observable by a strong magnon phonon interaction.

In order to further the investigation of the Invar effect, it would be of interest to perform additional measurements on the $Fe_{65}Ni_{35}$ alloy so that the effect of chemical order could be determined.

It is also important to compare the results with other Invar systems such as Fe_3Pt alloy. The Invar effect in Fe_3Pt is more pronounced than in $Fe_{65}Ni_{35}$ and is independent of the degree of order. The low temperature magnetisation varies as $T^{3/2}$ and the high field susceptibility is less than half that observed in $Fe_{65}Ni_{35}$. So the information about the way in which the magnetisation is coupled with Fe–Ni alloys.

REFERENCES

[1] K. Tajima, Y. Ishikawa and P. J. Webster, J.Phy.Soc. Jpn, 43, 483, (1977).

[2] B. Caroli and A. Blandin, J.Phys.Chem. Solids, 27, 503, (1966).

[3] Y. Ishikawa and Y. Noda, Spin Waves and Magnetic Interaction, 20th annual conference on magnetism, San Franciso, California, (1974).

[4] O. Yamada, F. Ono and I. Nakai, Solid State Phys. 27, 85, (1987).

[5] E. F. Wassermann, Adv. Solid State Phys. 27, 85 (1987).

[6] G. Hausch, Phys. Stat. Sol (a) 16, 371, (1973).

[7] S. Ishio and M. Takahashi, J.Magn. Mat. 50, 271, (1984).

[8] C. G. Shull, W. A. Strauser and E. O. Wollan, Phys. Rev. 83, 333 (1951).

[9] A. F Hames, J. Appl. Phys. 31, 307 (1960).

[10] P. J. Brown, I.K. Jassim, Y. Nakamura and K. R. A. Ziebeck, J.Physique, C8 – 307, (1988).

[11] H. A. Mook, Phys. Rev. Lett. 46, 508 (1981).

[12] H. A. Mook and J. Lynn, Phys. Rev. Lett 30, 556 (1973).

[13] J. Deportes and K. R. A. Ziebeck, J. Appl. Phys. 52, 2074, (1981).

[14] P. J. Brown, J. Deportes and K. R. A. Ziebeck, 53, 1973, (1982).

[15] W. Pauli, Z.Phys. 41, (1927).

[16] C. Herring, "Magnetism IV", Ed. G. T. Rado and H. Suhl, pub, Academic Press (1966).

[17] H. Capellmann and V. Vieia, Phys. Rev. B25, 3333 (1982).

[18] J. B. Sokoloff, J. Phys. F. : Metall Physics, 5, 1946 (1975).

[19] H. Capellmann, Solid State Commun, 30a, 7, (1979).

[20] B. Barbara, D. Gignoux and C. Vettier, Lectures on Modern magnetism, Science Press, 1988.

[21] D. E. G. Williams, The Magnetic Properties of Matter, Longmans, 1966.

[22] P. Langevin, J. de. Phys. 4, 678 (1905).

[23] P. Weiss, J. Phys. Radium, 6, 661, (1907).

[24] W. Heitler and F. London, Z. Phys. 44, 455 (1927).

[25] W. Heisenberg, Z. Phys. 57, 545, (1928).

[26] J. C. Slater, Phys. Rev. 36, 57, (1930).

[27] P. W. Anderson, Phys. Rev. 80, 922 (1950).

[28] M. A. Rudermann and Kittel, Phys. Rev. 96, 99, (1954).

[29] Y. Endoh and Y. Ishikawa, J. Phys. Soc. Japan 30 1614, (1971).

[30] M. Hayase and M. Shiga, J. Phys. Soc. Japan, 30 729, (1971).

[31] J. Crangle and G. C. Hallam, Proc. Roy. Soc. (London), A272, 119 (1963).

[32] M. Shiga, J. Phys. Soc. Japan, 22, 539, (1967).

[33] M. Hayase, M. Shiga and Y. Nakamura, J. Phys. State. Sol (b)50, 359, (1972).

[34] K. Gupta and C. H. Cheny, J. Phys. Chem. Solids, 25, 73, (1964).

[35] E. C. Stoner, Proc. Roy. Soc. A165, p372, (1938).

[36] E. C. Stoner, Rep. Prog. Phys. 11 , p43, (1947).

[37] S. Chikazumi, Physics of Magnetism, New York, (1964).

[38] G. Hausch and H. Warlimont, Phys. Letters, 41A, 437 (1972).

[39] G. A. Alers and J. R. Neighbours, J. Phys. Chem. Solids, 13, 40, (1960).

[40] E. P. Wohlfarth, Physica, B19, 203, (1983).

[41] D. J. Kim, Phys. Rev. B25, 6919, (1982).

[42] D. J. Kim and C. Tanaka, Phy. Rev. B37, 3948, (1987).

[43] D. J. Kim, J. De. Physique, C8, 289, (1988).

[44] D. J. Kim, Phys. Lett, 171, 129, (1988).

[45] J. Kanamori and Y. Teraoka, Proc. Alp. Conf. 24, 16, (1975).

[46] D. J. Kim, Physics Reports (Review Sec. of Physic. Lett), 171, No.4, (1988).

[47] Y. Endoh, J. Mag. Magne. Mater, 10, 177, (1979).

[48] C. Kittel, Introduction to Solid State Physics, fifth edition, (1976).

[49] J. De Launay, Solid State Physics, 2, 219, (1965).

[50] R. W. H. Stevenson, Phonons in perfect lattice, Scottish Universities Summer School, (1965).

[51] G. Hausch, J. Phys. Soc. Japan, 37, 819, (1974).

[52] M. Shiga, Solid State commun, 7, 559, (1969).

[53] K. Tajima and Y. Endoh, Phys. Rev. Lett, 37, 519, (1976).

[54] G. Hausch, Phys. Status Solidi (a), 15, 50, (1973).

[55] K. P. Belov, Magnetic Transitions consultants Bureau, New York, 1961.

[56] G. Burns, Solid State Physics, Academic Press, 408, 1985.

[57] G. E. Bacon, "Neutron Diffraction", 3rd Edn. pub. Oxford Clarendon Press, (1975).

[58] W. Marshall and S. W. Lovesey, Theory of Thermal Neutron Scattering, Oxford, (1971).

[59] G. L. Squires, Introduction to the Theory of Thermal Neutron Scattering, Cambridge University Press, (1978).

[60] W. Gavin Williams, Polarized Neutrons, Clarendon Press, Oxford, (1988).

[61] P. A. Egelstaff, Thermal Neutron Scattering, Academic Press, (1965).

[62] V. F. Sears, Thermal Neutron Scattering lengths and cross sections for Condensed Matter, Atomic Energy of Canada, (1984).

[63] R. Nathans, C. G. Shull and G. Shirance, J. Phys. Chem. Solids, 10, 138, (1959).

[64] R. M. Moon, T. Riste and W. C. Koehler, Phys. Rev. 181, 920, (1969).

[65] O. Steinsvoll, R. M. Moon and W. C. Koehler, Physi. Review B, 24, 4031, (1981).

[66] O. Steinsvoll, Neutron Physics Section Memo, No. 8 (Sept 1966), Institutt for Atomenergi, Kjellei.

[67] P. J. Brown and J. B. Forsyth, Brit. J. Appl. Phys. 15, 1529 (1964).

[68] K. R. A. Ziebeck and P. J. Brown, J. Phys. F10, 2015 (1980).

[69] J. Nelson and O. Riley, Proc. Roy. Soc. 57, 160, (1945).

[70] Guide to Neutron Research Facilities, Institut Max Von Laue, Grenoble, France, (1988).

[71] A. W. Hewat, Materials Science Forum, Vol.19, p.69–80, (1986).

[72] P. J. Bendall, D. Phil. Thesis, Oxford University, (1980).
P. J. Bendall and M. W. Thomas, AERA Report, (1980)
M. W. Thomas and R. J. Bendall, Act Crys, A34, s351, (1980).

[73] P. J. Brown, Treatise on materials science and technology, Vol.15, p69, (1979).

[74] John Temporal, Ph.D. Thesis, Dept of Physics, University of Sheffield, Feb. (1975).

[75] Gerald Burns, International Edition Solid State Physics, Academic Press, (1985).

[76] P. Leech and C Sykes, Phil. Mag. 27, 743, (1939).

[77] M. F. Collins, R. V. Jones and R. D. Lowds, J. Phys. Soc. Japan, 17, Suppl. B–III, 19, (1964).

[78] G. Shirance, Acta Cryst., 12, 282, (1959).

[79] R. E. Watson and A. J. Freeman, Act. Cryst., 14, 27, (1961).

[80] Y. Noda and Y. I. Shikawa, J. Phys. Soc. Japan, 40, 690, (1976).

[81] Y. Noda and Y. Ishikawa, J. Phys. Soc. Japan, 40, 699, (1976).

[82] K. Mooriani and J. M. D. Coey, Magnetic Glasses, Elsevier, (1984).

[83] L. E. Wenger and P. H. Keesom, Phys. Rev. B13, 4053, (1976).

[84] D. L. Martin, Phys. Rev, B21, 1902, (1980).

[85] E. I. Kondorsky and V. L. Sedov, J. Appl. Phys. 31, 331, (1960).

[86] G. E. Bacon and E. W. Mason, Proc. Phys. Soc. 92, 713, (1967).

[87] G. E. Bacon and J. S. Plant, J. Phys. F3, 2003, (1973).

[88] Y. Endoh, J. Magn. Magn. Mater 10, 177 (1979).

[89] S. Onodera, Y. Ishikawa and K. Tajima, J. Phys. Soc. Japan, 50, 1513, (1981)

[90] W. Bendick, H. H. Ettwig and W. Pepperhoff, J. Phys. F: Metal Phys. 8, 2525, (1978).

[91] W. J. Carr, Phys. Rev. 85, 590, (1952).

[92] J. C. Slater, J. Appl. Phys. 8, 385, (1937).

[93] L. Pauling, Phys. Rev., 54, 899, (1938)

[94] P. Weiss and G. Foex, J. Phys. Radium, 1, 744, (1911).

[95] V. L. Sedov, JETP Lett, 14, 341, (1971)

[96] W. F. Schlosser and G. M. Graham, J. Phys. Chem. Solids, 32, 927, (1971).

[97] V. I. Gomankov, Sov. Phys. Dok 1, 23, 851,, (1978).

[98] R. W. Cochrane, Can. J. Phys. 48, 264, (1970).

[99] T. Miyazaki, Y. Ando and M. Takahashi, J. Appl. Phys, 57, 3456, (1985).

[100] A. V. Deryabin, Sov. Phys. Solid State 27, 376, (1985).

[101] P. P. M. Meincke, Phys. Lett, A27, 390 (1969).

[102] R. Fletcher, J. Phys. C2, 2107, (1969).

[103] E. Claridge, Ph.D. Thesis, University of Leeds, (1968).

[104] G. Haush and H Warlimont, Acta. Metallurgica, 21, 401, (1973).

[105] M. Hansen, Constitution of Binary Alloys, McGraw –Hill Book Co. Inc., New York and London.

[106] E. A. Owen and A. H. Sully, Phil. Mag. 31, 314, (1941.)

[107] Y. Endoh, Y. Noda and Y. Ishikawa, Solid State commun, 23, 951, (1977).

[108] G. Hausch and H. Warlimont, Acta Met. 21, 401, (1973).

[109] M. Shiga, ICM88 Paris (1988).

[110] E. Endoh, J. Magne. Magn. Mate, 10, 177, (1979).

[111] D. I. Bower and E. Claridge, Phys. Stat. Sol, 29, 617, (1968).

[112] D. P. Morris and R. R. Preston, Proc. Phys. Soc. B.69, 849, (1956).

[113] R. W. Wyckoff, Crustal Structures, Vol.1, Interscience Publishers Ltd, London (1960).

[114] Y. Ishikawa and S. Onodera, J.Mag. Mag. Mater 10, 183, (1979).

[115] Y. Ishikawa, Y. Noda and K. R. A. Ziebeck, Solid State Communications, 57, 531, (1986).

[116] A. V. Gold, J. Low. Temp. Phys, 16, 13, (1974).

[117] P. Hohenberg and W. Kohn, Phys. Rev. 136, B864, (1964).

[118] T. Moriya, J. Magn. Magn. Mat. 14, 1, (1979).

[119] R. E. Prange and V. Korenman, Phys. Rev. B19, 4691 (1979).

[120] D. G. Pettifer, J. Phys. C3, 367, (1970).

[121] T. Kasya, Sol. State. Comm, 15, 1119, (1974).

[122] P. J. Brown, K. R. A. Ziebeck, J. A. C. Bland and P. J. Webster, J. Phys. D. Appl. Phys. 14, 511, (1981)

[123] S. M. Johnson, J. A. C. bland, P. J. Brown, P. J. Webster and K. R. A. Ziebeck, Journal de Physique, 43, p.67–119, (1982).

[124] P. J. Webster and R. S. Tebble, Phil. Mag. 16, 347, (1967).

[125] P. J. Webster and M. R. I. Ramadan, J. magn. Magn. Mat. 5, 51, (1977).

[126] P. J. Webster and M. R. I. Ramadan, J. magn. Magn. Mat. 13, 301, (1979).

[127] P. J. Webster and M. R. I. Ramadan, J. magn. Magn. Mat. 20, 271, (1980).

[128] P. J. Brown, Physica, 137B, 31–42, (1986).

[129] V. F. Sears, Atomic energy of Canda Limited, thermal neturon scattering lengths and cross sections for condensed matter, (1984).

[130] M.Hayasa, M. Shiga and Y. Nakamura, J. Phys. Soc. Japan, 30, 729 (1971).

[131] K. Gupta and C. Cheng, J. Phys. Chem. Solids, 25, 73, (1964).

[132] D. M. Roy and D. G. Pettifor, Solid State Commun, 27, 677, (1978).

[133] D. G. Pettifor, J. Phys. F7, L183, (1977).

[134] Pearson's Handbook of Crystallographic Data for Intermetallic Phases, by P. Villars and L. D. Calver, Vol. 12, (1985), American Society for Metals.

[135] International Tables for Crystallography, Vol. A. Space Group Symmetry by Theo Hahn, p. 679, (1987).

AN INELASTIC POLARISED NEUTRON SCATTERING INVESTIGATION OF THE DYNAMIC FORM FACTOR IN THE INVAR ALLOY $Fe_{65}Ni_{35}$

P. J. Brown ([1,2]), I. K. Jassim ([2]), R. M. Mankikar ([2]), Y. Nakamura ([3]) and K. R. A. Ziebeck ([2])

([1]) *Institut Laue-Langevin, Grenoble 38042, France*
([2]) *Department of Physics, Loughborough University of Technology, Loughborough, Leics. LE11 3TU, G.B.*
([3]) *Department of Metal Science and Technology, Sakyo-Ku, Kyoto 606, Japan*

Abstract. – Polarisation dependence of one phonon cross sections has been investigated in the Invar alloy $Fe_{65}Ni_{35}$. The variation of the polarisation ratios suggests that the magneto vibrational scattering is strongly dependent on the energy and wave vector of the phonon, indicating that the effective magnetic moments are reduced as the phonon energy increases.

Introduction

The thermal expansion anomaly associated with the onset of ferromagnetism in certain alloys, notably $Fe_{1-x}Ni_x$ with $x = 0.35$, and known as the Invar effect, has been the subject of much experimental and theoretical study [1]. In recent years attempts have been made using ultrasonic [2], neutron scattering [3, 4] and other techniques to elucidate the microscopic origin of the effect, but as yet no clear understanding has been reached. Nevertheless, in all models of the Invar effect it is recognised that the relationship between magnetic moment and the atomic volume or interatomic distance plays a crucial role, and hence the interactions between the vibrational and the magnetic degrees of freedom are of great importance. One very sensitive way to study such interactions is through the polarisation dependence of the magneto-vibrational neutron scattering. The polarised neutron technique was first used to study magneto-vibrational scattering by Steinsvoll *et al.* [5] who made measurements on metallic iron and nickel. They were able to show that whereas for nickel the magnetism density giving rise to magneto-vibrational scattering was indistinguishable from that giving rise to elastic scattering, for iron there was a small but significant difference. We have now used this same technique to study magneto-vibrational scattering in $Fe_{65}Ni_{35}$, for which it is expected that the magnetic moment is strongly coupled to the atomic vibrations.

Experimental

The experiments were carried out on a single crystal of $Fe_{65}Ni_{35}$ in the form of a cube 12 × 12 × 12 mm with edges parallel to $[1\bar{1}0]$, [001] and [110]. It was aligned with the $[1\bar{1}0]$ edge vertical and in the vertical field of a superconducting pair of Helmholtz coils on the IN20 polarised triple axis spectrometer at ILL, Grenoble. The field at the sample was set to 2 T which was sufficient for saturation at 100 K, the temperature of the experiment.

The spectrometer was set up with a vertically focussing Cu (200) monochrometer to produce an unpolarised monochromatic incident beam, the polarisation of the scattered beam was analysed using the (111) reflection of a Cu_2MnAl Heusler alloy and a Mezei flipper placed just in front of the analyser crystal. The collimation used starting from the monochromator was 30′, 40′, 40′, 40′ and the spectrometer was used in the constant K_f mode with K_f either 4.1 or 2.66 A^{-1} and a graphite filter to eliminate high order contamination of the beam.

Dispersion curves for the phonon and magnon modes in the [111] and [001] directions taken from the published work [3, 4] are shown in figure 1. They show the magnon mode crossing the LA [111] phonon mode at ≈ 12 meV and the LA [100] phonon mode at ≈ 7 meV.

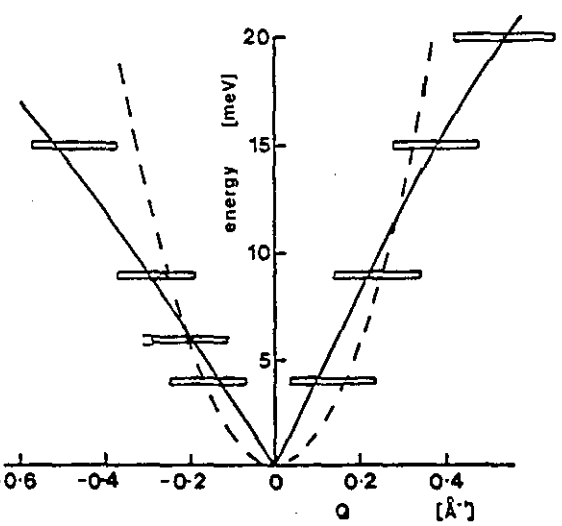

Fig. 1. – Dispersion curves for the magnon (dashed curve) and LA 111 and LA 001 phonons (full curves) in $Fe_{0.65}Ni_{0.35}$. The LA 111 branch is displayed in the positive Q direction and the 001 branch in the negative one. The horizontal oblongs indicate the scans carried out. The squares and triangles within the oblongs show the positions determined for the phonon and magnon peaks respectively.

A series of constant E scans were carried out which are indicated by the horizontal oblongs in figure 1. Those in the [111] direction were based on the 111 reciprocal lattice point and those in the [001] direction on 002. In each scan the scattered intensity was measured at each point with the flipper on, and then with it off, to obtain the polarisation dependence of the scattered intensity. For the scans in the [001] direction the magnon and phonon peaks were observed partially resolved from one another in the scans at 4 and at 6 meV; in the former the magnon peak, identified by its lack of polarisation dependence, was at higher q. These results indicate a deviation in the form of the dispersion curves from their ideal forms around the magnon phonon crossover, which may indicate anti-crossing behaviour due to interaction between them.

Analysis

The scattered intensity for both polarisation states measured in the scans was fitted to a sum of Gaussian peaks superposed on a linear background. The fits were constrained so that the centres and widths of the peaks for both polarisation states were the same, and the centres of peaks in scans at the same energy for $\tau + \mathbf{q}$ and $\tau - \mathbf{q}$ (where τ is a reciprocal lattice vector) were also at the same value of q. When one of the peaks in a scan was identified with a magnon, it was constrained to have the same intensity for both polarisation states. The centres of the fitted peaks are plotted as squares (phonon) and triangles (magnon) in figure 1. The ratios of the scattered peak intensities for the two polarisation states, after correction for incomplete polarisation of the beam, were used to calculate the ratio γ of magnetic to nuclear scattering in the phonon peaks.

Discussion

In the adiabatic approximation, and under the assumption that the magnetisation density around an atom is independent of its thermal displacement from its equilibrium position the ratio of the magneto-vibrational to the nuclear scattering cross-section is

$$\gamma^2 = \left(f(Q)\,\bar{\mu}\,/\,\bar{b}\right)^2$$

where $f(Q)$ is the magnetic form factor, $\bar{\mu}$ the mean magnetic moment per atom and $\bar{b}$ the mean of the nuclear scattering lengths. Using the value $\bar{b} = 0.981 \times 10^{-12}$ cm the product $\bar{\mu} f(Q)$ was evaluated and is plotted against Q in figure 2. It is clear from this figure that the product $\bar{\mu} f(Q)$ varies much more rapidly with Q than does the static form factor $f(Q)$ [6] indicated by the dotted line. Indeed it is not a monotonic function of Q but apears to decrease with increasing energy transfer as q increases on either side of the Bragg peak for both phonon branches that were measured.

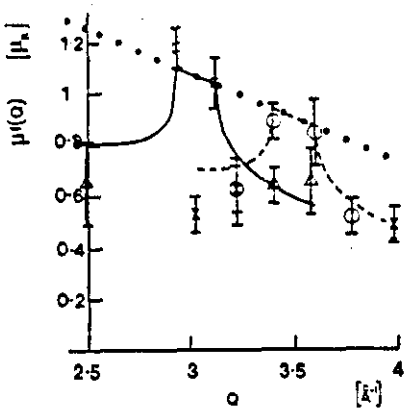

Fig. 2. – Experimental values of the product $\mu f(Q)$ plotted against Q. The points marked with squares and triangles are for the LA 111 phonon at $K_f = 2.66$ and 4.1 $Å^{-1}$ respectively; those marked with circles and crosses are similarly for the LA 001 phonon measured from 002. The dotted line indicates the moment variation due to the form factor $f(Q)$ and the full and dashed curves show the predictions of the simple model described in the text.

As yet a fully quantitative treatment of this behaviour cannot be given, but qualitatively it suggests that the mean moment $\bar{\mu}$ contributing to the magneto-vibrational scattering at high q and E is reduced by a factor of about two with respect to the mean periodic moment. The full and dashed curves of figure 2 correspond to a crude model in which the moment drops to zero in that part of the phonon vibration in which the near neighbour distance is reduced from its equilibrium value by a critical fraction which corresponds to about 0.01 for the curves shown. The reduction of the effective moment contributing to magneto vibrational scattering at high energy transfers may be due either to a collapse of the localised moment itself, or to a reduction in the mean moment though increased anti-parallel coupling. The former explanation implies coupling with Stoner modes, whereas the latter would imply coupling with the magnons. As yet the evidence is insufficient to permit a choice to be made between the two possibilities although the data given in figure 1 suggest that there is at least some magnon, phonon coupling.

[1] See Proc. Int. Symp. Invar Problems, *J. Magn. Magn. Mater.* **10** (1979).
[2] Haush, G., *J. Phys. Soc. Jpn* **37** (1974) 819.
[3] Endoh, Y., *J. Magn. Magn. Mater.* **10** (1979) 177.
[4] Onodera, S., Ishikawa, Y. and Tajima, K., *J. Phys. Soc. Jpn* **50** (1981) 1513.
[5] Steinsvoll, O., Moon, R. M., Koehler, W. C. and Windsor, C. G., *Phys. Rev. B* **24** (1981) 4031.
[6] Ho, Y., Akimitsu, J., Matsui, M. and Chikasumi, S., *J. Magn. Magn. Mater.* **10** (1979) 194.

Physica B [+] [1989] [page]
North-Holland, Amsterdam

NEUTRON SCATTERING FROM INVAR ALLOYS

P.J. BROWN*, I.K. JASSIM, K.-U. NEUMANN and K.R.A. ZIEBECK
Department of Physics, Loughborough University of Technology, Loughborough, Leics, LE11 3TU, UK
**Institut Laue-Langevin, Grenoble, France*

Neutron scattering experiments from invar alloys are reviewed. The discussion is restricted to results obtained on $Fe_{65}Ni_{35}$ and Fe_3Pt alloys. Particular attention is given to polarised neutron techniques which enable a detailed test of relevant theories to be made. These measurements suggest that many of the theories put forward to explain the invar effect are inappropriate. Finally, the results of some recent polarised-neutron measurements are presented.

1. Introduction

Alloys which exhibit invar behaviour have a small thermal expansion coefficient below the Curie temperature, a large forced volume magnetostriction and show a substantial pressure dependence of the magnetisation and Curie temperature, etc. For alloys in the Fe–Ni system, local fluctuations in composition resulting in heterogenous magnetisation are believed essential for the invar effect, which shows a maximum at the composition $Fe_{65}Ni_{35}$. This is not the case for Fe_3Pt, which orders in the $L1_2$ structure and exhibits a more pronounced invar effect than in $Fe_{65}Ni_{35}$. Both alloys are iron rich with an fcc structure and have compositions close to the phase boundary between fcc and bcc structures. Iron rich alloys in the Fe–Ni series which have a bcc structure do not exhibit invar behaviour. Various models have been proposed to explain the invar effect, and include latent antiferromagnetism, which is believed to be characteristic of fcc iron, or the collapse of the local moment, etc. Whereas $Fe_{65}Ni_{35}$ has been classified as a weak itinerant ferromagnet, Fe_3Pt does not exhibit such characteristic properties, since the low temperature magnetisation varies as $T^{3/2}$ and the high field susceptibility at low temperatures is less than half that observed in $Fe_{65}Ni_{35}$ [1]. Ultrasonic measurements on both $Fe_{65}Ni_{35}$ and Fe_3Pt reveal that the shear constants $\frac{1}{2}(C_{11} - C_{12})$ and C_{44} decrease below the Curie temperature [2].

On the basis of the bulk measurements, it may be concluded that a coupling of the magnetisation to the lattice is essential for the invar effect. Neutron scattering therefore provides a unique possibility of studying the temporal and spatial variation of the lattice and magnetic degrees of freedom and their possible interaction. Furthermore, if polarised neutrons are employed, then the various scattering mechanisms contributing to the total cross-section can be identified and placed on an absolute scale. Consequently, the importance of antiferromagnetism, moment stability, etc. to the invar effect can be established, and the validity of theories rigorously tested. Neutron scattering measurements on $Fe_{65}Ni_{35}$, Fe_3Pt and γ-Fe are discussed.

2. Static form factor

Polarised neutron diffraction enables the spatial distribution of magnetic electrons to be established and provides a unique method of establishing the ground state wave function. Measurements carried out on Fe and Ni have revealed that the magnetisation density localised around each atomic site is greater than the atomic moment given by the magnetisation measurements, and in the region between atoms the spin density is essentially constant but oppositely directed to the total magnetisation. The observed radial dependence of the density is almost exactly the same as that obtained for 3d electrons in a spin

0921-4526/89/$03.50 © Elsevier Science Publishers B.V.
(North-Holland Physics Publishing Division)

polarised Hartree–Fock calculation for a free atom, although Fe does show some deviation from the self-consistent calculations using a spin polarised exchange correlation potential. An important feature of the spin density distribution in both Fe [3] and Ni [4] is the large deviation from spherical symmetry. For spherical symmetry, the occupation of the T_{2g} and E_g orbitals should be in the ratio of 60 : 40, whereas in the case of Fe and E_g population is 53% and in the case of Ni, 19%. Measurements taken at high temperatures have revealed no change in the asymmetry of the spin density in Fe [5]. In the case of Ni it would appear that the spin splitting of the E_g and T_{2g} sub-bands have different temperature dependences [6]. A recent polarised neutron experiment [7] on Ni which extends above the Curie temperature has shown that the constant negative background density falls to zero at the Curie temperature.

Determination of the spin density distribution has been carried out on a chemically disordered sample of $Fe_{65}Ni_{35}$ at 300 and 77 K [8]. Analysis of the data was carried out in a similar manner to that used for Ni and Fe, and it was found that a satisfactory agreement with the observed form factor could be obtained using spherical Fe and Ni form factors. A projection of the spin density onto a [1 1 0] plane showing the approximately spherical distribution around the atoms is presented in fig. 1. Since measurements were only made in the zero layer of the [1, −1, 0] zone, it is not possible to calculate a section of the spin density. Quenching of the orbital contribution in comparison to the ionic state is consistent with spin resonance data [9] which indicates a decrease of the gyromagnetic ratio near the invar region. The amount of asphericity, as indicated by the percentage of 3d electrons in E_g orbitals, was small, e.g., 44.6% at 300 and 47.9% at 77 K. The level of constant negative background was found to be essentially temperature independent and of a level consistent with that observed in Fe. The average local moment associated with Ni atoms exhibits little temperature dependence below room temperature, so that the observed variation of the bulk magnetisation in this temperature range can be entirely attributed to that of the Fe atoms.

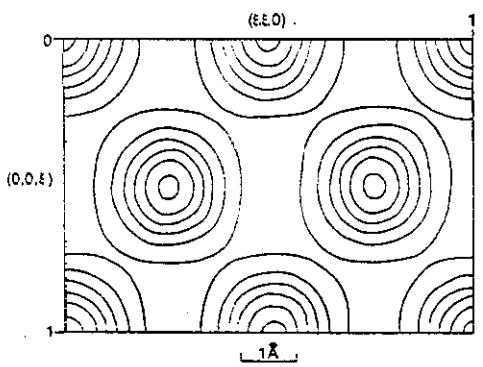

Fig. 1. A projection of the spin density in $Fe_{65}Ni_{35}$ onto the [1 1 0] plane [8].

3. Paramagnetic state

The thermal variation of the static susceptibility in both $Fe_{65}Ni_{35}$ [10] and Fe_3Pt [11] is substantial, indicating that a significant moment persists above the Curie temperature, and that as in other transition metal systems, the paramagnetic state is characterised by the thermal variation of long wavelength spin fluctuations. In the case of bcc iron, [12, 13] the polarised neutron measurements revealed that the long wavelength component of the response was enhanced above that expected for local disordered moments. Furthermore, at wave vectors greater than half the Brillouin zone boundary value, the energy width of the response was found to be small, 40 meV, and the total weight anomalously low. The observed scattering, when integrated throughout the Brillouin zone, yielded an amplitude per Fe atom lower than that observed in the ground state. The region in which the response becomes suppressed corresponds to the same region in the ground state in which the spin waves appear damped by single particle excitations. In the case of nickel [14], the long-wavelength response is significantly more enhanced, as might be expected on the basis of the large stiffness of the spin wave in the ground state. At large wave vectors,

a small paramagnetic response was found, unlike the case of iron, to persist up to very high energy transfers, i.e., >200 meV. Consequently the amplitude on the nickel atom was found to be substantially larger than the ground state moment. The response at large wave vectors was attributed to quantum fluctuations associated with states at the top of a hole band, and therefore having a long life-time. Thus, as may be expected, the paramagnetic state is characterised by thermal fluctuations of the spin density together with quantum fluctuations. The itinerant nature of the magnetic electrons characterises the degree of spatial correlation of the magnetic fluctuations and the importance of quantum fluctuations within the thermal energy range is determined by the details of the band structure.

The measurements on bcc iron were carried out on polycrystalline and single crystals in which the alpha phase has been stabilised by the addition of a few atomic per cent impurity atoms. Silicon, which is non-magnetic, was used as the impurity, with only 5 at% being necessary to stabilise the alpha phase beyond 1600 K. Pure iron undergoes a structural phase transition at 1183 K from the alpha (bcc) to the gamma (fcc) phase. Considerable effort, both theoretical and experimental, has been expended in an attempt to account for the alpha–gamma structural phase transition in pure iron. In general, it has been suggested that the driving mechanism for it, as well as more generally for the invar anomaly, originates from the differences in the magnetic character of iron in the two phases: the iron moment in the alpha phase is stable; in the gamma phase either its possible instability, or alternatively antiferromagnetic interactions between magnetic moments have been considered. The polarised neutron scattering measurements revealed that the scattering in pure gamma iron was characterised by spatial correlations of a ferromagnetic nature (fig. 2) [15]. Although the forward scattering in gamma iron was significantly reduced from that observed at the same temperature in the stabilised $Fe_{95}Si_5$, the correlations remained strongly ferromagnetic. The experiments did not reveal the presence of any

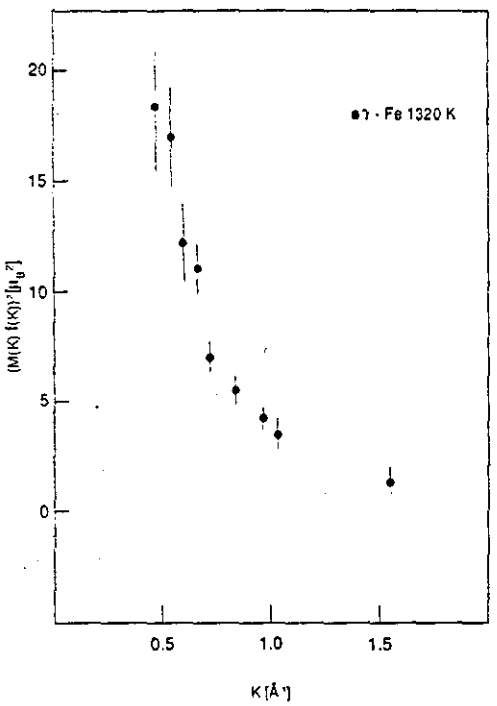

Fig. 2. The wave vector dependence of the paramagnetic scattering in pure γ-Fe at 1320 K, indicating the strong ferromagnetic correlations [15].

antiferromagnetic correlations, as is often quoted in literature on the basis of indirect experimental arguments. Consequently, these results indicate that if pure gamma iron were to order magnetically, it would do so ferromagnetically, not antiferromagnetically. Since the static susceptibility in the gamma phase is found to vary slowly with temperature, it was concluded that the spatial correlations do not vary significantly with temperature. Similar measurements on the invar alloys $Fe_{65}Ni_{35}$ and Fe_3Pt also indicated the absence of any antiferromagnetic correlations.

Polarised neutron scattering experiments on a single crystal of $Fe_{65}Ni_{35}$ in the paramagnetic phase at a temperature of 1.25 T_C have been carried out in the momentum range covered 0.1 to 0.9 $Å^{-1}$ [16]. Constant q-scans carried out in the [1 1 1] and [1 0 0] directions indicated that the response was isotropic and that $\Gamma = Aq^2$ with $A = 41$ meV $Å^2$. In fig. 3 the wave vector dependence of the scattering is displayed, together

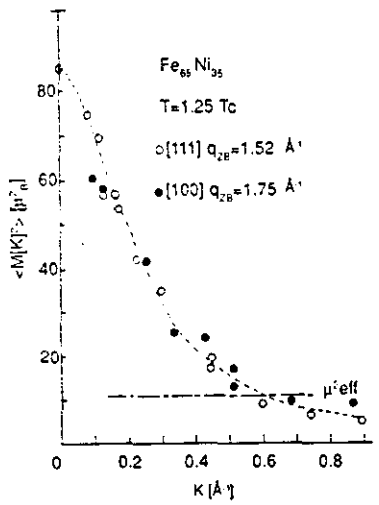

Fig. 3. The wave vector dependence of the paramagnetic scattering in $Fe_{65}Ni_{35}$ at 1.25 T_C. The horizontal dashed line corresponds to the level of scattering expected for local disordered moments, and is given by $\mu^2_{eff} = g^2S(S+1)$ [16].

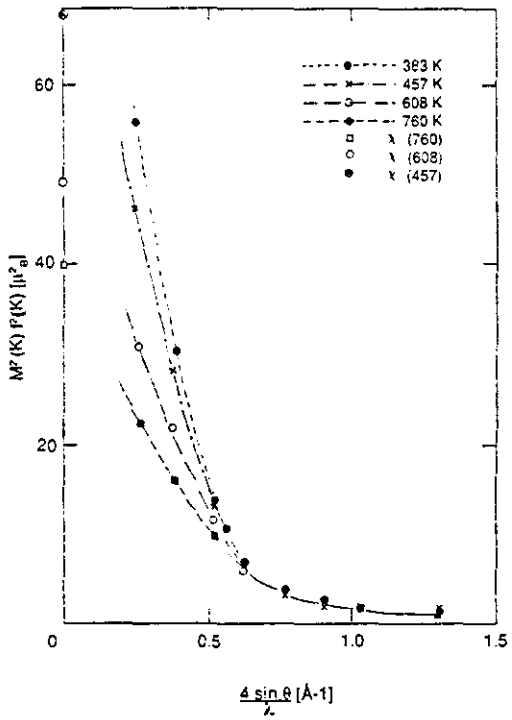

Fig. 4. The temperature variation of the paramagnetic scattering in Fe_3Pt. The enhanced forward scattering indicates the presence of strong ferromagnetic correlations [17].

with the level expected for completely disordered local moments corresponding to $\mu_{eff} = 3.3\mu_B$. It was concluded that the amplitude of the spin fluctuations could be described satisfactorily by a localised model in which the parameters were deduced from the measured spin wave dispersion at low temperatures, the magnetisation and uniform susceptibility. Measurements at larger wave vectors approaching the Brillouin zone boundaries were not reported, and it is in this region that the itinerant nature of the system can, depending upon the band structure, become important. At wave vectors corresponding to the zone boundary, the response is dominated by fluctuations on an atom whereas at small q, the response over large distances is being explored.

The paramagnetic scattering from Fe_3Pt has been determined throughout the Brillouin zone [17]. The forward scattering corresponding to the ferromagnetic correlations was found to be temperature dependent, as shown in fig. 4, and significant scattering was observed at large wavevectors towards the zone boundary. As in the case of $Fe_{65}Ni_{35}$, these measurements revealed that the moment persisted into the paramagnetic phase and that the response was dominated by ferromagnetic correlations. Consequently, models put forward to explain the invar effect, and based upon moment instability and/or the existence of antiferromagnetic correlations, are not supported by the above experiments.

4. Inelastic measurements

Inelastic neutron scattering measurements reveal that both $Fe_{65}Ni_{35}$ and Fe_3Pt exhibit similar phonon anomalies. A large softening of the [1 1 0] T_1 acoustic phonon mode occurs below the Curie temperature, but no significant shift in the phonon frequencies with changing temperature occurs in the paramagnetic phase, thus suggesting that the softening originates from magneto elastic coupling [18, 19]. The sound velocities obtained from the slopes of the dispersion curves agree with those obtained using ultrasonic techniques, and it has been suggested that the softening is associated with a fast relaxation pro-

cess. However, no appreciable softening was found in the longitudinal acoustic phonon modes, although ultrasonic measurements have demonstrated a significant decrease of the velocity associated with this mode. It was therefore concluded that a slow relaxation mechanism would be responsible for the variation in the LA mode.

Magnetic excitations in both alloys have been studied using inelastic neutron scattering [20, 21]. Well-defined magnon groups were observed up to the highest energies at which measurements could be carried out, i.e., 80 meV. The Stoner continuum was therefore assumed to lie above this energy, and single particle excitations could not be responsible for the invar effect, particularly at low temperatures. The spin wave stiffness constant is found to be isotropic in both compounds, with a thermal variation which may be accounted for using two magnon Heisenberg theory for temperatures up to 0.8 T_C. Over the temperature range covered by the experiment, the intensity of the magnon spectra is wave-vector independent, with a thermal variation in agreement with the magnetisation. However, the spin wave spectra can only account for half of the decrease of magnetisation with temperature (fig. 5). This is in contrast to Pd_2MnSn (a localised system) and Ni and $Fe_{50}Ni_{50}$, which are itinerant ferromagnets but do not exhibit invar behaviour. On the basis of these results, it may be concluded that Stoner excitations are not the primary mechanism controlling invar behaviour and that a dynamic effect involving magnon phonon interaction is responsible.

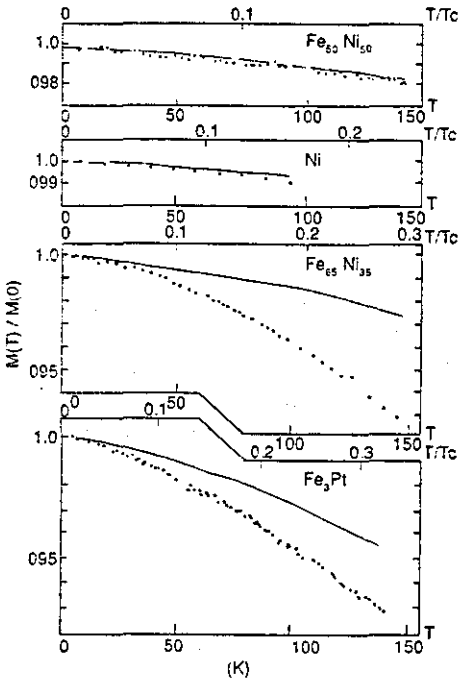

Fig. 5. The thermal variation of the magnetisation in $Fe_{50}Ni_{50}$, Ni, $Fe_{65}Ni_{35}$ and Fe_3Pt. The solid lines are calculated using spin wave theory and the open circles represent values obtained from magnetisation measurements [21].

5. Dynamic form factor

In all models of the invar effect it is recognised that the relationship between magnetic moment and atomic volume or interatomic distance plays a crucial role. Hence the interactions between the vibrational and magnetic degrees of freedom are of great importance. Information about the way in which the magnetisation is coupled to the phonon modes may be obtained by measurements of the phonon intensities in much the same way as the time averaged magnetisation density can be obtained from the polarisation dependence of the intensities of Bragg peaks. Consequently the polarisation ratios may be measured as a continuous function of q throughout the Brillouin zone and for different phonon polarisations. This is in contrast to elastic scattering measurements of the spin density distribution which are restricted to discrete values of q given by τ, i.e., Bragg peaks. To the extent that the magnetic electrons follow the nuclei exactly, the form factor of the magneto vibrational scattering will be identical with that obtained from the elastic scattering experiment. However, if particular components of the magnetisation density such as the E_g or T_{2g} components couple more strongly to particular vibrational modes, then this will be shown by differences between the effective magneto vibrational form factor and the elastic one. This technique was first used by Steinsvoll et al. to study iron and nickel [22].

Their measurements demonstrated that, whereas for nickel the magnetic density giving rise to the magneto vibrational scattering was indistinguishable from that giving rise to elastic scattering, for iron there was a small but significant difference.

The magneto vibrational scattering in $Fe_{65}Ni_{35}$ has recently been investigated [23]. These measurements reveal that there is indeed a strong coupling of the magnetic density to the lattice. In the adiabatic approximation, and under the assumption that the magnetisation density around an atom is independent of its themal displacement from its equilibrium position, the ratio of the magneto vibrational to the nuclear vibrational scattering is:

$$\gamma^2 = (f(K)\mu/b)^2$$

where $f(K)$ is the magnetic form factor, μ the mean magnetic moment per atom and b the mean of the nuclear scattering lengths. Using the value $b = 0.981 \times 10^{-12}$ cm, the product $\mu f(K)$ was evaluated and is plotted against K in fig. 6.

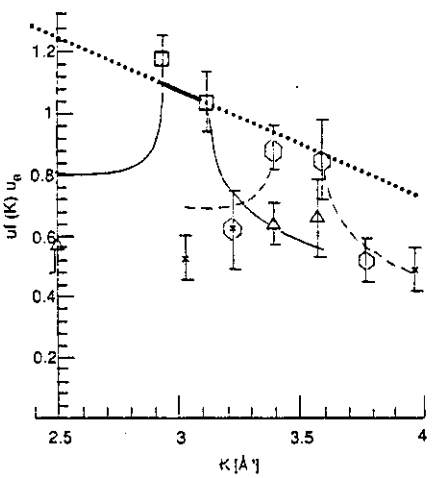

Fig. 6. Experimental values of the product $\mu f(K)$ plotted against K. The points marked with squares and triangles are for the LA 111 phonon, measured using final wave vectors of 2.66 and 4.1 $Å^{-1}$, respectively. Those marked with circles and crosses are for the LA 001 phonon measured in the 0 0 2 zone with final wave vectors of 2.66 and 4.1 $Å^{-1}$, respectively. The dotted line indicates the moment variation due to the form factor obtained from static measurements [8] and the full and dashed curves show the prediction of the simple model described in the text [22].

From this figure it may be seen that the product $\mu f(K)$ varies much more rapidly with K than does the static form factor $f(K)$ indicated by the dotted line. Indeed, it is not a monotonic function of K but appears to decrease with increasing energy transfer as K increases on either side of the Brillouin zone centre for both phonon branches measured. This behaviour suggests that the mean magnetic moment μ contributing to the magneto vibrational scattering at high q and E is reduced by a factor of about 2 with respect to the mean periodic moment. The full and dashed curves in the figure correspond to a crude model in which the moment drops to zero in that part of the phonon vibration in which the near neighbour distance is reduced from its equilibrium value by a critical fraction corresponding to about 0.01 for the curves shown. The reduction of the effective moment contributing to magneto vibrational scattering at high energy transfers may be due either to a collapse of the localised moment itself or to a reduction in the mean moment through increased anti-parallel coupling. The former explanation would imply coupling with the Stoner modes, whereas the latter may involve coupling with the magnons. Work is in progress to elucidate the origin of this reduction, but experimental evidence does suggest the existence of some magnon-phonon coupling, particularly in the [0 0 1] direction.

A series of constant energy scans made along the [0 0 1] direction with either $[1, -1, 0]$ and then the $[1, 0, 0]$ perpendicular to the plane of scattering revealed 3 excitations in the momentum range $q = 0.1$ to 0.25. In both geometries, only phonon scattering from the LA 001 branch should be observed, since the polarisation of the degenerate transverse modes are perpendicular to the scattering vector ($\boldsymbol{\varepsilon} \cdot \boldsymbol{K} = 0$) and therefore the cross-section for these modes is 0. The existence of the forbidden transverse mode was confirmed using two different orientations of the crystal and by repeating the scans using two different final wave vectors. The dispersion of the 3 modes is shown in fig. 7, in which the curves represented by circles and triangles can be identified with the LA 001 phonon and the magnon respectively. The observed dispersion of

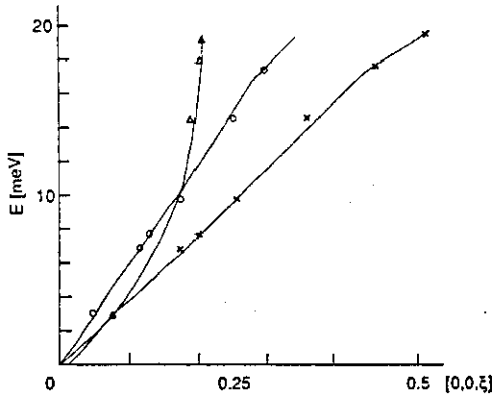

Fig. 7. The observed dispersion in the 001 direction indicating the expected magnon (△) and LA 001 (○) modes and the "forbidden" transverse acoustic mode TA 001 (X). The measurements were carried out at 100 K with a magnetic field of 2 T applied perpendicular to the scattering plane [22].

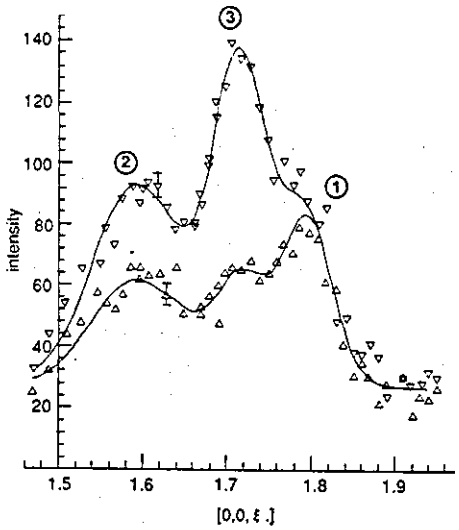

Fig. 8. A constant energy scan $E = 15$ meV carried out along the 0 0 1 direction indicating the 3 peak structure referred to in the text. The peak identified by 1 represents the magnon and therefore does not have a flipping ratio associated with it. Peak 3 is the LA phonon expected for the scattering geometry used in the scan. Peak 2 represents the "forbidden" TA mode [22].

these modes is in good agreement with that published previously. The third excitation, represented by crosses, has the same dispersion as the TA 001 phonon, which as mentioned above should not be visible for the scattering geometry used. The polarisation dependence of the intensities scattered by all 3 excitations was measured. As expected, the magnon intensity was found to have no polarisation dependence. The polarisation dependence of the other two modes was analysed as described above in terms of an effective normalised moment, defined as the fraction of the mean atomic moment which would be needed to give the observed polarisation dependence for magneto acoustic scattering. For the LA 001 phonon, effectively the whole moment contributes for measurements below 18 meV, but for increasing energy transfers there is evidence for a significant reduction. The "forbidden" TA 001 mode differs in that at low energy transfers only about one half the moment is observed in the scattering; this again falls off above 15 meV. The presence of the "forbidden" phonon mode could be explained by a strong coupling of the magnetic and lattice degrees of freedom. However, it must be emphasised that the intensity of the mode is substantial, as may be seen in fig. 8. Measurements made in the [1 1 0] direction, in which the TA_2 mode with polarisation parallel to [1, −1, 0] was reported to soften significantly with temperature, revealed that the effective moment contributing to the magneto vibrational scattering was close to unity. The results of these measurements, carried out at 100 K, were very similar to the results obtained at 5 K, except that the intensities of the peaks for measurements made in the [1 0 0] direction were significantly reduced and the corresponding values of the effective moment increased.

6. Summary

In the ground state of $Fe_{65}Ni_{35}$, the spin density distribution is essentially spherically symmetric, and there is no evidence of significant negative density. A substantial moment persists into the paramagnetic phase of both $Fe_{65}Ni_{35}$ and Fe_3Pt, and the properties are characterised by thermal fluctuation of the long wavelength components of the spin density. There is no evidence of the existence of antiferromagnetic correlations

in these compounds. Moreover, paramagnetic scattering experiments on γ-Fe reveal strong ferromagnetic correlations, indicating that if the system were to order it would do so ferromagnetically and not antiferromagnetically, as often quoted in literature. It may be concluded from these measurements that single particle excitations are not predominant in characterising the paramagnetic state. This is consistent with the observation in the ground state that the spin waves propagate up to 80 meV, which again suggests that the spectrum of single particle excitations lies outside the thermal range. However, the magnon density of states is unable to account for the observed decrease in the magnetisation with temperature, indicating that other degrees of freedom must be involved. On the basis of the spin and lattice dynamics, it is clear that the invar effect is associated with the coupling of the magnetic and lattice degrees of freedom in a dynamic process. Support for this interpretation is provided by measurements of the dynamic form factor, which not ony reveal a deviation from the elastic form factor, but also the presence of a "forbidden" phonon mode, rendered observable by a strong magnon–phonon interaction.

References

[1] Y. Nakamura, IEEE Trans. Magn. MAG-12 (1976) 278.
[2] G. Hausch and H. Warlimont, Acta. Met. 21 (1973) 401.
[3] C.G. Shull and Y. Yamada, J. Phys. Soc. Jpn. 17 Suppl. B111 (1962) 1.
[4] H.A. Mook, Phys. Rev. 148 (1966) 495.
[5] R.C. Maglic, A.I.P. Proc. no. 5 (1972) 1420.
[6] J.W. Cable, Phys. Rev. B 23 (1981) 6168.
[7] P.J. Brown, J. Deportes and K.R.A. Ziebeck (to be published).
[8] Y. Ito, J. Akimitsu, M. Matsui and S. Chikazumi, J. Magn. Magn. Mat. 10 (1979) 194.
[9] C.A. Bauer and P.E. Wigen, Phys. Rev. B 5 (1972) 4516.
[10] F. Ono, J. Phys. Soc. Jpn. 50 (1981) 2231.
[11] K. Sumiyama, M. Shiga and Y. Nakamura, J. Phys. Soc. Jpn. 4 (1973) 1393.
[12] P.J. Brown, H. Capellmann, J. Deportes and K.R.A. Ziebeck, J. Magn. Magn. Mat. 30 (1982) 243.
[13] J.P. Wicksteed, G. Shirane and O. Steinsvoll, Phys. Rev. B 29 (1984) 488.
[14] P.J. Brown, H. Capellmann, J. Deportes, D. Givord, S.M. Johnson and K.R.A. Ziebeck, J. de Phys. 47 (1986) 491.
[15] P.J. Brown, H. Capellmann, J. Deportes, D. Givord and K.R.A. Ziebeck, J. Magn. Magn. Mat. 30 (1983) 335.
[16] K. Tajima, P. Boni, G. Shirane, Y. Ishikawa and M. Kohgi, Phys. Rev. B 35 (1987) 274.
[17] K.R.A. Ziebeck, P.J. Webster, P.J. Brown and H. Capellmann, J. Magn. Magn. Mat. 36 (1983) 151.
[18] K. Tajima, Y. Endoh, Y. Ishikawa and W.G. Stirling, Phys. Rev. Lett. 37 (1976) 519.
[19] Y. Endoh, J. Magn. Magn. Mat. 10 (1979) 177.
[20] Y. Ishikawa, S. Onodera and K. Tajima, J. Magn. Magn. Mat. 10 (1979) 183.
[21] S. Onodera, Y. Ishikawa and K. Tajima, J. Phys. Soc. Jpn. 50 (1981) 1513.
[22] O. Steinsvoll, R.M. Moon, W.C. Koehler and C.G. Windsor, Phys. Rev. B 24 (1981) 4031.
[23] P.J. Brown, I.K. Jassim, R.M. Mankikar, Y. Nakamura and K.R.A. Ziebeck.
Proc. Int. Conf. on Magnetism, D. Givord, ed. (Les Éditions de Physique, Paris, 1989) p. 307.

THE INSTITUTE OF PHYSICS

Solid State Physics Division Committee

SOLID STATE PHYSICS CONFERENCE

20 - 22 December 1988

University of Nottingham

FP28

Magnetic and Thermal Properties of Transition Metal Heisenberg Antiferromagnets

I.K. Jassim, W. Hussen and K-U. Neumann
Physics Department
Loughborough University of Technology
Loughborough, Leics. LE11 3TU United Kingdom

ABSTRACT

The magnetic and thermal properties of transition metal antiferromagnets are presented. The compounds are based on the Heusler $L2_1$ structure, and provide good candidates for the study of localised antiferromagnetism in metallic systems. A strong coupling exists between the magnetic and lattice degrees of freedom and the symmetry of the lattice distortion below the Neel temperature is discussed in relation to the magnetic structure.